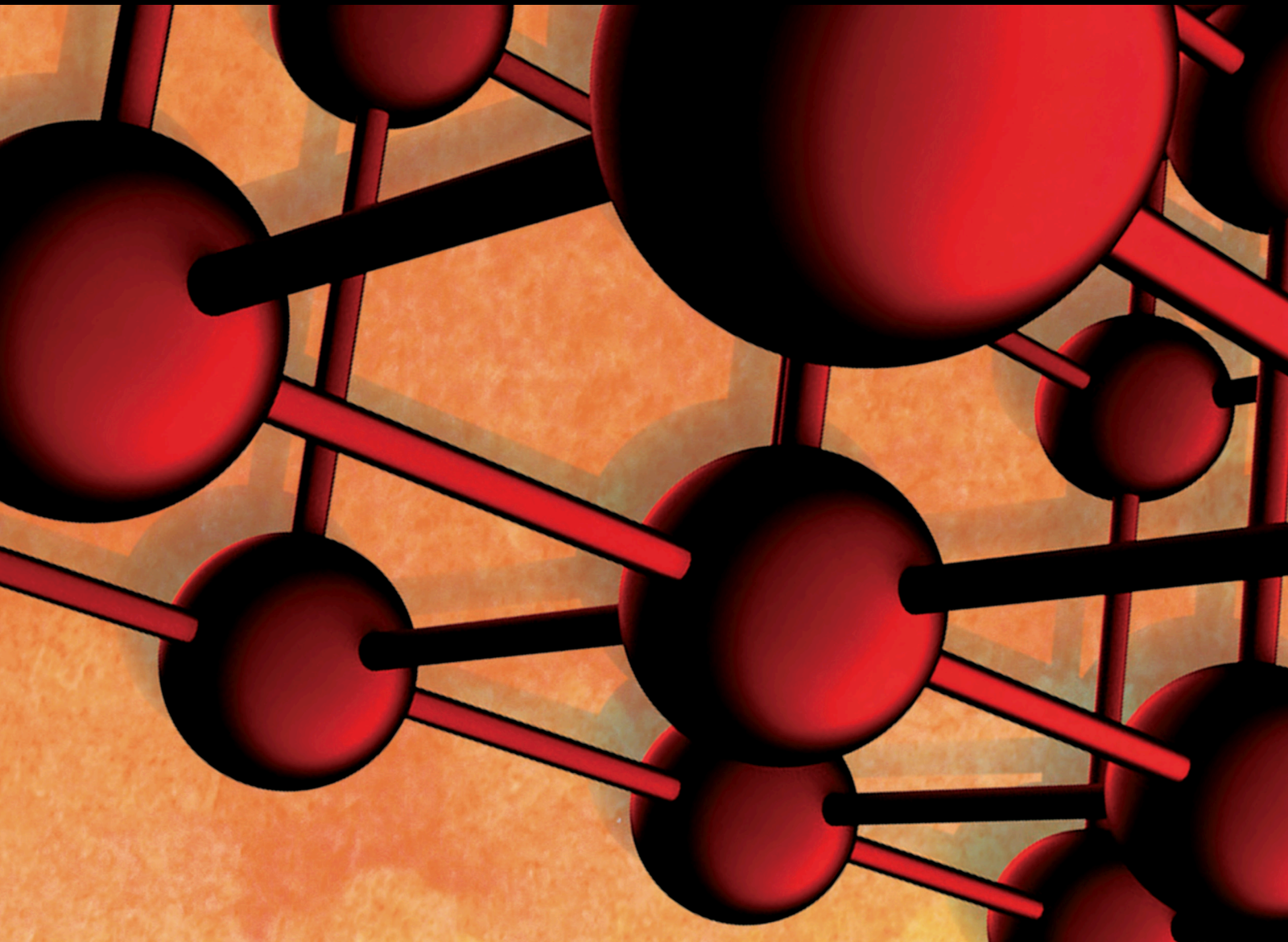


# Experimental and Numerical Investigations in Mechanical Machining of Fibre-Reinforced Composite Materials

Special Issue Editor in Chief: Jinyang Xu

Guest Editors: J. Paulo Davim, Mohamed El Mansori, and Vijayan Krishnaraj





---

**Experimental and Numerical Investigations  
in Mechanical Machining of Fibre-Reinforced  
Composite Materials**

Advances in Materials Science and Engineering

---

**Experimental and Numerical  
Investigations in Mechanical Machining  
of Fibre-Reinforced Composite  
Materials**

Special Issue Editor in Chief: Jinyang Xu

Guest Editors: J. Paulo Davim, Mohamed El  
Mansori, and Vijayan Krishnaraj



---

Copyright © 2021 Hindawi Limited. All rights reserved.

This is a special issue published in "Advances in Materials Science and Engineering." All articles are open access articles distributed under the Creative Commons Attribution License, which permits unrestricted use, distribution, and reproduction in any medium, provided the original work is properly cited.

# Chief Editor

Amit Bandyopadhyay, USA

## Editorial Board

Antonio Abate, Germany  
H.P.S. Abdul Khalil, Malaysia  
Michael Aizenshtein, Israel  
Hamed Akhavan, Portugal  
Jarir Aktaa, Germany  
Amelia Almeida, Portugal  
Rajan Ambat, Denmark  
Santiago Aparicio, Spain  
Raul Arenal, Spain  
Alicia E. Ares, Argentina  
Apostolos Avgeropoulos, Greece  
Renal Backov, France  
Markus Bambach, Germany  
Massimiliano Barletta, Italy  
Brahim Benmokrane, Canada  
Jamal Berakdar, Germany  
Jean-Michel Bergheau, France  
Guillaume Bernard-Granger, France  
Giovanni Berselli, Italy  
Patrice Berthod, France  
Michele Bianchi, Italy  
Hugo C. Biscaia, Portugal  
Antonio Boccaccio, Italy  
Heinz-Günter Brokmeier, Germany  
Steve Bull, United Kingdom  
Gianlorenzo Bussetti, Italy  
Jose M. Cabrera, Spain  
Antonio Caggiano, Germany  
Veronica Calado, Brazil  
Marco Cannas, Italy  
Qi Cao, China  
Gianfranco Carotenuto, Italy  
Paolo Andrea Carraro, Italy  
Victor M. Castaño, Mexico  
Michelina Catauro, Italy  
Robert Černý, Czech Republic  
Jose Cesar de Sa, Portugal  
Wensu Chen, Australia  
Daolun Chen, Canada  
Francisco Chinesta, France  
Er-Yuan Chuang, Taiwan  
Gianluca Cicala, Italy  
Francesco Colangelo, Italy  
Marco Consales, Italy

María Criado, Spain  
Lucas da Silva, Portugal  
J. Paulo Davim, Portugal  
Angela De Bonis, Italy  
Abílio De Jesus, Portugal  
José António Fonseca de Oliveira Correia, Portugal  
Luca De Stefano, Italy  
Francesco Delogu, Italy  
Luigi Di Benedetto, Italy  
Maria Laura Di Lorenzo, Italy  
Marisa Di Sabatino, Norway  
Luigi Di Sarno, Italy  
Ana María Díez-Pascual, Spain  
Guru P. Dinda, USA  
Nadka Tzankova Dintcheva, Italy  
Mingdong Dong, Denmark  
Hongbiao Dong, China  
Frederic Dumur, France  
Stanislaw Dymek, Poland  
Kaveh Edalati, Japan  
Philip Eisenlohr, USA  
Claude Estournès, France  
Luis Evangelista, Norway  
Michele Fedel, Italy  
Francisco Javier Fernández Fernández, Spain  
Isabel J. Ferrer, Spain  
Paolo Ferro, Italy  
Dora Foti, Italy  
Massimo Fresta, Italy  
Pasquale Gallo, Finland  
Germà Garcia-Belmonte, Spain  
Santiago Garcia-Granda, Spain  
Carlos Garcia-Mateo, Spain  
Georgios I. Giannopoulos, Greece  
Ivan Giorgio, Italy  
Antonio Gloria, Italy  
Vincenzo Guarino, Italy  
Daniel Guay, Canada  
Gianluca Gubbiotti, Italy  
Jenő Gubicza, Hungary  
Xuchun Gui, China  
Benoit Guiffard, France

Ivan Gutierrez-Urrutia, Japan  
Simo-Pekka Hannula, Finland  
Sandip Harimkar, USA  
Akbar Heidarzadeh, Iran  
David Holec, Austria  
Yue Hou, China  
David Houivet, France  
Yi Huang, United Kingdom  
Michele Iafisco, Italy  
Erdin Ibrahim, United Kingdom  
Saliha Ilican, Turkey  
Md Mainul Islam, Australia  
Ilia Ivanov, USA  
Hom Kandel, USA  
kenji Kaneko, Japan  
Fuat Kara, Turkey  
Akihiko Kimura, Japan  
Paweł Kłosowski, Poland  
Jan Koci, Czech Republic  
Lingxue Kong, Australia  
Ling B. Kong, Singapore  
Fantao Kong, China  
Prמוד Koshiy, Australia  
Hongchao Kou, China  
Alexander Kromka, Czech Republic  
Ravi Kumar, India  
Andrea Lamberti, Italy  
Luciano Lamberti, Italy  
Fulvio Lavecchia, Italy  
Marino Lavorgna, Italy  
Laurent Lebrun, France  
Joon-Hyung Lee, Republic of Korea  
Cristina Leonelli, Italy  
Ying Li, USA  
Yuanshi Li, Canada  
Yuning Li, Canada  
Guang-xing Liang, China  
Barbara Liguori, Italy  
Shaomin Liu, Australia  
Yunqi Liu, China  
Jun Liu, China  
Zhiping Luo, USA  
Fernando Lusquiños, Spain  
Peter Majewski, Australia  
Georgios Maliaris, Greece  
Muhamamd A. Malik, United Kingdom  
Dimitrios E. Manolakis, Greece

Necmettin Maraşlı, Turkey  
Enzo Martinelli, Italy  
Alessandro Martucci, Italy  
Bobby Kannan Mathan, Australia  
Roshan Mayadunne, Australia  
Mamoun Medraj, Canada  
Shazim A. Memon, Kazakhstan  
Philippe Miele, France  
Andrey E. Miroshnichenko, Australia  
Ajay Mishra, South Africa  
Hossein Moayedi, Vietnam  
Sakar Mohan, India  
Jose M. Monzo, Spain  
Alfonso Muñoz, Spain  
Roger Narayan, USA  
Rufino M. Navarro, Spain  
Miguel Navarro-Cia, United Kingdom  
Behzad Nematollahi, Australia  
Luigi Nicolais, Italy  
Peter Niemz, Switzerland  
Hiroschi Noguchi, Japan  
Dariusz Oleszak, Poland  
Laurent Orgéas, France  
Togay Ozbakkaloglu, United Kingdom  
Nezih Pala, USA  
Marián Palcut, Slovakia  
Gianfranco Palumbo, Italy  
Davide Palumbo, Italy  
Zbyšek Pavlík, Czech Republic  
Alessandro Pegoretti, Italy  
Gianluca Percoco, Italy  
Andrea Petrella, Italy  
Claudio Pettinari, Italy  
Giorgio Pia, Italy  
Silvia M. Pietralunga, Italy  
Daniela Pilone, Italy  
Teresa M. Piqué, Argentina  
Candido Fabrizio Pirri, Italy  
Marinos Pitsikalis, Greece  
Alain Portavoce, France  
Simon C. Potter, Canada  
Ulrich Prael, Germany  
Anjanapura V. Raghu, India  
Carlos R. Rambo, Brazil  
Baskaran Rangasamy, Zambia  
Manijeh Razeghi, USA  
Paulo Reis, Portugal

Yuri Ribakov, Israel  
Aniello Riccio, Italy  
Anna Richelli, Italy  
Antonio Riveiro, Spain  
Marco Rossi, Italy  
Pascal Roussel, France  
Fernando Rubio-Marcos, Spain  
Francesco Ruffino, Italy  
Mark H. Rummeli, China  
Pietro Russo, Italy  
F.H. Samuel, Canada  
Maria Gabriella Santonicola, Italy  
Hélder A. Santos, Finland  
Carlo Santulli, Italy  
Fabrizio Sarasini, Italy  
Michael J. Schütze, Germany  
Raffaele Sepe, Italy  
Mercedes Solla, Spain  
Donato Sorgente, Italy  
Charles C. Sorrell, Australia  
Andres Sotelo, Spain  
Damien Soulat, France  
Adolfo Speghini, Italy  
Antonino Squillace, Italy  
Koichi Sugimoto, Japan  
Baozhong Sun, China  
Sam-Shajing Sun, USA  
Shengwen Tang, China  
Youhong Tang, Australia  
Kohji Tashiro, Japan  
Miguel Angel Torres, Spain  
Laszlo Toth, France  
Achim Trampert, Germany  
Tomasz Trzpiecieński, Poland  
Matjaz Valant, Slovenia  
Luca Valentini, Italy  
Zhongchang Wang, Portugal  
Lijing Wang, Australia  
Jörg M. K. Wiezorek, USA  
Jiang Wu, China  
Guoqiang Xie, China  
Jinyang Xu, China  
Zhonghua Yao, China  
Yee-wen Yen, Taiwan  
Wenbin Yi, China  
Hao Yi, China  
Tetsu Yonezawa, Japan

Hiroshi Yoshihara, Japan  
Lenka Zajíčková, Czech Republic  
Zhigang Zang, China  
Michele Zappalorto, Italy  
Gang Zhang, Singapore  
Jinghuai Zhang, China  
Mikhail Zheludkevich, Germany  
Wei Zhou, China  
You Zhou, Japan  
Hongtao Zhu, Australia

# Contents

## **Experimental and Numerical Investigations in Mechanical Machining of Fibre-Reinforced Composite Materials**

Jinyang Xu , J. Paulo Davim, Mohamed El Mansori, and Vijayan Krishnaraj  
Editorial (1 page), Article ID 9780790, Volume 2021 (2021)

## **Experimental Study on Mechanical Properties of Interface between Basalt Fiber-Reinforced Polymer/Glass Fiber-Reinforced Polymer Composite Cement Plate and Concrete**

Lifeng Zhang , Hui Liu , Wenqiang Li , Hangjun Liu , Xuehui An , and Xiaoruan Song   
Research Article (13 pages), Article ID 6616898, Volume 2021 (2021)

## **Influence of Blade Profiles on Plastic Centrifugal Pump Performance**

Hui Zhang , Lingfeng Tang, and Yongtao Zhao  
Research Article (17 pages), Article ID 6665520, Volume 2020 (2020)

## **A Stochastic Model of Stress Evolution in a Bolted Structure in the Presence of a Joint Elastic Piece: Modeling and Parameter Inference**

Mohammed Haiek , Youness El Ansari , Nabil Ben Said Amrani , and Driss Sarsri   
Research Article (11 pages), Article ID 9601212, Volume 2020 (2020)

## **A Supporting Design Method When Longwall Face Strides across and Passes through a Roadway**

Weidong Pan, Xinyuan Li , YiWei Li, Xiaobin Li , Qing Qiao, and Haoran Gong  
Research Article (15 pages), Article ID 8891427, Volume 2020 (2020)

## **Optimized Polynomial Virtual Fields Method for Constitutive Parameters Identification of Orthotropic Bimaterials**

Xueyi Ma , Yu Wang, and Jian Zhao   
Research Article (27 pages), Article ID 2974723, Volume 2020 (2020)

## **The Influence of Blade Angle on the Performance of Plastic Centrifugal Pump**

Jun Li , Lingfeng Tang, and Yaoyao Zhang  
Research Article (20 pages), Article ID 7205717, Volume 2020 (2020)

## **Prediction of Tool Lifetime and Surface Roughness for Nickel-Based Waspaloy**

Shao-Hsien Chen  and Chung-An Yu  
Research Article (12 pages), Article ID 2013487, Volume 2020 (2020)

## Editorial

# Experimental and Numerical Investigations in Mechanical Machining of Fibre-Reinforced Composite Materials

Jinyang Xu <sup>1</sup>, J. Paulo Davim,<sup>2</sup> Mohamed El Mansori,<sup>3</sup> and Vijayan Krishnaraj<sup>4</sup>

<sup>1</sup>School of Mechanical Engineering, Shanghai Jiao Tong University, Shanghai 200240, China

<sup>2</sup>Department of Mechanical Engineering, University of Aveiro, Campus Santiago, Aveiro 3810-193, Portugal

<sup>3</sup>MSMP-EA 7350, Arts et Métiers ParisTech, Châlons-en-Champagne 51006, France

<sup>4</sup>Department of Production Engineering, PSG College of Technology, Coimbatore 641004, India

Correspondence should be addressed to Jinyang Xu; [xujinyang@sjtu.edu.cn](mailto:xujinyang@sjtu.edu.cn)

Received 19 July 2021; Accepted 19 July 2021; Published 15 August 2021

Copyright © 2021 Jinyang Xu et al. This is an open access article distributed under the Creative Commons Attribution License, which permits unrestricted use, distribution, and reproduction in any medium, provided the original work is properly cited.

The emergence of fibre-reinforced composites can be regarded as a significant breakthrough in the development era of new materials in human society. This can be seen by their substantial impact on the material distribution in diverse industrial fields due to their superior mechanical/physical properties and excellent structural functionality. To meet the eventual application requirements, machining operations such as turning, milling, and drilling are frequently used to precisely fabricate these fibrous composites. Despite their widespread applications, composite materials are quite difficult to cut due to their anisotropic behaviour and heterogeneous architecture. Particular issues are associated with severe defect formation, rapid tool wear progression, and short tool life, resulting in a large number of composite part rejections. To solve fundamentally the technical issues, experimental and theoretical investigations concerning the composite cutting mechanisms, surface quality issues, and wear control are of vital importance.

The objective of this special issue is to report on the newest studies in the field of various machining processes for fibre-reinforced composites covering a variety of aspects, including the physical modelling of force and heat generation, optimization of process parameters, damage detection, and wear control. High-quality papers were rigorously selected to integrate the present issue that emphasizes the need, interest, and importance of this topic. It is hoped that

the contributions collected in this special issue can provide readers with a good overview of the advances achieved in the machining of fibre-reinforced composite materials. We also wish that the publication of this special issue can motivate more scholars to work in this highly promising and challenging research field.

### Conflicts of Interest

The Guest Editors declare that there are no conflicts of interest involved in this special issue.

### Acknowledgments

The editors would like to thank all authors and contributors who submitted their high-quality work for consideration in this special issue. The editors also want to express their gratitude to the reviewers for their dedicated support during the review process by providing constructive comments to improve the quality of the papers in a timely manner.

Jinyang Xu  
J. Paulo Davim  
Mohamed El Mansori  
Vijayan Krishnaraj

## Research Article

# Experimental Study on Mechanical Properties of Interface between Basalt Fiber-Reinforced Polymer/Glass Fiber-Reinforced Polymer Composite Cement Plate and Concrete

Lifeng Zhang <sup>1</sup>, Hui Liu <sup>1</sup>, Wenqiang Li <sup>1</sup>, Hangjun Liu <sup>1</sup>, Xuehui An <sup>2</sup>,  
and Xiaoruan Song <sup>3</sup>

<sup>1</sup>Power China Road Bridge Group, Beijing 100048, China

<sup>2</sup>School of Civil Engineering, Tsinghua University, Beijing 100084, China

<sup>3</sup>Department of Civil Engineering, North China University of Technology, Beijing 100144, China

Correspondence should be addressed to Hui Liu; [lqliuhui@powerchina.cn](mailto:lqliuhui@powerchina.cn) and Xiaoruan Song; [sxr@ncut.edu.cn](mailto:sxr@ncut.edu.cn)

Received 29 October 2020; Revised 22 December 2020; Accepted 3 March 2021; Published 17 March 2021

Academic Editor: Jinyang Xu

Copyright © 2021 Lifeng Zhang et al. This is an open access article distributed under the Creative Commons Attribution License, which permits unrestricted use, distribution, and reproduction in any medium, provided the original work is properly cited.

The bonding behaviors of the plate-concrete interface of a composite structure consisting of a concrete block in the middle and two cement plates at both sides play a key role in its overall mechanical performance. In this paper, the authors conduct 3 groups of push-out shear tests on a total of 39 composite samples to assess the bonding performance. The influence of the FRP cement plates, the concrete strength, and the ribs installed in the cement plate on the interfacial shear strength, the relative bond-slip, strain, and the failure modes of the composite samples is recorded and analyzed. The results show that (1) the shear strength and bond-slip performance of the interface are largely improved if the GFRP/BRRP cement plates are used; (2) shear strength of the interface increases with the concrete strength, while the deformation behaviors show no significant improvement; (3) an inclusion of the ribs to the interface enhances the shear strength and shear stiffness but decreases the maximum relative slip at failure; (4) most of the samples present the shear failures along the interface; however, the bending shear failure prior to the interface shear failure is also observed on the concrete block for low concrete strength samples and the samples with ribs; and (5) regression method is used to develop a constitutive model of the stress-slip at the interface to describe the relationship between the shear strength with the cement plates, the concrete strength, and ribs.

## 1. Introduction and Background

The fiber-reinforced polymer (FRP) material has become one of the most popular construction materials and has been widely used in civil engineering in recent years [1, 2]. As compared to traditional materials, the FRP material has higher strength, lighter weight, easier construction procedures, and more reliable performance. Of the FRP materials, the glass fiber-reinforced polymer (GFRP) and the basalt fiber-reinforced polymer (BFRP) are two of the most commonly used fiber materials. The lightweight GFRP has a long service life, good corrosion resistance, and many other advantages. The electric-insulating BFRP also shows good resistance to corrosion as well as to high temperature [3, 4]. Both the two types of new FRP materials have become the

most important materials in structure strengthening engineering [5, 6].

This paper has utilized the BFRP/GFRP materials for the construction of a composite structure. The composite structure consists of a concrete block in the middle and two FRP reinforced cement plates at both sides (see Figure 1). The cement plate is reinforced with the fiber mesh and can be used as a permanent mold/plate. The concrete is poured between the two permanent plates during construction; thus, a composite structure is easily created. As compared to the traditional cement plates, the permanent composite plate offers advantages in terms of the overall costs, the construction period, and materials saving including steel, wood, and bamboo. It also saves demolding operations and transportation cost. As a composite structure, both the

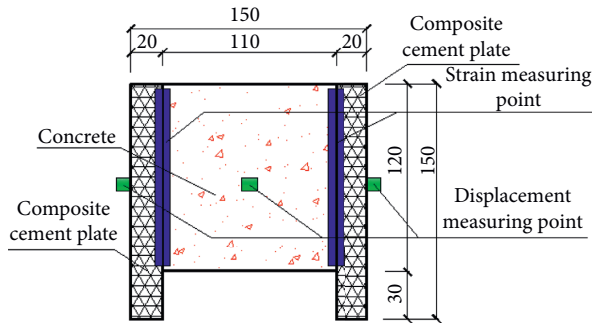


FIGURE 1: A schematic of the composite sample showing the structure and geometry.

middle concrete and the reinforced composite cement plates at two sides can sustain loads, and therefore, the overall mechanical performance is improved. However, the bonding performance between the reinforced permanent plates and concrete becomes the major concern for this composite structure.

From the field application of the composite structures, it is observed that the early separation of the FRP reinforced cement plates from the concrete block greatly impairs the load-bearing capacity of the composite structure. Therefore, extensive studies have been made to investigate the bonding behaviors of the concrete-plate interface. Ma et al. performed the simple shear tests to study the bonding properties of a concrete beam reinforced by CFRP sheets under the cyclic loading condition [7]. They found that the length and thickness of the CFRP sheets and the concrete grade have a major impact on the bonding between the CFRP sheets and the concrete and that a larger loading rate reduces the fatigue endurance of the interface. Chen et al. reinforced the manually precracked single trabeculae by attaching FRP sheets on its sides and tested the bonding performance [8]. The influence of dimensions of the FRP sheets and the applied loading conditions were included in their work. Nanni et al. studied the interfacial bonding performance of the interface between FRP reinforced laminated plates and the middle concrete and found that the stiffness of the laminated plate significantly impacts the failure load of the interface [9]. Nakaba et al. proposed a constitutive model to describe the relationship between the local bond stress and the slip at the interface between the FRP reinforced laminated plate and the concrete based on a number of double shear tests [10]. Li et al. performed the simple shear tests on the concrete samples with embedded CFRP sheets [11]. The length of the embedding CFRP sheets was found to have a great influence on the bonding behaviors.

Other researchers improved the bonding performance of the composite structures by material modification and the connection modes at the interface. Gravina et al. investigated the bonding behavior between the FRP laminated sheets preimpregnated with resin [12]. The resin was also used for concrete modification and the thickness of the bonding interface was included in their experiment to study the adhesive performance of the composite structure. The material modification can improve the bonding force. Zhou et al. improved

the bonding properties of the composite structure by increasing the mechanical fastening pressures between the FRP-concrete interfaces [13]. Chen et al. designed a horizontal slot at the interface to improve the bonding and deformation capacity of the composite structure [14]. Studies on the endurance of the interface were also documented in previous works. Wang et al. concluded that the bonding force between the FRP plates and the concrete was reduced when subjected to water, seawater, high temperature, the cyclic damp heat condition, and the corrosion under acid and alkali conditions [15]. They found from their tests that the high temperature presented worse deterioration to the interface properties than the low temperature and the presence of mortar joint in the composite structure further reduced the bonding capacity of the interface. The endurance of the composite structure interface under the extreme weather and loading conditions was included in Wang et al. [16].

The bonding between the FRP cement plates and the concrete is the key factor largely determining the overall performance of the composite structures. A number of researchers have developed the constitutive models to describe the bonding stress and slip deformation at the interface. Lin and Cao investigated the bonding performance at the pure bending section of the CFRP concrete structure and developed an analytical model to describe the bond and slip behaviors at the interface [17]. Woo and Yun conducted the pull-out tests to composite structures with CFRP sheets attaching to the concrete and developed their constitutive model from back analysis [18]. Baky et al. and Dai et al. analyzed the seismic performance of an FRP reinforced dam using a nonlinear bond-slip model [19, 20]. Wang et al. updated their constitutive model based on a beam test on the CFRP composite structures [21]. Gao et al. proposed a continuous curved bonding-slip model based on a summary of the previous constitutive models [22]. Lu et al. developed a bonding-slip constitutive model with a consideration of the interface stiffness [23]. The model was used to predict the separation of the interface. Ko et al. conducted the double shear tests on 18 composite samples to investigate the bonding between the GFRP sheets and the concrete, based on which a bilinear stress-slip model was proposed [24]. Hao et al. performed the pull-out tests to study the bonding between the steel strand and the concrete on 180 samples, with a consideration of the placement of the strand and the dimensions of the concrete [25]. They improved their bonding-slip constitutive model based on the experimental results.

The previous studies have improved our understandings of the bonding performance of the composite structures between the FRP materials and the concrete. However, the CFRP and GFRP sheets rather than the FRP cement plates were used for most of the composite structures in previous works. This paper attempts to evaluate the bonding performance between the BFRP/GFRP reinforced cement plates and the concrete block with a consideration of the types of the fiber mesh, the concrete grade, and the inclusion of steel ribs in the cement plates. Three sets of experiments were designed and were used to conduct the push-out tests in the present work. The first set compares the bonding performance of the composite structures with three different cement

plates, that is, the regular cement plates for the GS samples, the BFRP reinforced plates for the GB samples, and the GFRP reinforced plates for the DG samples. The second set consists of different composite structures made of the C15, C30, and C50 concrete. The third set includes the composite samples with and without ribs to investigate the influence of the mechanical interaction at the interface. The failure characteristics of the composite samples and the relation between the shearing capacity and the slip deformation at the interface were recorded. The shearing strength as a function of the slip deformation was obtained using the regression approach. The results from this paper may provide a reference for improving the bonding performance and promoting the industrial applications of the composite structures.

## 2. Experiment Design

**2.1. Sample Preparation.** In this research, the push-out shear test is performed to study the influence of the fiber-reinforced cement plate, concrete strength, and ribs in the plate on the bonding performance of the plate-concrete interface. Figure 1 gives a front view of the composite structure. The cement plate at both ends is 20 mm thick, 150 mm high, and 150 mm long, and the middle concrete body is 110 mm thick, 120 mm high, and 150 mm long. Therefore, the overall dimension of the composite specimen prepared in this study is  $150 \times 150 \times 150$  mm. Efforts were made during the sample construction to make sure that all specimens have the same size. The concrete is poured 30 mm above the bottom; thus, the push-out shearing test can be performed.

The cement plate is constructed using cement, fly ash, expanded perlite, sand, water reducing agent, and coupling agent with a proportion of 1 : 0.25 : 0.015 : 0.15 : 0.007 : 0.015 by weight. During construction, the GFRP plate uses low alkalinity cement while the BFRP plate uses the Portland cement [26]. Fiber meshes are placed on both side surfaces of the plate. The fiber meshes used in the GFRP and BFRP plates have the same density ( $160 \text{ g/m}^2$ ).

The construction of the BFRP and GFRP composite samples includes three procedures: (1) preparation of the experimental mold and cement slabs; (2) concrete pouring between the composite cement plates; and (3) sample curing at room temperature for 28 days. For ease of demolding, the inner surface of the mold was cleaned and coated with lubricating oil before pouring. Two pieces of cement plates are placed at both sides of the mold, and a 30 mm thick foam block is placed at the bottom between the two plates for reserving space for the later push-out test. The foam is tightly pressed on cement plates to prevent slurry leakage. The concrete is poured at a designed strength (i.e., C15, C30, and C50 in this study) for comparing the concrete strength influence on the bonding behaviors of the plate-concrete interface. After demolding, the composite samples are cured for a period of 28 days at room temperature.

**2.2. Loading Condition and Data Measuring System.** The push-out shearing test is performed on a compression testing machine. Figure 2 plots the loading condition of the

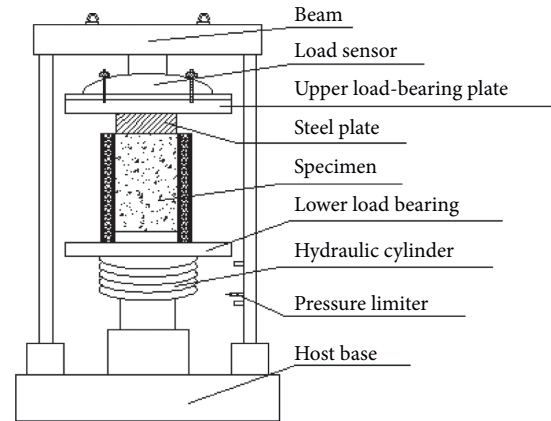


FIGURE 2: A schematic of the loading condition of the composite sample.

composite sample. The composite sample is placed between the upper and lower bearing plates. A steel plate slightly less than 110 mm wide is put between the upper bearing plate and the sample for performing the push-out shearing test. The test is ceased when the sample is damaged.

The bonding performance of the plate-concrete interface (including the shear strength and relative bond-slip) is the major concern of this study. The layout of the measuring points is also shown in Figure 1. A total of 3 displacement measuring points can be found on the left and right sides of the two plates and on the front surface of the concrete body, respectively. The relative slip of the plate-concrete interface can therefore be obtained. The strain data of the interface, however, were measured by 2 strain gauges placed at the plate-concrete boundaries. The testing machine (type SANS) is used to load, the sensor (type CFBLY) is used to record the load data, and the data acquisition system (type BETC) is used to collect data. The shear stress, relative movement, and strain data of the interface are recorded during the test. The failure characteristics and development of fractures on the sample are also observed by a camera.

**2.3. Material Strength Test.** In the process of making specimens, the concrete samples with different strength grades are reserved, which are  $150 \text{ mm} \times 150 \text{ mm} \times 150 \text{ mm}$ . The ordinary plain cement board samples, BFRP reinforced cement composite board samples, and GFRP reinforced cement composite board samples are all reserved for material mechanics tests, which are  $20 \text{ mm} \times 250 \text{ mm} \times 250 \text{ mm}$ . The compressive strength of concrete is shown in Table 1. The flexural strength of the cement board is shown in Table 2.

## 3. Results and Analysis

**3.1. Effect of Fiber Mesh Type on Interface Bonding Performance.** As mentioned above, the inclusion of fiber mesh in the cement plate and its type should influence the bonding performance of the plate-concrete interface. Therefore, the first group of tests compares the influence of three kinds of cement plates, that is, the plain Portland

TABLE 1: The 28-day compressive strength of concrete.

Concrete type	Average compressive strength (MPa)
C15	15.3
C30	31.1
C50	51.2

TABLE 2: The flexural strength of cement board.

Cement board type	Average flexural strength (MPa)
Plain cement board	5.4
BFRP reinforced cement composite board	12.1
GFRP reinforced cement composite board	12.3

cement plate without fiber reinforcement (GS); BFRP reinforced ordinary Portland composite cement plate (GB), and GFRP reinforced low alkalinity composite cement plate (DG). All the three sets of composite specimens utilize C30 for the middle concrete during the sample preparation. In each set, 3 samples are prepared. Therefore, the total number of samples in this group is 9. The samples are assigned with different numbers for better analysis. Sample GS C30-1, for instance, represents the first sample with the GS cement plates on both sides and C30 middle concrete.

**3.1.1. Failure Modes of Specimens.** Figure 3 shows the failure characteristics of the samples after the shear test. It is found that all 3 GS samples present brittle failure (see Figure 3(a)). Of those, samples GS C30-1 and GS C30-3 show both shear failure along the interface and failure on the cement plate, and sample GS C30-2 only finds brittle failure and fractures on the cement plate. All the failures occur on the relatively weak side of the sample. For the 3 GB samples, the shear failure along the interface is found on both GB C30-2 and GB C30-3 samples, while GB C30-1 sees failure in the concrete body (Figure 3(b)). By contrast, all three DG composite samples see shear failure along the interface (Figure 3(c)) and separations between the cement plates and the concrete are observed.

The shearing test reveals that the fiber-reinforced composite sample fails along the plate-concrete interface prior to the cement plate, indicating that the overall load-bearing capacity of the cement plate is largely improved by the fiber materials. The bonding performance of the interface is also enhanced for the fiber-reinforced samples as compared to the nonfiber samples and the interfacial shear strength of the fiber-reinforced sample is even higher than that of C30 concrete itself.

**3.1.2. Shear Strength of the Interface.** Table 3 compares the shear strength of the plate-concrete interface for the composite samples with different fiber-reinforced cement plates. The shear strength of the nonfiber composite sample (GS samples) is noticeably lower than the fiber-reinforced samples. The mean value of the shear strength for the GS samples is 0.64 MPa, which is only 63.63% and 55.77% of the

GB (1.00 MPa) and DG (1.14 MPa) composite samples, respectively. Hence, the fiber mesh significantly improves the shear strength of the plate-concrete interface. It is also noted that DG composite samples with GFRP cement plates have a slightly larger shearing performance than the GB samples with BFRP plates.

**3.1.3. Relative Bond-Slip of the Interface.** Table 4 lists the maximum relative slip of the plate-concrete interface with different fiber meshes. The average displacement values of the GS, GB, and DG composite samples are 0.27, 0.54, and 0.45 mm, respectively. Therefore, the composite samples with fiber-reinforced plates allow a larger relative displacement on the plate-concrete interface compared to the composite samples with nonfiber plates.

Figure 4 plots the relationship of the shearing stress over the relative displacement. It shows that the shearing stresses of the GB and DG composite samples increase at a large and similar rate. The fast growth of shearing stresses ends when the relative displacement is about 0.14 mm. The stresses then reach a plateau and only increase slightly over a large displacement; that is, the interface of the fiber-reinforced samples shows plastic deformation characteristics. The slope of the curve for the GS sample, however, is much lower. Therefore, the fiber-reinforced cement plate also improves the deformation performance of the interface.

**3.1.4. Shearing Stress-Strain Relationship of the Interface.** Table 5 summarizes the maximum and mean strain values of the interface for the 3 sets of samples. It shows that the mean strain value of GS C30 samples is only 10.6% of GB C30 and 18% of DG C30 samples. The mean maximum strain of GB C30 samples is 1.7 times that of DG C30 specimen.

The shearing stress-strain curve is given in Figure 5. An approximately linear relationship is observed between the stress and strain for all the three sets of samples. It can also be found from the curves that the GB and DG samples show some plastic behaviors at the later stage, which corresponds to the stress-displacement curves.

**3.2. Effect of Concrete Strength on Interface Bonding Performance.** The bonding performance of the plate-concrete interface is also influenced by the concrete strength. The composite samples in this group use C15, C30, and C50 for middle concrete, respectively. The cement plates at both sides are BFRP reinforced ordinary Portland composite cement plate (GB) and GFRP reinforced low alkalinity composite cement plate (DG). Therefore, this group of experiments prepares 6 sets of tests with 18 samples in total. Each sample is assigned a unique number. For instance, the composite structure with BFRP cement plates and C15 concrete has 3 samples, that is, GB C15-1, GB C15-2, and GB C15-3.

**3.2.1. Failure Modes of Specimens.** Figure 6 gives the fracture development and failure characteristics of the samples after the test. Note that the GB C30 and DG C30 samples have

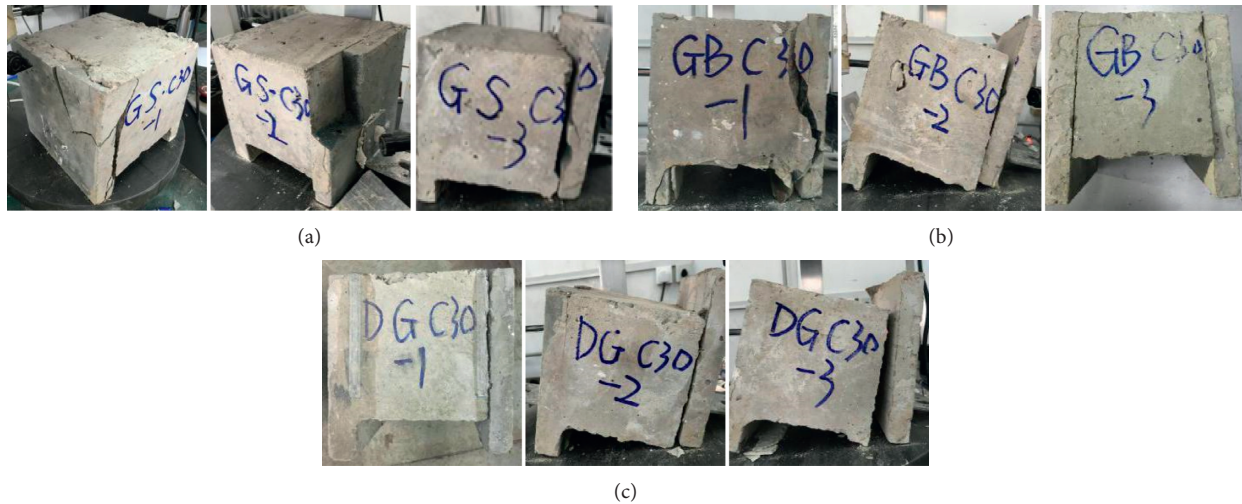


FIGURE 3: Failure characteristics of the composite samples after the shear test: (a) GS C30, (b) GB C30, and (c) DG C30.

TABLE 3: A summary of the shear load at failure and shear strength of the plate-concrete interfaces for samples with different cement plates.

Composite sample	Maximum load at failure, kN			Average	Shear strength, MPa
	Sp1	Sp2	Sp3		
GS C30	24.33	20.84	23.75	22.97	0.64
GB C30	41.30	30.89	36.72	36.10	1.00
DG C30	42.07	40.31	42.60	41.19	1.14

TABLE 4: The maximum relative bond-slip of the plate-concrete interfaces at failure for composite samples with different cement plates.

Composite sample	Maximum relative displacement at failure, mm			
	Sp1	Sp2	Sp3	Average
GS C30	0.257	0.276	0.265	0.266
GB C30	0.537	0.548	0.541	0.542
DG C30	0.442	0.474	0.434	0.450

been included in Figure 3. Thus, Figure 6 only shows the results of the C15 and C30 samples. It is observed that most of the GB samples see shear failure along the interface, except the GB C30-1 and GB C50-3 with failures also observed on the concrete body. GB C30-1 finds failure on both the cement plate and the middle concrete rather than fails in shear along the interface (Figure 3(b)). The GB C50-3 sample, however, finds tensile damage on top of the sample beside the shear failure along the interface (Figure 6(b)).

By comparison, the DG samples show different failure modes. Samples DG C15-1 and C15-3 find tensile failure in the middle concrete due to bending (see Figure 6(c)). The fracture initiates from the bottom of the concrete and extends upwards. Sample DG C15-2, however, sees the common shear failure along the plate-concrete interface; that is, the middle concrete separates from the cement plate when the limit relative displacement is reached. Likewise, all

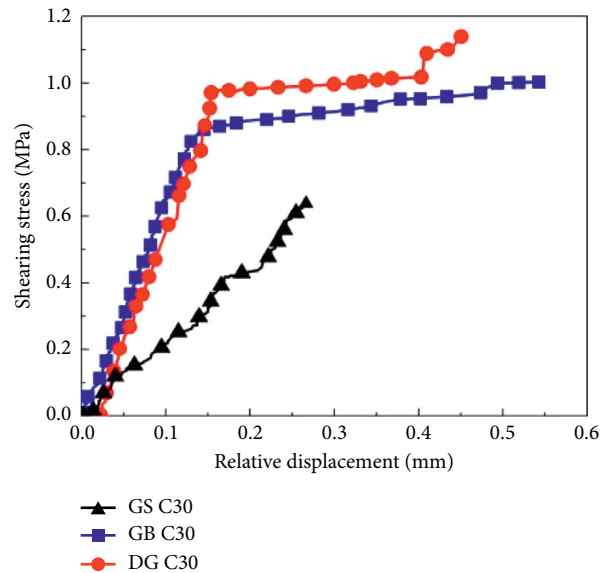


FIGURE 4: Relationship of the shearing stress over the relative displacement of the interface.

TABLE 5: The maximum strain of the interface at failure for composite samples with different cement plates.

Composite sample	Maximum strain, $\mu\epsilon$			
	Sp1	Sp2	Sp3	Average
GS C30	32.5	28.6	27.1	29.4
GB C30	289.4	257.8	282.6	276.4
DG C30	168.5	157.3	162.6	162.8

the DG C30 and C50 samples fail in shear along the concrete-plate interface (see Figures 3(c) and 6(d)). The DG C50-3 sample shows a slightly different failure mode, although with the fracture first developing along the interface and then extending to the concrete before cutting through the entire sample.

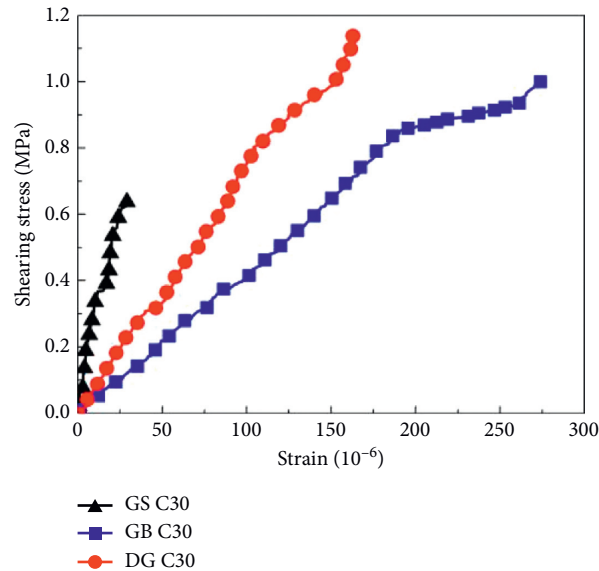


FIGURE 5: Stress-strain curves of the interface for composite samples with different cement plates.



FIGURE 6: Failure characteristics of the composite samples after the shear test: (a) GB C15, (b) GB C50, (c) DG C15, and (d) DG C50.

From the above analysis, we learn that most of the failure occurs in shear along the interface. However, it is also interesting to note that bending shear failure in concrete is observed for Samples DG C15-1 and C15-3, and compression shear failure on both cement plate and concrete is found in Sample GB C30-1. In other words, failure in the concrete or cement plate may occur prior to the interfacial shear failure, indicating that the shear strength of the interface may be larger than the cement plate and the concrete body, especially when the concrete strength is low (say, the C15 samples).

**3.2.2. Shear Strength of the Interface.** Table 6 compares the shear strength of the composite samples with different cement plates and concrete. It shows that the shear strength of the interface increases with the concrete strength for

both GB and DG samples. For instance, the shear strength for GB C50 sample is 1.43 MPa, which is 1.43 times the GB C30 sample (1.00 MPa) and 2.46 times the GB C15 (0.58 MPa). By contrast, maximum shear strength is found at 1.36 MPa for DG C50, compared to 1.14 MPa for DG C30 and 0.56 MPa for DG C15. On the other hand, the GB and DG samples show no significant discrepancy in the interfacial shear strength when the same middle concrete is used.

**3.2.3. Relative Bond-Slip of the Interface.** The maximum relative bond-slip along the concrete-plate interface is provided in Table 7. It is noticed that the relative displacement of the interface shows no significant difference. This differs from the positive relationship between the shear strength and the concrete strength.

TABLE 6: A summary of the maximum shear load at failure and shear strength of the plate-concrete interfaces for composite samples with different cement plates and concretes.

Cement plate	Concrete	Maximum load at failure, kN				Average	Shear strength, MPa
		Sp1	Sp2	Sp3			
GB	C15	19.56	22.18	18.74	20.16	0.58	
	C30	41.30	30.89	36.72	36.10	1.00	
	C50	52.16	50.83	51.12	51.37	1.43	
DG	C15	20.01	21.38	21.28	20.98	0.56	
	C30	42.07	40.31	42.60	41.19	1.14	
	C50	48.79	51.23	47.01	49.07	1.36	

TABLE 7: The maximum relative bond-slip of the plate-concrete interfaces at failure for composite samples with different cement plates and concretes.

Cement plate	Concrete	Maximum relative displacement at failure, mm				Average
		Sp1	Sp2	Sp3		
GB	C15	0.478	0.485	0.513	0.492	
	C30	0.537	0.546	0.543	0.542	
	C50	0.516	0.528	0.516	0.520	
DG	C15	0.487	0.499	0.514	0.500	
	C30	0.463	0.451	0.436	0.450	
	C50	0.477	0.469	0.485	0.477	

Figure 7 plots the shearing stress-relative displacement curves for composite samples with different cement plates and concretes. The deformation behavior along the interface shows different characteristics for samples with different concrete strength, although the maximum relative displacements are generally the same. It shows that the shearing stress for C30 and C50 samples increases rapidly at the early stage of loading, which means the samples pick up the shear load quickly but at a small displacement. After the relative displacement reaches about 0.14 mm, the C30 and C50 samples reach a plateau and show clear plastic deformation behavior, with a large amount of displacement but a small increase in shearing stress. By comparison, the C15 sample shows an approximately linear relationship between the shearing stress and the displacement. It is also observed from the slope of the curves that the overall shearing stiffness of the composite samples is increased with the increase of concrete strength.

### 3.2.4. Shearing Stress-Strain Relationship of the Interface.

Table 8 gives the maximum and mean values of the interface strain. Figure 8 shows the shearing stress-strain curves. It is observed that the interfacial shearing stiffness and deformation performance for both GB and DG samples are increased with enhanced concrete strength. In particular, the C50 samples show obvious plastic displacement behavior at the late stage of loading. The maximum strain, however, does not show a specific relationship with relation to the concrete strength. This is consistent with the results of the interface slip test, which shows that the interface deformation properties can also be reflected by measuring the interfacial strain.

3.3. *Effect of Rib on Interface Bonding Performance.* The addition of ribs in the cement plate and its layout are also influential to the bonding performance of the plate-concrete interface. The authors have designed cement plates with horizontal (HL) and vertical (ZL) ribs, which are compared to the nonrib samples (WL). The rib is 10 mm in width and 5 mm in height. A total of 2 ribs are symmetrically placed in the cement plate with a spacing of 100 mm. During construction, the BFRP (GB) and GFRP (DG) materials are used for cement plates and C30 for concrete. The sample ID is assigned to each sample. Sample GB HL-1 represents the first sample with BFRP cement plate and HL rib.

3.3.1. *Failure Modes of Specimens.* Figure 9 plots the failure characteristics of the samples after the test. All the 3 GB HL samples see shear failure near the plate-concrete interface in both the cement plate and the concrete (Figure 9(a)). This differs from the smooth shear failure of the interface and complete separation of the plate and concrete for the WL samples. The GB ZL samples also see shear failure along the plate-concrete interface (Figure 9(b)). However, fractures extend towards the middle concrete and damage is found in the concrete at top of the sample, especially for the GB ZL-3 sample.

Shear failure along the interface is observed for Samples DG HL-1 and DG HL-2 (Figure 9(c)). The middle concrete for Sample DG HL-1 also sees shear failure near the failure interface side at the top. DG HL-3, however, fails in bending shear in the concrete. The bending shear crack initiates from the bottom and extends upward to the top surface, but the interfaces on both sides still remain intact. Similar to the GB ZL samples, the DG ZL samples find shear failure along the interface and splitting failure on the concrete at the top.

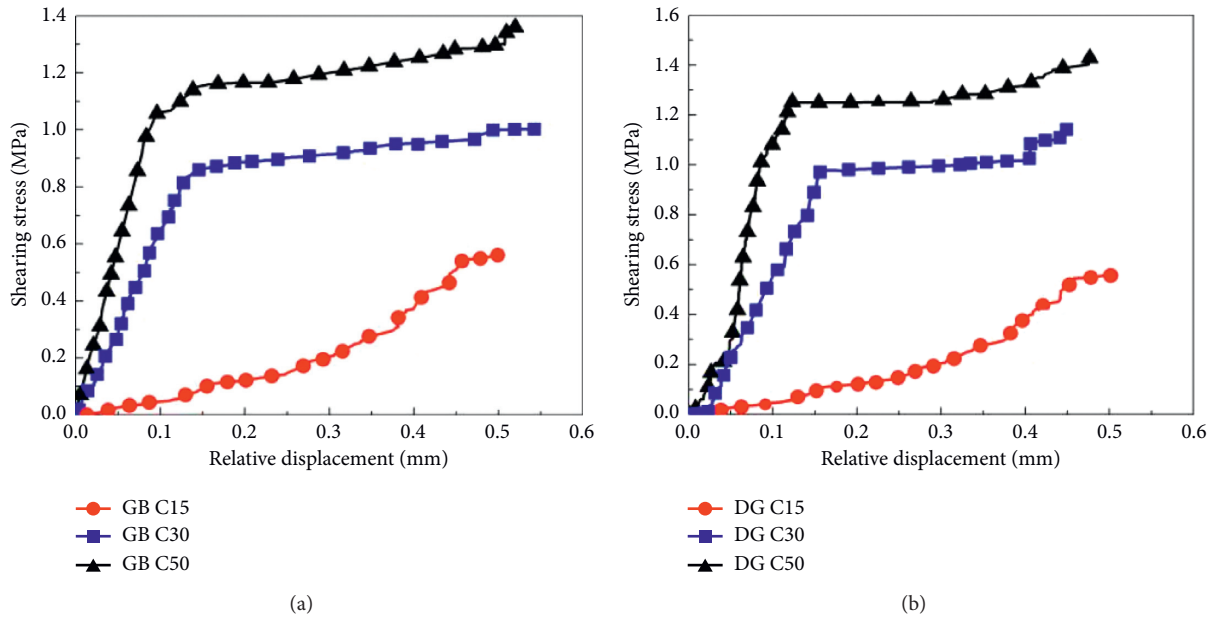


FIGURE 7: Relationship of the shearing stress over the relative displacement of the interface: (a) GB and (b) DG.

TABLE 8: Maximum strain of the interface at failure for composite samples with different cement plates and concretes.

Cement plate	Concrete	Maximum strain, $\mu\epsilon$			Average
		Sp1	Sp2	Sp3	
GB	C15	118.7	136.5	106.0	120.4
	C30	289.4	257.8	282.6	276.4
	C50	231.5	219.3	233.5	228.1
DG	C15	187.3	210.2	198.9	198.8
	C30	168.5	157.3	162.6	162.8
	C50	254.3	259.4	259.7	257.8

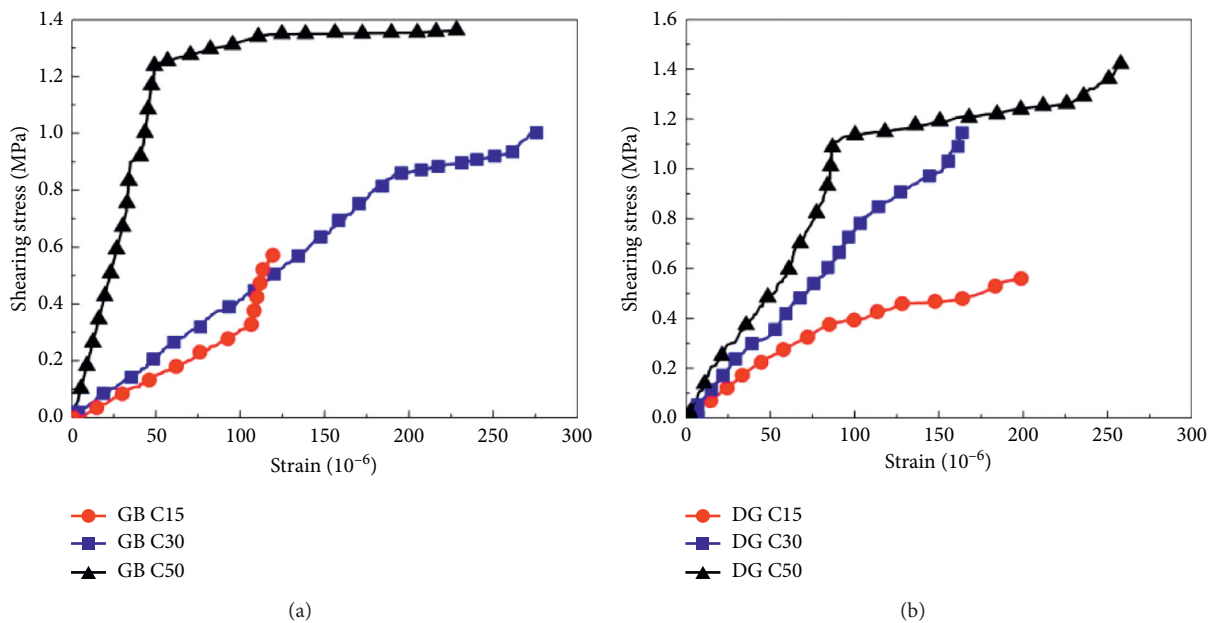


FIGURE 8: Stress-strain curves of the interface for composite samples with different cement plates and concretes: (a) GB and (b) DG.



FIGURE 9: Shear fracture of cement plate and concrete composite specimens with different ribs: (a) GB HL, (b) GB ZL, (c) DG HL, and (d) DG ZL.

Sample DG ZL-3, however, shows an inclined compression shear failure mode with a 45° fracture (in relation to the interface) developing upward obliquely from the bottom edge (Figure 9(d)).

**3.3.2. Shear Strength of the Interface.** Table 9 summarizes the maximum shear load of the interface and the shear strength at failure. It is obvious that the samples with ribs in the plate present much larger shear strength than the nonrib ones. The shear strength values for the rib samples almost double those for the nonrib. This is because the presence of ribs in the cement plate not only increases the bonding area but also improves the load transmission between the cement plate and the concrete. The ribs provide extra mechanical interaction at the interface rather than the pure friction for WL samples. Therefore, the ribbed samples are more reliable.

It is also noted that the samples with HL ribs have better interface bonding performance compared to the samples with ZL ribs. The HL ribs play a more important part than the ZL ribs in improving the mechanical interaction at the interface.

**3.3.3. Relative Bond-Slip of the Interface.** The maximum relative bond-slip of the interface is listed in Table 10 and the curve of the interfacial shear stress-relative displacement is shown in Figure 10. It can be seen that, due to the mechanical interlocking between the rib and the concrete, not only is the interfacial shear bearing capacity of the composite samples increased, but also the interfacial shear stiffness of the composite samples is greatly increased, the HL rib samples present the largest shearing stiffness. The maximum interface slip of the samples after being ribbed is significantly reduced. The sample with HL ribs has the lowest relative displacement, followed by the ZL rib sample and the WL sample. It is also observed that no plastic deformation behavior is found for the rib samples.

TABLE 9: Maximum load at failure and the shear strength of the interface for composite samples with different ribs.

Cement plate	Rib	Maximum load at failure, kN				Shear strength, MPa
		Sp1	Sp2	Sp3	Average	
GB	HL	84.10	83.88	83.78	83.92	2.33
	ZL	75.40	72.89	76.23	74.84	2.08
	WL	41.30	30.89	36.72	36.10	1.00
DG	HL	90.01	89.62	87.55	89.06	2.47
	ZL	76.34	79.21	76.86	77.47	2.15
	WL	42.07	40.31	42.60	41.19	1.14

TABLE 10: Maximum relative bond-slip of the plate-concrete interfaces at failure for composite samples with different ribs.

Cement plate	Rib	Maximum relative displacement, mm			
		Sp1	Sp2	Sp3	Average
GB	HL	0.123	0.119	0.130	0.124
	ZL	0.249	0.267	0.249	0.255
	WL	0.537	0.546	0.543	0.542
DG	HL	0.208	0.224	0.225	0.219
	ZL	0.257	0.249	0.274	0.260
	WL	0.463	0.451	0.436	0.450

**3.3.4. Shearing Stress-Strain Relationship of the Interface.** Table 11 gives the maximum strain of the interface at failure. The WL samples have the highest strain values, while the ribbed samples show significant lower strain. The stress-strain curves are plotted in Figure 11. The HL rib sample has the largest shear modulus and the ZL rib sample is the second, while the WL sample has the lowest shear modulus. The ribs at the interface increase the mechanical friction of the sample but allow less relative movement, which is consistent with the previous results of interfacial bond-slip tests.

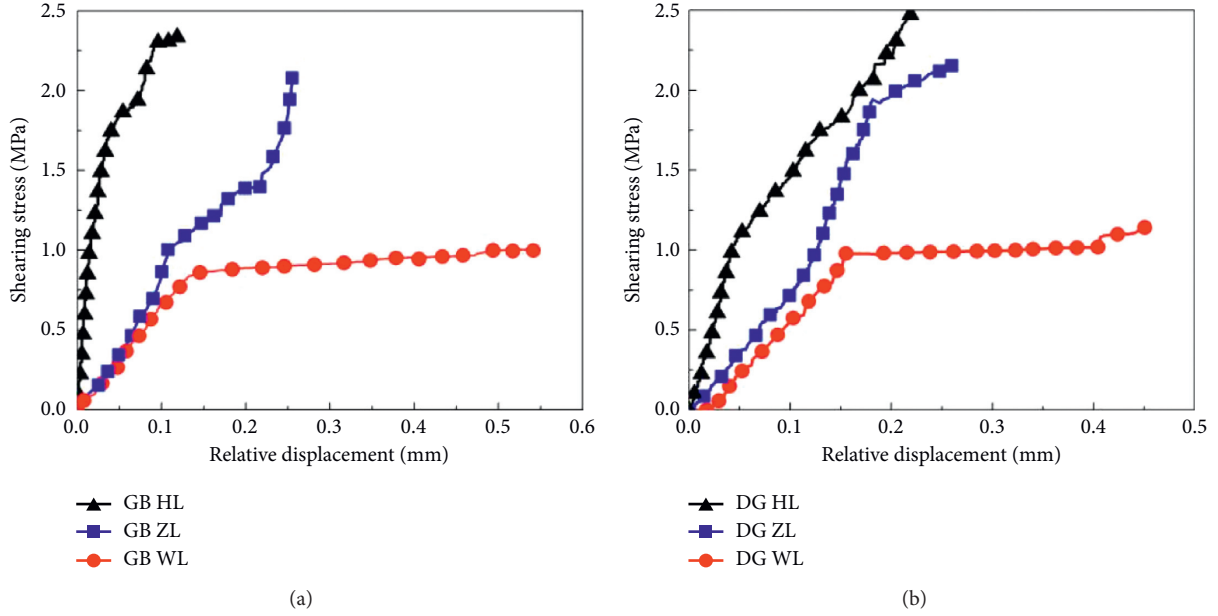


FIGURE 10: Relationship of the shearing stress over the relative displacement of the interface for composite samples with different ribs: (a) GB and (b) DG.

TABLE 11: Maximum strain of the interface at failure for composite samples with different ribs.

Cement plate	Rib	Maximum strain, $\mu\epsilon$			
		Sp1	Sp2	Sp3	Average
GB	HL	169.3	172.1	182.1	174.5
	ZL	180.2	185.6	197.3	187.7
	WL	283.4	270.3	275.5	276.4
DG	HL	143.5	149.2	148.6	147.1
	ZL	215.4	210.2	219.1	214.9
	WL	301.2	316.5	308.7	308.8

3.4. Regression Expression for the Shear Strength of the Interface. The influence of the cement plate, concrete strength, and rib on the bonding performance of the interface has been studied using the push-out shear test in this paper. The regression analysis is then utilized to establish a mathematical relation between the shear strength and the 3 influencing factors, which is given in equation (1):

$$\tau_u = 0.638 \cdot \alpha \cdot \gamma \cdot (0.0217 f_{cuk} + 0.261), \quad (1)$$

where  $\tau_u$  is the shear strength of the plate-concrete interface in MPa;  $\alpha$  is a dimensionless factor representing the influence of the fiber mesh type ( $\alpha=1$  for the nonfiber cement plate,  $\alpha=1.793$  for the GFRP cement plate, and  $\alpha=1.572$  for the BFRP cement plate);  $\gamma$  is also dimensionless expressing the influence of rib in the cement plate ( $\gamma=1$  for WL sample,  $\gamma=2.244$  for the sample with HL rib, and  $\gamma=1.977$  for the ZL rib);  $f_{cuk}$  is the standard cube compressive strength of the concrete.

The shear strength of the plate-concrete interface is computed using equation (1). Table 12 compares the calculated shear strength with the shear test results in this study. The ratio of the calculated value over the test result is

also provided. It is found that in most cases the GB samples show slightly larger shear test results, while the DG samples slightly larger calculated shear strength. However, the ratios are very close to 1, showing good agreement between the calculation equation and the shear test results. Therefore, equation (1) can be used to calculate the shear strength of the interface and provide good results, when the shear test is not available.

#### 4. A Constitutive Model for the Shear Strength-Relative Slip of the Interface

According to the test results, all the samples show a linear relationship between the shear strength and the relative slip at the early loading stage. After reaching the maximum, the shear strength plateaus over a long relative displacement, but only for the samples with fiber-reinforced nonrib cement plates. However, for the nonfiber, nonrib samples, or the ribbed samples with no fiber-reinforced cement plates, the stress-slip curve only has the rising linear stage, and there is no obvious plastic deformation stage. These samples fail after the peak shear strength is reached and no plastic behavior is observed.

Figure 12 is used to express the relationship of the shearing stress and relative slip, where  $\tau$  is the shearing stress in MPa and  $S$  is the value of the relative slip in mm. The shear stress of the interface increases linearly with the relative displacement before it reaches the characteristic value of the relative displacement,  $S_0$ . The shear stress then maximizes at  $\tau_u$  over the displacement range of  $S_0 < S < S_u$ . The curve is divided into elastic (OA) and plastic (AB) sections according to the load-deformation characteristics. Note that only the linear growth Section OA is used for expressing the stress-displacement relationship for the nonfiber and ribbed

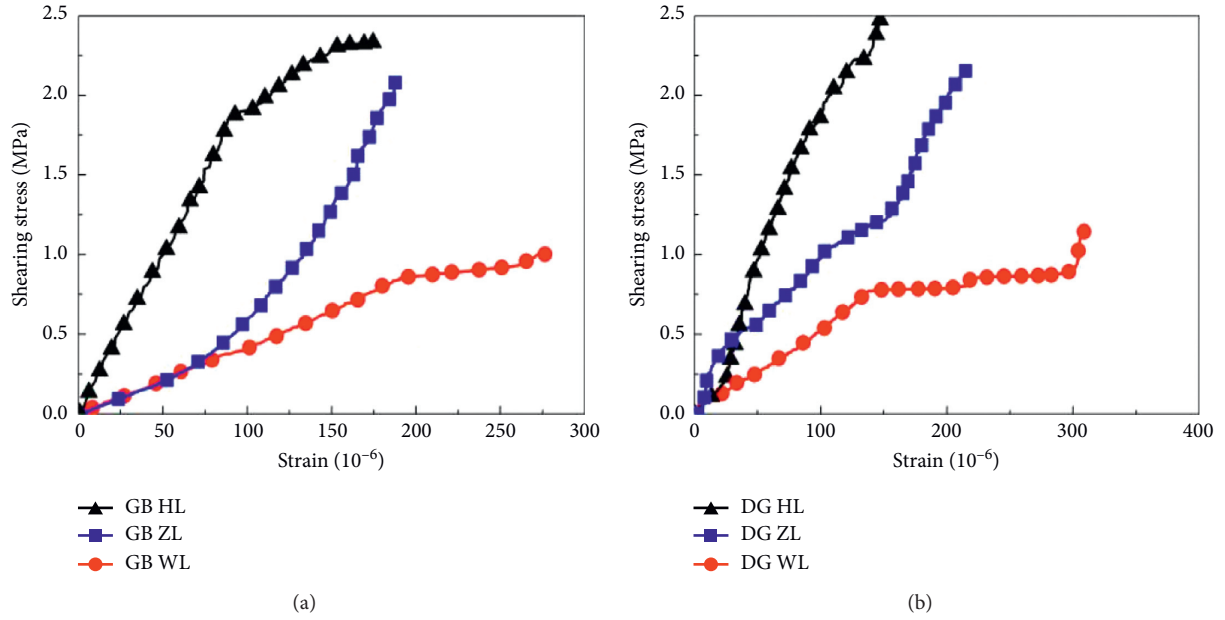


FIGURE 11: Stress-strain curves of the interface: (a) GB and (b) DG.

TABLE 12: Comparisons between calculated and test shear strength.

Sample ID	Mean value of test results, MPa	Mean value of calculated results, MPa	Calculated results/test results
GS C30	0.64	0.582	0.912
GB C15	0.58	0.588	1.008
GB C30	1.00	0.915	0.912
GB C50	1.43	1.350	0.946
GB HL	2.33	2.053	0.881
GB ZL	2.08	2.053	0.987
DG C15	0.56	0.671	1.198
DG C30	1.14	1.043	0.912
DG C50	1.36	1.540	1.130
DG HL	2.47	2.341	0.946
DG ZL	2.15	2.063	0.959

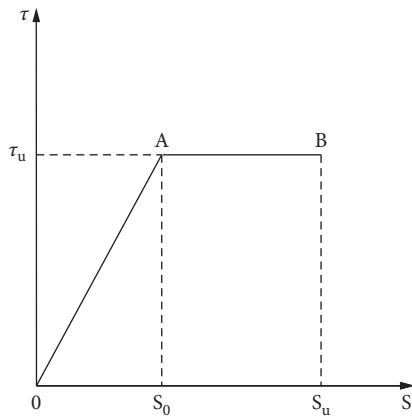


FIGURE 12: Constitutive model for the shearing stress-relative slip of the interface.

samples. The load-deformation behavior of the samples using fiber-reinforced cement plates includes both sections.

4.1. *Elastic Behavior of the Sample (Section OA).* The experimental data are used to obtain the mathematical relationship between the shearing stress and relative slip using the regression method. Equation (2) gives the expression for the linear growth of stress over displacement in Section OA.

$$\tau = 2.409 \cdot \beta \cdot \eta \cdot (0.243 f_{cuk} - 1.526) \cdot S, \quad (0 < S \leq S_0), \quad (2)$$

where  $\tau$  is the shear stress of the plate-concrete interface;  $\beta$  is the dimensionless factor concerning the influence of fiber mesh on the stress-slip relationship ( $\beta=1$  for the nonfiber cement plate,  $\beta=2.633$  for the GFRP cement plate, and

$\beta = 2.619$  for the BFRP cement plate);  $\eta$  is a dimensionless parameter explaining the influence of rib in the cement plate ( $\eta = 1$  for WL sample,  $\eta = 1.735$  for the sample with HL rib, and  $\eta = 1.304$  for the ZL rib);  $f_{cuk}$  is the standard cube compressive strength of the concrete;  $S$  is the relative slip of the plate-concrete interface ( $0 < S < S_0$ ).

4.2. *Plastic Behavior of the Sample (Section AB)*. In the following section of the curve, the shear stress of the interface maximizes at  $\tau_u$ , while the relative slip continues to increase. Equation (3) shows the relationship of shear stress over the relative slip.

$$\tau = \tau_u, (S > S_0), \quad (3)$$

where  $\tau_u$  is the shear strength of the interface. The shear strength can be obtained using equation (1).

4.3. *Characteristic Value of the Relative Slip*.  $S_0$  is the characteristic value of relative slip referring to the amount of relative displacement when the shear stress reaches its peak value. Combining equations (1) and (2) yields the expression for  $S_0$ :

$$S_0 = \frac{0.638 \cdot \alpha \cdot \gamma \cdot (0.0217 f_{cuk} + 0.261)}{2.409 \cdot \beta \cdot \eta \cdot (0.243 f_{cuk} - 1.526)}. \quad (4)$$

In Figure 12,  $S_u$  represents the maximum relative displacement when the samples fail completely. Note that, for the samples without plastic behavior,  $S_u = S_0$  and is normally less than 0.3 mm. For samples with plastic behavior, however, the relative slip characteristic values fall in the range of 0.45–0.55 mm.

It should be noted that the maximum concrete strength in this study uses the C50. Hence, the obtained equations above only apply for C50 concrete or less, and further research needs to be done for concrete strength grade higher than C50.

## 5. Summaries and Conclusions

This paper has analyzed the bonding performance of the plate-concrete interface by performing push-out shear test in the laboratory. A total of 3 groups of experiments have been conducted to assess the influence of the fiber mesh type, the concrete strength, and the inclusion of ribs in the cement plate. The failure characteristics of the sample, shear strength of the interface, and the relationship of load-deformation have been discussed for different samples. The regression method is adopted to compute the shear strength and the stress-displacement slip of the interface using the experimental data. The results provide guidance for improving the bonding performance of the interface. Important findings of this paper are listed as follows:

- (1) Instead of brittle failure, the composite sample with fiber-reinforced cement plate shows plastic behavior following the elastic stage. The deformation performance of the interface is therefore improved by using the fiber-reinforced cement plate. These fiber-

reinforced cement plates increase not only the buckling strength but also the shear stress of the plate-concrete interface. There is no appreciable difference between the GFRP and BFRP composite samples, although the GFRP samples have slightly larger shear strength, while the BFRP samples show slightly better deformation performance.

- (2) The shear strength of the plate-concrete interface is improved when using higher strength of concrete. However, the maximum relative slip at failure is not increased with the increase of concrete strength. Composite samples with larger concrete strength (say C50) show good shear stiffness and plastic behavior following the elastic stage.
- (3) The shear strength and shear stiffness of the interface are largely improved by setting ribs in the cement plate. However, the maximum relative slip of the interface is decreased for the rib samples. The layout of the rib is also influential to the interface bonding performance. The HL rib has larger shear strength and stiffness but lower maximum displacement.
- (4) Good consistency is found between the stress-strain and stress-slip relationship of the interface. Therefore, the deformation characteristics of the interface can also be represented by measuring the strain data.
- (5) The regression analysis gives the mathematical expression for the shear strength and the constitutive relationship of the stress-slip of the interface. The approximate elastic-perfectly plastic behavior is found for the samples using fiber-reinforced cement plates, while only linearly elastic behavior is observed for both nonfiber and rib samples.

## Abbreviations

Sp1, Sp2, and Sp3: Specimens 1, 2, and 3

Sp3:

$\tau$ :	Shear stress of the plate-concrete interface
$\tau_u$ :	Shear strength of the plate-concrete interface
$S$ :	Relative bond-slip of the plate-concrete interface
$S_0$ :	Characteristic value of relative bond-slip when the shear stress reaches maximum
$S_u$ :	Maximum relative bond-slip when the samples fail completely
$f_{tk}$ :	Standard cube compressive strength of the concrete
$\alpha$ :	A dimensionless factor representing the influence of fiber mesh type on shear strength
$\gamma$ :	A dimensionless factor expressing the influence of rib on shear strength
$\beta$ :	A dimensionless factor concerning the influence of fiber mesh on stress-slip relationship
$\eta$ :	A dimensionless factor concerning the influence of rib on stress-slip relationship.

## Data Availability

The data used to support the findings of this study are included within the article.

## Conflicts of Interest

The authors declare no conflicts of interest.

## Acknowledgments

This research was supported by the Key Science and Technology Projects in Transportation Industry (2018-MS2-051) and the Excellent Research Team of North China University of Technology (107051360021XN083/019). The authors are grateful for Dr. Gaofeng Song's help in improving English writing.

## References

- [1] L.-P. Ye and F. Peng, "Applications and development of fiber-reinforced polymer in engineering structures," *China Civil Engineering Journal*, vol. 39, no. 3, pp. 24–36, 2006.
- [2] X. Fan, J. Liu, S. Hu, and J. Lu, "Experimental study on dynamic mechanical properties of concrete beams strengthened with CFRP at different loading rates," *Journal of Building Structures*, vol. 41, no. 7, pp. 201–206, 2020.
- [3] G. Alaim, A. Valenza, D. Enea, and V. Fiore, "The durability of basalt fibres reinforced polymer (BFRP) panels for cladding," *Materials & Structures*, vol. 49, no. 6, pp. 2053–2064, 2016.
- [4] Y.-X. Yang, W. Chen, and M.-S. Ma, "Durability of basalt fiber sheets under wet-dry cycling in seawater," *Industrial Construction*, vol. 47, no. 4, pp. 5–8, 2010.
- [5] A. K. El-Sayed, E. El-Salakawy, and B. Benmokrane, "Shear strength of FRP reinforced concrete beams without transverse reinforcement," *ACI Structural Journal*, vol. 3, no. 2, pp. 235–243, 2006.
- [6] Z. F. Chen, L. L. Wan, S. Lee et al., "Evaluation of CFRP, GFRP and BFRP material systems for the strengthening of RC slabs," *Journal of Reinforced Plastics and Composites*, vol. 27, no. 12, pp. 1233–1243, 2008.
- [7] T. Ma, P. Jin-Long, and W. Hong-Li, "Experimental study of bond behavior between CFRP and concrete under cyclic loading," *Building Structure*, vol. 45, no. 19, pp. 15–18, 2013.
- [8] G.-M. Chen, D. Liu, L. Yun-Lei, L. Shi-Wei, C. Jian-Fei, and X. Hao-Bin, "Bond behavior between shear strengthening FRP and concrete: an experimental study," *Engineering Mechanics*, vol. 32, no. 7, pp. 164–175, 2015.
- [9] A. Nanni, B. Miller, and L. D. Lorenzis, "Bond of fiber-reinforced polymer laminates to concrete," *ACI Materials Journal*, vol. 98, no. 3, pp. 256–264, 2001.
- [10] K. Nakaba, T. Kanakubo, T. Furuta, and H. Yoshizawa, "Bond behavior between fiber-reinforced polymer laminates and concrete," *ACI Structural Journal*, vol. 98, no. 3, pp. 359–367, 2001.
- [11] L. Rong, T. Jin-Guang, and Y. Qing-Rui, "Experimental study on bond behavior of NSM CFRP strips-concrete interface," *Industrial Construction*, vol. 42, no. 8, pp. 31–34, 2005.
- [12] R. J. Gravina, S. A. Hadigheh, and S. Setunge, "Interfacial bond strength of resin-impregnated fibre-reinforced polymer laminates bonded to concrete using vacuum and heat: experimental study," *Australian Journal of Structural Engineering*, vol. 15, no. 2, pp. 189–201, 2014.
- [13] Y. Zhou, X. Wang, L. Sui et al., "Effect of mechanical fastening pressure on the bond behaviors of hybrid-bonded FRP to concrete interface," *Composite Structures*, vol. 204, 2018.
- [14] C. Chen, L. Xue, X. Wang et al., "Effect of transverse groove on bond behavior of FRP-concrete interface: experimental study, image analysis and design," *Composites Part B*, vol. 161, 2019.
- [15] Z. Wang, S. Shen, Y. Ju, and M. Shao, "Research progress on durability of bonding interface of FRP cloth reinforced structure," *Composite Materials Science and Engineering*, vol. 47, no. 7, pp. 117–122, 2020.
- [16] S. Wang, Y. Yao, and H. Lei, "Durability of FRP-high strength concrete adhesive joints under aggressive exposure conditions and loads," *Journal of Disaster Prevention and Mitigation Engineering*, vol. 37, no. 1, pp. 127–133, 2017.
- [17] X.-Y. Lin and S.-Y. Cao, "Study on bond behavior of inter-crack CFRP and concrete in beams strengthened with fibers," *Engineering Mechanics*, vol. 25, no. 11, pp. 149–155, 2008.
- [18] S.-K. Woo and Y. Yun, "Experimental study on interfacial behavior of CFRP-bonded concrete," *KSCE Journal of Civil Engineering*, vol. 14, no. 3, pp. 385–393, 2010.
- [19] H. A. Baky, U. A. Ebead, and K. W. Neale, "Nonlinear micromechanics-based bond-slip model for FRP/concrete interfaces," *Engineering Structures*, vol. 39, no. 6, pp. 11–23, 2003.
- [20] J.-G. Dai, W. Y. Gao, and J. G. Teng, "Bond-slip model for FRP laminates externally bonded to concrete at elevated temperature," *Journal of Composites for Construction*, vol. 17, no. 2, pp. 217–228, 2013.
- [21] X.-L. Wang, Y. Jia-Jia, H.-Y. Sun, K. Li, and X.-D. Kang, "Experimental study on bond-slip model for CFRP-concrete interface based on beam test," *Journal of Disaster Prevention and Mitigation Engineering*, vol. 34, no. 3, pp. 314–319, 2014.
- [22] D.-Y. Gao, H.-T. Zhu, and J.-J. Xie, "The constitutive models for bond slip relation between FRP rebars and concrete," *Industrial Construction*, vol. 40, no. 7, pp. 41–43, 2003.
- [23] X. Lu, L. Ye, J. Teng, and J. Zhuang, "Bond-slip model for FRP-to-concrete interface," *Journal of Building Structures*, vol. 26, no. 4, pp. 10–18, 2005.
- [24] H. Ko, S. Matthys, A. Palmieri, and Y. Sato, "Development of a simplified bond stress-slip model for bonded FRP-concrete interfaces," *Construction and Building Materials*, vol. 68, no. 4, pp. 142–157, 2014.
- [25] H. Qing-duo, Y.-L. Wang, J.-L. Hou, and O. Jin-Ping, "Bond-slip constitutive model between GFRP/steel wire composite rebars and concrete," *Engineering Mechanics*, vol. 26, no. 5, pp. 62–72, 2009.
- [26] S. Xiao-Ruan, J.-L. Gao, and J.-Y. Qu, "Experimental study on physical and mechanical properties of GRC formwork," *Journal of Beijing University of Technology*, vol. 34, no. 7, pp. 708–713, 2008.

## Research Article

# Influence of Blade Profiles on Plastic Centrifugal Pump Performance

Hui Zhang , Lingfeng Tang, and Yongtao Zhao

School of Mechanical Engineering, Anhui Polytechnic University, Wuhu, Anhui 241000, China

Correspondence should be addressed to Hui Zhang; 2190110111@stu.ahpu.edu.cn

Received 9 October 2020; Revised 26 November 2020; Accepted 2 December 2020; Published 22 December 2020

Academic Editor: Jinyang Xu

Copyright © 2020 Hui Zhang et al. This is an open access article distributed under the Creative Commons Attribution License, which permits unrestricted use, distribution, and reproduction in any medium, provided the original work is properly cited.

To study the influence of blade profiles of the plastic centrifugal pump on pump performance, the impeller blade profiles were designed and drawn by the single arc method, double arc method, logarithmic spiral method, and B-spline curve method, respectively, with the known structural parameters. The shape and size of four profiles were drawn, and two-dimensional models and three-dimensional models of four impellers and volute were completed, respectively. The impeller models were printed by 3D printing technology, and the performance experiments of the plastic centrifugal pump were carried out. The numerical simulation of the internal flow field was performed. From the contours of the velocity and pressure, the vapor volume fraction distribution, and fluid-structure interaction analysis of impellers, the impeller drawn by the logarithmic spiral method was better than others. The optimization of the logarithmic spiral method was completed. The impeller inlet and outlet diameters ( $D_1$  and  $D_2$ ) and impeller inlet and outlet installation angles ( $\beta_1$  and  $\beta_2$ ) were taken as control variables, and the total power loss and the minimum NPSH<sub>r</sub> of the pump were taken as the objective functions. The optimization results were that  $D_1 = 58$  mm and  $D_2 = 162$  mm and  $\beta_1 = 17^\circ$  and  $\beta_2 = 31^\circ$ . The hydraulic efficiency was increased by 1.68%.

## 1. Introduction

As a type of general machinery, centrifugal pumps are widely used such as in mechanical engineering, aerospace, and petrochemical industries [1–3]. The flow components of plastic centrifugal pumps are made of engineering plastic, with less manufacturing costs and better corrosion resistance. Plastic centrifugal pumps are suitable for most corrosive environments such as acid, alkali, and salt and can be applied to the transportation of corrosive materials in chemical and petroleum industries. However, it is well known that inevitable cavitation in centrifugal pumps will affect the pump performance and cause noise and vibrations [4–10].

The impeller is the core part of the centrifugal pump, and the impeller blade profile plays a vital role in the fluid flow which will directly impact the performance of centrifugal pumps. At present, there have been many studies on the influence of the impeller parameters on the flow characteristics of centrifugal pumps [11–20]. Tao et al. [21] used the

numerical method to study how the blade thickness influenced the flow characteristics in the impeller passages and volute casing. They concluded that the pressure pulsations increased at the leading edges but decreased at the trailing edges according to the increase in the blade thickness. However, their work was only helpful for the design of ceramic pumps. Tao et al. [22] studied the influence of blade leading-edge shape on the cavitation and concluded it delayed the inception cavitation and critical cavitation. Peng et al. [23] analyzed various blade outlet angles without changing other impeller parameters and concluded that if the blade outlet angle was increased, the flow separation and the axial vortex along the blade working surface would be more serious. However, their work was aimed at low specific speed submersible pumps. Yu-Qin and Ze-Wen [24] studied how different blade numbers influenced the flow-induced noise of the centrifugal pump based on the idea of acoustic-vibration coupling. They found that the 6-blade model pump was the optimal value. Han et al. [25] presented an impeller and volute shape optimization design method that improved

the hydraulic performance of the pump. Zhang et al. and Wang et al. [26, 27] explored the effects of slotted blades on the performance of centrifugal pumps. Li et al. [28] studied the influence of the blade angle of a low specific speed plastic centrifugal pump on the pump performance. They applied the one-way fluid-structure interaction but did not take the impact of structural deformation on performance into consideration.

The blade profile directly affects the bending of the blade and has an important impact on the fluid flow in the impeller channel. Studying the impact of the blade profile on the performance of the centrifugal pumps is beneficial to improve the performance and efficiency of the centrifugal pumps. Hu et al. [29] designed an iterative method of double arc blade profile for drawing cylindrical blade profile which overcame the shortcomings of blade profile drawing methods. El-Gazzar and Hawash [30] used the splitting technique to change the shape of the impeller and concluded that the impeller blade split caused the uneven mass distribution around the impeller, which led to the imbalance of the impeller. Ming et al. [31] proposed a new variable-angle spiral equation that was complementary to the traditional variable-angle spiral equation by changing the blade placement angle function.

In existing research studies, the studies on blade profile are mainly focused on metal pumps and a single profile, while only a few pieces of research are on the performance of plastic centrifugal pumps. Moreover, there is no regularity between the various blade profiles and the performance parameters of centrifugal pumps. In this paper, four design methods of blade profiles, which are the single arc method, double arc method, logarithmic spiral method, and B-spline curve method, are proposed and the influence of four kinds of blade profile on plastic centrifugal pump performance is studied. The flow field simulation of pumps with various impellers is analyzed in detail.

## 2. Design Methods of Blade Profiles

**2.1. Single Arc Method.** Figure 1 shows the design principle of the single arc method. In Figure 1,  $D_1$  and  $D_2$  are impeller inlet and outlet diameters, respectively,  $\beta_1$  and  $\beta_2$  are the impeller inlet and outlet installation angles, respectively, and arc  $AB$  is the blade profile.

Take a random point (point  $A$ ) on the entrance circle  $D_1$ . Take point  $A$  as the fixed point. Draw a line with a  $\beta_1$  angle and a length of  $\rho$  in the negative direction of the  $x$ -axis. Take point  $E$  as the endpoint. Then, take point  $E$  as the center and  $\rho$  as the radius to make the arc intersect the inlet and outlet circles at  $A$  and  $B$ . Therefore, the arc  $AB$  is the blade profile of the single arc method.

The radius of curvature of the single arc:

$$\rho = \frac{R_2^2 - R_1^2}{2(R_2 \cos \beta_2 - R_1 \cos \beta_1)}, \quad (1)$$

where  $\rho = EA$ —radius of curvature of the single arc (mm) and  $R_1, R_2$ —impeller inlet and outlet radii (mm).

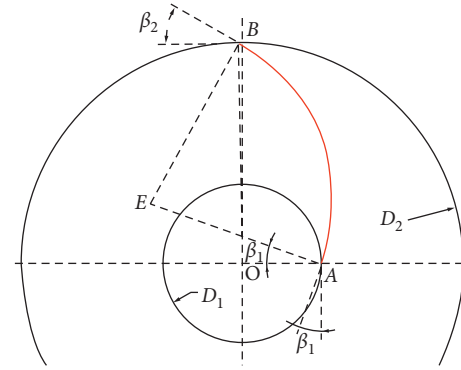


FIGURE 1: Blade profile of single arc method.

**2.2. Double Arc Method.** The principle of the double arc method is to find the radius of rotation according to the drawing method to determine the first arc and then calculate the value of the radius of rotation to determine the second arc according to the formula.

In Figure 2,  $D_1$  and  $D_2$  are impeller inlet and outlet diameters and  $\beta_1$  and  $\beta_2$  are the impeller inlet and outlet installation angles. Take  $D_1$  as the diameter to make a circle and divide the circle into equal parts according to the number of blades  $Z$ . The equal points are  $A_1, A_2, A_3, A_4, A_5,$  and  $A_6$ . Take the diameter  $\delta = D_1 \sin \beta_1$  as the concentric circle with the diameter  $D_1$ . Make tangent lines  $A_1E_1, A_2E_2, A_3E_3, A_4E_4, A_5E_5,$  and  $A_6E_6$  from each equal point to the circle of diameter  $\delta$ . Take  $E_1$  as the center of the circle ( $\angle E_1A_1O = \beta_1$ ) and  $E_1A_1$  as the radius to make an arc, which intersects the auxiliary circle (point  $F$ ); then, the arc  $FA_1$  is the first profile of the blade. The second arc needs to meet three conditions which determine the position of point  $P$ . Three conditions are that (1)  $F, E_1,$  and  $M$  points are colinear; (2)  $\angle OPM = \beta_2$ ; and (3)  $PM = MF = \rho$ .

The value of  $\rho$  is

$$\rho = \frac{1}{2} \frac{R_2^2 - R_f^2}{R_2 \cos \beta_2 - R_f \cos \beta_f}, \quad (2)$$

where  $\rho$ —radius of rotation of the second arc (mm);  $R_f$ —radius of rotation of the point  $F$  (mm); and  $\beta_f$ —blade angle of point  $F$  ( $^\circ$ ).

After the position of point  $P$  is determined, the center point  $M$  can be determined and the second arc can be determined according to  $\rho$ .

**2.3. Logarithmic Spiral Method.** After determining the impeller inlet and outlet installation angles and the impeller inlet and outlet diameters, the blade wrap angle has a larger value range. Therefore, the advantage of the logarithmic spiral method in the shape of the cylindrical impeller's blade is also more prominent. Design and draw the impeller blade profile according to the equivariant angle spiral, and its design principle of the profile is shown in Figure 3.

In Figure 3,  $\beta$  is impeller installation angle ( $^\circ$ );  $\beta_1$  and  $\beta_2$  are impeller inlet and outlet installation angles ( $^\circ$ );  $D_1$  and  $D_2$

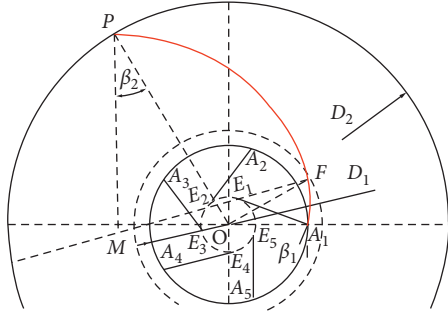


FIGURE 2: Blade profile of double arc method.

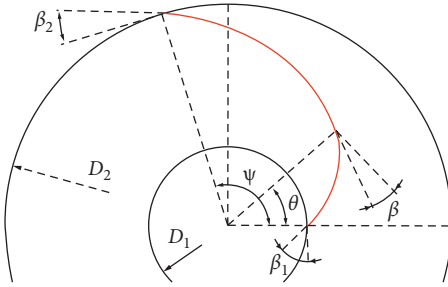


FIGURE 3: Blade profile of logarithmic spiral method.

are the impeller inlet and outlet diameters (mm); and  $\theta$  is the variation of wrap angle  $\psi$  ( $^\circ$ ).

When  $\beta_1 \neq \beta_2$ , the change law of  $\beta$  is

$$\beta = (\beta_2 - \beta_1) \cdot \frac{\theta}{\varphi} + \beta_1. \quad (3)$$

Profile equation:

$$r = r_1 \left[ \frac{\cos \beta_1}{\cos[(\beta_2 - \beta_1/\varphi)\theta + \beta_1]} \right]^{(\psi/\beta_2 - \beta_1)}. \quad (4)$$

Wrap angle:

$$\varphi = \frac{(\beta_2 - \beta_1) \ln(r_2/r_1)}{\ln(\cos \beta_1 / \cos \beta_2)}. \quad (5)$$

Substitute  $\beta_1 = 20$ ,  $\beta_2 = 30$ ,  $D_1 = 58$  mm, and  $D_2 = 162$  mm into the program written by MATLAB software, and the resulting blade profile is shown in Figure 4(a).

**2.4. B-Spline Curve Method.** Use 5-point (or 4-point) Bezier curve to fit the studied impeller profile, which eliminates the inconvenience of curve adjustment caused by traditional cubic polynomial fitting and makes the design of blade profile simpler, smoother, and easier to control. Determine the coordinates of the control points first. According to the Bezier equation,  $n = 4$ ,

$$P(t) = (1-t)^4 P_0 + 4t(1-t)^3 P_1 + 6t^2(1-t)^2 P_2 + 4t^3(1-t) P_3 + t^4 P_4. \quad (6)$$

The coordinate of any point  $P(x_p, y_p)$  on the Bezier curve is

$$\begin{aligned} x_p &= (1-t)^4 x_0 + 4t(1-t)^3 x_1 + 6t^2(1-t)^2 x_2 \\ &\quad + 4t^3(1-t) x_3 + t^4 x_4, \\ y_p &= (1-t)^4 y_0 + 4t(1-t)^3 y_1 + 6t^2(1-t)^2 y_2 \\ &\quad + 4t^3(1-t) y_3 + t^4 y_4. \end{aligned} \quad (7)$$

Figure 5 shows the design principle of the B-spline curve method. In Figure 5, the impeller inlet and outlet installation angles  $\beta_1$  and  $\beta_2$  and the impeller inlet and outlet diameters  $D_1$  and  $D_2$  are the known parameters.

Substitute  $\beta_1 = 20$ ,  $\beta_2 = 30$ ,  $D_1 = 58$  mm,  $D_2 = 162$  mm, and  $\psi = 88.3$  into the calculation and obtain  $P_0(0, 29)$ ,  $P_1(-26.32, 38.58)$ ,  $P_2(60.87, 12.77)$ ,  $P_3(-66.79, 25.49)$ , and  $P_4(-81, 2.83)$ . From the obtained coordinates of  $P_0$ ,  $P_1$ ,  $P_2$ ,  $P_3$ , and  $P_4$ , the designed blade profile can be drawn by MATLAB software, as shown in Figure 4(b).

### 3. Numerical Simulation Method

**3.1. Computation Model.** Take the plastic centrifugal pump designed by a certain unit as an example, and its main design parameters are shown in Table 1. According to the known structural parameters of a plastic centrifugal pump, the impeller blade profiles were designed and drawn by the single arc method, double arc method, logarithmic spiral method, and B-spline curve method, respectively.

Figure 6 shows a two-dimensional diagram of the impeller. According to the parameters of the impeller in Figure 6, the UG software is used to design the three-dimensional model of the impeller. The three-dimensional models of the impeller with four profile design methods are shown in Figure 7.

Figure 8 shows a two-dimensional diagram of the volute. According to the parameters of the volute in Figure 8, the UG software is used to design the three-dimensional model of the volute. The three-dimensional model of the volute is shown in Figure 9.

**3.2. Meshing.** According to the above completed three-dimensional models, ANSYS-ICEM software is employed to utilize to mesh the computational domains. When we mesh the models, the actual grid cannot reach the ideal shape. If the grid deforms or deformation exceeds a certain limit, the accuracy of the calculation results will change accordingly. Therefore, in the initial division of the grid, it is necessary to use appropriate measures to control or measure the quality of the grid and try to achieve the best grid. The final determination of the number of grid cells in each part of the computational domains is shown in Table 2.

The final meshing is shown in Figure 10.

**3.3. Computational Setup.** Numerical calculations were performed in FLUENT software. The turbulence model was a k-epsilon (equation (2)) turbulence model. The computational impeller domain was set to a rotational domain. All other computational domains were set to static.

The boundary conditions were set to velocity inlet and outflow. The relevant setting parameters were set by default. The reference pressure was set to standard atmospheric

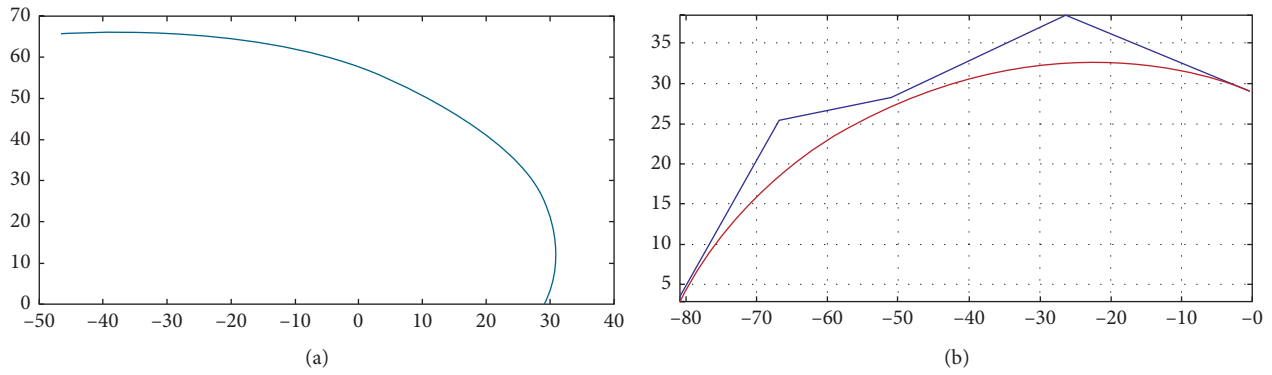


FIGURE 4: Blade profiles drawn by MATLAB software. (a) Logarithmic spiral method. (b) B-spline curve method.

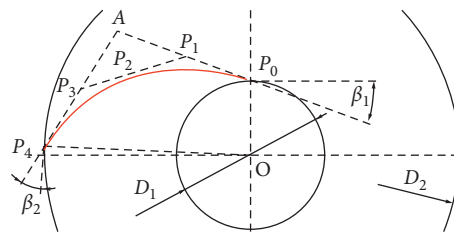


FIGURE 5: Blade profile of B-spline curve method.

TABLE 1: Design parameters of plastic centrifugal pump.

Performance parameters		Geometrical dimension	
Q (m <sup>3</sup> /h)	20	Impeller inlet diameter (mm)	58
H (m)	30	Impeller outlet diameter (mm)	162
n (r/min)	2900	Impeller inlet width (mm)	23
n <sub>s</sub>	60.871	Impeller outlet width (mm)	10
P <sub>t</sub> (kW)	5.5	Impeller inlet installation angle (°)	20
NPSH <sub>a</sub> (m)	4	Impeller outlet installation angle (°)	30
Volute width (mm)	33	Base circle diameter of volute (mm)	175

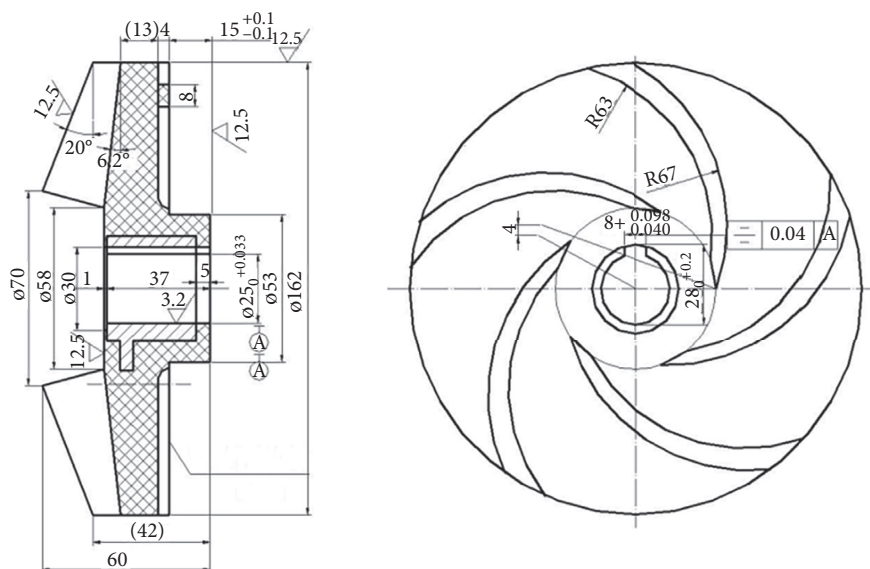


FIGURE 6: Two-dimensional diagram of the impeller.

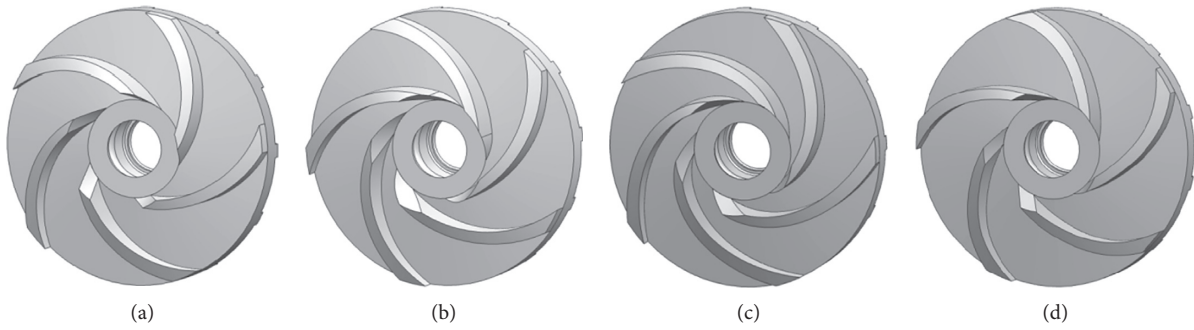


FIGURE 7: Models of impellers drawn by four profile design methods. (a) Single arc. (b) Double arc. (c) Logarithmic spiral. (d) B-spline curve.

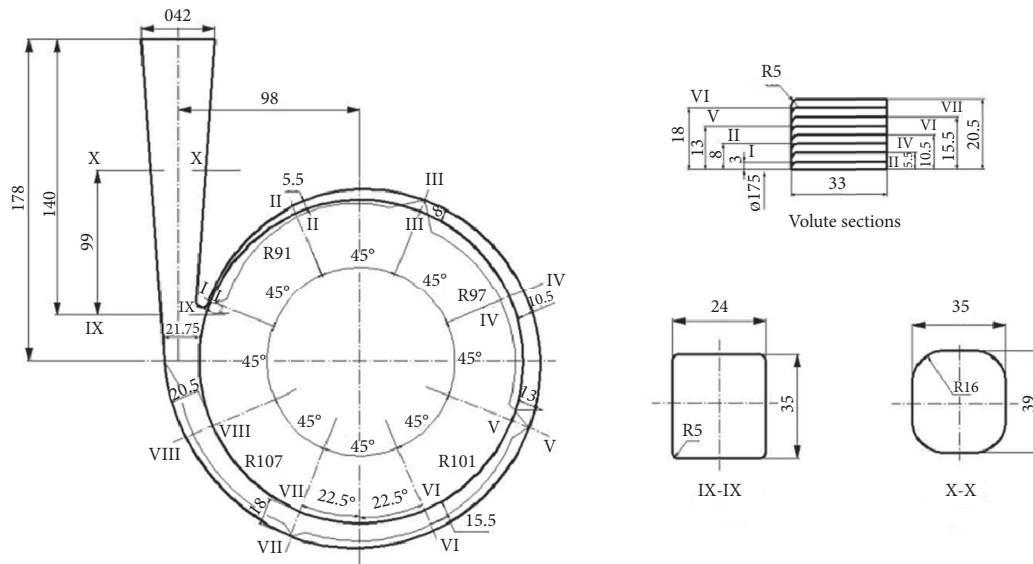


FIGURE 8: Two-dimensional diagram of the volute.



FIGURE 9: Model of volute.

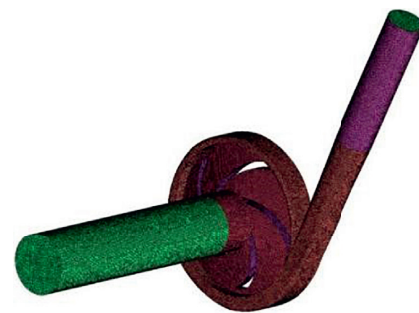


FIGURE 10: Meshing.

TABLE 2: The number of grid cells.

Computational domains	Inlet extension	Impeller	Volute	Outlet extension
The number of grid cells	581102	397526	393266	1502055

pressure. The wall surface was placed under a non-slip boundary condition, and a standard wall surface function was applied. The calculation method was SIMPLEC. The convergence accuracy was set to  $10^{-4}$ .

#### 4. Test Verification

4.1. 3D Printing of Plastic Centrifugal Pump Impellers. UTR9000 material was used for 3D printing of impellers, which was an ABS-like stereo light modeling resin with

accurate and durable characteristics. The durability of components made of UTR9000 resin was more than 6.5 months. According to the three-dimensional models of the impellers drawn by four profile design methods (Figure 6), the impeller models printed by 3D printing technology are shown in Figure 11.

**4.2. Performance Tests of Plastic Centrifugal Pump.** Figure 12 shows the pump performance test bench, which mainly included a motor and a flow control valve.

The pump test system (electrical measurement method) V8.97 software on the data acquisition platform was used to collect data at each operating point by adjusting the flow control valve. The pump performance experiments were performed on the impellers of the four types of profiles. The parameter settings before the experiment are shown in Table 3, and the collected data are shown in Tables 4–7.

**4.3. Data Analysis.** Figures 13 and 14 show the comparison of head and efficiency in performance experiments of four types of impellers. From the shut-off point to the maximum flow condition during the test, 13 flow condition points were selected to completely reflect the external characteristic variation curve. It can be seen that the efficiency of the logarithmic spiral method was better than that of the other three methods, and the efficiency of the single arc method was the worst.

## 5. Analysis of Numerical Simulation Results

**5.1. Velocity in the Flow Field.** Figure 15 shows the contours of the velocity of the four impellers, respectively. As shown in Figure 15, when the other parameters were consistent, the impellers drawn by four profile design methods had insufficient fluid flow, and the internal flow fields in the impellers drawn by the single arc method and B-spline curve method had obvious vortex. The internal flow fields in the impellers drawn by the double arc method and logarithmic spiral method were significantly better than those drawn by the B-spline curve method and single arc method.

**5.2. Pressure in the Flow Field.** Figure 16 shows the contours of the pressure of the four impellers, respectively. As shown in Figure 16, when the other parameters were consistent, the internal pressure trends of the impellers drawn by four design methods were correct, and the stratification was obvious. There was negative pressure near the impeller inlet in the flow fields of impellers drawn by the single arc method and B-spline method, while negative pressure did not occur in the other two flow fields of impellers. The maximum pressure values corresponding to the four methods were 437563 Pa, 441628 Pa, 438368 Pa, and 435518 Pa. The pressure fields in the impellers drawn by the double arc method and logarithmic spiral method were significantly better.

**5.3. Cavitation in the Flow Field.** Figure 17 shows the vapor volume fraction distribution in four impellers when  $NPSH_r$  was 1 m. As shown in Figure 17, when  $NPSH_r$  was 1 m, the bubbles almost filled the entire impellers. The vapor volume fractions of the impellers drawn by the double arc method and logarithmic spiral method were 0.9455 and 0.9449, which were significantly lower than those in the other two impellers. The impeller drawn by the single arc method had the largest value.

Figure 18 shows the vapor volume fraction distribution in four impellers when  $NPSH_r$  was 2 m. As shown in Figure 18, when  $NPSH_r$  was 2 m, bubbles filled one third of the entire impellers. The vapor volume fractions of the impellers drawn by the double arc method and logarithmic spiral method were 0.861 and 0.8174, which were significantly lower than those in the other two impellers. The impeller drawn by the B-spline curve had the largest value.

In summary, when  $NPSH_r = 1$  m and 2 m, the impeller drawn by the logarithmic spiral method is significantly better than the other three impellers, which means that the logarithmic spiral method is the best design method.

**5.4. Analysis of Efficiency.** According to the above conclusion, CFD-Post software was used to calculate the performance parameters of the four profiles, as shown in Table 8. From Table 8, it can be concluded that the impeller of the logarithmic spiral method was the optimal impeller under the design condition.

**5.5. Analysis of Blade Profiles Based on Fluid-Structure Interaction.** The purpose of fluid-structure interaction was to find how the flow field influenced the impeller, which was mainly reflected in the deformation of the impeller caused by the fluid, and the force on the impeller. ANSYS-CFX software was used to complete the fluid-structure interaction analysis.

Figure 19 shows the total deformation of the impellers drawn by four profile design methods under the same working condition. As a whole, the total deformation distribution of the four impellers was symmetrical and stratified obviously. The deformation of the impellers increased continuously with the increase of the radius, the maximum deformation occurred at the edge of the impellers, and the minimum deformation occurred at the inlet of the impellers.

The maximum total deformation of the impellers drawn by four profile design methods was 0.61503 mm, 0.58614 mm, 0.57442 mm, and 0.61609 mm, respectively. The following can be concluded for total deformation: B-spline curve method > single arc method > double arc method > logarithmic spiral method.

Figure 20 shows the equivalent stress of the impellers drawn by four profile design methods under the same working conditions. As a whole, the impeller stress was mainly concentrated on the blade root, where the equivalent stress was significantly greater than that in other areas. Therefore, compared to other positions, the blade root near the impeller inlet was more prone to stress concentration.

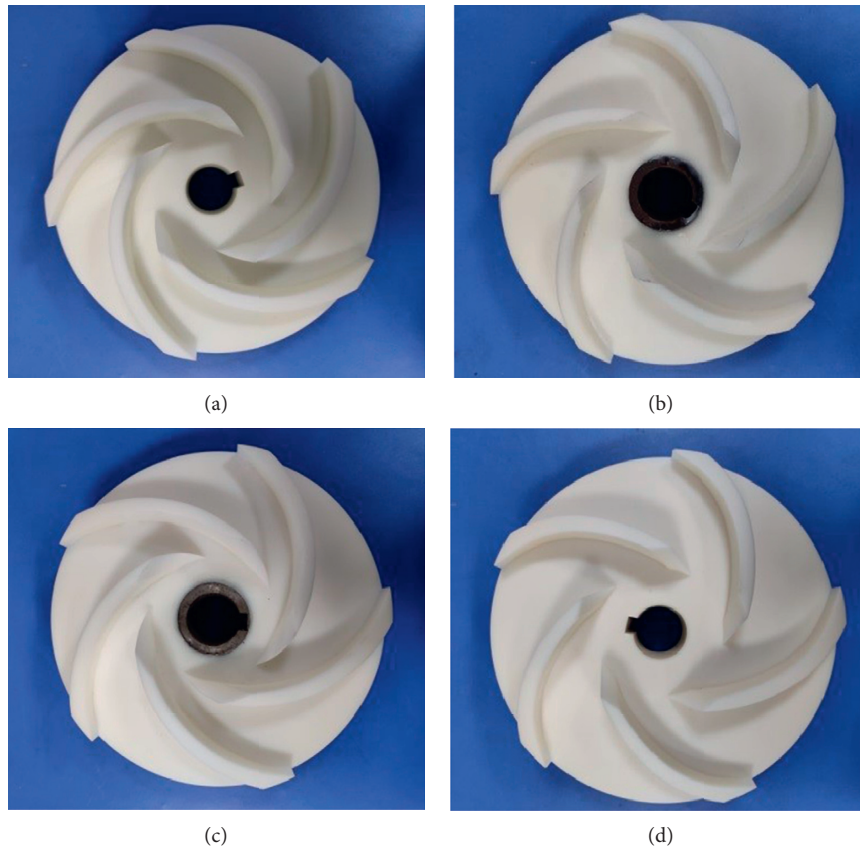


FIGURE 11: 3D printing of impellers. (a) Single arc. (b) Double arc. (c) Logarithmic spiral. (d) B-spline curve.



FIGURE 12: Pump performance test bench.

TABLE 3: Parameter settings of pump performance experiment.

Product number	Fluid density (kg/m <sup>3</sup> )	Fluid viscosity (CST)	Meter factor ( <i>f</i> /1)	Inlet diameter (m)	Outlet diameter (m)
50UHB15-32	Water	Water	79.89	0.05	0.032

TABLE 4: Performance experiment of single arc method.

	Measured value						<i>n</i> = 2900 (r/min)		
	Inlet pressure (kPa)	Outlet pressure (kPa)	<i>Q</i> (m <sup>3</sup> /h)	<i>n</i> (r/min)	<i>P</i> <sub>in</sub> (kW)	<i>Q</i> (m <sup>3</sup> /h)	<i>H</i> (m)	<i>P</i> <sub>in</sub> (kW)	$\eta$ (%)
1	-70.00	170.00	20.95	2998.60	5.85	20.26	25.72	5.29	26.83
2	-80.00	220.00	19.93	3001.44	5.83	19.26	31.19	5.26	31.11
3	-70.00	240.00	18.92	3002.21	5.81	18.28	31.94	5.24	30.37

TABLE 4: Continued.

	Measured value					$n = 2900$ (r/min)			
	Inlet pressure (kPa)	Outlet pressure (kPa)	$Q$ (m <sup>3</sup> /h)	$n$ (r/min)	$P_{in}$ (kW)	$Q$ (m <sup>3</sup> /h)	$H$ (m)	$P_{in}$ (kW)	$\eta$ (%)
4	-60.00	260.00	16.35	3001.81	5.56	15.80	32.47	5.01	27.87
5	-50.00	280.00	14.86	3001.81	5.37	14.36	33.21	4.84	26.82
6	-40.00	300.00	12.93	3002.06	5.12	12.49	33.90	4.62	24.99
7	-30.00	310.00	10.91	3002.36	4.96	10.54	33.66	4.47	21.62
8	-20.00	330.00	8.28	3001.63	4.68	8.00	34.39	4.22	17.76
9	-20.00	340.00	6.33	3001.54	4.53	6.12	35.21	4.09	14.36
10	-10.00	350.00	2.44	3001.34	4.26	2.36	35.06	3.84	5.86
11	-10.00	360.00	1.49	3001.16	4.22	1.44	36.00	3.81	3.71
12	-10.00	360.00	0.21	3000.81	4.15	0.20	35.99	3.75	0.53
13	0.00	380.00	0.00	3000.90	4.03	0.00	36.94	3.64	0.00

TABLE 5: Performance experiment of double arc method.

	Measured value					$n = 2900$ (r/min)			
	Inlet pressure (kPa)	Outlet pressure (kPa)	$Q$ (m <sup>3</sup> /h)	$n$ (r/min)	$P_{in}$ (kW)	$Q$ (m <sup>3</sup> /h)	$H$ (m)	$P_{in}$ (kW)	$\eta$ (%)
1	-80.00	190.00	21.19	3000.59	5.47	20.48	28.60	4.94	32.31
2	-80.00	220.00	19.98	2998.58	5.33	19.32	31.26	4.82	34.13
3	-70.00	240.00	18.09	2997.92	5.21	17.50	31.89	4.72	32.23
4	-70.00	250.00	16.89	2998.15	5.18	16.34	32.64	4.69	30.98
5	-50.00	280.00	14.25	2998.20	5.01	13.78	33.20	4.53	27.50
6	-40.00	290.00	12.63	2998.18	4.82	12.22	33.00	4.36	25.17
7	-30.00	310.00	10.85	2997.94	4.60	10.50	33.76	4.16	23.18
8	-20.00	330.00	8.56	2998.14	4.44	8.28	34.50	4.02	19.36
9	-20.00	340.00	6.70	2998.48	4.32	6.48	35.31	3.91	15.95
10	-10.00	350.00	4.83	2998.58	4.20	4.67	35.20	3.80	11.79
11	-10.00	360.00	2.06	2998.72	3.99	1.99	36.06	3.61	5.42
12	-10.00	370.00	0.24	2999.02	3.82	0.23	36.99	3.45	0.68
13	-10.00	380.00	0.00	2999.52	3.71	0.00	37.93	3.35	0.00

TABLE 6: Performance experiment of logarithmic spiral method.

	Measured value					$n = 2900$ (r/min)			
	Inlet pressure (kPa)	Outlet pressure (kPa)	$Q$ (m <sup>3</sup> /h)	$n$ (r/min)	$P_{in}$ (kW)	$Q$ (m <sup>3</sup> /h)	$H$ (m)	$P_{in}$ (kW)	$\eta$ (%)
1	-70.00	180.00	21.33	2998.60	5.58	20.63	26.75	5.05	29.79
2	-80.00	190.00	21.08	2998.07	5.36	20.39	28.62	4.85	32.77
3	-80.00	210.00	20.24	3001.45	5.21	19.56	30.30	4.70	34.35
4	-80.00	230.00	18.98	3002.29	5.20	18.33	31.95	4.69	34.05
5	-60.00	250.00	16.50	3001.64	5.01	15.94	31.55	4.52	33.32
6	-50.00	280.00	14.65	3001.62	4.80	14.15	33.18	4.33	29.55
7	-30.00	310.00	11.30	3001.65	4.48	10.92	33.72	4.04	24.82
8	-30.00	320.00	1.54	3001.62	4.42	10.18	34.59	3.99	24.08
9	-20.00	330.00	8.46	3001.77	4.20	8.17	34.40	3.79	20.23
10	-20.00	340.00	7.35	3001.72	4.11	7.10	35.27	3.71	18.41
11	-20.00	340.00	5.93	3001.50	3.98	5.73	35.19	3.59	15.30
12	-10.00	350.00	2.63	3001.25	3.74	2.54	35.06	3.37	7.19
13	-10.00	370.00	0.00	3001.34	3.43	0.00	36.93	3.09	0.00

The maximum equivalent stress of the impellers drawn by four profiles was 41.357 MPa, 41.43 MPa, 40.909 MPa, and 44.891 MPa, respectively. The following can be

concluded for equivalent stress: B-spline curve method > double arc method > single arc method > logarithmic spiral method.

TABLE 7: Performance experiment of B-spline curve method.

	Measured value					$n = 2900$ (r/min)			
	Inlet pressure (kPa)	Outlet pressure (kPa)	$Q$ (m <sup>3</sup> /h)	$n$ (r/min)	$P_{in}$ (kW)	$Q$ (m <sup>3</sup> /h)	$H$ (m)	$P_{in}$ (kW)	$\eta$ (%)
1	-80.00	180.00	21.27	2998.15	5.40	20.57	27.70	4.89	31.77
2	-80.00	220.00	20.05	3001.80	5.31	19.37	31.21	4.79	34.39
3	-80.00	240.00	17.69	3001.60	5.13	17.09	32.69	4.63	32.90
4	-80.00	250.00	16.65	3001.51	5.03	16.09	33.48	4.54	32.34
5	-60.00	280.00	14.91	3001.36	4.81	14.41	34.17	4.34	30.91
6	-40.00	300.00	12.75	3001.13	4.60	12.32	33.90	4.15	27.41
7	-30.00	310.00	11.08	3000.93	4.44	10.71	33.71	4.01	24.54
8	-30.00	330.00	8.29	3000.63	4.26	8.01	35.37	3.85	20.07
9	-20.00	340.00	7.06	3000.61	4.17	6.82	35.28	3.76	17.42
10	-20.00	350.00	5.81	3000.56	4.05	5.62	36.16	3.66	15.13
11	-10.00	350.00	4.75	3000.45	3.92	4.59	35.16	3.54	12.42
12	-10.00	360.00	3.29	3000.55	3.82	3.18	36.05	3.45	9.05
13	-10.00	370.00	2.14	3000.56	3.72	2.07	36.97	3.36	6.20

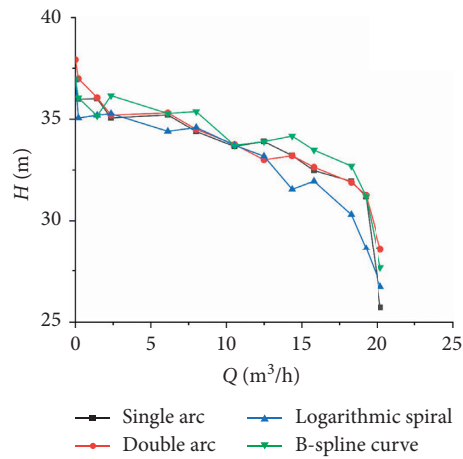


FIGURE 13:  $Q$ - $H$  curves of four profiles.

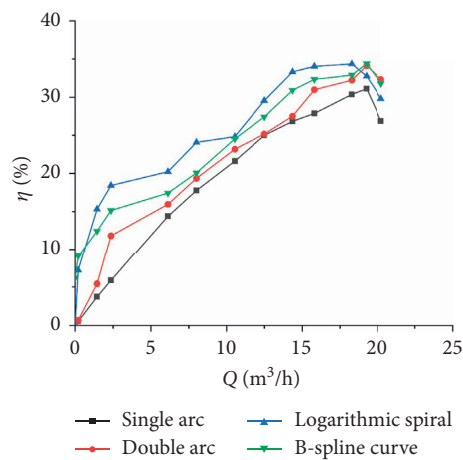


FIGURE 14:  $Q$ - $\eta$  curves four profiles.

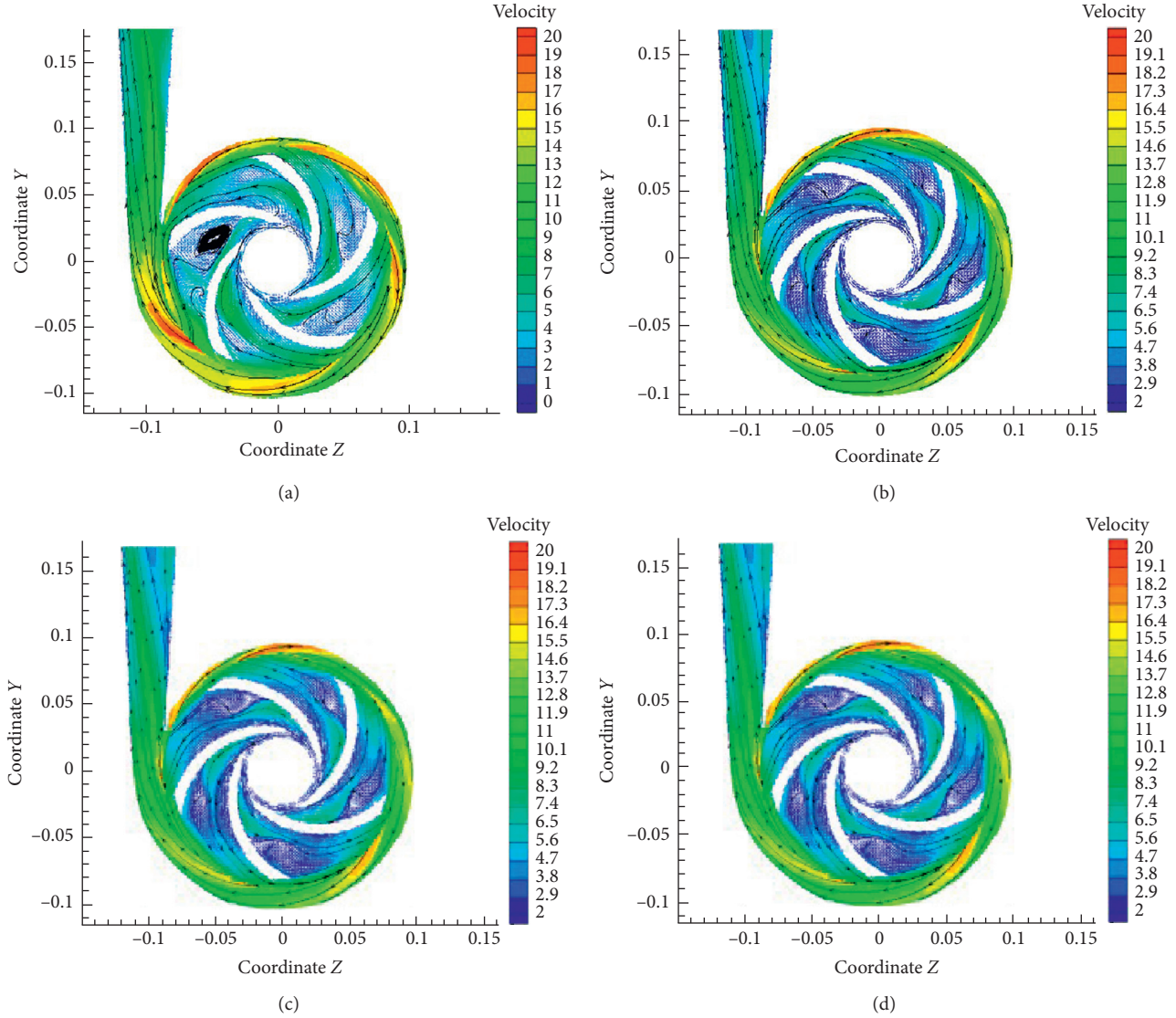


FIGURE 15: Contours of the velocity of the four impellers. (a) Single arc. (b) Double arc. (c) Logarithmic spiral. (d) B-spline curve.

## 6. Optimization of the Logarithmic Spiral Method

**6.1. Objective Function.** Based on the above analysis, it is shown that the logarithmic spiral method has the highest efficiency. To maximize the efficiency, the impeller inlet and outlet diameters ( $D_1$  and  $D_2$ ) and impeller inlet and outlet installation angles ( $\beta_1$  and  $\beta_2$ ) were taken as control variables and the total power loss and the minimum  $NPSH_r$  of the pump were taken as the objective functions to optimize the impeller structure of the logarithmic spiral method.

**6.1.1. Minimum  $NPSH_r$ .** The basic equation of  $NPSH_r$ :

$$NPSH_r = \frac{v_0^2}{2g} + \lambda \frac{\omega_0^2}{2g}. \quad (8)$$

Assuming that there is no prerotation at impeller inlet,

$$\begin{aligned} v_{u0} &= 0, \\ \omega_0^2 &= v_0^2 + u_0^2, \\ v_0 &= k_2 \frac{4Q}{(D_1^2 - d_h^2)\pi\eta_v}, \\ u_0 &= k_1 \frac{\pi n D_j}{60}, \end{aligned} \quad (9)$$

where  $k_1 = 0.876$ ;  $k_2 = 0.91$ ;  $D_j$ —impeller inlet diameter (m);  $d_h$ —impeller hub diameter (m);  $\eta_v = Q/Qt$ ;  $\lambda$ —blade inlet pressure drop coefficient,  $\lambda = 0.15-0.3$ ;  $v_0$ —the absolute velocity of the slightly forward part of the blade inlet (m/s); and  $\omega_0$ —the relative velocity of the slightly forward part of the blade inlet ( $^\circ/s$ ).

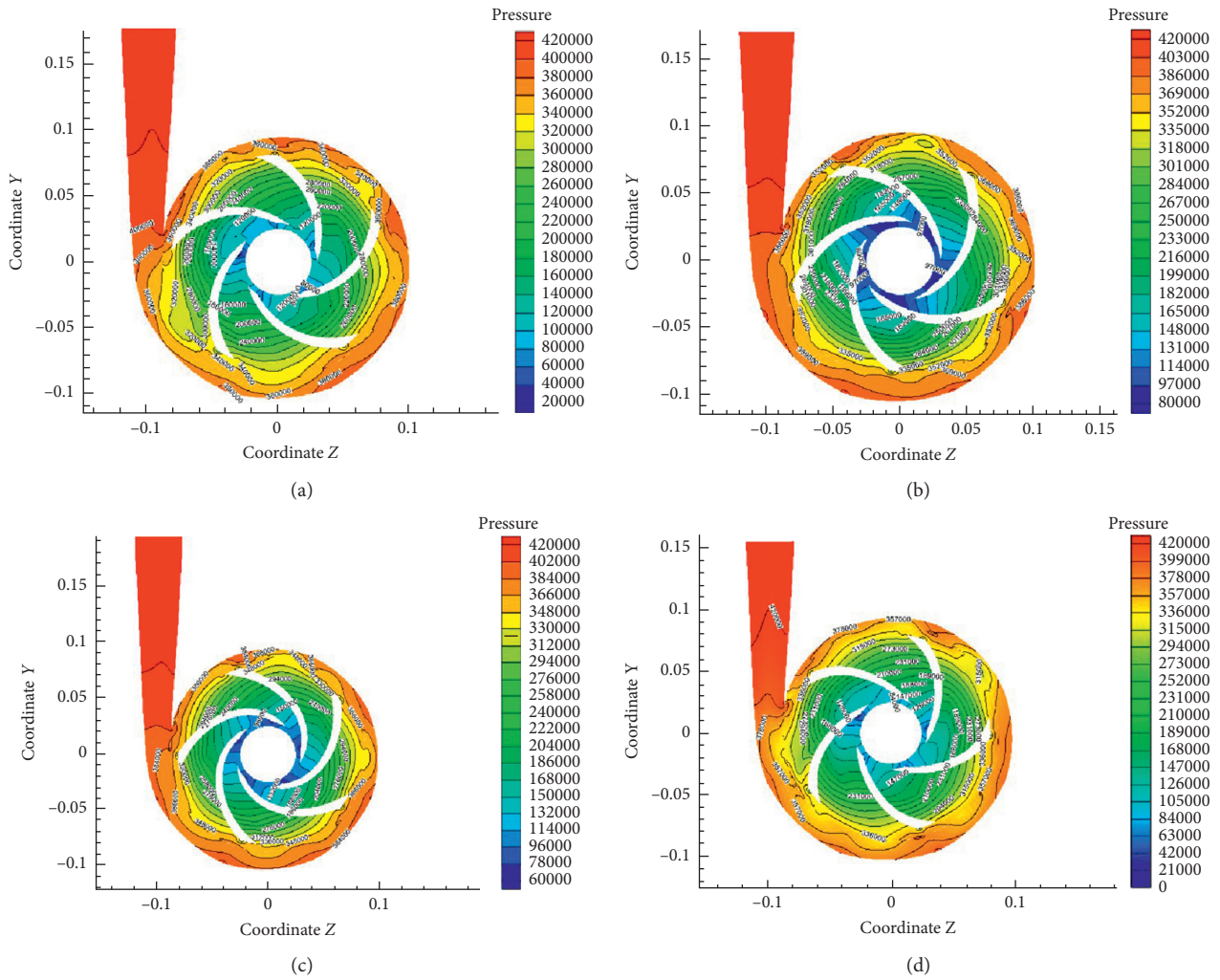


FIGURE 16: Contours of the pressure of the four impellers. (a) Single arc. (b) Double arc. (c) Logarithmic spiral. (d) B-spline curve.

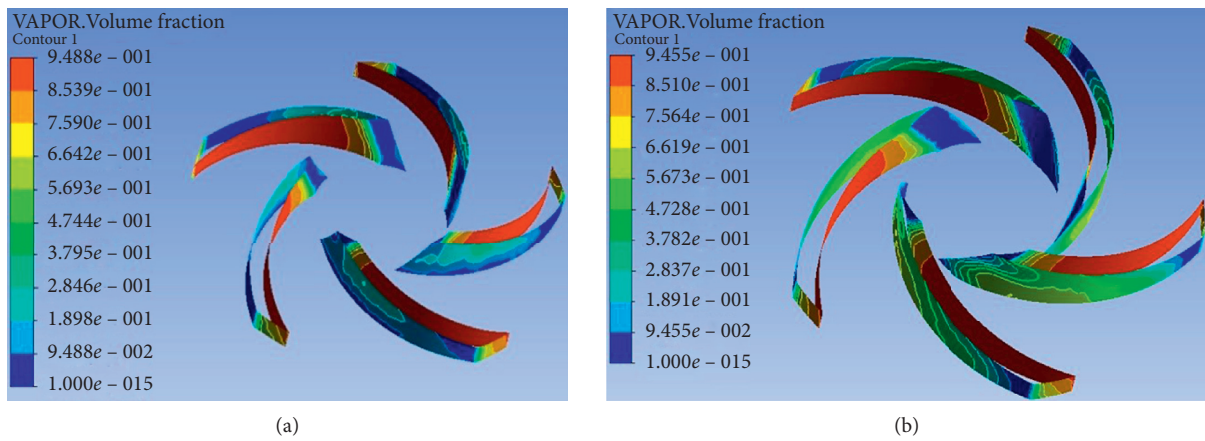


FIGURE 17: Continued.

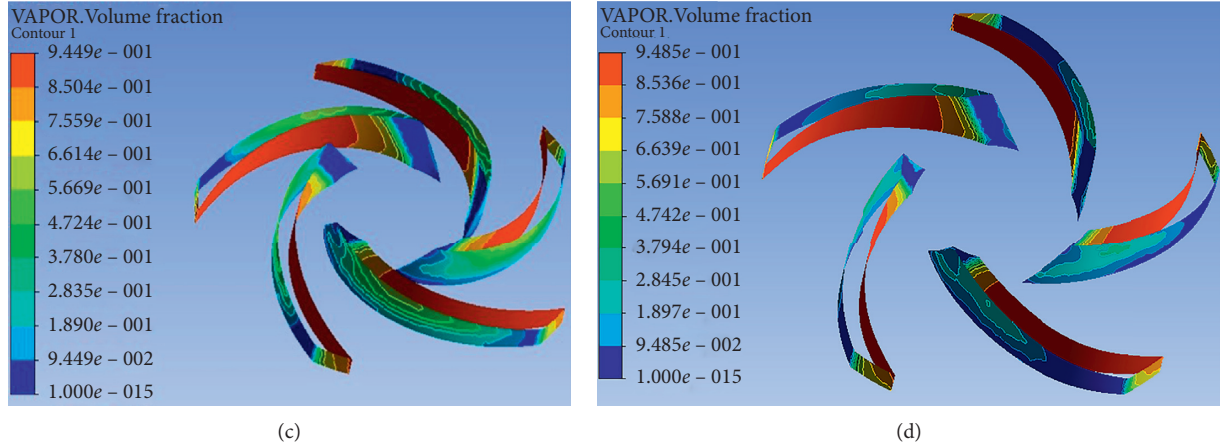


FIGURE 17: Vapor volume fraction distribution ( $NPSH_r = 1$  m). (a) Single arc. (b) Double arc. (c) Logarithmic spiral. (d) B-spline curve.

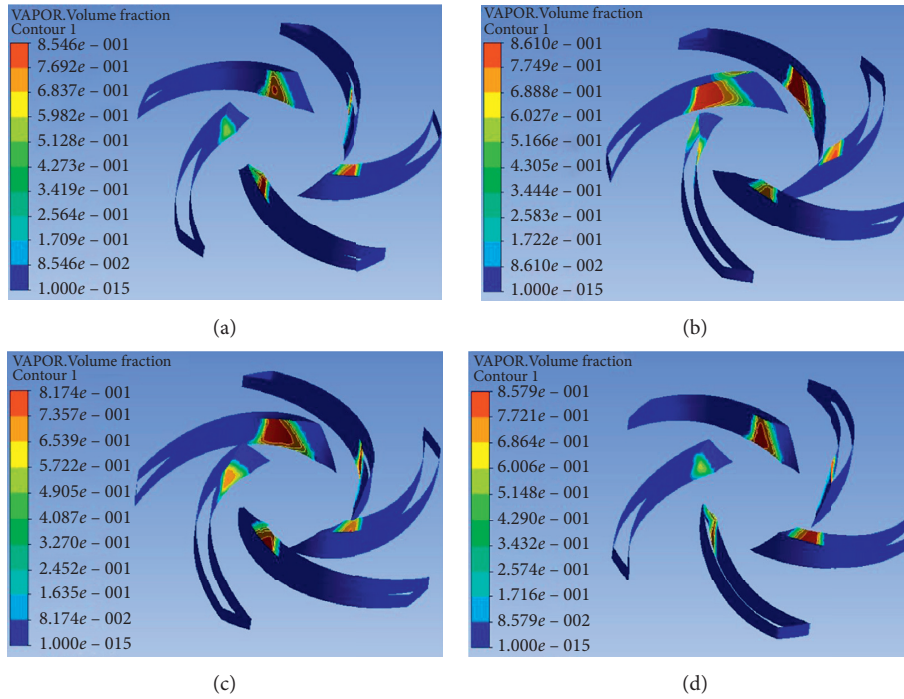


FIGURE 18: Vapor volume fraction distribution ( $NPSH_r = 2$  m). (a) Single arc. (b) Double arc. (c) Logarithmic spiral. (d) B-spline curve.

TABLE 8: Performance parameters comparison of four methods.

Method	Single arc	Double arc	Logarithmic spiral	B-spline curve
H (m)	35.4435	35.4653	35.541	35.3835
P (kW)	3.50485	3.3662	3.30089	3.51129
$\eta$ (%)	76.99	81.53	81.98	76.72

Then,

$$NPSH_r = \frac{1}{2g} (1 + \lambda) \frac{k_2^2 4^2 Q^2}{(D_1^2 - d_h)^2 \pi^2 \eta_v^2} + \lambda \frac{k_1 \pi^2 n^2 D_j^2}{60^2 \times 2g}. \quad (10)$$

Therefore, the minimum objective function of  $NPSH_r$  is  $\min [f_1(x) = NPSH_r]$ .

**6.1.2. Minimum Power Loss.** The centrifugal pump losses mainly include volume, mechanical, and hydraulic losses. The volume loss accounts for a small proportion of the total loss, so the volume loss can be ignored. The optimization model is established with the mechanical loss and hydraulic loss.

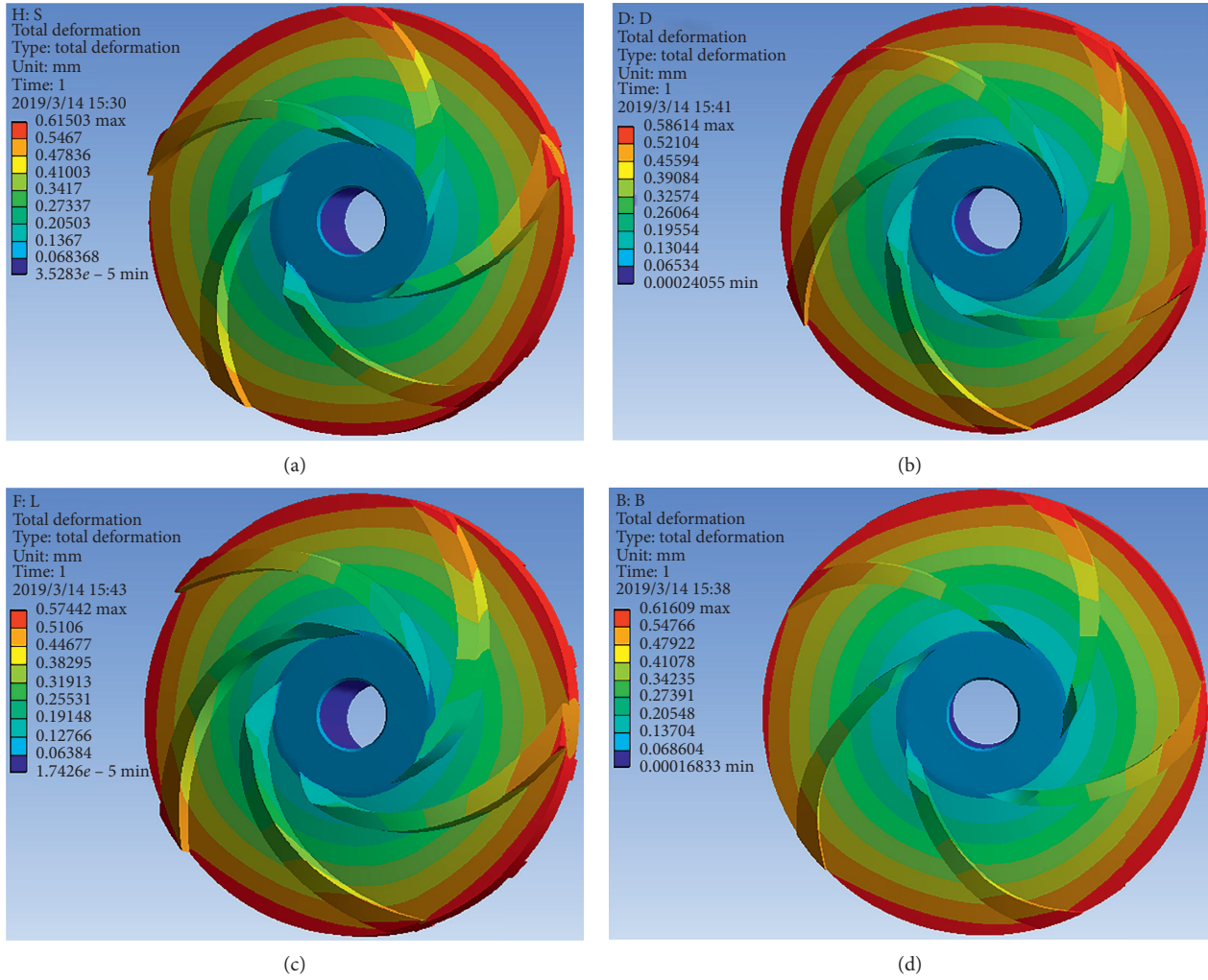


FIGURE 19: Total deformation of the impellers. (a) Single arc. (b) Double arc. (c) Logarithmic spiral. (d) B-spline curve.

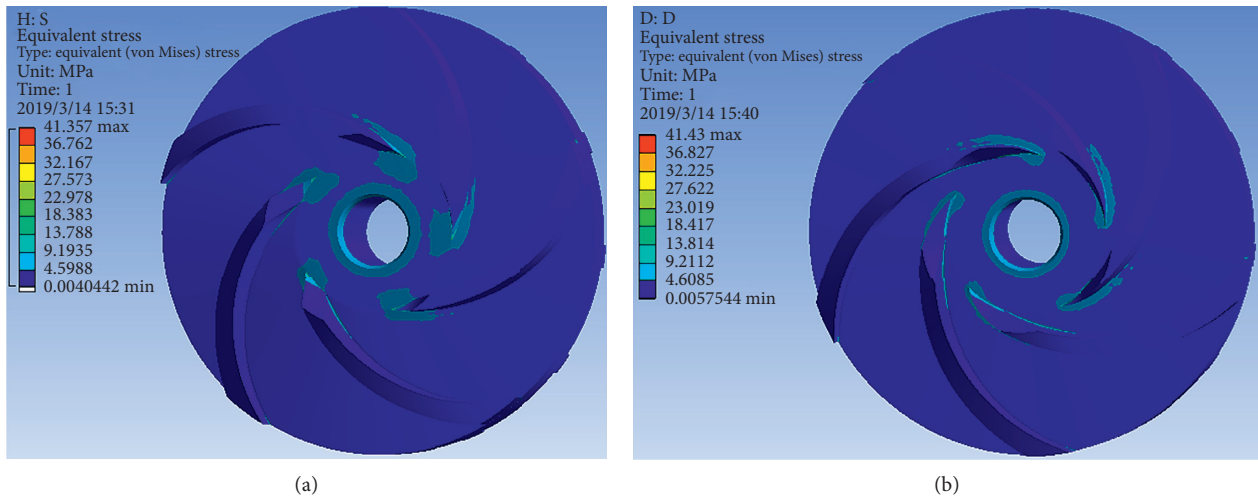


FIGURE 20: Continued.

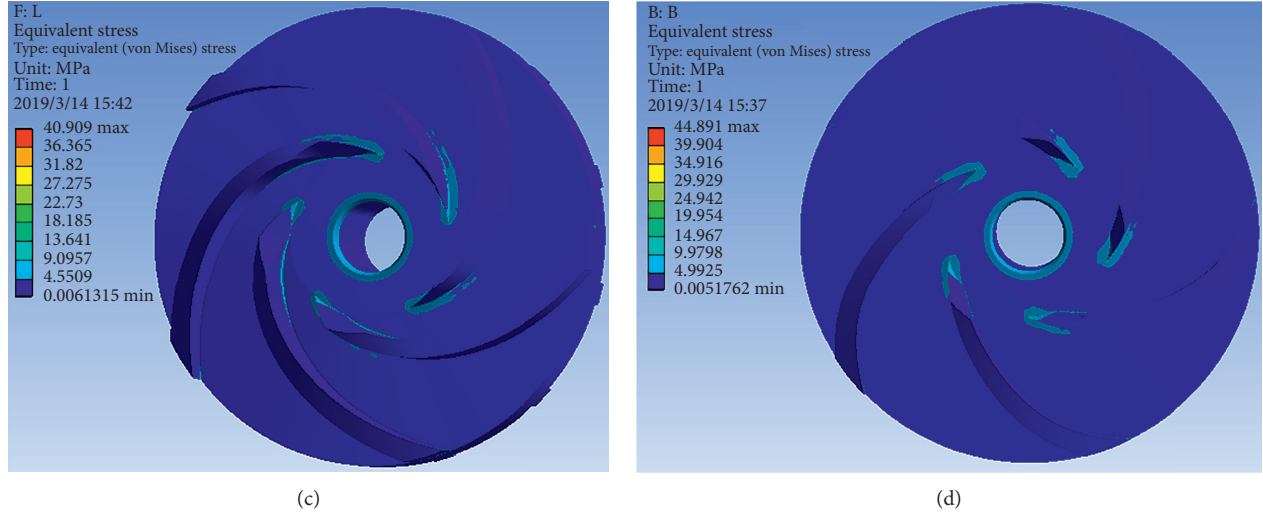


FIGURE 20: Equivalent stress of the impellers. (a) Single arc. (b) Double arc. (c) Logarithmic spiral. (d) B-spline curve.

$$P = P_{m1} + P_{m2}, \quad (11)$$

where  $P$ —total loss power (kW);  $P_{m1}$ —hydraulic loss power (kW); and  $P_{m2}$ —mechanical loss power (kW).

$$P_{m1} = \frac{t_1 \rho Q v_2^2}{2}, \quad (12)$$

$$P_{m2} = 0.35 t_2 \times 10^{-2} \rho \omega^3 R_2^5,$$

where  $t_1$ —velocity energy loss coefficient in the pressurized water chamber,  $t_1 = 0.15 \sim 0.25$ ;  $t_2$ —dimensionless disc friction coefficient,  $t_2 = 0.8 \sim 1.0$ ;  $v_2$ —the absolute velocity of impeller outlet (m/s);  $\omega$ —the rotational angular velocity of the shaft ( $^\circ/s$ ); and  $R_2$ —impeller radius (m).

Assuming that there is no prerotation at impeller inlet,  $u_1 = 0$ . According to Stodola's equation,

$$H_t = \frac{u_2}{g} \left( \sigma u_2 - \frac{V_{m2}}{\tan \beta_2} \right),$$

$$u_2 = \frac{n \pi R_2}{30}, \quad (13)$$

$$\sigma = 1 - \frac{\pi}{2} \sin \beta_2,$$

$$V_{m2} = \frac{2Q_t}{b_2 \psi_2 R_2 \pi}.$$

Then,

$$H_t = \frac{1}{g} \left[ \left( \frac{n \pi R_2}{30} \right)^2 \left( 1 - \frac{\pi \sin \beta_2}{Z} \right) - \frac{n Q_t}{60 b_2 \psi_2 \tan \beta_2} \right], \quad (14)$$

where  $u_1, u_2$ —the circumferential velocity of inlet and outlet (m/s);  $v_{u1}, v_{u2}$ —the circumferential absolute velocity of inlet and outlet (m/s);  $H_t$ —theoretical head of the pump (m);

$n$ —rotational speed (rad/s);  $\psi_2$ —crowding coefficient of impeller outlet,  $\psi_2 = 0.842$ ; and  $\sigma$ —Stodola's slip coefficient.

Impeller outlet speed triangle:

$$v_2^2 = v_{m2}^2 + v_{u2}^2,$$

$$v_{m2} = \frac{2Q_t}{\pi R_2 b_2 \psi_2}, \quad (15)$$

$$v_{u2} = \frac{g H_t}{u_2}.$$

Then,

$$P = \frac{(1 - (\pi \sin \beta_2 / Z))}{g H_t + (n Q_t / 60 b_2 \psi_2 \tan \beta_2)}$$

$$\bullet \left\{ \frac{t_1 \rho Q}{2} \left[ g^2 H_t^2 + \left( \frac{n Q_t}{60 b_2 \psi_2} \right)^2 \right] + \frac{1}{4 \times 60^2} \right.$$

$$\bullet \left. \left[ 0.35 \times 10^{-2} t_2 \rho (n \pi)^2 \left( \frac{60 g H_t}{n \pi} \right)^3 \left( 1 + \frac{n Q_t}{60 g H_t b_2 \psi_2} \right)^{(3/2)} \right] \right\}. \quad (16)$$

Therefore, the minimum objective function of  $P$  is  $\min[f_2(x) = P]$ .

**6.1.3. Unified Objective Function.** The weighting coefficient transformation method is used to deal with the two objective functions. According to the actual situation, the power loss of the plastic centrifugal pump has a greater impact on the total efficiency of the pump than NPSH<sub>r</sub>. Therefore, it is assumed that NPSH<sub>r</sub> accounts for 30% and the power loss accounts for 70% for optimization and the unified objective function is  $\min [f(x) = 0.3P + 0.7NPSH_r]$ .

**6.2. Constraint Conditions.** The constraint ranges of design variables were determined by combining the statistical

TABLE 9: Comparison of optimization design variables.

Parameters	$D_1$ (mm)	$D_2$ (mm)	$\beta_1$ (°)	$\beta_2$ (°)
Before optimization	58	162	20	30
After optimization	58	162	17	31

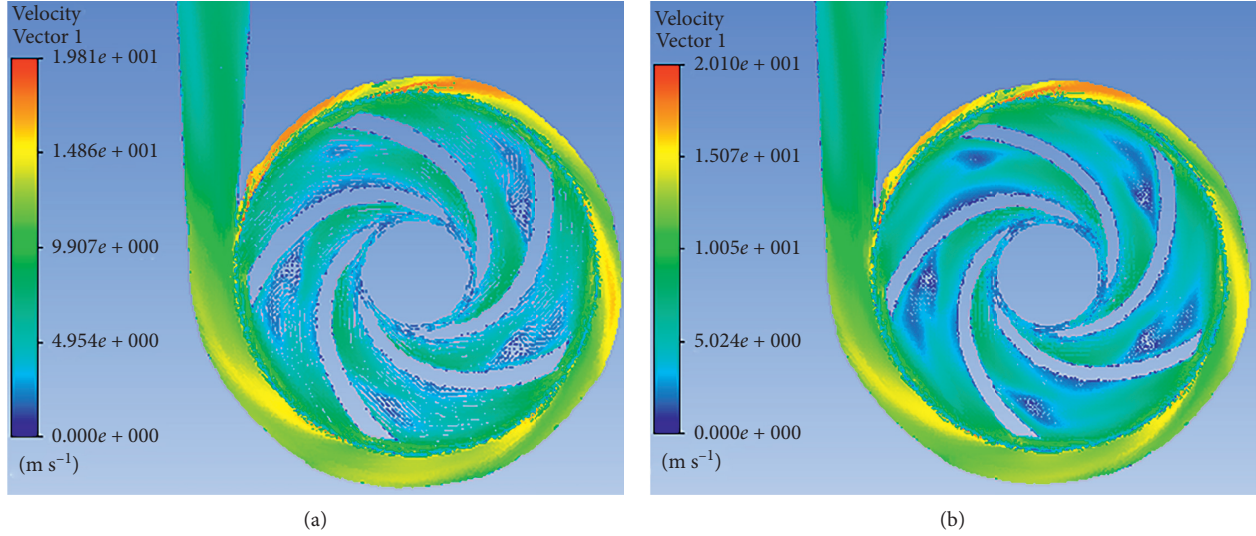


FIGURE 21: Optimization results.

formula of the velocity coefficient method with the actual excellent model pump. Then, we increased the constraint ranges appropriately.

Constraint formulas:

$$\begin{aligned}
 2\sqrt[3]{\frac{\bar{Q}}{n}} < D_1 < 4\sqrt[3]{\frac{\bar{Q}}{n}}, \\
 9.35\left(\frac{n_s}{100}\right)^{(1/2)}\sqrt[3]{\frac{\bar{Q}}{n}} < D_2 < 10.5\left(\frac{n_s}{100}\right)^{(1/2)}\sqrt[3]{\frac{\bar{Q}}{n}}, \\
 10^\circ < \beta_1 < 30^\circ, \\
 20^\circ < \beta_2 < 40^\circ.
 \end{aligned} \quad (17)$$

**6.3. Multiobjective Function Optimization.** According to the creation of a multiobjective optimization program, the four parameters of impeller inlet and outlet diameters and impeller inlet and outlet installation angles were optimized. The final optimization results were that the impeller inlet and outlet diameters were 57.778 mm and 161.57 mm and the impeller inlet and outlet installation angles were 16.836° and 30.68°. The optimization results were rounded and compared with those before optimization, and the design variables are shown in Table 9.

**6.4. Simulation Comparison and Verification.** The optimized parameters were used to remodel the impeller. Under the same working conditions, the internal flow field simulation was performed. The results after analysis are shown in

Figure 21. It can be seen that after optimization, the flow in the impeller was more sufficient. The efficiency was 83.66% after calculation, which was 1.68% higher than before. Therefore, the performance of the optimized impeller had been improved.

## 7. Conclusions

- (1) According to the basic parameters of the centrifugal pump and the four different design methods of impeller profile, the shapes and sizes of several profiles were determined. Three-dimensional models were drawn by UG software. ANSYS-ICEM software was utilized to mesh the computational domains.
- (2) According to the three-dimensional models drawn by four profile design methods, the impeller models were printed by 3D printing technology. The performance experiments of the plastic centrifugal pumps were carried out. The experimental results showed that the logarithmic spiral method was the best and the single arc method was the worst.
- (3) The analysis of numerical simulation was performed by FLUENT software. From the contours of velocity and pressure, the flow field in the impeller drawn by the logarithmic spiral method was significantly better. The maximum pressure values corresponding to the four methods were 437563 Pa, 441628 Pa, 438368 Pa, and 435518 Pa. From the vapor volume fraction distribution, when  $NPSH_r = 1$  m and 2 m,

the impeller drawn by the logarithmic spiral method was significantly better than the other three impellers. According to the calculation of performance parameters, it can be concluded that the impeller drawn by the logarithmic spiral method was the optimal impeller under the design condition.

- (4) ANSYS-CFX software was used to complete the fluid-structure interaction analysis. The maximum total deformation of the impellers drawn by the four profile design methods was 0.61503 mm, 0.58614 mm, 0.57442 mm, and 0.61609 mm, respectively. Deformation: B-spline curve method > single arc method > double arc method > logarithmic spiral method. The maximum equivalent stress of the impellers drawn by the four profile design methods was 41.357 MPa, 41.43 MPa, 40.909 MPa, and 44.891 MPa, respectively. Equivalent stress: B-spline curve method > double arc method > single arc method > logarithmic spiral method.
- (5) Based on the analysis, the impeller drawn by the logarithmic spiral method had the highest efficiency. To maximize the efficiency, the impeller inlet and outlet diameters ( $D_1$  and  $D_2$ ) and impeller inlet and outlet installation angles ( $\beta_1$  and  $\beta_2$ ) were taken as control variables and the total power loss and the minimum NPSH<sub>r</sub> of the pump were taken as the objective functions. The final optimization results were that the impeller inlet and outlet diameters were 58 mm and 162 mm and the impeller inlet and outlet installation angles were 17° and 31°. The hydraulic efficiency was increased by 1.68% after calculation, which indicated that the impeller structure had been improved.

## Abbreviations

$D_1$ :	Impeller inlet diameter, mm
$D_2$ :	Impeller outlet diameter, mm
$\beta_1$ :	Impeller inlet installation angle, °
$\beta_2$ :	Impeller outlet installation angle, °
$\rho$ :	Radius of curvature, mm
$R_1$ :	Impeller inlet radius, mm
$R_2$ :	Impeller outlet radius, mm
$R_f$ :	Radius of rotation of the point $F$ , mm
$\beta_f$ :	Blade angle of point $F$ , °
$Z$ :	Number of blades
$\beta$ :	Impeller installation angle, °
$\psi$ :	Wrap angle, °
$\theta$ :	Variation of wrap angle $\psi$ , °
$Q$ :	Flow rate, m <sup>3</sup> /h
$H$ :	Pump head, m
$n$ :	Rotational speed, r/min
$n_s$ :	Specific speed
$P_t$ :	Shaft power, kW
$D_j$ :	Impeller inlet diameter, m
$d_h$ :	Impeller hub diameter, m
$\lambda$ :	Blade inlet pressure drop coefficient
$v_0$ :	Absolute velocity of the slightly forward part of the blade inlet, m/s

$\omega_0$ :	Relative velocity of the slightly forward part of the blade inlet, °/s
$P$ :	Total loss power, kW
$P_{m1}$ :	Hydraulic loss power, kW
$P_{m2}$ :	Mechanical loss power, kW
$t_1$ :	Velocity energy loss coefficient in the pressurized water chamber
$t_2$ :	Dimensionless disc friction coefficient
$v_2$ :	Absolute velocity of impeller outlet, m/s
$u_1$ :	Circumferential velocity of inlet, m/s
$u_2$ :	Circumferential velocity of outlet, m/s
$v_{u1}$ :	Circumferential absolute velocity of inlet, m/s
$v_{u2}$ :	Circumferential absolute velocity of outlet, m/s
$H_t$ :	Theoretical head of the pump, m
$\psi_2$ :	Crowding coefficient of impeller outlet
$\sigma$ :	Stodola's slip coefficient.

## Data Availability

The data used to support the findings of this study are included within the article.

## Conflicts of Interest

The authors declare that they have no conflicts of interest.

## Acknowledgments

This work was supported by the University Synergy Innovation Program of Anhui Province (GXXT-2019-004), the Teaching Research Project of Anhui Education Department (2019jyxm0229), and the Natural Science Foundation of Anhui Province Education Department (KJ2017ZD12).

## References

- [1] M. Tan, Y. Lu, X. Wu, H. Liu, and X. Tian, "Investigation on performance of a centrifugal pump with multi-malfunction," *Journal of Low Frequency Noise, Vibration and Active Control*, Article ID 146134842094234, 2020.
- [2] M. Liu, L. Tan, and S. Cao, "Theoretical model of energy performance prediction and BEP determination for centrifugal pump as turbine," *Energy*, vol. 172, pp. 712–732, 2019.
- [3] X. Li, B. Chen, X. Luo, and Z. Zuchao, "Effects of flow pattern on hydraulic performance and energy conversion characterisation in a centrifugal pump," *Renewable Energy*, vol. 151, pp. 475–487, 2020.
- [4] D. Wu, Y. Ren, J. Mou et al., "Unsteady flow and structural behaviors of centrifugal pump under cavitation conditions [J]," *Chinese Journal of Mechanical Engineering*, vol. 32, no. 01, pp. 127–141, 2019.
- [5] X. Li, Z. Jiang, and Z. Zhu, "Entropy generation analysis for the cavitating head-drop characteristic of a centrifugal pump," *Archive Proceedings of the Institution of Mechanical Engineers Part C Journal of Mechanical Engineering Science*, vol. 203-210, 2018. <https://www.semanticscholar.org/author/Q.-Si/2164738><https://www.semanticscholar.org/author/Y.-Li/47002268>, Article ID 095440621775345.
- [6] P. A. Kumar, R. J. Shruti, and T. Rajiv, "Prediction of flow blockages and impending cavitation in centrifugal pumps using

- Support Vector Machine (SVM) algorithms based on vibration measurements,” *Measurement*, vol. 130, pp. 44–56, 2018.
- [7] X. He, W. Jiao, C. Wang, and C. Weidong, “Influence of surface roughness on the pump performance based on computational fluid dynamics,” *IEEE Access*, vol. 99, p. 1, 2019.
- [8] H. S. Shim, K. Y. Kim, and Y. S. Choi, “Three-objective optimization of a centrifugal pump to reduce flow recirculation and cavitation,” *Journal of Fluids Engineering*, vol. 140, no. 9, 14 pages, Article ID 091202, 2018.
- [9] Y. Li, G. Feng, and X. Li, Z. Zuchao, An experimental study on the cavitation vibration characteristics of a centrifugal pump at normal flow rate,” *Journal of Mechanical Science and Technology*, vol. 32, no. 10, pp. 4711–4720, 2018, [https://www.researchgate.net/profile/Quiorui\\_Si](https://www.researchgate.net/profile/Quiorui_Si).
- [10] A. R. Al-Obaidi, “Investigation of effect of pump rotational speed on performance and detection of cavitation within a centrifugal pump using vibration analysis,” *Heliyon*, vol. 5, no. 6, 2019.
- [11] D. O. W. Dimar, V. D. S. Martijn, and N. P. Kruyt, “Prediction of the effect of impeller trimming on the hydraulic performance of low specific-speed centrifugal pumps,” *Journal of Fluids Engineering*, vol. 140, no. 8, 2018.
- [12] Y. Yuan, S. Yuan, and L. Tang, “Investigation on the effect of complex impeller on vibration characteristics for a high-speed centrifugal pump,” *Proceedings of the Institution of Mechanical Engineers Part A Journal of Power and Energy*, vol. 234, no. 5, Article ID 095765091987831, 2019.
- [13] B. Cui, C. Zhang, Y. Zhang, and Z. Zhu, “Influence of cutting angle of blade trailing edge on unsteady flow in a centrifugal pump under off-design conditions,” *Applied Sciences*, vol. 10, no. 2, p. 580, 2020.
- [14] Y. Song, Z. Yu, G. Shi et al., “Influence of impeller staggered arrangement on radial force and pressure fluctuation for a double-suction centrifugal pump,” *Advances in Mechanical Engineering*, vol. 10, p. 6, 2018.
- [15] J. M. Jin, K. J. Jung, Y. H. Kim, and Y.-J. Kim, “Effects of gap between impeller and volute tongue on a pressure fluctuation in double-suction pump,” *Journal of Mechanical Ence and Technology*, pp. 1–7, 2020.
- [16] D. C. Fu, F. J. Wang, P. J. Zhou et al., “Impact of impeller stagger angles on pressure fluctuation for a double-suction centrifugal pump,” *Chinese Journal of Mechanical Engineering*, vol. 31, no. 1, p. 10, 2018.
- [17] H. Yousefi, Y. Noorollahi, M. Tahani, R. Fahimi, and S. Saremian, “Numerical simulation for obtaining optimal impeller’s blade parameters of a centrifugal pump for high-viscosity fluid pumping,” *Sustainable Energy Technologies and Assessments*, vol. 34, pp. 16–26, 2019.
- [18] N. A. Mandhare, K. Karunamurthy, and S. Ismail, “Computational investigation of flow over nose cap of closed impeller of mixed flow centrifugal pump,” *Journal of Pressure Vessel Technology*, vol. 142, no. 3, 2019.
- [19] L. Dong, Y. Zhao, H. Liu et al., “The effect of front streamline wrapping angle variation in a super-low specific speed centrifugal pump,” *Journal of Mechanical Engineering Science*, vol. 232, no. 23, Article ID 095440621877260, 2018.
- [20] D. Zindani, A. K. Roy, and K. Kumar, “Design of mixed flow pump impeller blade using mean stream line theory and its analysis,” *Scientia Iranica*, 2018.
- [21] Y. Tao, S. Yuan, and J. Liu, T. Jianping, The influence of the blade thickness on the pressure pulsations in a ceramic centrifugal slurry pump with annular volute,” *Journal of Power and Energy*, vol. 231, no. a5, pp. 415–431, 2017, [https://www.researchgate.net/profile/Fan\\_Zhang410](https://www.researchgate.net/profile/Fan_Zhang410).
- [22] R. Tao, R. Xiao, and Z. Wang, “Influence of blade leading-edge shape on cavitation in a centrifugal pump impeller,” *Energies*, vol. 11, no. 10, p. 11, 2018.
- [23] G. Peng, Q. Chen, L. Zhou, B. Pan, and Y. Zhu, “Effect of blade outlet angle on the flow field and preventing overload in a centrifugal pump,” *Micromachines*, vol. 11, no. 9, p. 811, 2020.
- [24] W. Yu-Qin and D. Ze-Wen, “Influence of blade number on flow-induced noise of centrifugal pump based on CFD/CA,” *Vacuum*, vol. 172, Article ID 109058, 2019.
- [25] X. Han, Y. Kang, J. Sheng et al., “Centrifugal pump impeller and volute shape optimization via combined NUMECA, genetic algorithm, and back propagation neural network,” *Structural and Multidiplinary Optimization*, vol. 61, no. 3, 2019.
- [26] R. H. Zhang, L. C. Yun, and J. Li, “Investigation on the effect of impeller slot jet on centrifugal pump performance,” *Journal of Hydrodynamics*, vol. 31, no. 3, 2018.
- [27] H. Wang, B. Long, C. Wang et al., “Effects of the impeller blade with a slot structure on the centrifugal pump performance,” *Energies*, vol. 13, no. 7, 2020, <https://www.researchgate.net/deref/http%3A%2F%2Fdx.doi.org%2F10.3390%2Fen13071628>.
- [28] J. Li, L. Tang, and Y. Zhang, “The influence of blade angle on the performance of plastic centrifugal pump,” *Advances in Materials Science and Engineering*, vol. 2020, Article ID 7205717, 20 pages, 2020.
- [29] J. Hu, Y. Chen, Y. Wang, J. Cheng, and J. Zhao, “New method for drawing two arc cylindrical blade of centrifugal pump,” *Chemical Equipment Technology*, vol. 37, no. 2, pp. 24–26, 2016.
- [30] D. M. S. El-Gazzar and S. A. A. F. Hawash, “Optimizing centrifugal pump performance by different blade configuration patterns,” *American Journal of Mechanical and Industrial Engineering*, vol. 3, no. 1, p. 1, 2018.
- [31] J. Ming, L. Dong, H. Liu et al., “Research of variable angle spiral method for cylindrical blade profile in centrifugal pump,” *Water Resources and Power*, vol. 35, no. 1, pp. 180–183, 2017.

## Research Article

# A Stochastic Model of Stress Evolution in a Bolted Structure in the Presence of a Joint Elastic Piece: Modeling and Parameter Inference

Mohammed Haiek <sup>1</sup>, Youness El Ansari <sup>2</sup>, Nabil Ben Said Amrani <sup>1</sup>, and Driss Sarsri <sup>1</sup>

<sup>1</sup>Laboratory of Innovative Technologies, National School of Applied Sciences of Tangier, Abdelmalek Essaâdi University, B. P. 1818, Tangier, Morocco

<sup>2</sup>High School of Technology, Ibn Zohr University, B. P. 80150, Agadir, Morocco

Correspondence should be addressed to Mohammed Haiek; [haiek.mohammed@gmail.com](mailto:haiek.mohammed@gmail.com)

Received 19 August 2020; Revised 30 September 2020; Accepted 20 October 2020; Published 31 October 2020

Academic Editor: Jinyang Xu

Copyright © 2020 Mohammed Haiek et al. This is an open access article distributed under the Creative Commons Attribution License, which permits unrestricted use, distribution, and reproduction in any medium, provided the original work is properly cited.

In this paper, we propose a stochastic model to describe over time the evolution of stress in a bolted mechanical structure depending on different thicknesses of a joint elastic piece. First, the studied structure and the experiment numerical simulation are presented. Next, we validate statistically our proposed stochastic model, and we use the maximum likelihood estimation method based on Euler–Maruyama scheme to estimate the parameters of this model. Thereafter, we use the estimated model to compare the stresses, the peak times, and extinction times for different thicknesses of the elastic piece. Some numerical simulations are carried out to illustrate different results.

## 1. Introduction

The bolted structures are widely used in automotive and aeronautical applications, and they ensure very good rigidity of the assembly and high level of security. The dynamic modeling of bolted structures is the subject of numerous works in the industrial as well as in the academic community, and it represents a real challenge for mechanical engineers. Several studies [1–3] have been carried out to model this kind of structure, with taking into account the influence of diverse solicitations such as creep, pressure, thermal charging, vibration, and fatigue. In this framework, putting an elastic joint piece between two plates of the assembly allows to obtain a great stability of the structure. The purpose of this technique is to absorb the distribution of stresses causing by the existing of significant vibration transfer and von Mises stress, from one plate to another.

Our original contribution in this paper consists to model the influence of the existence of an elastic piece on the dynamic behavior bolted mechanical structure which is

under the effect of von Mises stress. We start out in Section 1 with a description of the studied bolted structure; then, we use in first time a finite element (EF) analysis approach to investigate the parameters that may affect the stress concentration in a bolted assembly, depending of different thicknesses of the elastic piece. The EF numerical simulation by ABAQUS software is described, and the results of the simulations are presented (simulation inputs and obtained data) in Section 2.

Thereafter, this data are exploited to evaluate the correlation between the stress applied and the thickness of the joint elastic piece. In other terms, we are modeling stochastically the stress variation over time of a bolted structure in function of the thickness of a joint elastic piece. This correlation is made by a Pearson test.

Therefore, a stochastic model is built, and its parameters are estimated; this new model allows predicting the point of stress stability (stress peak) of behavior of bolted structure studied, its time (stress peak time) and its extinction time. First step is to verify the stress distribution normality by a

graphical test, which is carried out by the Q-Q plot (Quantile-Quantile plot) model; this tool is used to determine the best fit for the duration of phonemes. The q-q plot shows the relationship between the quantiles of expected distribution and actual data. Also, a Shapiro–Wilk test is made to demonstrate the distribution normality by the analytical method.

Section 3 aims to validate the effectiveness of the proposed stochastic model and to estimate its parameter by the Euler-maximum likelihood estimation method. Section 4 is dedicated to predict the stress peak and the stress extinction time and to discuss the results of our modeling. In Section 5, new simulations are carried out with a steel piece with different thicknesses, in order to compare their results with the previous results obtained for the bolted structure with the joint elastic piece. We finish by a conclusion and some perspectives.

*1.1. State of Art.* In the literature, several mathematical methods have been handled in order to ensure the validity of bolted structures. The finite element (FE) analysis has been used to examine the bolt hole clearance effect on the mechanical behavior of a bolted structure [4]. Also, Hashin's failure criteria have been used to predict the failure onset load (see [5, 6]). These studies applied principally analytical methods supported with some included experimental results and lead to draw several conclusions to model more complex structures.

Also, several stochastic models have remained an effective tool to analyze the behaviors of mechanical structures by taking into consideration the randomness of mechanical properties. These models introduce uncertainties in the parameters of deterministic models by supposing that they are subject to environmental fluctuations, which gives more realism to the results.

Constructing and studying deterministic and stochastic models belong to the most beneficial methods to estimate the relation between the input parameters of the structure finite element model and the response parameters of interest. In this context, McCarthy and Gray [7] proposed and analyzed a deterministic model for predicting the distribution of loads in multibolt composite joints [8]. In other investigation, Lacour et al. [9] have modeled the von Mises stress, stiffness, and displacements by a nonlinear stochastic model at each degree of freedom.

In order to formulate a stochastic finite element method for nonlinear material models, the same authors have applied a discrete approach to develop a constitutive algorithm which can be implemented on a global level of the context 3D nonlinear stochastic finite element method [10]. In this work, our proposed modeling is done by the continuous stochastic model, and it should be noticed that it has not been treated before in the literature.

## 2. Experiment Numerical Simulation and Data

*2.1. Description of the Studied Structure.* For aeronautic and automotive applications, bolted assemblies are subjected to

traction, compression, torsional torque, and thermal and centrifugal forces. As presented in Figure 1, the studied bolted structure is submitted to compressive stress, and an elastic piece is put between the two steel plates in the assembly area. Figure 1 indicates all the ratings used. The parameters related to the substrate are the thickness of the elastic piece, the width, and the length of the two plates, as well as the diameter of the hole from the middle to the contact zone.

*2.2. Compression Test Simulation.* First, we aim to simplify the meshing of the finite element (FE) model of the studied structure, by substituting its geometry with elements having an equivalent behavior. The simulations using ABAQUS software are carried out. ABAQUS is an excellent software tool which can incorporate the nonlinearity of materials, geometry, asticity (strain hardening), large displacement, contact problem, etc. The geometry of the structure was created by using the modules Parts and Assembly in ABAQUS software (see Figure 2).

The material properties for the different pieces of the structure have been chosen according to the type of material. For the materials of construction, the two plates and the bolt are made of steel, while the elastic piece is made of rubber. The material properties of the different pieces of the structure are detailed in Table 1:

In this simulation, compression loads of  $50 \text{ N/mm}^2$  was applied to the side face of the upper plate (see Figure 2), and we modified the thickness of the elastic piece to study the dynamic response of the structure and then, to model the von Mises constraint distribution in the lower plate of the structure, which depends on time and thickness.

All the simulations below are performed using an explicit dynamic step. The contact properties between the parts of the structure are defined. During this meshing, we obtain a three-dimensional continuum of 8 inclined brick elements. Finally, we can run the simulation and extract the results.

*2.3. Result Finite Element Simulation.* Finite element (FE) analysis is a relatively inexpensive and fast alternative to physical experiments. Reliable test data are essential to calibrate an FE model. If the validity of FE analysis is ensured, it is possible to model the dynamic response of the structure with the number of parameters.

The elastic piece thickness is modified from 0 mm to 2 mm and for each thickness a numerical simulation is made. For each simulation step, we apply the same conditions in order to investigate thickness effect in the distribution of the vonMises stress applied in the lower plate of the structure. Figure 3 shows the simulation results for only 7 types of thicknesses, in order to study the stresses distribution on the lower plate in function of the thickness of the elastic part.

The results of the simulations show that the stresses are concentrated in the contact zone, between the lower plate and the elastic piece. In the case of the structure without elastic piece, the stresses are distributed around the holes. With a thickness of 0 mm, it can be seen that the stresses are

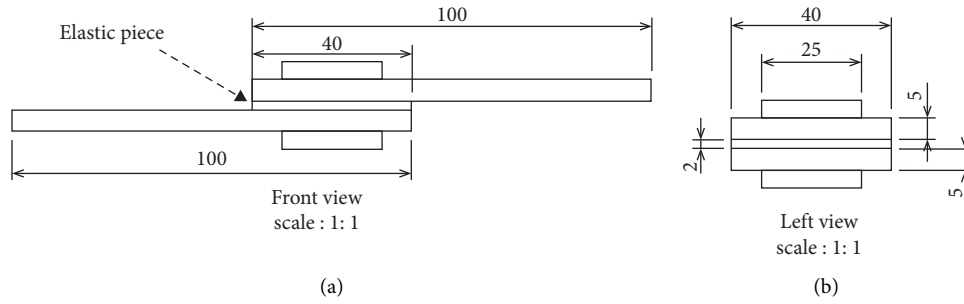


FIGURE 1: The overall drawing of the studied structure with elastic piece.

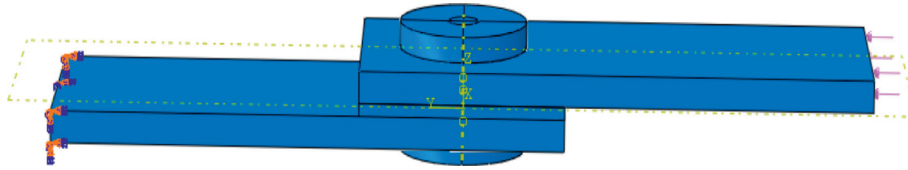


FIGURE 2: Numerical experiment of bolted structure compression test.

TABLE 1: Material properties of the structure components.

	Young modulus $E$ (MPa)	Poisson ratio	Density ( $T/mm^2$ )
Steel plates	$210e3$	0.3	$7.8e-9$
Elastic piece	100	0.46	$9.45e-10$
Bolt	$210e3$	0.3	$7.8e-9$

distributed over the entire lower plate and that its distribution reaches its maximum in the periphery of the hole.

For each simulation, an element of the lower plate is chosen in the contact area where the stress distribution is maximum. In order to efficiently observe the influence of the thickness change on the stress evolution and to properly interpret the results, we make a representation of this stress as function of time. The simulation results for 7 thicknesses are presented in Figure 4.

It can be seen that the stress in the bolted structure with elastic piece thickness 0, 0.1, 0.7, and 1 is significantly higher compared to the stress in the structure bolted with elastic piece thickness 0.4 and 0.9. Accordingly, the simulation result reveals that there exists any correlation between the stress evolution and the elastic piece thickness. In order to confirm the last hypothesis, a Pearson test is carried out. Table 2 summarizes the results of this test.

As can be see from the results above the  $p$  value of the test is 0.7794, which is bigger than the significance level  $\alpha = 0.05$ . We can conclude that the stress and the joint elastic piece thickness are not correlated. Officially, the thickness does not affect the stress.

In the following section, a stochastic model is built, and its parameters are estimated.

### 3. Model and Parameter Estimation

*3.1. Stochastic Model of Modelisation.* The QQ plot (or quantile-quantile plot) establishes the correlation between a

given sample and the normal distribution. A 45-degree reference line is also drawn. In a QQ plot, each observation is plotted as a single point. If the data are normal, the points should form a straight line. The following figure gives the QQ plot linked to the stress sample of each elastic piece thickness.

We can remark from Figure 5 that all points lie approximately along this reference line, and we can assume the normality of the stress sample linked the given elastic piece thicknesses. Visual inspection, as described in previously, is generally unreliable. A significance test comparing the sample distribution to a normal distribution can be used to determine whether or not the data shows a significant deviation from the normal distribution. There are several methods for assessing normality, including the Kolmogorov–Smirnov (K-S) normality test and the Shapiro–Wilk test. The Shapiro–Wilk test is widely recommended for normality testing and provides better power than K-S test. It is based on the correlation between the data and the corresponding normal scores (see Ghasemi and Zahediasl [11]). The following table summarizes the results of the Shapiro–Wilks test for all the samples of stresses with different elastic piece thicknesses.

According to Table 3, for each elastic piece thickness, the  $p$  value  $>0.05$  indicates that the corresponding stress distribution is not significantly different from the normal distribution. In other words, we can assume normality of all the distribution. Thus, if  $x(t)$  is the one-dimensional variable that represents the stress density linked to a piece elastic thickness per second, so

$$x(t) = c_0 \exp\left(-\frac{1}{2} \left(\frac{t - \mu}{\sigma}\right)^2\right), \quad (1)$$

where  $c_0$ ,  $\mu$ , and  $\sigma$  are constant characteristics. By deriing  $x(t)$  along time, we obtain

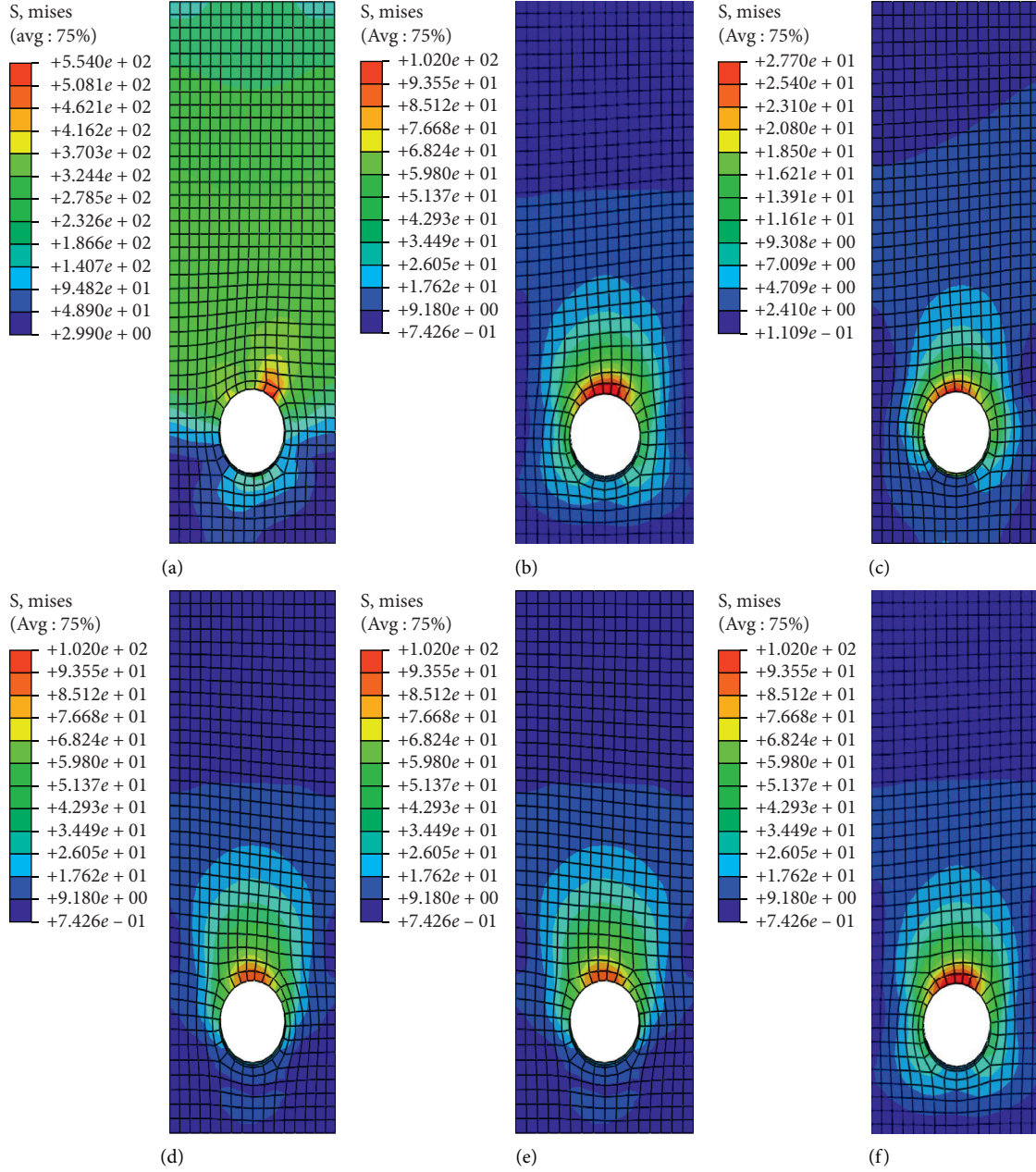


FIGURE 3: Results of experiment numerical simulation: (a) thickness=0, (b) thickness=0.1, (c) thickness=0.4, (d) thickness=0.7, (e) thickness=0.9, and (f) thickness=1.

$$dx(t) = \frac{1}{\sigma^2} (\mu - t)x(t)dt, \quad (2)$$

and we suppose that the parameter  $\mu$  is subject to random fluctuations. We replace  $\mu$  by  $\mu + \rho(dB/dt)$  in equation (2), where  $B(t)$  is a standard one-dimensional Brownian motions and  $\rho$  is the intensity of the perturbation. We obtain the following stochastic model:

$$dx(t) = \frac{1}{\sigma^2} (\mu - t)x(t)dt + \frac{\rho}{\sigma^2} x(t)dB(t). \quad (3)$$

3.2. *Parameter Estimation.* Let  $[0, T]$  a time interval and  $(t_i)_{0 \leq i \leq K}$  be a subdivision of this interval. We suppose that the step  $\Delta_i = t_i - t_{i-1} = \Delta$  for all  $i \in (0, 1, \dots, K)$ . The numerical approximation of model (3) by Euler-Maruyama scheme gives

$$x(t_i) = x(t_{i-1}) \frac{1}{\sigma^2} (\mu - t_{i-1})x(t_{i-1})\Delta_t + x(t_{i-1})\xi_i, \quad (4)$$

$$0 \leq i \leq K,$$

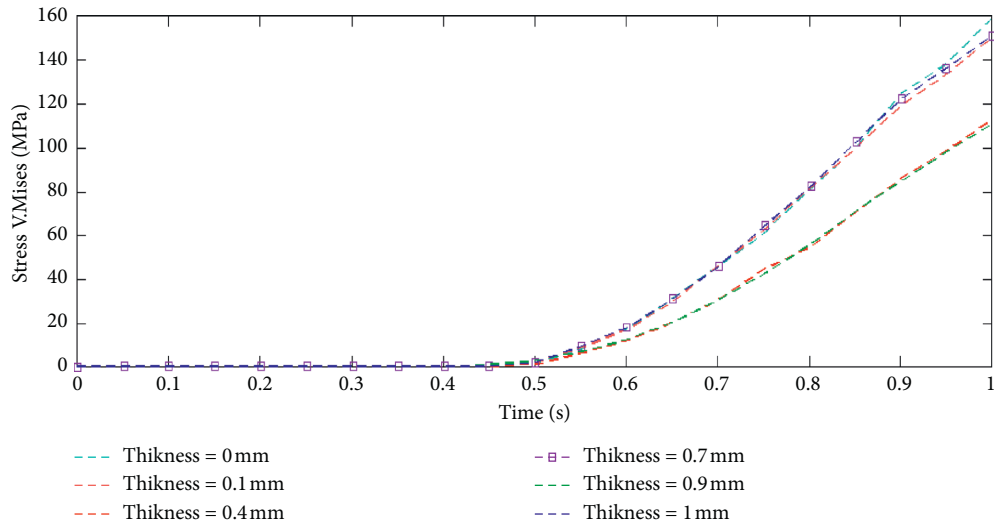


FIGURE 4: Stress evolution as function of time and of elastic piece thickness at an element of the lower plate.

TABLE 2: The results of the Pearson test of correlation between the stress and the elastic piece thickness.

		Thickness	Stress
Thickness	Pearson correlation	1	-0.0906
	Sig.(bilateral)		<b>0.7794</b>
	<i>N</i>	10	10
Stress	Pearson correlation	-0.0906	1
	Sig.(bilateral)	<b>0.7794</b>	
	<i>N</i>	10	10

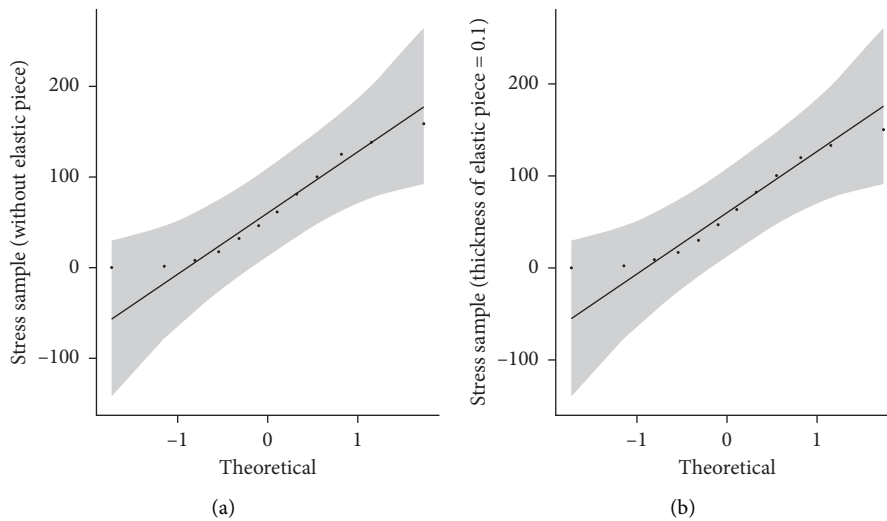


FIGURE 5: Continued.

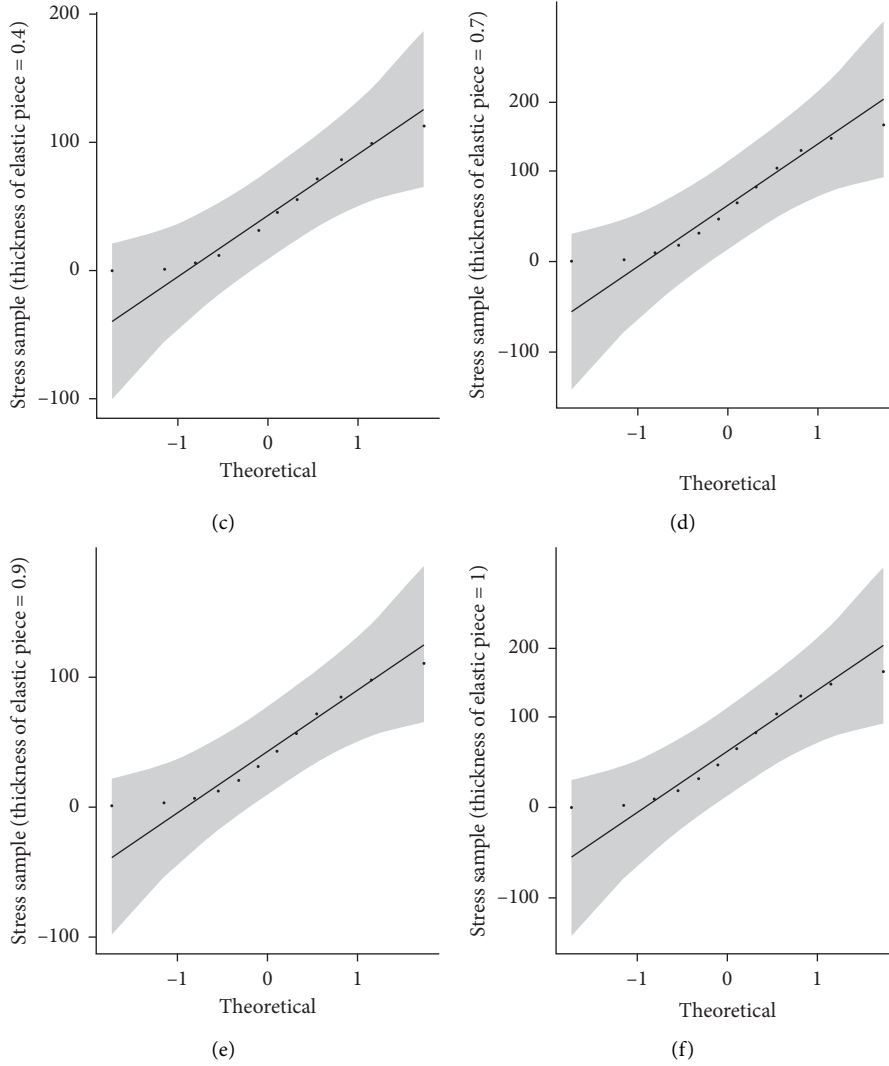


FIGURE 5: QQ plots testing the normality of the stress's distribution: (a) thickness = 0, (b) thickness = 0.1 (c) thickness = 0.4, (d) thickness = 0.7, (e) thickness = 0.9, and (f) thickness = 1.

TABLE 3: Normality test between the von Mises stress and the thickness of elastic piece.

Thickness (mm)	0	0.1	0.4	0.7	0.9	1.0
$p$ test	0.280	0.278	0.265	0.264	0.240	0.264

where  $\xi_i \sim N(0, (\rho^2/\sigma^4)\Delta)$ . We suppose that  $x_i = x(t_i) \neq 0, 0 \leq i \leq K$ , so the variables

$$Y_i = \frac{x_i - x_{i-1} - (1/\sigma^2)(\mu - t_{i-1})x_{i-1}\Delta}{x_{i-1}}, \quad 0 \leq i \leq K, \quad (5)$$

are independent and identically distributed (iid) and that all follows the law  $N(0, (\rho^2/\sigma^4)\Delta)$ . Thus, the density function of any  $Y_i$  is

$$f(\xi_i, \theta) = \frac{1}{(\rho/\sigma^2)\sqrt{2\pi\Delta}} \exp\left(-\frac{\sigma^4}{2\rho^2\Delta} \left(\frac{x_i - x_{i-1} - (1/\sigma^2)(\mu - t_{i-1})x_{i-1}\Delta}{x_{i-1}}\right)^2\right), \quad (6)$$

where  $\theta = (\mu, \sigma^2, \rho)^T$ . The Euler-ML estimator  $\hat{\theta}$  of  $\theta$  is concerned to find the parameter vector  $\theta$  that maximizes the log-likelihood function:

$$\log L(\theta, \xi_i) = -K \log\left(\frac{\rho}{\sigma^2} \sqrt{2\pi\Delta}\right) - \frac{\sigma^4}{2\rho^2\Delta} \sum_{i=1}^K \left(\frac{x_i - x_{i-1} - (1/\sigma^2)(\mu - t_{i-1})x_{i-1}\Delta}{x_{i-1}}\right)^2. \quad (7)$$

The MLEs  $\hat{\mu}$ ,  $\hat{\rho}$ , and  $\hat{\sigma}^2$  for the parameters  $\mu$ ,  $\rho$ , and  $\sigma^2$  verify

$$\begin{aligned} \hat{\mu} &= \arg \max_{\mu} (\log L(\theta, \xi_i)), \\ \hat{\rho} &= \arg \max_{\rho} (\log L(\theta, \xi_i)), \\ \hat{\sigma}^2 &= \arg \max_{\sigma^2} (\log L(\theta, \xi_i)), \end{aligned} \quad (8)$$

i.e.,

$$\frac{\partial \log L(\theta, \xi_i)}{\partial \mu} = \frac{\partial \log L(\theta, \xi_i)}{\partial \rho} = \frac{\partial \log L(\theta, \xi_i)}{\partial \sigma^2} = 0. \quad (9)$$

By resolving this problem, we found the estimators  $\hat{\mu}$ ,  $\hat{\rho}$ , and  $\hat{\sigma}^2$  of  $\mu$ ,  $\rho$ , and  $\sigma^2$ :

$$\hat{\mu} = \frac{T - ZF}{Z - KF}, \quad (10)$$

$$\hat{\sigma}^2 = \frac{K\Delta\hat{\mu} - \Delta Z}{X - K}, \quad (11)$$

where

$$\begin{aligned} X &= \sum_{i=1}^K \frac{x_i}{x_{i-1}}, \\ Y &= \sum_{i=1}^K \frac{x_i t_{i-1}}{x_{i-1}}, \\ Z &= \sum_{i=1}^K t_{i-1}, \\ T &= \sum_{i=1}^K t_{i-1}^2, \\ F &= \frac{Y - Z}{X - K}. \end{aligned} \quad (12)$$

For  $\hat{\rho}$ , we have

$$\hat{\rho} = \frac{\hat{\sigma}^2}{\sqrt{K\Delta}} \sqrt{\sum_{i=1}^K \left(\frac{x_i - x_{i-1} - (1/\hat{\sigma}^2)(\hat{\mu} - t_{i-1})x_{i-1}\Delta}{x_{i-1}}\right)^2}. \quad (13)$$

Thus, the stochastic model

$$\begin{cases} x(t_i) = x(t_{i-1}) + \frac{1}{\sigma^2} (\hat{\mu} - t_{i-1})x(t_{i-1})\Delta + \frac{\hat{\rho}}{\sigma^2} x(t_{i-1})\xi_i, \\ x(t_0) = x_0, \end{cases} \quad (14)$$

can describe the evolution of von Mises stress in a time interval  $[0, T]$ .

In the remainder of this paper, it is assumed that the mechanical action is suppressed when the stress reaches the point of stability (peak of the stress).

#### 4. Simulations and Discussion

Depending on experimental sample  $(x_i)_{0 \leq i \leq K}$  of each thickness, we calculate the linked estimators  $\hat{\mu}$ ,  $\hat{\sigma}^2$ , and  $\hat{\rho}$  using formulas (10), (11), and (13). Table 4 gathers the results.

As example, the estimating model for the elastic piece thickness 0.2 mm is

$$\begin{cases} x(t_i) = x(t_{i-1}) + 5.69(1.19 - t_{i-1})x(t_{i-1}) + x(t_{i-1})\xi_i, & 0 \leq i \leq K, \\ x(t_0) = 0.05. \end{cases} \quad (15)$$

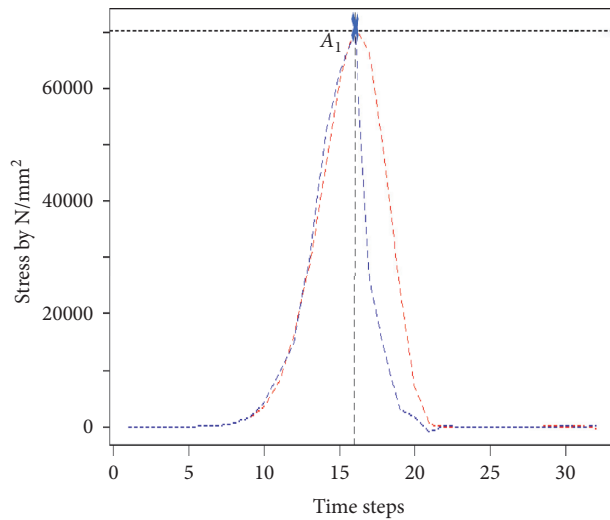
In the following simulations and table, the peak stress (stress point of stability) and its peak time are stochastically estimated using model (14). We recall that when the stress reaches the point of stability, it is assumed that the mechanical action is suppressed. The stress extinction time is also estimated.

As indicated in Figure 6 and Table 5, we can analyze these results in two levels; first, the stress peak time and the extinction time are not correlated with the elastic piece thickness, but the variance of their evolution are very small. In other words, the elastic piece thickness affects slowly the stress peak time and the stress extinction time, although there exist no correlation between the elastic piece thickness and the other two variables. In the second level, the stress peak is also not correlated with the elastic piece thickness; on top of that the variance of the evolution of this variable with change of the elastic piece thickness is very large.

In general, the mechanical loads applied to the upper plate are transferred to the lower plate and this transfer is reflected in the concentration of stresses on the lower plate. According to the result of Figure 3, the stress is well distributed on all the lower plate in the case of absence of the elastic piece; however, its presence concentrates the stress in the lower plate in the contact area around the hole. Thus, the elastic part allows to concentrate the stresses in the contact

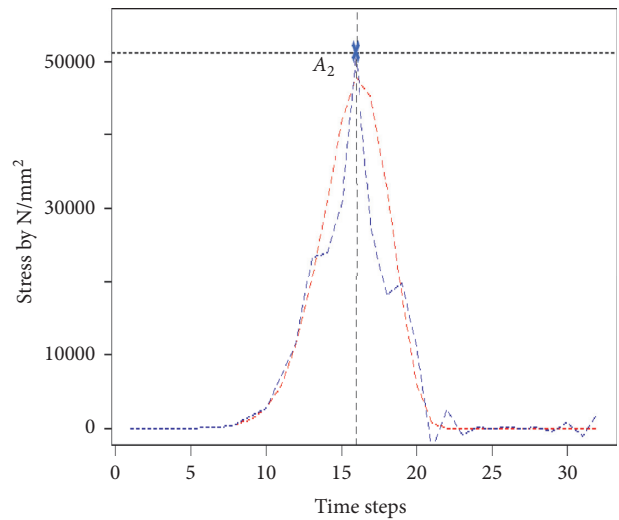
TABLE 4: Euler-maximum likelihood estimation of the parameters  $\mu$ ,  $\sigma^2$ , and  $\rho$  for different elastic piece thicknesses.

Thickness (mm)	Parameter estimation		
	$\hat{\mu}$	$\hat{\sigma}^2$	$\hat{\rho}$
0	1.18468927	0.01167707	0.22097886
0.1	1.18581822	0.01228712	0.22727400
0.2	1.180558422	0.008790051	0.225317436
0.3	1.181756874	0.009602489	0.221970306
0.4	1.182099792	0.009846698	0.215053257
0.5	1.18509170	0.01187883	0.22262422
0.6	1.18583600	0.01242017	0.22572033
0.7	1.18519627	0.01178613	0.22318094
0.8	1.182537373	0.009997622	0.221740906
0.9	1.2522960	-0.2012549	-0.8309588
1.0	1.18519627	0.01178613	0.22318094
1.1	1.182297143	0.009987085	0.217539627
1.2	1.181672416	0.009427385	0.218533872
1.3	1.181976021	0.009628434	0.218214562
1.4	1.18539929	0.01215588	0.22313173
1.5	1.18322684	0.01045432	0.22340075
1.6	1.1852761	0.01204753	0.22369206
1.7	1.18501296	0.01188262	0.21906066
1.8	1.181932970	0.009618655	0.216498734
1.9	1.181091762	0.009271733	0.224089725
2.0	1.18589145	0.01253209	9.22427855



-- Deterministic stress  
 - - Stochastic stress

(a)



-- Deterministic stress  
 - - Stochastic stress

(b)

FIGURE 6: Continued.

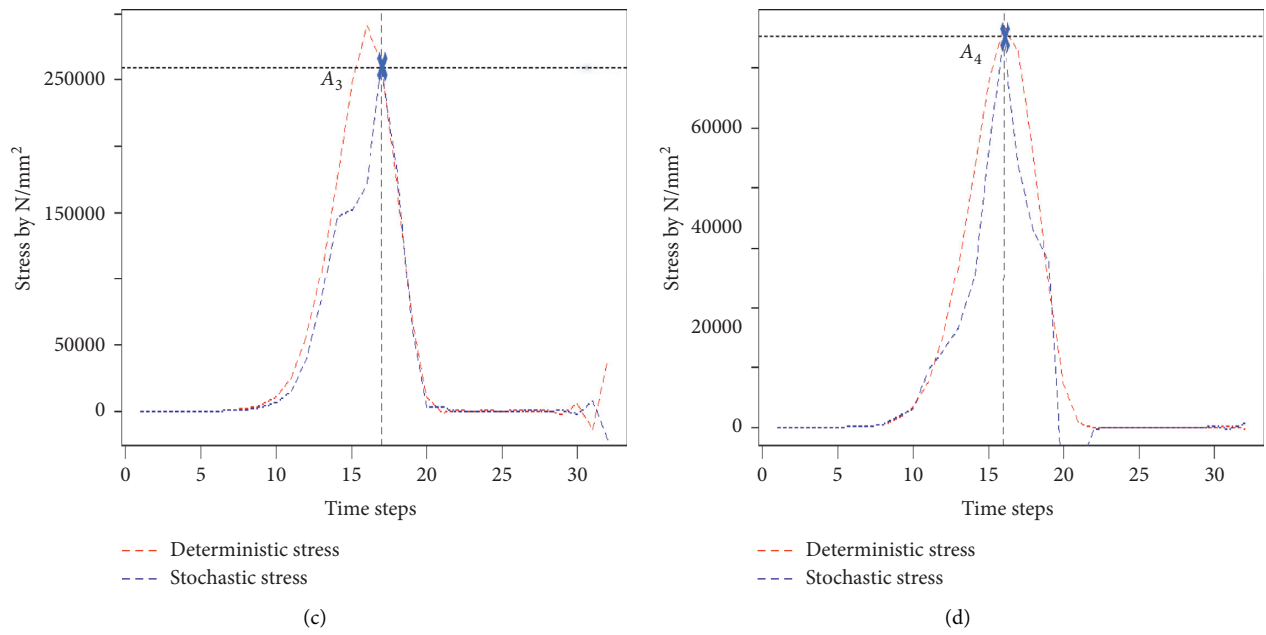


FIGURE 6: Simulation of the stress density for some joint elastic piece thicknesses using their corresponding estimating models. (a) Thickness=0,  $A_1$  (16, 70236), (b) thickness=0.1,  $A_2$  (16, 51191), (c) thickness=0.4,  $A_3$  (17, 259276), and (d) thickness=0.7,  $A_4$  (16, 65108).

TABLE 5: Results of the simulation: stress peak value, stress peak time, and stress extinction time.

Elastic piece thickness (mm)	Stress peak (N/mm) <sup>2</sup>	Stress peak time by second	Stress extinction time by second
0	70237	17	22
0.1	51191	16	24
0.3	3376175	16	22
0.4	259276	17	20
0.7	65108	16	22.2
1.0	61803	18	23.5
1.3	319817	16	21
1.5	172692	17	21
1.7	55142	15	21
2.0	39104	16	19

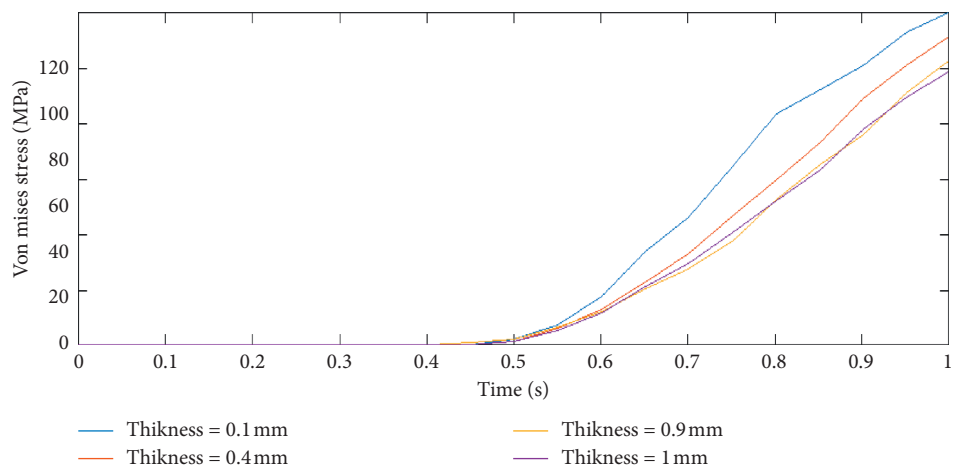


FIGURE 7: Stress evolution as function of time and thickness of the steel piece at an element of the lower plate.

TABLE 6: The results of the Pearson test of correlation between the stress and the steel piece thickness.

		Thickness	Stress
Thickness	Pearson correlation	1	0.93
	Sig.(bilateral)		<b>0.03</b>
	<i>N</i>	10	10
Stress	Pearson correlation	0.93	1
	Sig.(bilateral)	<b>0.03</b>	
	<i>N</i>	10	10

area or in the assembly area, where there is the bolt and its action. This helps to reduce the damage of the structure because the assembly area is one of the hardest part in this structure.

On the contrary, as deduced in the correlation and stochastic model results, the change in the thickness of the elastic piece does not influence the evolution of stress in the case of the presence of mechanical actions or in the case of their absence. The noninfluence of the thickness on the stress evolution as a function of time in a finite element of the structure is caused perhaps by the material properties of this elastic piece.

The paper of Saxena et al. [12] allows us to consider the last hypothesis. In fact, their paper shows that the stress evolution depends on the piezoelectric layer length and the thickness variation of the plate, which has the same material properties of the global structure and affects the stress evolution.

#### 4.1. Dynamic Behavior of Bolted Structure with Steel Piece.

In order to verify this hypothesis, we carry out the same simulations on the ABAQUS Software, but this time, we replace the elastic piece by a steel piece which has the same material properties of the structure. The results of this numerical simulation as well as the correlation test are presented in Figure 7 and Table 6.

The stress evolution is presented as function of time in a lower plate element and the change of the steel piece are strongly correlated. This result is confirmed by the Pearson correlation test in Table 6 (the  $p$  value is  $<0.05$ ).

This result is consistent with the hypothesis that we have previously proposed. Therefore, the noncorrelation between the stress evolution and the change in the thickness of the elastic piece is mainly caused by the material properties of the latter.

## 5. Conclusion

In this paper, an experiment numerical simulation has been conducted to study the von Mises stress evolution into a bolted structure in presence of an elastic piece. The experiment changes the thickness of the elastic piece to deduce its effect in the evolution of the stress. The results of this investigation are various. First, the presence of the elastic piece makes possible to concentrate the stress in the assembly area in the lower plate. The second result also showed that there is no correlation between the stress evolution and

the change of the thickness. This uncorrelation is caused by the difference of material properties between the elastic piece and the other pieces of the structure.

A stochastic model has been built from the graph of the stress evolution as well as by a normality test, and its pentameters have been estimated by the Euler-Maximum Likelihood estimation method. The model has been used to predict the stress peak, the stress peak time, and the stress extinction time into the bolted structure. The proposed stochastic model remains a relevant model which gives good predictions of the last three parameters by changing the thickness of the elastic piece despite the fact that there is no correlation between the change in thickness and the stress evolution.

As a perspective, we can consider this work as a basis for several future studies, for example,

- (i) Build a stochastic model or a time series that predicts the evolution of the stress in function of the time and the thickness of the elastic piece
- (ii) Study the mechanical reliability of bolted structures with and without elastic part
- (iii) Search the optimal joint configuration that ensures the stability and reliability of the bolted structure

## Data Availability

The datasets used to support the results of this study are available from the corresponding author upon request.

## Conflicts of Interest

The authors declare that there are no conflicts of interest regarding the publication of this paper.

## References

- [1] Y. D. Kwon, H. W. Kwon, J. H. Hwangbo, and S. H. Jang, "Finite element modeling for static and dynamic analysis of structures with bolted joint," *Key Engineering Materials*, vol. 306–308, pp. 547–552, 2006.
- [2] J. KimD, T. C. Yoon, and B. S. Kang, "Finite element analysis and modeling of structure with bolted joints," *Applied Mathematical Modelling*, vol. 31, no. 5, pp. 895–911, 2007.
- [3] E. Parroissien, "Contribution to the hybrid (bolted/bonded) joining - application to aeronautical joints," Thesis, Toulouse University III, Toulouse, France, 2006.
- [4] M. A. McCarthy, C. T. McCarthy, V. P. Lawlor, and W. F. Stanley, "Three-dimensional finite element analysis of single-bolt, single-lap composite bolted joints: part I-model development and validation," *Composite Structures*, vol. 71, no. 2, pp. 140–158, 2005.
- [5] C. T. McCarthy and M. A. McCarthy, "Three-dimensional finite element analysis of single-bolt, single-lap composite bolted joints: part II. Effects of bolt-hole clearance," *Composite Structures*, vol. 71, no. 2, pp. 159–175, 2005.
- [6] M. A. McCarthy, V. P. Lawlor, W. F. Stanley, and C. T. McCarthy, "Bolt-hole clearance effects and strength criteria in single-bolt, single-lap, composite bolted joints," *Composites Science and Technology*, vol. 62, no. 10-11, pp. 1415–1431, 2002.

- [7] C. T. McCarthy and P. J. Gray, "An analytical model for the prediction of load distribution in highly torqued multi-bolt composite joints," *Composite Structures*, vol. 93, no. 2, pp. 287–298, 2011.
- [8] G. S. Padhi, M. A. McCarthy, and C. T. McCarthy, "BOLJAT: a tool for designing composite bolted joints using three-dimensional finite element analysis," *Composites Part A: Applied Science and Manufacturing*, vol. 33, no. 11, pp. 1573–1584, 2002.
- [9] M. Lacour, J. Macedo, and N. A. Abarhamson, "Stochastic finite element method for non-linear material models," *Computers and Geotechnics*, vol. 125, Article ID 103641, 2020.
- [10] M. Lacour and N. A. Abarhamson, "Stochastic constitutive modeling of elastic-plastic materials with uncertain properties," *Computers and Geotechnics*, vol. 125, Article ID 103642, 2020.
- [11] A. Ghasemi and S. Zahediasl, "Normality tests for statistical analysis: a guide for non-statisticians," *International Journal of Endocrinology and Metabolism*, vol. 10, no. 2, pp. 486–489, 2012.
- [12] S. Saxena, R. Sharma, and B. D. Pant, "Piezoelectric layer length and thickness variation effects on displacement, von-mises stress and electric potential generated by cantilever type piezoelectric energy harvester," *Materiels Today: Proceedings*, vol. 30, pp. 23–27, 2020.

## Research Article

# A Supporting Design Method When Longwall Face Strides across and Passes through a Roadway

Weidong Pan,<sup>1,2</sup> Xinyuan Li ,<sup>1,2</sup> YiWei Li,<sup>1,2</sup> Xiaobin Li ,<sup>2</sup> Qing Qiao,<sup>3</sup> and Haoran Gong<sup>4</sup>

<sup>1</sup>State Key Laboratory of Coal Resources and Safe Mining, China University of Mining and Technology-Beijing, Ding No. 11 Xueyuan Road, Haidian District, Beijing, China

<sup>2</sup>School of Energy and Mining Engineering, China University of Mining and Technology-Beijing, Ding No. 11 Xueyuan Road, Haidian District, Beijing, China

<sup>3</sup>School of Mechanics and Civil Engineering, China University of Mining and Technology-Beijing, Ding No. 11 Xueyuan Road, Haidian District, Beijing, China

<sup>4</sup>School of Emergency Management and Safety Engineering, China University of Mining and Technology-Beijing, Ding No. 11 Xueyuan Road, Haidian District, Beijing, China

Correspondence should be addressed to Xinyuan Li; [lx199521@student.cumtb.edu.cn](mailto:lx199521@student.cumtb.edu.cn)

Received 15 September 2020; Accepted 29 September 2020; Published 19 October 2020

Academic Editor: Jinyang Xu

Copyright © 2020 Weidong Pan et al. This is an open access article distributed under the Creative Commons Attribution License, which permits unrestricted use, distribution, and reproduction in any medium, provided the original work is properly cited.

In coal underground mining, situation of longwall face striding across (SAR) or passing through roadway (PTR) is very common, especially in an inclined coal seam mining. A roadway supporting design method, consisting of a model using to determine the minimal rock strata thickness and a segmental supporting scheme, is developed. In addition, to represent the mechanical behaviour of the caved material authentically, an elastic model was developed. The results showed that the elastic model has a good agreement with the caved material mechanical behaviours at a relatively lower stress condition. By using a FDEM method, a real case in Xutuan coal mine is studied. Compared with the process without backfill, the  $z$ -displacement of cross-cut roof decreased shapely after backfilling, with a maximum  $z$ -displacement, decreases from 0.76 m to 0.13 m and from 0.39 m to 0.064 m in PTR and SAR section, respectively. Therefore, the possibility of fall of ground (FOG) and crushing accidents can be reduced effectively with backfilling material of wood cribs. And the maximum subsidence (SAR section side) of face floor is 0.16 m, which is small enough to ensure normal production. The results of this study are likely to be useful as a reference for the safe and efficient mining of coal resources under similar conditions.

## 1. Introduction

In underground coal mining, many roadways are excavated in coal or rock strata at different depths. Each of them plays a functional role in the coal mine production; a few are used for transportation while others are used for ventilation. Collectively, these roadways constitute a complex system. In the longwall mining field practice, it is common to encounter a situation in which roadways are laid ahead or below the longwall face [1–3], in particular, in the inclined coal seam mining. As the mining activity proceeds, it is inevitable for the longwall face to stride across (SAR) or pass through roadways (PTR). In China, particularly, owing to the large demand of coal consumption, this situation is more

common. This imposes a significant safety challenge on the mining activity, e.g., with respect to the stability of the roadway surrounding rock and the possibility of the fall of ground (FOG).

Much research has been done on SAR and PTR. Regarding SAR, when a longwall face is far away from a roadway in the advancing direction, the roadway is in a stable state. With the advance of the longwall face, the abutment pressure starts to increase [4]. The abutment pressure, together with the coal seam gravity, is transmitted to the face floor, which could increase the stress to several-fold above that of the primary rock and thus can affect the face floor and supporting structures. The mining-induced redistribution of the stress field leads to the initiation and

growth of preexisting cracks [5], leading to the formation of a face floor failure area. Thus, maximal floor failure depth plays a vital role in SAR. Once the maximal floor failure depth exceeds its critical value, the roadway is destroyed and the supports of the longwall face fall down. In addition, the roadway loosening zone cannot be ignored. After the roadway excavation, the stress in the surrounding rock becomes concentrated [6], which may exceed the bearing capacity of the surrounding rock and may damage the surrounding rock [7]. Therefore, the maximal floor failure depth and roadway loosening zone affect SAR. Regarding PTR, as the longwall face advances toward the roadway, the roof's hanging length increases gradually. When the hanging length reaches its critical value, the main roof breaks ahead of the longwall face, which sharply increases the load on the hydraulic supports and leads to the FOG and crushing of supports, especially when the longwall face suddenly advances into the roadway. In view of this, supporting schemes have been proposed to prevent possible accidents [2, 8], and these schemes provide guidelines and reference when doing supporting design for similar field conditions.

However, because of the inclination of the coal seam, it is inevitable to encounter a situation, in which both SAR and PTR appear simultaneously. Yet, little research was done to address these issues. In the work described in this paper, a mechanical model using to determine minimal rock strata thickness is proposed, and a segmental supporting scheme was introduced for different section of the roadway. Based on geological and mining condition of Xutuan coal mine, a FDEM numerical analysis is conducted by comparing the behaviour of the cross-cut rock mass with or without supporting.

## 2. Roadway Supporting Design Method

Figure 1 is an example of a longwall face striding across and passing through a roadway, simultaneously, because of the inclination of the coal seam. And there is a position where the rock strata, with a certain thickness, can hold the longwall face and the mining activity can carry out safely. Therefore, it is necessary to compute the minimal thickness of the rock strata. The calculation is guided by the realization that the rock strata at the minimal thickness should be able to support the weight of the longwall face equipment and should not collapse during the mining process.

**2.1. Supporting Range Division.** When the longwall face strides across a roadway, the thickness of the rock strata has three components, namely, the face floor failure depth ( $T_1$ ), the bearing rock strata thickness ( $T_2$ ), and the roadway broken height ( $T_3$ ), as shown in Figure 2.

Owing to the existence of a bedding plane between the coal seam and the floor strata, the coal rib can be regarded as a deep foundation with a rough contact with plane OA [9]. Owing to the presence of unmined solid coal in the face-advancing direction, a half model compared with the model based on Terzaghi's principle [10] is established to deduce the longwall face failure depth  $T_1$ , as shown in Figure 3.

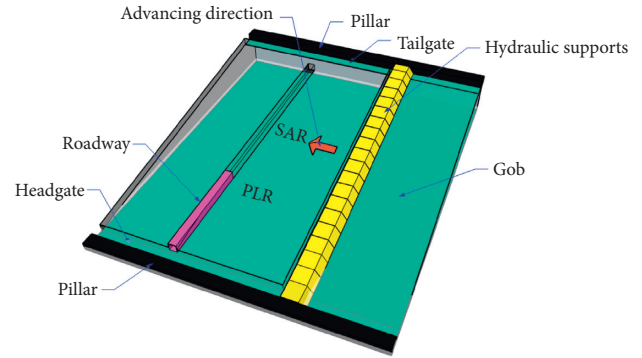


FIGURE 1: Longwall face striding across and passing through a roadway.

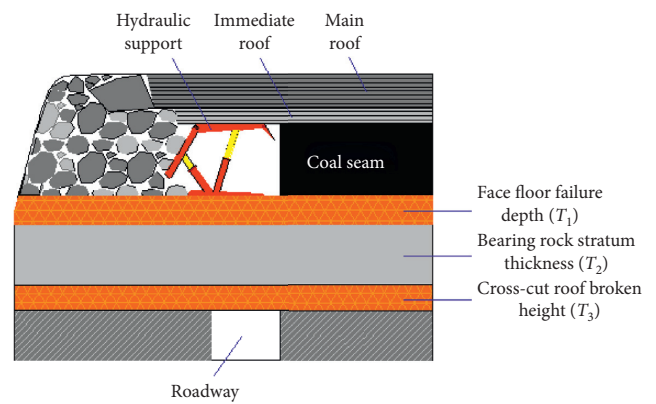


FIGURE 2: The components of rock strata.

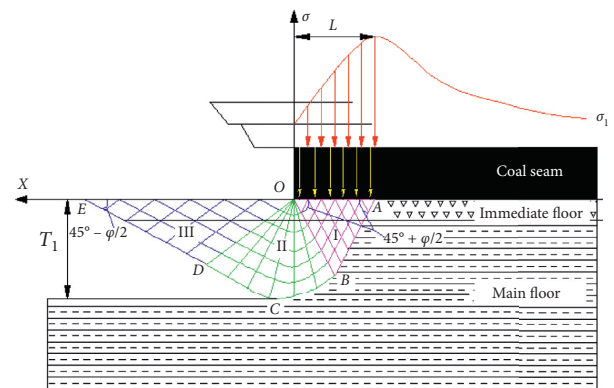


FIGURE 3: Failure model of the 7# coal seam floor.

In the proposed model, under the coal rib, the floor is plastically deformed owing to the abutment pressure, and the rock mass forms a continuous slip surface. As shown in Figure 3, curve ACE represents the slip curve of the floor, where section BCD is a logarithmic spiral with B as the starting point. The plastic failure area of the floor is divided into three zones by the two radiation lines OB and OD: (1) the active stress area of zone I, (2) the transition area of zone II, and (3) the passive stress area of zone III. As shown in Figure 3, the failure depth  $T_1$  is calculated as

$$T_1 = r \cos \theta = r_0 e^{\alpha \tan \varphi} \cos \theta,$$

$$\theta = \alpha - \frac{\pi}{4} + \frac{\varphi}{2}, \quad (1)$$

$$r_0 = \frac{L}{2 \cos((\pi/4) + (\varphi/2))},$$

where  $r$  represents the distance between the logarithmic spiral and the original point ( $O$ );  $\theta$  is the angle between the helical radius ( $r$ ) and the vertical line;  $\alpha$  is the angle between the waist line ( $OB$ ) and the helical radius;  $r_0$  is the waist length ( $OB$ ) of the isosceles triangle  $OAB$ ;  $\varphi$  is the inner-friction angle; and  $L$  is the distance between the peak abutment pressure and the longwall face. Hence,

$$T_1 = r_0 e^{\alpha \tan \varphi} \cos\left(\alpha - \frac{\pi}{4} + \frac{\varphi}{2}\right). \quad (2)$$

From the functional relationship, the value of  $T_1$  is maximal when  $(dT_1/d\alpha) = 0$ . Thus,

$$\frac{dT_1}{d\alpha} = r_0 e^{\alpha \tan \varphi} \cos\left(\alpha - \frac{\pi}{4} + \frac{\varphi}{2}\right) - r_0 e^{\alpha \tan \varphi} \sin\left(\alpha - \frac{\pi}{4} + \frac{\varphi}{2}\right) = 0. \quad (3)$$

Then,  $T_1$  can be estimated using the following equation:

$$T_1 = \frac{L \cos \varphi}{2 \cos((\pi/4) + (\varphi/2))} e^{((\pi/4) + (\varphi/2)) \tan \varphi}. \quad (4)$$

The bearing rock strata can be simplified as a clamped beam, as shown in Figure 4.

In Figure 4,  $L'$  is the width of the roadway;  $q$  is the pressure acted by the hydraulic support; and part of the strata weight above. The shear force and the bending moment at any point on the cross-section of the strata beam can be expressed as

$$F(x) = \frac{qL}{2} \left(1 - \frac{2x}{L'}\right), \quad (5)$$

$$M(x) = \frac{q}{12} (8L'x - 6x^2 - L'^2).$$

If the rock strata fractures in the shear form, the thickness of the strata ( $T_{2S}$ ) becomes

$$T_{2S} = \frac{3F_{\max}}{2R_s}, \quad (6)$$

where  $T_{2S}$  is the thickness of the rock strata when it fractures in the shear form,  $F_{\max}$  is the maximal shear force the strata can withstand, and  $R_s$  is the shear strength.

If the rock strata fractures in the tensile form, the thickness of the strata ( $T_{2T}$ ) becomes

$$T_{2T} = \sqrt{\frac{6M_{\max}}{R_T}}, \quad (7)$$

where  $T_{2T}$  is the thickness of the rock strata when it fractures in the extension form,  $M_{\max}$  is the maximal bending moment the strata can withstand, and  $R_T$  is the tensile strength.

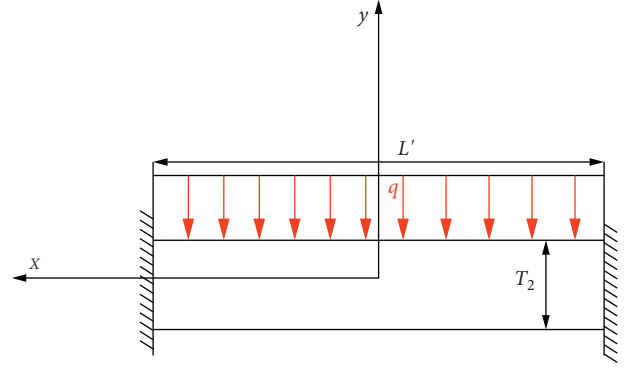


FIGURE 4: Clamped beam model.

The thickness of the bearing rock strata ( $T_2$ ) should be larger than the minimal thickness of the strata to minimize the risk of shear or tensile fractures:

$$T_2 > \max(T_{2S}, T_{2T}). \quad (8)$$

After the excavation of the roadway, the stress in the surrounding rock starts to concentrate; eventually, the bearing capacity of the surrounding rock may be exceeded, damaging the surrounding rock [11]. The area of the damaged rock can be described by Protodjakonov's theory [12], which utilizes the values of the angle of the internal friction of the rock to characterize the rock mass. Such characterization of the area of the damaged rock is often adopted for the rock arch description, because it yields good results.

According to Protodjakonov's theory, a natural arch is formed above the roadway, and along this natural arch, the rocks may loosen or separate from the rock mass, as shown in Figure 5. The arch height can be determined by

$$T_3 = b = \frac{a}{f}, \quad (9)$$

$$f = \frac{R_c}{10}.$$

Then, the minimal thickness of the rock strata can be calculated by

$$T = T_1 + T_2 + T_3. \quad (10)$$

And this thickness would be a boundary between backfilling section and no-backfilling section, beyond which the roadway needs no supporting measure.

**2.2. Roadway Supporting Scheme.** In this mining situation, it becomes imperative for normal production to design a reasonable supporting scheme to reinforce and support the roadway and prevent the subsidence of the longwall face, FOG, and support-crushing accidents. Since lower supporting cost, the backfilling technology, with waste rock, has been widely used in gob filling [13], which also have a great advantage in backfilling of SAR section.

As for PTR section, the longwall face at the PTR section passes through the roadway. During this process, the floor of the longwall face is hollow and the coal located in the roof of

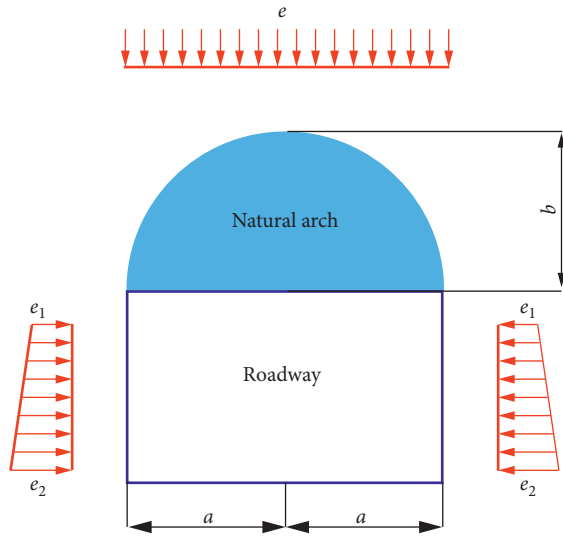


FIGURE 5: Natural arch theory model.

the roadway has a tendency to collapse and cave. Therefore, the main objective in this stage is to prevent the subsidence of the hydraulic support and provide enough supporting force to the roadway roof. Meanwhile, the support material cannot affect the production of the shearer. To improve the firmness of the face floor, concrete can be used to fill a certain height of the PTR section. Moreover, an intensive wood cribs should be laid previously and integrated with the concrete, which does not affect normal production, but provide supporting force to the roadway roof.

### 3. Case Study

**3.1. Geological and Mining Condition.** Xutuan coal mine, located at the Huaibei city, Anhui Province, China, was selected for a case study. In the Xutuan coal mine, No. 7 coal seam is one of the main minable seams and has a buried depth from 480 m to 510 m, with an average buried depth of 500 m. The vertical stress is 13.29 MPa, and the stress ratios are 0.43 and 0.21 in the advancing and inclined directions, respectively. No. 7 coal seam has a dip angle of  $12^\circ$ , thickness in the 4.0 m to 6.3 m range, with an average thickness of 5 m. The affiliated No. 7219 longwall face has an inclined length of 168 m and strike length of 420 m, and its succession face is No. 7229 longwall face. Moreover, there is a 100 m wide protective pillar between the two longwall faces, covering No. 7118 cross-cut. The cross-section of the cross-cut is rectangular, with 5 m width and 4.5 m height. The positions of the cross-cut and the longwall faces are shown in Figure 6.

The No. 7219 longwall face is a large mining height face with each of hydraulic shield supports weighing 36 t. Considering that the plan for moving the original face involved a long route with a significant amount of work, it was decided to extend the headgate and tailgate to the new stop line. As shown in Figure 6, No. 7219 longwall face continued to advance beyond the older stop line to the new stop line. In this way, additional coal resources could be recovered and the face-moving issue could also be resolved.

**3.2. Supporting Design.** The minimal thickness of the safety rock strata is the gap between the backfilling and non-backfilling of the SAR section. Based on field observations and measurements, the distance between the peak abutment pressure and the longwall face is 5 m (i.e.,  $L = 5$  m). The inner friction angle of the main floor was used because it is the median of the floor inner friction angle, as listed in Table 1. According on (4),

$$T_1 = 9.52 \text{ m.} \quad (11)$$

The width of the No. 7118 cross-cut ( $L'$ ) is 5 m; the pressure acted by the hydraulic support and part of the strata weight above ( $q$ ) is 0.51 MPa. The shear force ( $F_{\max}$ ) reaches the maximal value at the position  $x = \pm(L/2)$ , and the maximal bending moment ( $M_{\max}$ ) reaches the maximal value at the centre position of the strata ( $x=0$ ). According to (6) and (7),  $T_{2S}$  and  $T_{2T}$  are 0.15 m and 0.86 m, respectively. Thus,

$$T_2 = 0.86 \text{ m.} \quad (12)$$

Based on the parameters in Table 1, the height of the natural arch can be calculated from (9), and the maximal cross-cut broken height ( $T_3$ ) is

$$T_3 = 0.54 \text{ m.} \quad (13)$$

Therefore, the minimal thickness of the safety rock strata can be determined by (10),

$$T = T_1 + T_2 + T_3 = 9.52 + 0.86 + 0.54 = 10.92 \text{ m.} \quad (14)$$

According to the analysis above, the cross-cut can be sectioned using a rock strata thickness of 10.92 m. Therefore, the length of backfilling section is 52.5 m and PTR section are 30.5 m, as shown in Figure 7. Due to easy access, granular coal with radius in the 0.1–0.2 m range, corresponding to the field crashed coal dimensions, was used to backfill the roadway. And a concrete wall, with a thickness of 1 m, is built to prevent granular coal from flowing in SAR section near the backfilling material. In PTR section, the supporting material of concrete and wood cribs is used.

### 4. Numerical Model Construction

**4.1. Global Model.** In accordance with the geological characteristics of the coal measure strata, a numerical calculation model was established, as shown in Figure 8. The model dimensions were  $200 \text{ m} \times 276 \text{ m} \times 150 \text{ m}$  ( $X \times Y \times Z$ ). In this model, three roadways, namely, the headgate, the tailgate, and the cross-cut, were excavated, and the cross-cut intersected with the headgate. The headgate and tailgate measured  $4 \text{ m} \times 3 \text{ m}$  ( $Y \times Z$ ) and the cross-cut was rectangular (width, 5 m; height, 4.5 m). Around the panel, 50 m wide pillars were left to eliminate the boundary effect. To monitor displacement, three measure lines were set at the middle position of the walls and roof of the cross-cut, and the distance between every two measure points was 4 m.

FLAC3D was used for the numerical calculations. Atop the model, a vertical stress (13.286 MPa) was applied to

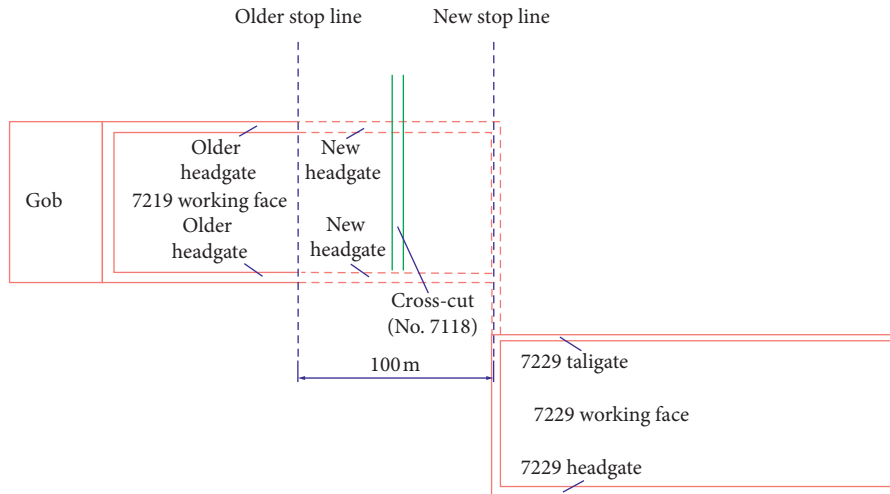


FIGURE 6: Positional relationship between the working faces and cross-cut.

TABLE 1: Physical and mechanical properties of main floor.

Lithology	Compressive strength (MPa)	Tensile strength (MPa)	Shear strength (MPa)	Inner friction angle (deg.)
Fine siltstone	45.9	9.0	13.0	35

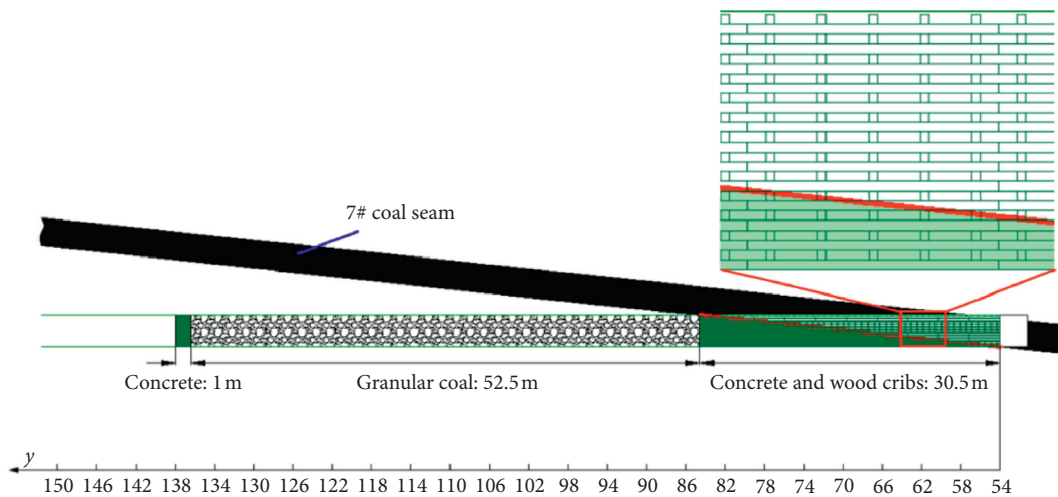


FIGURE 7: No. 7118 cross-cut supporting design.

simulate the load applied by the overburden, and the bottom sides were roller-constrained. A horizontal stress was applied according to the in situ stress condition. Coal and rock, as an elastic-plastic medium [14], are suitable to modelling by the Mohr-Coulomb criterion. The Mohr-Coulomb criterion was used to simulate the rock and coal strata behaviours in this model.

Before this simulation, a laboratory test task was conducted to obtain the physical and mechanical properties of the surrounding rock. Much research has been conducted [15, 16], which validated that young modulus, cohesion, and tensile strength of the rock mass and coal seam are 0.1–0.25 times the laboratory result, and the Poisson ratio is 1.2–1.4 times the laboratory result. The parameters used in this model are listed in Table 2.

*4.2. Elastic Model for Gob Modelling.* In the longwall mining method, the roof strata behind the longwall face are abandoned and collapse is allowed. When the face advances sufficiently far, the immediate roof behind it collapses at a distance that depends on the specific geological conditions. Failure of the roof continues until the roof and caved material come in contact. Under the load of the roof, the caved material is compacted gradually until the roof is balanced by the coal rib and the caved material. Thus, it is necessary to model the gob and its compaction [17]. The caved material does not behave as an intact rock; however, its stiffness varies with the stress to which it is subjected. In fact, it also exhibits certain strain-hardening characteristics.

The stress-strain behaviour of the caved material can be described by [18, 19], which were suggested for backfill materials by Salamon [20]:

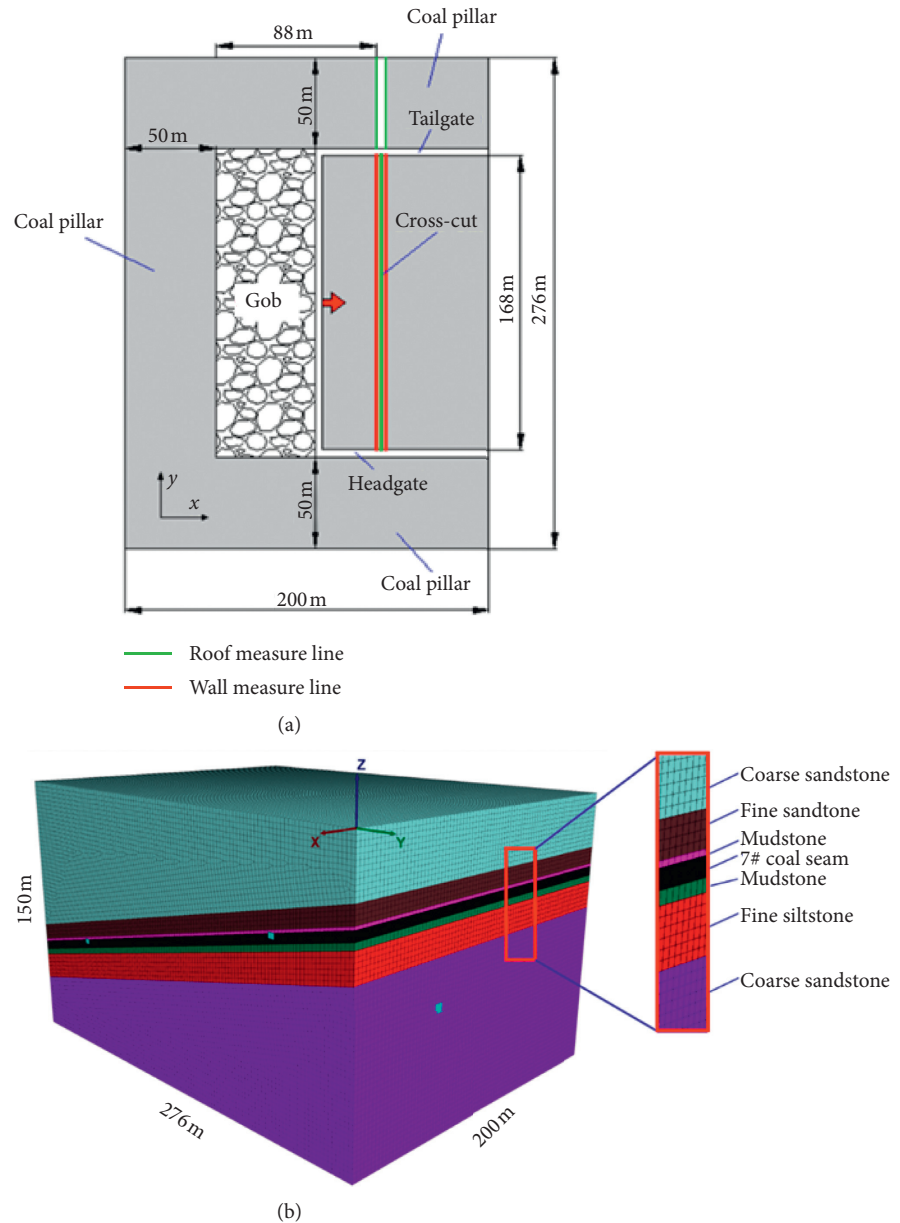


FIGURE 8: Numerical model configuration and measure line layout.

TABLE 2: Coal-rock layers and mechanical parameters used in the numerical model.

Rock strata	Thickness (m)	Density (kg/m <sup>3</sup> )	Bulk modulus (GPa)	Shear modulus (GPa)	Friction angle (deg.)	Cohesion (MPa)	Tensile strength (MPa)
Coarse sandstone	30.0–86.5	2580	10.3	8.4	37	4.3	5.9
Fine sandstone	9.0	2650	7.4	4.8	38	2.2	1.5
Mudstone	1.5	2540	2.3	1.2	27	1.2	0.8
7# coal seam	5.0	1400	0.3	0.12	18	0.3	0.15
Mudstone	3.4	2420	2.4	1.3	32	1.1	1.2
Fine siltstone	14.6	2500	3.0	1.9	35	2.4	4.3
Coarse sandstone	30.0–86.5	2660	8.1	4.9	37	2.8	2.2

$$\sigma = \frac{E_0 \varepsilon}{1 - (\varepsilon/\varepsilon_m)}, \quad (15)$$

$$\varepsilon_m = \frac{b - 1}{b}, \quad (16)$$

$$E_0 = \frac{10.39 \sigma_c^{1.042}}{b^{7.7}}, \quad (17)$$

where  $\sigma$  is the uniaxial stress applied to the material,  $\varepsilon$  is the strain under the applied stress,  $E_0$  is the initial tangent modulus,  $\varepsilon_m$  is the maximal possible strain of the bulk rock material,  $b$  is the initial bulk factor, and  $\sigma_c$  is the compressive strength of the rock.

Behind the longwall face, the strata bends downward and breaks into different-size blocks until the lowest uncaved strata receives the support of the caved and bulk rock pile [19]. Therefore, the initial bulk factor  $b$  is closely related to the caving height and can be calculated as

$$b = \frac{H_c + h}{H_c}, \quad (18)$$

where  $H_c$  is the caving height and  $h$  is the mining height.

The caving height can be predicted by the following empirical criterion [21], which is consistent with field statistics of 4–11 times the thickness of the coal seam height [22]:

$$H_c = \frac{100h}{c_1 h + c_2}, \quad (19)$$

where  $c_1$  and  $c_2$  are coefficients that depend on the strata lithology, as shown in Table 3 [21, 23].

According to (15)–(19), the height of the roof caving zone  $H_c$ , the initial bulk factor  $b$ , the maximal strain  $\varepsilon_m$ , and the initial gob modulus  $E_0$  are calculated (Table 4). The stress-strain behaviour of Salamon's model is shown in Figure 9 (blue line). The behaviour is approximately linear for stresses under 20 MPa, and it is exponential for higher stress values. This suggests that the caved material behaves like an elastic material for low stress values. As the objective of the present work was to analyse the deformability of the cross-cut (rather than observe failed zones), and because these material properties may change the stress level well behind the advancing longwall face rather than in front of the advancing longwall face, it is reasonable to assume elastic material properties in simulations of the caved material. An important practical advantage of using an elastic global model is computational efficiency, which allows to conduct a large number of analysis and parametric evaluations [24]. Kose and Cebi [25] suggested that the deformation modulus of the gob material ranges from 15 MPa to 3500 MPa, whereas, based on experiments, Shabanimashcool and Li [26] suggested that the deformation modulus of the caved material ranges from 60 MPa to 100 MPa. Jiang et al. [27] used a somewhat stiffer gob material with the deformation modulus and Poisson's ratio of 190 MPa and 0.25, respectively. To generate reasonable input parameters for the elastic model, a test material, with dimensions of

1 m × 1 m × 1 m, was simulated using FLAC3D. Loading was simulated by applying a velocity to the top surface; the parameters are listed in Table 5. The system's stress-strain behaviour was recorded and is shown in Figure 9 (red line).

As shown in Figure 9, the elastic model satisfactorily captures the caved material for stresses under 20 MPa. In practice, the stress behind the longwall face increases gradually with time. However, the stress cannot return to the original magnitude within a short-term period. In addition, the maximal in situ stress around the panel is 16 MPa, which is less than the limiting value of 20 MPa.

**4.3. Supporting Material Modelling.** Discrete Element Method (DEM) method has been used to simulation the behaviour of granular materials for a long time [28, 29]. In this paper, the granular coal, with the radius in the 0.1–0.2 m range, is used as the backfilling material. It is described as a cloud of discrete balls that were coupled to the FLAC3D continuous model via the "wall" medium, and this method is referred to as FDEM method. A uniform distribution model was used to represent the real distribution of the backfilling material of coal. Some parameters, including normal stiffness, shear stiffness, and friction coefficient, that were used here to model the granular coal were taken from literature [30]. Table 6 lists the parameters of the granular coal in our discrete model.

Three types of materials constitute the cross-cut supporting: concrete, wood, and granular coal. In this study, concrete was considered as a Mohr–Coulomb material [31]. Wood was simplified as an elastic material, although its actual mechanical behaviour is more complex [32]. However, the function of wood is just to support the cross-cut roof, and it only weakly affects the entire project. The parameters of the concrete and the wood cribs are listed in Table 7.

## 5. Simulation Results and Discussion

**5.1. Cross-Cut Deformation during the Longwall Face Advancement.** During the longwall face advancement, the stress around the cross-cut is disturbed. Subjected to the advancing abutment pressure, the walls and the roof of the cross-cut exhibit shape distortions in the form of displacement. The displacement of the surrounding rock was registered to obtain the displacement distribution.

**5.1.1. SAR Section Deformation.** As shown in Figure 10(a), when the longwall face advances, the distance between the longwall face and the cross-cut decreases ( $x$ -direction). The  $z$ -displacement of the cross-cut roof increases and then decreases, subjected to the advancing abutment pressure. However, the displacement along the cross-cut is different, owing to the thickness of the rock strata between the longwall face floor and the cross-cut roof, and the magnitude of the advancing abutment pressure. The  $z$ -displacement gradually increases with the advancement of the longwall face and as the advancing abutment pressure increases. However, the  $z$ -displacement begins to decrease when the longwall face advances 68–84 m, and the amount of reduction varies across the different

TABLE 3: Coefficients for average height of caving zone.

Strata lithology	Compressive strength ( $\sigma_c$ , MPa)	Coefficients	
		$c_1$	$c_2$
Strong and hard	>40	2.1	16
Medium strong	20–40	4.7	19
Soft and weak	<20	6.2	32

TABLE 4: Parameters for Salamon's model.

$H_c$ (m)	$B$	$\epsilon_m$	$E_0$ (MPa)
14.88	1.34	0.25	55.9

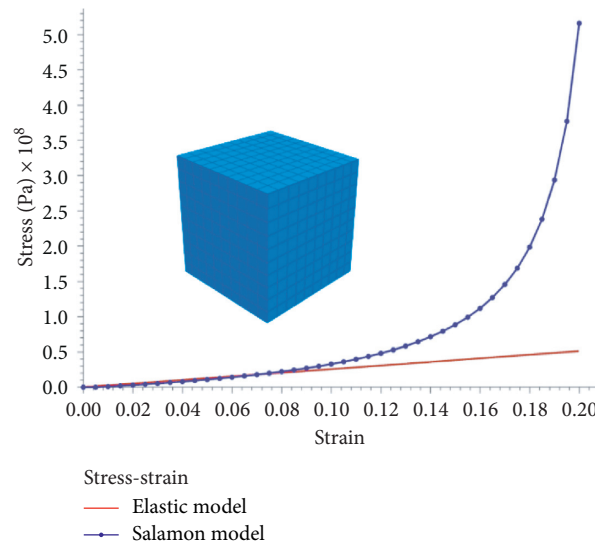


FIGURE 9: Stress-strain behaviour of caved material in gob.

TABLE 5: Parameters used in the elastic model for caved material.

Density ( $\text{kg/m}^3$ )	Young's modulus (MPa)	Poisson's ratio
1848	256.4	0.2

measured points. The maximal  $z$ -displacement decreases from 0.39 m to 0.064 m after backfilling. Moreover, as shown in Figure 10(b), the rate of change in the  $z$ -displacement gradually stabilizes when the  $y$ -coordinate is larger than 130 (the corresponding rock strata thickness is 9.78 m), which agrees with the calculation using the proposed model.

In Figure 11, after backfilling, the backfilling material interacts with the surrounding rock whenever a displacement occurs in any direction. Compared with the maximal  $x$ -displacement without backfilling, the maximal  $x$ -displacement decreases from 0.1 m to 0.03 m.

**5.1.2. PTR Section Deformation.** Several curves showing the variation of the  $z$ -displacement of the cross-cut roof when the longwall face advances were obtained and are shown in

Figure 12(a). When the longwall face advances, the distance between the longwall face and the cross-cut decreases ( $x$ -direction). The displacement along the  $z$ -direction of the cross-cut roof increases, subjected to the advancing abutment pressure. However, the displacement along the cross-cut is different, owing to the different thickness of the backfilling material and the magnitude of the advancing abutment pressure. The  $z$ -displacement gradually increases with the advancing longwall face and as the advancing abutment pressure increases. However, the  $z$ -displacement at the measured points  $y=74$ ,  $y=78$ , and  $y=82$  starts to decrease, while that at the measured points  $y=54$ ,  $y=58$ ,  $y=62$ ,  $y=66$ , and  $y=70$  continues to increase when the longwall face advances 68 m. The maximal  $z$ -displacement decreases from 0.76 m to 0.13 m after backfilling. In this way, the longwall face can pass through the cross-cut smoothly without worrying about the FOG and support-crushing accidents.

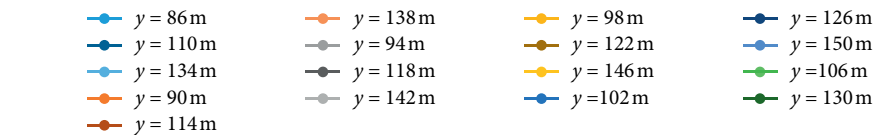
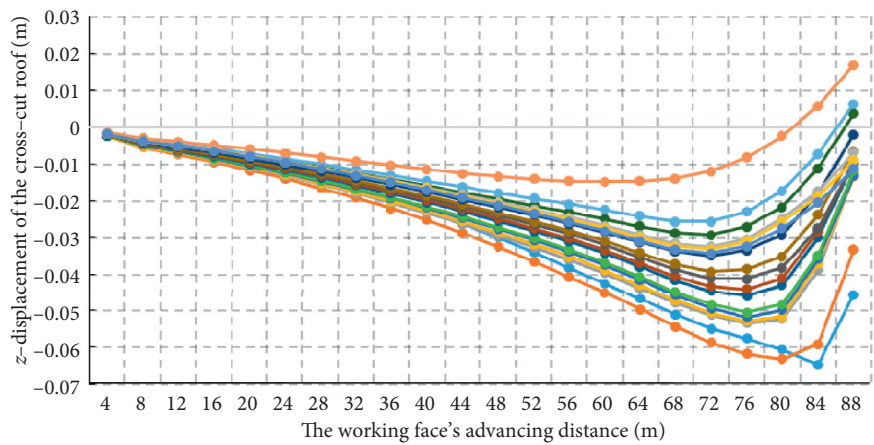
In Figure 13, after backfilling, the backfilling material and the surrounding rock are integrated with each other. Compared with the maximal  $x$ -displacement without

TABLE 6: Parameters for granular coal.

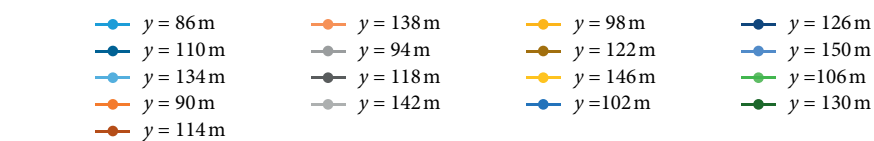
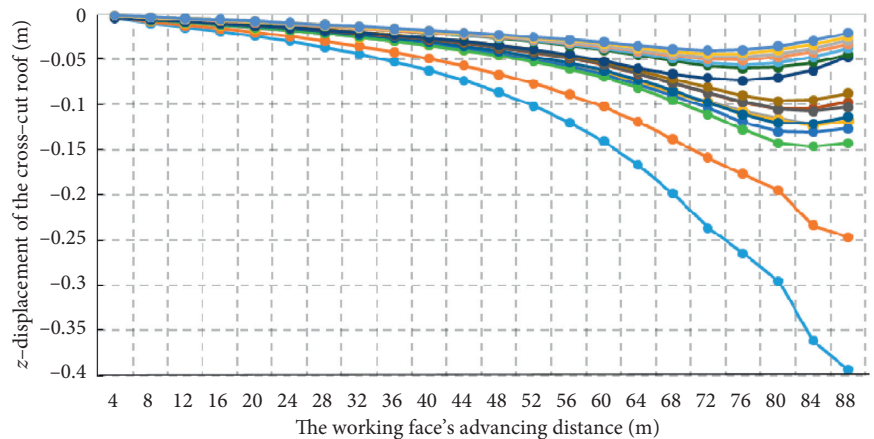
Radius (m)	Density (kg/m <sup>3</sup> )	Normal stiffness (N/m)	Shear stiffness (N/m)	Friction coefficient	Cohesion (MPa)	Damp
0.1-0.2	1400	2 × 10 <sup>8</sup>	2 × 10 <sup>8</sup>	0.4	0	0.7

TABLE 7: Parameters for the concrete and the wood cribs.

Material	Constitutive model	Density (kg/m <sup>3</sup> )	Young's modulus (GPa)	Poisson's ratio	Cohesive (MPa)	Friction angle (deg.)	Tension (MPa)
Concrete	Mohr-Coulomb	2400	30	0.2	3.18	55	1.43
Wood cribs	Elastic	364	4.3	0.38	—	—	—



(a)



(b)

FIGURE 10: z-displacement of SAR section: (a) z-displacement of SAR section with backfilling and (b) z-displacement of SAR section without backfilling.

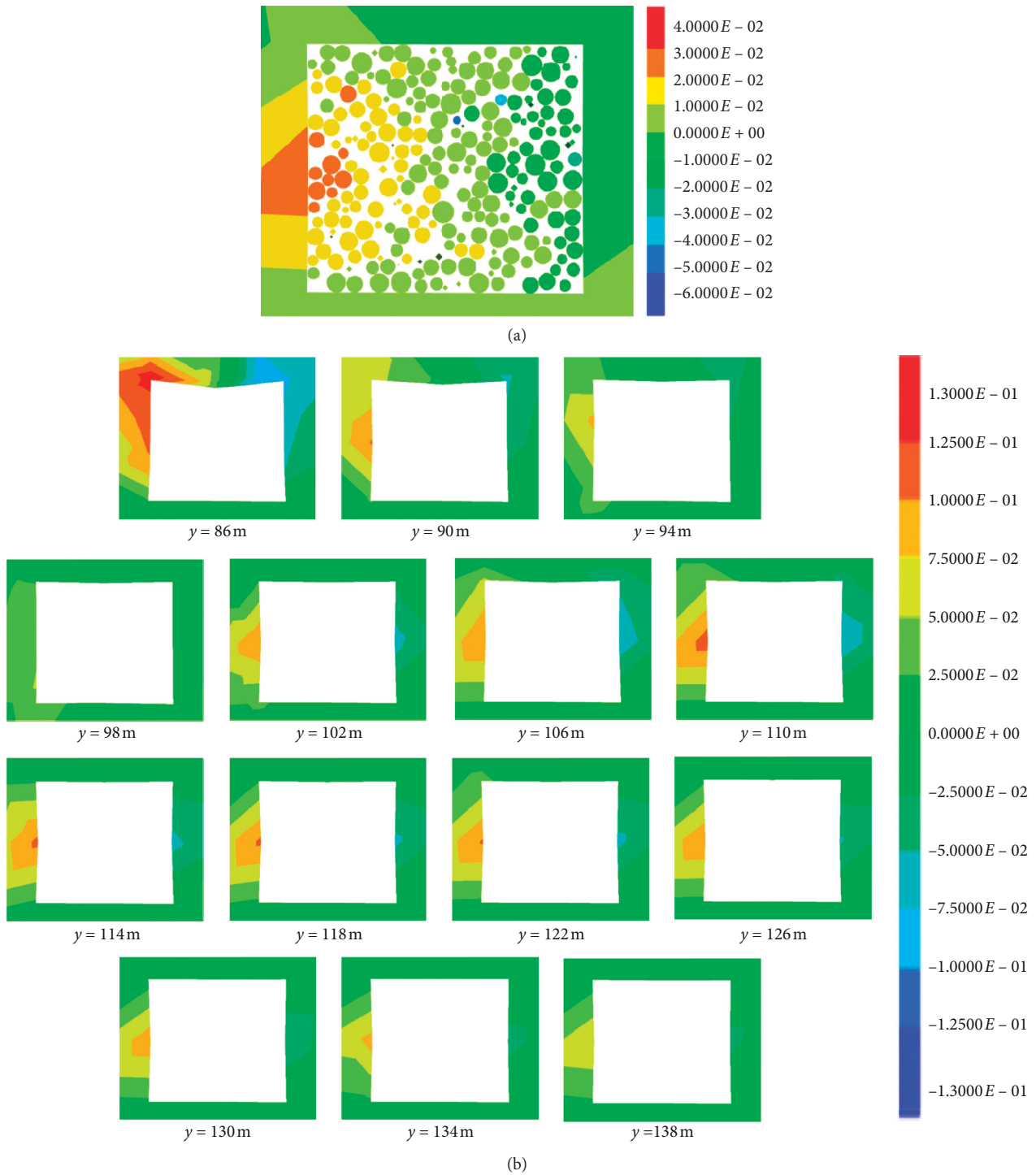


FIGURE 11:  $x$ -displacement of the cross-cut walls in SAR section. (a) Maximum  $x$ -displacement of the cross-cut walls after backfilling in measure point  $y = 126$  m. (b)  $x$ -displacement of the cross-cut walls without backfilling.

backfilling, the maximal  $x$ -displacement decreases from 0.4 m to 0.014 m, which indicates that the wood cribs are stable and the rib spalling can be avoided. Thus, the normal production of the longwall face is guaranteed.

5.2. Face Floor Subsidence (SAR Section Side) When the Longwall Face Is above the Cross-Cut. When the longwall face is above the cross-cut, the face floor subsides at a maximum value. As shown in Figure 14, along the

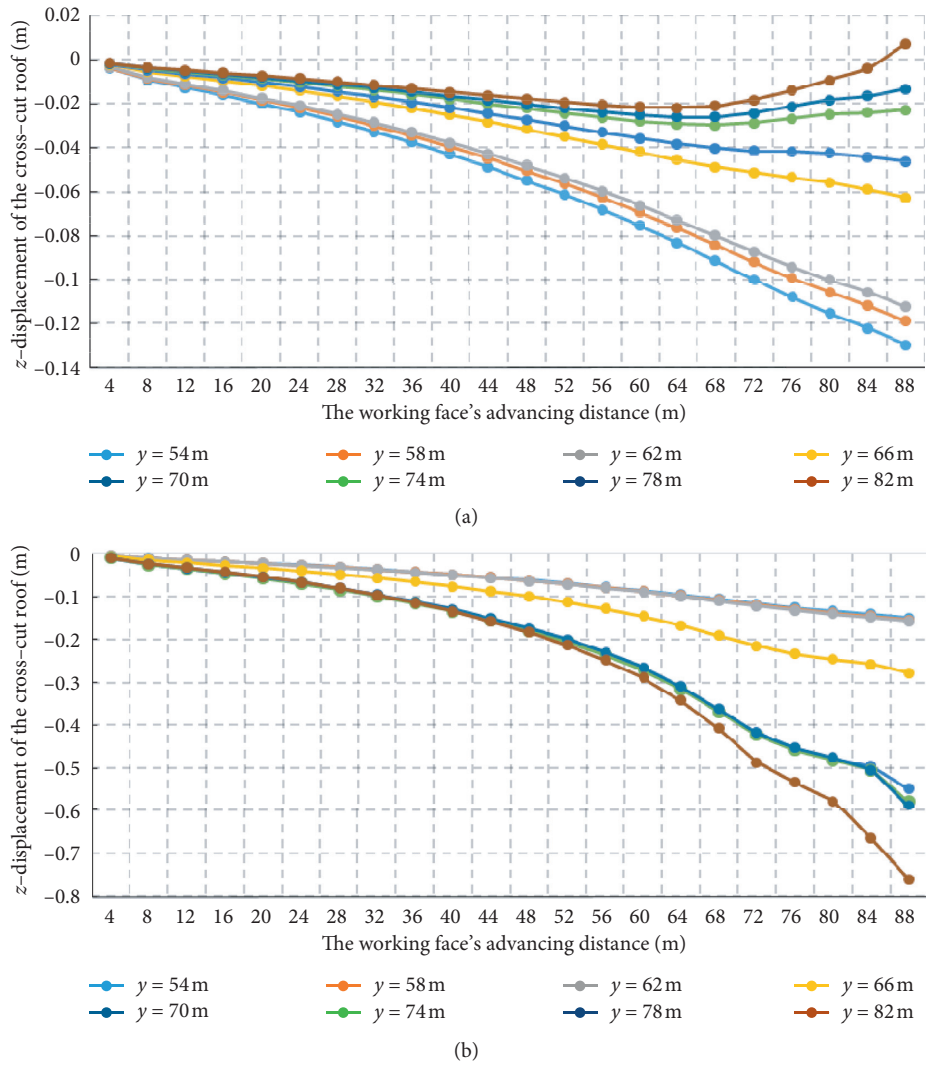
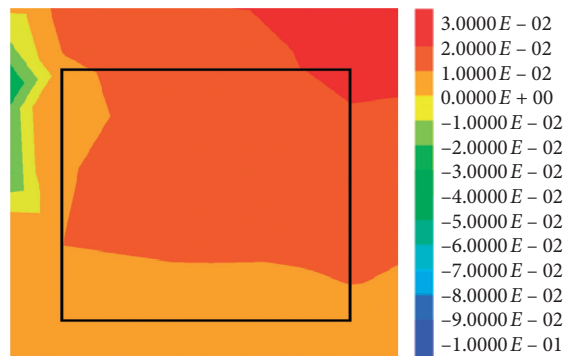


FIGURE 12: z-displacement of PTR section. (a) z-displacement of PTR section with backfilling. (b) z-displacement of PTR section without backfilling.



(a)  
FIGURE 13: Continued.

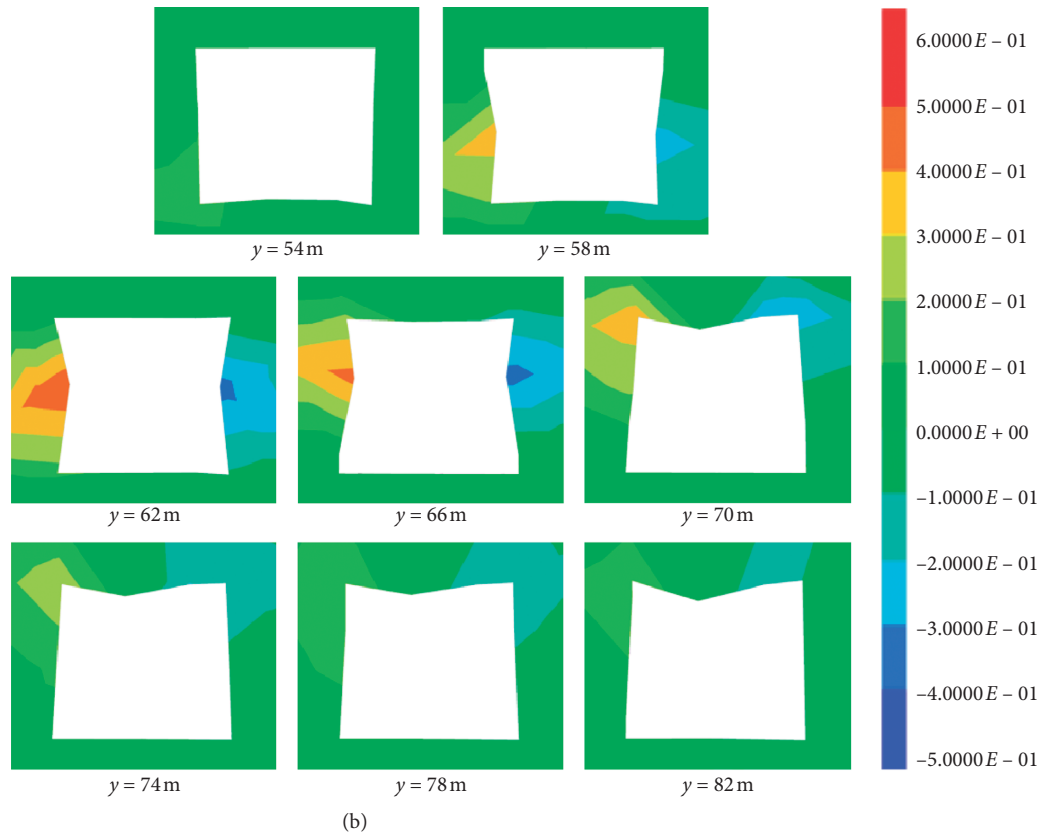


FIGURE 13:  $x$ -displacement of the cross-cut walls in PTR section. (a) Maximum  $x$ -displacement of the cross-cut walls after backfilling in measure point  $y = 70$  m. (b)  $x$ -displacement of the cross-cut walls without backfilling.

direction of the cross-cut axis, the magnitude of the subsidence decreases from 0.16 m to 0 m, then begins to increase in the opposite direction, and eventually stabilizes at 0.025 m. Note that the subsidence that occurs at the position  $y$  in the 132.5–140.5 m range is too small to affect normal production, for which the rock strata thickness is in an excellent agreement with the value calculated by the proposed model.

**5.3. Effect of the Backfilling Material.** The wood cribs and concrete, which are filled in PTR section as a backfilling material, provide support to the walls and the roof. The wood, which has a large Poisson's ratio, is a good material for maintaining the stability of the cross-cut, owing to its admirable Poisson effect and elastic deformability. The deformation of the PTR section is relatively larger than that of the SAR section. During the advancement of the longwall face, the displacement, either in the  $x$ -direction or in the  $z$ -direction, first increases and then decreases, because the peak advancing abutment pressure is at a certain distance in front of the longwall face. When a  $z$ -displacement occurs at the roof, the wood provides support to the roof and simultaneously generates lateral deformation, which provides support pressure to the walls. Meanwhile, the  $x$ -displacement that occurs at the walls provides confined

pressure to the backfilling material and increases its strength. In this way, both the FOG and the rib spalling can be controlled. As a soft material, the wood would not affect the shearer cutting coal, and the concrete would provide strong support to the supports and shearer when the longwall face passes through the cross-cut.

As an accessible material, the granular coal also exhibits a good performance in resisting deformation, and the continuity of displacements between the granular coal and rock mass indicates that the granular coal has a good displacement transmissibility, as shown in Figure 11(a). Subjected to the squeeze coming from the cross-cut deformation, the granular coal is compacted. The contact force between the coal and the cross-cut surface increases as the longwall face advances, especially in the middle of the walls ( $z$ -direction) and the roof ( $x$ -direction), as shown in Figure 15. However, this trend is interrupted when the face advances to 80 m; then, the contact force decreases as the face continues to advance. Note that the position of the peak contact force does not correspond to the field observations and measurements of the position of the advancing abutment pressure. The occurrence of this phenomenon may be related to excavation of the cross-cut, which may disturb the in-situ stress distribution and therefore would change the position of the advancing abutment pressure.

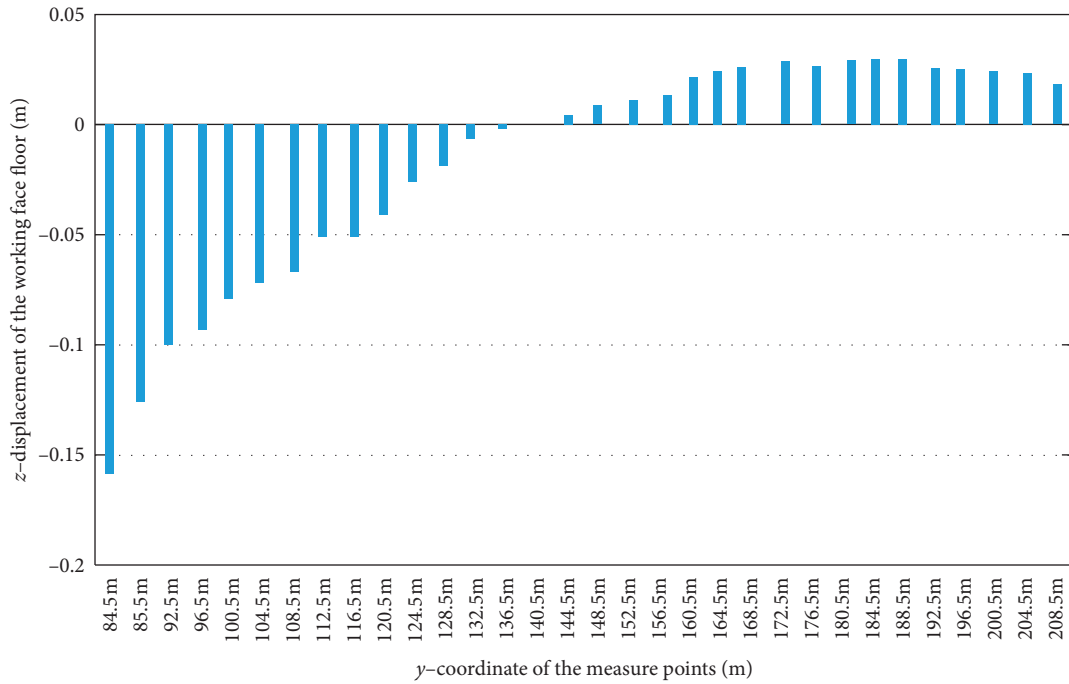


FIGURE 14: z-displacement of the face floor after backfilling.

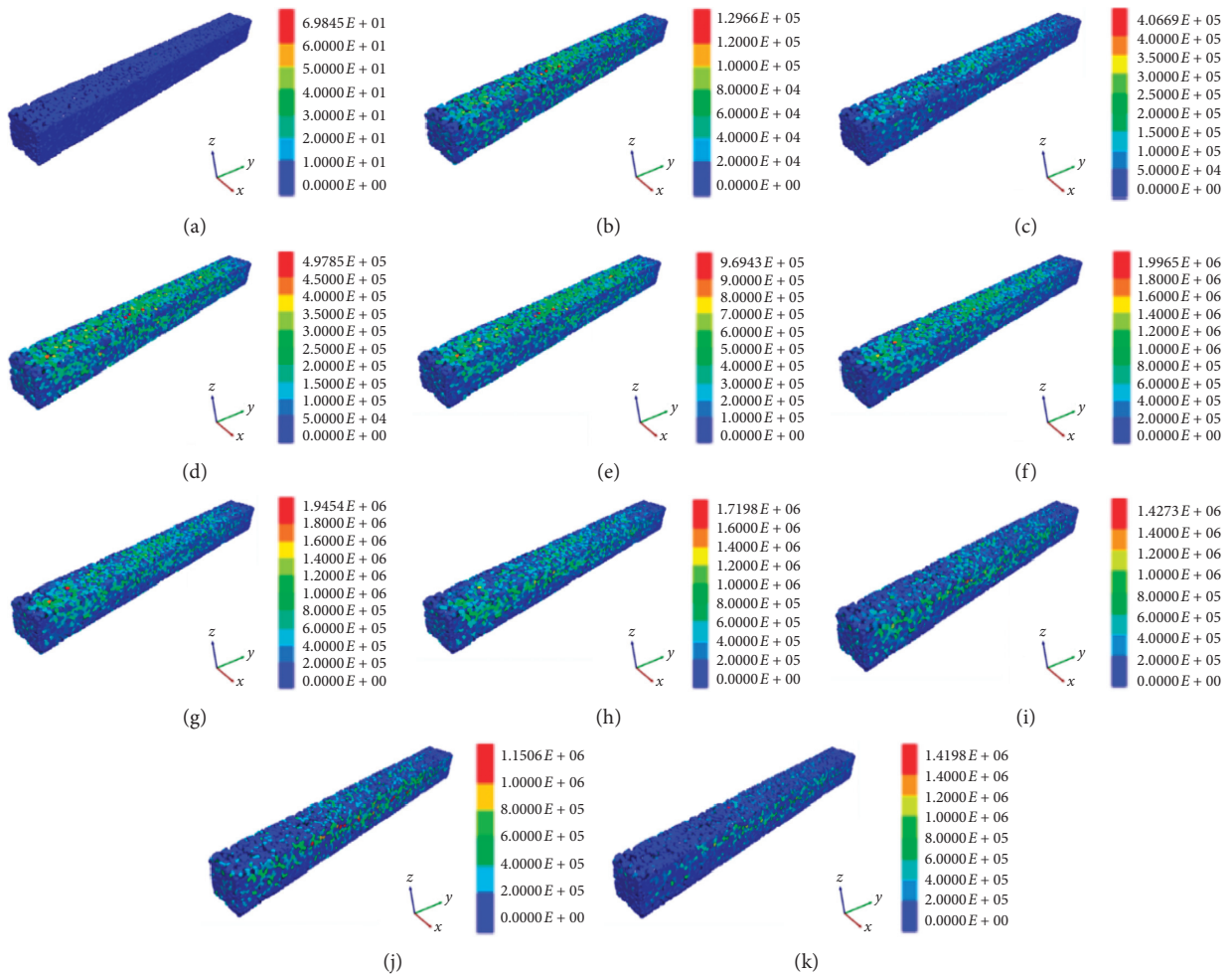


FIGURE 15: Contact force between granular coal and cross-cut with working face advancing. (a) 0 m. (b) 16 m. (c) 32 m. (d) 48 m. (e) 64 m. (f) 80 m. (g) 84 m. (h) 88 m. (i) 92 m. (j) 96 m. (k) 100 m.

## 6. Conclusions

- (1) A support design method is proposed when longwall face strides across and passes through a roadway, which is consisting of a model to determine the roadway supporting range and support scheme. The model is built based on Terzaghi's principle, rock beam, and Protodjakonov's theory. The developed model was used to determine the range of the roadway needing supporting. And a segmental support scheme is introduced based on the developed model.
- (2) An elastic model was developed to represent the mechanical behaviour of the crashed material in the gob. Comparing with Salamon's model, the elastic model provided more efficient computation and better results when the vertical stress below 20 MPa. The elastic model will be used in follow-up studies as a reference.
- (3) Based on a real case, the rationality of this model was validated using a FDEM method. The results indicate that this backfilling design can meet the production requirements and is likely to significantly reduce the support cost. The results suggest that the proposed model can be used for determining the minimal thickness of the rock strata, with the error rate ranging from  $-10.44\%$  to  $9.97\%$ . The results of this study are likely to be useful as a reference for the safe and efficient mining of coal resources under similar conditions.

## Data Availability

Some or all data, models, or codes that support the findings of this study are available from the corresponding author upon reasonable request.

## Conflicts of Interest

The authors declare no conflicts of interest.

## Acknowledgments

This work was supported by the National Key Research and Development Program of China (no. 2018YFC0604501) and the Fundamental Research Funds for the Central Universities (no. 2020YQNY09).

## References

- [1] C. Liu, Z. Yang, P. Gong et al., "Accident analysis in relation to main roof structure when longwall face advances toward a roadway: a case study," *Advances in Civil Engineering*, vol. 2018, Article ID 3810315, 11 pages, 2018.
- [2] D. C. Oyler, C. Mark, D. R. Dolinar, and R. C. Frith, "A study of the ground control effects of mining longwall faces into open or backfilled entries," *Geotechnical and Geological Engineering*, vol. 19, no. 2, pp. 137–168, 2001.
- [3] W. D. Pan, G. D. Liu, and L. K. Wei, "Safety rock stratum thickness and reinforced support technology during mining face striding crosscuts," *Journal of China Coal Society*, vol. 38, no. 4, 2013.
- [4] D.-Z. Kong, Z.-B. Cheng, and S.-S. Zheng, "Study on the failure mechanism and stability control measures in a large-cutting-height coal mining face with a deep-buried seam," *Bulletin of Engineering Geology and the Environment*, vol. 78, no. 8, pp. 6143–6157, 2019.
- [5] Y. Lu and L. Wang, "Numerical simulation of mining-induced fracture evolution and water flow in coal seam floor above a confined aquifer," *Computers and Geotechnics*, vol. 67, pp. 157–171, 2015.
- [6] M. Chen, S.-Q. Yang, Y.-C. Zhang, and C.-W. Zang, "Analysis of the failure mechanism and support technology for the Dongtan deep coal roadway," *Geomechanics and Engineering*, vol. 11, no. 3, pp. 401–420, 2016.
- [7] W. Zheng, Q. Bu, and Y. Hu, "Plastic failure analysis of roadway floor surrounding rocks based on unified strength theory," *Advances in Civil Engineering*, vol. 2018, Article ID 7475698, 10 pages, 2018.
- [8] H. Kang, H. Lv, X. Zhang, F. Gao, Z. Wu, and Z. Wang, "Evaluation of the ground response of a pre-driven longwall recovery room supported by concrete cribs," *Rock Mechanics and Rock Engineering*, vol. 49, no. 3, pp. 1025–1040, 2016.
- [9] W. Pan, X. Nie, and X. Li, "Effect of premining on hard roof distress behavior: a case study," *Rock Mechanics and Rock Engineering*, vol. 52, no. 6, pp. 1871–1885, 2019.
- [10] K. Terzaghi, *Theoretical Soil Mechanics*, John Wiley & Sons, Inc., vol. 1, Hoboken, NJ, USA, 1943.
- [11] S. Mahdevari, K. Shahriar, M. Sharifzadeh, and D. D. Tannant, "Stability prediction of gate roadways in longwall mining using artificial neural networks," *Neural Computing and Applications*, vol. 28, no. 11, pp. 3537–3555, 2017.
- [12] R. Šňuparek and P. Konečný, "Stability of roadways in coalmines alias rock mechanics in practice," *Journal of Rock Mechanics and Geotechnical Engineering*, vol. 2, no. 3, pp. 281–288, 2010.
- [13] Q. Chang, J. Chen, H. Zhou, and J. Bai, "Implementation of paste backfill mining technology in Chinese coal mines," *The Entific World Journal*, vol. 2014, Article ID 821025, 8 pages, 2014.
- [14] L. Fan and S. Liu, "Numerical prediction of in situ horizontal stress evolution in coalbed methane reservoirs by considering both poroelastic and sorption induced strain effects," *International Journal of Rock Mechanics and Mining Sciences*, vol. 104, pp. 156–164, 2018.
- [15] M. Cai, M. He, and D. Liu, *Rock Mechanics and Engineering*, Science Press, Beijing, China, 2002.
- [16] N. Mohammad, D. J. Reddish, and L. R. Stace, "The relation between in situ and laboratory rock properties used in numerical modelling," *International Journal of Rock Mechanics and Mining Sciences*, vol. 34, no. 2, pp. 289–297, 1997.
- [17] G. S. P. Singh and U. K. Singh, "A numerical modeling approach for assessment of progressive caving of strata and performance of hydraulic powered support in longwall workings," *Computers and Geotechnics*, vol. 36, no. 7, pp. 1142–1156, 2009.
- [18] Z.-L. Li, X.-Q. He, L.-M. Dou, D.-Z. Song, and G.-F. Wang, "Numerical investigation of load shedding and rockburst reduction effects of top-coal caving mining in thick coal seams," *International Journal of Rock Mechanics and Mining Sciences*, vol. 110, pp. 266–278, 2018.
- [19] H. Yavuz, "An estimation method for cover pressure re-establishment distance and pressure distribution in the goaf of

- longwall coal mines,” *International Journal of Rock Mechanics and Mining Sciences*, vol. 41, no. 2, pp. 193–205, 2004.
- [20] M. Salamon, “Mechanism of caving in longwall coal mining,” in *Proceedings of the 31st US Symposium on Rock Mechanics Contributions and Challenges*, pp. 161–168, Golden, CO, USA, June 1990.
- [21] M. Bai, F. S. Kendorski, and D. J. Van Roosendaal, *Chinese and North American High-Extraction Underground Coal Mining Strata Behavior and Water Protection Experience and Guidelines*, West Virginia University, Morgantown, WV, USA, 1995.
- [22] A. Liu, S. Liu, G. Wang, and D. Elsworth, “Predicting fugitive gas emissions from gob-to-face in longwall coal mines: coupled analytical and numerical modeling,” *International Journal of Heat and Mass Transfer*, vol. 150, Article ID 119392, 2020.
- [23] S. S. Peng, *Longwall Mining*, CRC Press, Boca Raton, FL, USA, 3rd edition, 2019.
- [24] H. Basarir, Y. Sun, and G. Li, “Gateway stability analysis by global-local modeling approach,” *International Journal of Rock Mechanics and Mining Sciences*, vol. 113, no. 1, pp. 31–40, 2019.
- [25] H. Kose and Y. Cebi, “Investigation the stresses forming during production of thick coal seam,” in *Proceedings of the 6th Coal Congress of Turkey*, pp. 371–383, Zonguldak, Turkey, January 1988.
- [26] M. Shabanimashcool and C. C. Li, “Numerical modelling of longwall mining and stability analysis of the gates in a coal mine,” *International Journal of Rock Mechanics and Mining Sciences*, vol. 51, pp. 24–34, 2012.
- [27] Y. Jiang, H. Wang, S. Xue, Y. Zhao, J. Zhu, and X. Pang, “Assessment and mitigation of coal bump risk during extraction of an island longwall panel,” *International Journal of Coal Geology*, vol. 95, pp. 20–33, 2012.
- [28] F. E. Garcia and J. D. Bray, “Modeling the shear response of granular materials with discrete element assemblages of sphere-clusters,” *Computers and Geotechnics*, vol. 106, pp. 99–107, 2019.
- [29] Y. Hu, W. Li, Q. Wang, S. Liu, and Z. Wang, “Study on failure depth of coal seam floor in deep mining,” *Environmental Earth Sciences*, vol. 78, no. 24, 2019.
- [30] J. Wang, S. Yang, Y. Li, L. Wei, and H. Liu, “Caving mechanisms of loose top-coal in longwall top-coal caving mining method,” *International Journal of Rock Mechanics and Mining Sciences*, vol. 71, pp. 160–170, 2014.
- [31] L. Li and M. Aubertin, “An improved method to assess the required strength of cemented backfill in underground stopes with an open face,” *International Journal of Mining Science and Technology*, vol. 24, no. 4, pp. 549–558, 2014.
- [32] M. Pattonmallory, S. M. Cramer, F. W. Smith, and P. J. Pellicane, “Nonlinear material models for analysis of bolted wood connections,” *Journal of Structural Engineering (ASCE)*, vol. 123, no. 8, pp. 1063–1070, 1997.

## Research Article

# Optimized Polynomial Virtual Fields Method for Constitutive Parameters Identification of Orthotropic Bimaterials

Xueyi Ma , Yu Wang, and Jian Zhao 

*School of Technology, Beijing Forestry University, Beijing 100083, China*

Correspondence should be addressed to Jian Zhao; [zhaojian1987@bjfu.edu.cn](mailto:zhaojian1987@bjfu.edu.cn)

Received 2 July 2020; Accepted 13 July 2020; Published 28 August 2020

Academic Editor: Jinyang Xu

Copyright © 2020 Xueyi Ma et al. This is an open access article distributed under the Creative Commons Attribution License, which permits unrestricted use, distribution, and reproduction in any medium, provided the original work is properly cited.

Heterogeneous materials are widely applied in many fields. Owing to the spatial variation of its constitutive parameters, the mechanical characterization of heterogeneous materials is very important. The virtual fields method has been used to identify the constitutive parameters of materials. However, there is a limitation: constitutive parameters of one material have to be a priori; then, constitutive parameters of the other one can be identified. Aiming at this limitation, this article presents a method to identify the constitutive parameters of heterogeneous orthotropic bimaterials under the condition that constitutive parameters of both materials are all unknown from a single test. A constitutive parameter identification method of orthotropic bimaterials based on optimized virtual field and digital image correlation is proposed. The feasibility of this method is verified by simulating the deformation fields of a two-layer material under three-point bending load. The results of numerical experiments with FEM simulations show that the weighted relative error of the constitutive parameter is less than 1%. The results suggest that the variation coefficient-to-noise ratio can perform a priori evaluation of a confidence interval on the identified stiffness components. The results of numerical experiments with DIC simulations show that the weighted relative error is 1.44%, which is due to the noise in the strain data calculated by DIC method.

## 1. Introduction

Heterogeneous materials, such as functionally gradient materials, wood [1, 2], polymeric foams [3], biological materials [4], and composites [5], have been widely applied in engineering. Constitutive parameters identification of heterogeneous materials is not only the important subject in experimental mechanics but also has attracted extensive notice in the fields of solid mechanics, structure health monitoring, and medical diagnosis. The traditional method of identifying constitutive parameters can directly determine all constitutive parameters of constitutive models through standard experiments (e.g., uniaxial tensile test). However, the investing of experimental involved in such standard test methods may increase when using anisotropic models and inhomogeneous materials, as well as bimaterial [6].

With the development of the photomechanics, full-field measurement methods (e.g., digital image correlation and moiré interferometry) combined with inverse methods have been developed so that the multiple constitutive parameters can be identified by a heterogeneous strain field [7]. The inverse methods belong to the updating methods (e.g., finite element updating method) and nonupdating methods (e.g., virtual fields method). The finite element updating method (FEUM) extract constitutive parameters through minimizing the cost function between the response of the finite element model and the real behavior iteratively; its simulation must be close to experimental conditions and its initial guess choice will affect the identification result [8]. The virtual fields method (VFM), which was put forward by Perrion and Grédiac [9, 10], is a typical nonupdating method used in a linear material model. Compared with the updating methods, the

advantage of VFM is that it requires less specimen boundary conditions and geometric configurations [11, 12].

A volume of research has focused on full-field measurement and VFM to identify the constitutive parameters of materials. The VFM within peridynamic framework was proposed to identify material properties in linear elasticity [13]. The special virtual fields method was adopted to resolve the difficulty in identifying constitutive properties of incompressible and nonhomogeneous solids [14]. The VFM was combined with an elaborately designed test configuration in order to realize the identification of the anisotropic yield constitutive parameters [15]. Several inverse methods based on the VFM have been developed, including the Fourier series-based VFM [16, 17], the sensitivity-based VFM [18], the eigenfunction VFM [19, 20], and several optimizations to improve the accuracy of identification results [21, 22].

The heterogeneity of strain field caused by multiple constitutive parameters of the complex constitutive model has been solved by the traditional VFM. For heterogeneous materials, the heterogeneity of strain field caused by the spatial variation of constitutive parameters requires further improvement of the virtual field method. According to the available literature studies, several methods and applications have been studied to identify constitutive parameters identification of heterogeneous material using VFM [6, 23, 24]. For instance, a bimaterial constitutive parameter identification method based on the combination of VFM and Moiré interference was proposed [25], and the VFM was also extended to identify the parameters [26]. In addition, several methods have been researched to lower the effects of noise in strain fields [26–29]. The optimized fields method, such as polynomial optimized virtual field [30] and piecewise optimized virtual field [31], was developed to improve convenience and accuracy. Although the above researches make identification of constitutive parameters more rapid and convenient, there is still a limitation for bimaterials: the constitutive parameters of one material must be a priori in order to determine the constitutive parameters of the other material. The purpose of this work is to propose an optimized virtual field that can not only extract the constitutive parameters of the heterogeneous orthotropic bimaterials without knowing any material constitutive parameters but also require only one single test.

In this study, to extract constitutive parameters of the bimaterials under the condition that constitutive parameters of the both materials are unknown, special optimized polynomial virtual fields combined with three-point bending test was proposed. In Section 2, the basic principle of optimized polynomial VFM and its improvement applied in bimaterials without knowing any material constitutive parameters are introduced. In Section 3, the FEM simulated experiments and the simulated DIC experiments are conducted to verify the feasibility of the abovementioned method. Finally, Section 4 is the conclusions.

## 2. Methodology

*2.1. Basic Principle of Optimized Polynomial Virtual Fields Method.* The integral form of the mechanical equilibrium equation of the VFM based on virtual work for a continuous solid can be expressed as [31]

$$\begin{aligned} & - \int_S \boldsymbol{\sigma} : \boldsymbol{\varepsilon}^* dS + \int_S \bar{\mathbf{T}} \cdot \mathbf{u}^* dS + \int_V \mathbf{b} \cdot \mathbf{u}^* dV \\ & = \int_V \rho \mathbf{a} \cdot \mathbf{u}^* dV \quad \forall \mathbf{u}^* \text{ KA}, \end{aligned} \quad (1)$$

where  $\boldsymbol{\sigma}$  is the Cauchy stress tensor,  $\mathbf{u}^*$  is the virtual displacement vector,  $\boldsymbol{\varepsilon}^*$  denotes the strain tensor corresponding to  $\mathbf{u}^*$ ,  $\bar{\mathbf{T}}$  represents the external force associated with the stress tensor  $\boldsymbol{\sigma}$  by the boundary,  $S$  is a vector which is the volume force applied over the volume  $V$  of the specimen, and  $\mathbf{a}$  denotes the distribution of acceleration. Such a distribution will cause an additional volumetric force distribution equal to  $-\rho \mathbf{a}$  with D'Alembert's principle, the virtual displacement field being kinematically admissible (KA).

For an orthotropic material in a plane-stress state, the principle of virtual work is suitable for every KA virtual field. This equation (see equation 2) uses four independent KA virtual fields  $\boldsymbol{\varepsilon}^{*(1)}$ ,  $\boldsymbol{\varepsilon}^{*(2)}$ ,  $\boldsymbol{\varepsilon}^{*(3)}$ , and  $\boldsymbol{\varepsilon}^{*(4)}$  instead of  $u^{*(1)}$ ,  $u^{*(2)}$ ,  $u^{*(3)}$ , and  $u^{*(4)}$ , respectively (see Appendix A1 for the detailed equation derivations):

$$\mathbf{A}\mathbf{Q} = \mathbf{B}, \quad (2)$$

where

$$\begin{aligned}
\mathbf{A} &= \begin{bmatrix} \int_S (\varepsilon_1 \varepsilon_1^*) dS & \int_S (\varepsilon_2 \varepsilon_2^*) dS & \int_S (\varepsilon_1 \varepsilon_2^* + \varepsilon_2 \varepsilon_1^*) dS & \int_S (\varepsilon_6 \varepsilon_6^*) dS \\ \int_S (\varepsilon_1 \varepsilon_1^*) dS & \int_S (\varepsilon_2 \varepsilon_2^*) dS & \int_S (\varepsilon_1 \varepsilon_2^* + \varepsilon_2 \varepsilon_1^*) dS & \int_S (\varepsilon_6 \varepsilon_6^*) dS \\ \int_S (\varepsilon_1 \varepsilon_1^*) dS & \int_S (\varepsilon_2 \varepsilon_2^*) dS & \int_S (\varepsilon_1 \varepsilon_2^* + \varepsilon_2 \varepsilon_1^*) dS & \int_S (\varepsilon_6 \varepsilon_6^*) dS \\ \int_S (\varepsilon_1 \varepsilon_1^*) dS & \int_S (\varepsilon_2 \varepsilon_2^*) dS & \int_S (\varepsilon_1 \varepsilon_2^* + \varepsilon_2 \varepsilon_1^*) dS & \int_S (\varepsilon_6 \varepsilon_6^*) dS \end{bmatrix}, \\
\mathbf{Q} &= \begin{pmatrix} Q_{11} \\ Q_{22} \\ Q_{12} \\ Q_{66} \end{pmatrix}, \\
\mathbf{B} &= \begin{pmatrix} \int_{L_f} (\bar{T}_i u_i^*) dl \\ \int_{L_f} (\bar{T}_i u_i^*) dl \\ \int_{L_f} (\bar{T}_i u_i^*) dl \\ \int_{L_f} (\bar{T}_i u_i^*) dl \end{pmatrix},
\end{aligned} \tag{3}$$

where  $Q_{11}$ ,  $Q_{22}$ ,  $Q_{12}$ , and  $Q_{66}$  are the in-plane stiffness components.

The constraints of KA virtual fields  $u^{*(1)}$ ,  $u^{*(2)}$ ,  $u^{*(3)}$ , and  $u^{*(4)}$  are as follows:

$$\begin{cases} \int_S (\varepsilon_1 \varepsilon_1^*) dS = 1 & \int_S (\varepsilon_2 \varepsilon_2^*) dS = 0 & \int_S (\varepsilon_1 \varepsilon_2^* + \varepsilon_2 \varepsilon_1^*) dS = 0 & \int_S (\varepsilon_6 \varepsilon_6^*) dS = 0 \\ \int_S (\varepsilon_1 \varepsilon_1^*) dS = 0 & \int_S (\varepsilon_2 \varepsilon_2^*) dS = 1 & \int_S (\varepsilon_1 \varepsilon_2^* + \varepsilon_2 \varepsilon_1^*) dS = 0 & \int_S (\varepsilon_6 \varepsilon_6^*) dS = 0 \\ \int_S (\varepsilon_1 \varepsilon_1^*) dS = 0 & \int_S (\varepsilon_2 \varepsilon_2^*) dS = 0 & \int_S (\varepsilon_1 \varepsilon_2^* + \varepsilon_2 \varepsilon_1^*) dS = 1 & \int_S (\varepsilon_6 \varepsilon_6^*) dS = 0 \\ \int_S (\varepsilon_1 \varepsilon_1^*) dS = 0 & \int_S (\varepsilon_2 \varepsilon_2^*) dS = 0 & \int_S (\varepsilon_1 \varepsilon_2^* + \varepsilon_2 \varepsilon_1^*) dS = 0 & \int_S (\varepsilon_6 \varepsilon_6^*) dS = 1. \end{cases} \tag{4}$$

The exact values and white noise constitute the measured strain component. Assume that the noise components are uncorrelated to each other, and presume that the noise

between points is also uncorrelated. Therefore, the principle of virtual work is as equation (5) (see Appendix A2 for the detailed equation derivations).

$$\begin{aligned}
& Q_{11} \int_S (\varepsilon_1 \varepsilon_1^*) dS + Q_{22} \int_S (\varepsilon_2 \varepsilon_2^*) dS + Q_{12} \int_S (\varepsilon_1 \varepsilon_2^* + \varepsilon_2 \varepsilon_1^*) dS + Q_{66} \int_S (\varepsilon_6 \varepsilon_6^*) dS \\
& - \gamma \left[ Q_{11} \int_S \varepsilon_1^* \mathcal{N}_1 dS + Q_{22} \int_S \varepsilon_2^* \mathcal{N}_2 dS + Q_{12} \int_S (\varepsilon_2^* \mathcal{N}_1 + \varepsilon_1^* \mathcal{N}_2) dS + Q_{66} \int_S \varepsilon_6^* \mathcal{N}_6 dS \right] = \int_{L_f} (T_i u_i^*) dl,
\end{aligned} \tag{5}$$

where  $\mathcal{N}_1$ ,  $\mathcal{N}_2$ , and  $\mathcal{N}_6$  denote the processes of scalar zero-mean stationary Gaussian generalized by the corresponding strain components  $\varepsilon_1$ ,  $\varepsilon_2$ , and  $\varepsilon_6$ , respectively, and  $\gamma$  denotes the measured amplitude of the random variable strain.

If the noise is ignored, approximate parameters expressed as  $Q^{\text{app}}$ , these components are defined by equation (6). So, directly identify  $Q_{11}$ ,  $Q_{22}$ ,  $Q_{12}$ , and  $Q_{66}$  using these four special virtual displacement fields as equation (7) (see Appendix A3 for the detailed equation derivations).

$$\left\{ \begin{array}{l} Q_{11}^{\text{app}} = \int_{L_f} (T_i u_i^{*(1)}) dl, \\ Q_{22}^{\text{app}} = \int_{L_f} (T_i u_i^{*(2)}) dl, \\ Q_{12}^{\text{app}} = \int_{L_f} (T_i u_i^{*(3)}) dl, \\ Q_{66}^{\text{app}} = \int_{L_f} (T_i u_i^{*(4)}) dl, \end{array} \right. \quad (6)$$

$$\left\{ \begin{array}{l} Q_{11} = \gamma \left[ Q_{11}^{\text{app}} \int_S \varepsilon_1^{*(1)} \mathcal{N}_1 dS + Q_{22}^{\text{app}} \int_S \varepsilon_2^{*(1)} \mathcal{N}_2 dS + Q_{12}^{\text{app}} \int_S (\varepsilon_2^{*(1)} \mathcal{N}_1 + \varepsilon_1^{*(1)} \mathcal{N}_2) dS + Q_{66}^{\text{app}} \int_S \varepsilon_6^{*(1)} \mathcal{N}_6 dS \right] + Q_{11}^{\text{app}}, \\ Q_{22} = \gamma \left[ Q_{11}^{\text{app}} \int_S \varepsilon_1^{*(2)} \mathcal{N}_1 dS + Q_{22}^{\text{app}} \int_S \varepsilon_2^{*(2)} \mathcal{N}_2 dS + Q_{12}^{\text{app}} \int_S (\varepsilon_2^{*(2)} \mathcal{N}_1 + \varepsilon_1^{*(2)} \mathcal{N}_2) dS + Q_{66}^{\text{app}} \int_S \varepsilon_6^{*(2)} \mathcal{N}_6 dS \right] + Q_{22}^{\text{app}}, \\ Q_{12} = \gamma \left[ Q_{11}^{\text{app}} \int_S \varepsilon_1^{*(3)} \mathcal{N}_1 dS + Q_{22}^{\text{app}} \int_S \varepsilon_2^{*(3)} \mathcal{N}_2 dS + Q_{12}^{\text{app}} \int_S (\varepsilon_2^{*(3)} \mathcal{N}_1 + \varepsilon_1^{*(3)} \mathcal{N}_2) dS + Q_{66}^{\text{app}} \int_S \varepsilon_6^{*(3)} \mathcal{N}_6 dS \right] + Q_{12}^{\text{app}}, \\ Q_{66} = \gamma \left[ Q_{11}^{\text{app}} \int_S \varepsilon_1^{*(4)} \mathcal{N}_1 dS + Q_{22}^{\text{app}} \int_S \varepsilon_2^{*(4)} \mathcal{N}_2 dS + Q_{12}^{\text{app}} \int_S (\varepsilon_2^{*(4)} \mathcal{N}_1 + \varepsilon_1^{*(4)} \mathcal{N}_2) dS + Q_{66}^{\text{app}} \int_S \varepsilon_6^{*(4)} \mathcal{N}_6 dS \right] + Q_{66}^{\text{app}}. \end{array} \right. \quad (7)$$

Similar results are obtained for  $Q_{22}$ ,  $Q_{12}$ , and  $Q_{66}$ . Denoting  $V(Q)$ , the vector containing the variances of  $Q_{11}$ ,  $Q_{22}$ ,  $Q_{12}$ , and  $Q_{66}$ , one can write as equation (8) (see Appendix A4 for the detailed equation derivations).

$$\left\{ \begin{array}{l} V(Q_{11}) = (\eta^{(1)})^2 \gamma^2, \\ V(Q_{22}) = (\eta^{(2)})^2 \gamma^2, \\ V(Q_{12}) = (\eta^{(3)})^2 \gamma^2, \\ V(Q_{66}) = (\eta^{(4)})^2 \gamma^2, \end{array} \right. \quad (8)$$

and  $(\eta^{(i)})^2$  have two kinds of unknowns: the constitutive parameters and the unknown coefficients of the virtual fields. So,  $(\eta^{(i)})^2$  can be expressed as

$$(\eta^{(i)})^2 = \frac{1}{2} \mathbf{Y}^{*(i)} \mathbf{H} \mathbf{Y}^{*(i)} = \left( \frac{S_c}{n_c} \right)^2 \mathbf{Q}^{\text{app}} \mathbf{G}^{(i)} \mathbf{Q}^{\text{app}}, \quad (9)$$

where  $\mathbf{Y}^*$  is the vector related to the coefficients of virtual strain fields,  $\mathbf{H}$  is the Hessian matrix of all monomials in  $\varepsilon^*$ , and  $\mathbf{G}^{(j)}$ ,  $j = 1, 2, 3, 4$ , is the following square matrix:

$$\left[ \begin{array}{cccc} \sum_{i=1}^n (\varepsilon_1^{*(j)}(M_i))^2 & 0 & \sum_{i=1}^n \varepsilon_1^{*(j)}(M_i) \varepsilon_2^{*(j)}(M_i) & 0 \\ 0 & \sum_{i=1}^n (\varepsilon_2^{*(j)}(M_i))^2 & \sum_{i=1}^n \varepsilon_1^{*(j)}(M_i) \varepsilon_2^{*(j)}(M_i) & 0 \\ \sum_{i=1}^n \varepsilon_1^{*(j)}(M_i) \varepsilon_2^{*(j)}(M_i) & \sum_{i=1}^n \varepsilon_1^{*(j)}(M_i) \varepsilon_2^{*(j)}(M_i) & \sum_{i=1}^n (\varepsilon_1^{*(j)}(M_i))^2 + \sum_{i=1}^n (\varepsilon_2^{*(j)}(M_i))^2 & 0 \\ 0 & 0 & 0 & \sum_{i=1}^n (\varepsilon_6^{*(j)}(M_i))^2 \end{array} \right], \quad (10)$$

and the  $(\eta^{(i)})^2$  coefficients  $i = 1, 2, 3, 4$  depend on the selected virtual fields. Also, the virtual fields are selected for the  $Q_{ij}$  parameters extraction. Thus, select the appropriate virtual field that can reduce the influence of

strain. In this article, the virtual fields were expanded by the polynomials. The displacement fields and the virtual strain are as shown in equations (11) and (12), respectively.

$$\begin{cases} u_1^* = \sum_{i=0}^m \sum_{j=0}^n A_{ij} \left(\frac{x_1}{L}\right)^i \left(\frac{x_2}{w}\right)^j, \\ u_2^* = \sum_{i=0}^m \sum_{j=0}^n B_{ij} \left(\frac{x_1}{L}\right)^i \left(\frac{x_2}{w}\right)^j, \end{cases} \quad (11)$$

$$\begin{cases} \varepsilon_1^* = \sum_{i=1}^m \sum_{j=0}^n A_{ij} \left(\frac{x_1}{L}\right)^{i-1} \left(\frac{x_2}{w}\right)^j, \\ \varepsilon_2^* = \sum_{i=0}^m \sum_{j=1}^n B_{ij} \left(\frac{x_1}{L}\right)^i \left(\frac{x_2}{w}\right)^{j-1}, \\ \varepsilon_6^* = \sum_{i=0}^m \sum_{j=1}^n A_{ij} \frac{i}{L} \left(\frac{x_1}{L}\right)^i \left(\frac{x_2}{w}\right)^{j-1} + \sum_{i=1}^m \sum_{j=0}^n B_{ij} \frac{i}{L} \left(\frac{x_1}{L}\right)^{i-1} \left(\frac{x_2}{w}\right)^j, \end{cases} \quad (12)$$

where  $A_{ij}$  and  $B_{ij}$  are the coefficients of the monomials,  $m$  and  $n$  are the polynomial degrees that define that the maximum number of monomials has used, and  $L$  and  $w$  are the typical dimensions of the  $x_1$  and  $x_2$  directions, respectively.

Using the Lagrange multiplier approach, the Lagrangian function  $\mathcal{L}^{(i)}$  can be constructed for each constitutive parameter sought, and its constraint is equation (13), and the objective function is  $(\eta^{(i)})^2$ . Therefore, the expression of the Lagrange function is

$$\mathcal{L}^{(i)} = \frac{1}{2} \mathbf{Y}^{*(i)} \mathbf{H} \mathbf{Y}^{*(i)} + \lambda^{(i)} (\mathbf{A} \mathbf{Y}^{*(i)} - \mathbf{Z}^{(i)}), \quad (13)$$

where  $\lambda^{(i)}$  is the vector containing Lagrange multipliers.

The KA condition can produce several linear equations, and the number of this equations is depending on the number of supports. The special virtual field condition also leads to several linear equations, the number of which depends on the type of constitutive model of specimen material. The two types of conditions can produce the following linear system as equation (14) (see Appendix A5 for the detailed equation derivations).

$$\begin{bmatrix} \mathbf{H} & \mathbf{A} \\ \mathbf{A} & \mathbf{0} \end{bmatrix} \begin{pmatrix} \mathbf{Y}^{(i)} \\ \boldsymbol{\lambda}^{(i)} \end{pmatrix} = \begin{pmatrix} \mathbf{0} \\ \mathbf{Z}^{(i)} \end{pmatrix}. \quad (14)$$

Attention that  $(\eta^{(i)})^2$  coefficients also correspond on the unknown  $Q_{ij}$  parameters. Thus, the optimization problem is solved for a given set of  $Q_{ij}$  parameters, and the process is

iterative: the first guess of the  $Q_{ij}$  parameters is used to find the first group of four special virtual fields. Then, these four special virtual fields are used to find a new set of  $Q_{ij}$  parameters, and repeat abovementioned steps until the optimal  $Q_{ij}$  parameter is found. In practice, no matter what the parameter  $Q_{ij}$  is initially selected, this iterative process will converge quickly. Usually, only two loops are sufficient to converge.

**2.2. Optimized Polynomial Virtual Fields Applied to the Bimaterials without Knowing Any Material Constitutive Parameters.** As shown in Figure 1, for the plane-stress specimen with two different materials Part A and Part B, and both of them are set with the elastic orthotropic material. But the constitutive parameters of A and B are unknown. As mentioned above, the sum of exact values and white noise is the measured strain. Assume that the noise components are uncorrelated to each other, and presume that the noise between points is also uncorrelated. Therefore, the governing equation of the virtual fields method for the total specimen is as equation (15) (see Appendix B1 for the detailed equation derivations).

$$\begin{aligned} & Q_{11a} \int_{S_a} \varepsilon_1 \varepsilon_1^* dS + Q_{22a} \int_{S_a} \varepsilon_2 \varepsilon_2^* dS + Q_{12a} \int_{S_a} (\varepsilon_1 \varepsilon_2^* + \varepsilon_2 \varepsilon_1^*) dS \\ & + Q_{66a} \int_{S_a} \varepsilon_6 \varepsilon_6^* dS + \\ & Q_{11b} \int_{S_b} \varepsilon_1 \varepsilon_1^* dS + Q_{22b} \int_{S_b} \varepsilon_2 \varepsilon_2^* dS + Q_{12b} \int_{S_b} (\varepsilon_1 \varepsilon_2^* + \varepsilon_2 \varepsilon_1^*) dS \\ & + Q_{66b} \int_{S_b} \varepsilon_6 \varepsilon_6^* dS - \\ & \gamma \left[ Q_{11a} \int_{S_a} \varepsilon_1^* \mathcal{N}_1 dS + Q_{22a} \int_{S_a} \varepsilon_2^* \mathcal{N}_2 dS \right. \\ & \left. + Q_{12a} \int_{S_a} (\varepsilon_2^* \mathcal{N}_1 + \varepsilon_1^* \mathcal{N}_2) dS + Q_{66a} \int_{S_a} \varepsilon_6^* \mathcal{N}_6 dS \right. \\ & \left. Q_{11b} \int_{S_b} \varepsilon_1^* \mathcal{N}_1 dS + Q_{22b} \int_{S_b} \varepsilon_2^* \mathcal{N}_2 dS \right. \\ & \left. + Q_{12b} \int_{S_b} (\varepsilon_2^* \mathcal{N}_1 + \varepsilon_1^* \mathcal{N}_2) dS + Q_{66b} \int_{S_b} \varepsilon_6^* \mathcal{N}_6 dS \right] \\ & = \int_{L_f} (T_i u_i^*) dl. \end{aligned} \quad (15)$$

The constraints of the eight special virtual fields denoted that  $u^{*(1)}$ ,  $u^{*(2)}$ ,  $u^{*(3)}$ ,  $u^{*(4)}$ ,  $u^{*(5)}$ ,  $u^{*(6)}$ ,  $u^{*(7)}$ , and  $u^{*(8)}$  must satisfy the following equation:

$$\left[ \begin{array}{l}
\int_{S_a} (\varepsilon_1 \varepsilon_1^{*(1)}) dS = 0 \quad \int_{S_a} (\varepsilon_2 \varepsilon_2^{*(1)}) dS = 0 \quad \int_{S_a} (\varepsilon_1 \varepsilon_2^{*(1)} + \varepsilon_2 \varepsilon_1^{*(1)}) dS = 1 \quad \int_{S_a} (\varepsilon_6 \varepsilon_6^{*(1)}) dS = 0, \\
\int_{S_b} (\varepsilon_1 \varepsilon_1^{*(1)}) dS = 0 \quad \int_{S_b} (\varepsilon_2 \varepsilon_2^{*(1)}) dS = 0 \quad \int_{S_b} (\varepsilon_1 \varepsilon_2^{*(1)} + \varepsilon_2 \varepsilon_1^{*(1)}) dS = 0 \quad \int_{S_b} (\varepsilon_6 \varepsilon_6^{*(1)}) dS = 0, \\
\int_{S_a} (\varepsilon_1 \varepsilon_1^{*(2)}) dS = 0 \quad \int_{S_a} (\varepsilon_2 \varepsilon_2^{*(2)}) dS = 0 \quad \int_{S_a} (\varepsilon_1 \varepsilon_2^{*(2)} + \varepsilon_2 \varepsilon_1^{*(2)}) dS = 1 \quad \int_{S_a} (\varepsilon_6 \varepsilon_6^{*(2)}) dS = 0, \\
\int_{S_b} (\varepsilon_1 \varepsilon_1^{*(2)}) dS = 0 \quad \int_{S_b} (\varepsilon_2 \varepsilon_2^{*(2)}) dS = 0 \quad \int_{S_b} (\varepsilon_1 \varepsilon_2^{*(2)} + \varepsilon_2 \varepsilon_1^{*(2)}) dS = 0 \quad \int_{S_b} (\varepsilon_6 \varepsilon_6^{*(2)}) dS = 0, \\
\int_{S_a} (\varepsilon_1 \varepsilon_1^{*(3)}) dS = 0 \quad \int_{S_a} (\varepsilon_2 \varepsilon_2^{*(3)}) dS = 0 \quad \int_{S_a} (\varepsilon_1 \varepsilon_2^{*(3)} + \varepsilon_2 \varepsilon_1^{*(3)}) dS = 1 \quad \int_{S_a} (\varepsilon_6 \varepsilon_6^{*(3)}) dS = 0, \\
\int_{S_b} (\varepsilon_1 \varepsilon_1^{*(3)}) dS = 0 \quad \int_{S_b} (\varepsilon_2 \varepsilon_2^{*(3)}) dS = 0 \quad \int_{S_b} (\varepsilon_1 \varepsilon_2^{*(3)} + \varepsilon_2 \varepsilon_1^{*(3)}) dS = 0 \quad \int_{S_b} (\varepsilon_6 \varepsilon_6^{*(3)}) dS = 0, \\
\int_{S_a} (\varepsilon_1 \varepsilon_1^{*(4)}) dS = 0 \quad \int_{S_a} (\varepsilon_2 \varepsilon_2^{*(4)}) dS = 0 \quad \int_{S_a} (\varepsilon_1 \varepsilon_2^{*(4)} + \varepsilon_2 \varepsilon_1^{*(4)}) dS = 1 \quad \int_{S_a} (\varepsilon_6 \varepsilon_6^{*(4)}) dS = 0, \\
\int_{S_b} (\varepsilon_1 \varepsilon_1^{*(4)}) dS = 0 \quad \int_{S_b} (\varepsilon_2 \varepsilon_2^{*(4)}) dS = 0 \quad \int_{S_b} (\varepsilon_1 \varepsilon_2^{*(4)} + \varepsilon_2 \varepsilon_1^{*(4)}) dS = 0 \quad \int_{S_b} (\varepsilon_6 \varepsilon_6^{*(4)}) dS = 0, \\
\int_{S_a} (\varepsilon_1 \varepsilon_1^{*(5)}) dS = 0 \quad \int_{S_a} (\varepsilon_2 \varepsilon_2^{*(5)}) dS = 0 \quad \int_{S_a} (\varepsilon_1 \varepsilon_2^{*(5)} + \varepsilon_2 \varepsilon_1^{*(5)}) dS = 1 \quad \int_{S_a} (\varepsilon_6 \varepsilon_6^{*(5)}) dS = 0, \\
\int_{S_b} (\varepsilon_1 \varepsilon_1^{*(5)}) dS = 0 \quad \int_{S_b} (\varepsilon_2 \varepsilon_2^{*(5)}) dS = 0 \quad \int_{S_b} (\varepsilon_1 \varepsilon_2^{*(5)} + \varepsilon_2 \varepsilon_1^{*(5)}) dS = 0 \quad \int_{S_b} (\varepsilon_6 \varepsilon_6^{*(5)}) dS = 0, \\
\int_{S_a} (\varepsilon_1 \varepsilon_1^{*(6)}) dS = 0 \quad \int_{S_a} (\varepsilon_2 \varepsilon_2^{*(6)}) dS = 0 \quad \int_{S_a} (\varepsilon_1 \varepsilon_2^{*(6)} + \varepsilon_2 \varepsilon_1^{*(6)}) dS = 1 \quad \int_{S_a} (\varepsilon_6 \varepsilon_6^{*(6)}) dS = 0, \\
\int_{S_b} (\varepsilon_1 \varepsilon_1^{*(6)}) dS = 0 \quad \int_{S_b} (\varepsilon_2 \varepsilon_2^{*(6)}) dS = 0 \quad \int_{S_b} (\varepsilon_1 \varepsilon_2^{*(6)} + \varepsilon_2 \varepsilon_1^{*(6)}) dS = 0 \quad \int_{S_b} (\varepsilon_6 \varepsilon_6^{*(6)}) dS = 0, \\
\int_{S_a} (\varepsilon_1 \varepsilon_1^{*(7)}) dS = 0 \quad \int_{S_a} (\varepsilon_2 \varepsilon_2^{*(7)}) dS = 0 \quad \int_{S_a} (\varepsilon_1 \varepsilon_2^{*(7)} + \varepsilon_2 \varepsilon_1^{*(7)}) dS = 1 \quad \int_{S_a} (\varepsilon_6 \varepsilon_6^{*(7)}) dS = 0, \\
\int_{S_b} (\varepsilon_1 \varepsilon_1^{*(7)}) dS = 0 \quad \int_{S_b} (\varepsilon_2 \varepsilon_2^{*(7)}) dS = 0 \quad \int_{S_b} (\varepsilon_1 \varepsilon_2^{*(7)} + \varepsilon_2 \varepsilon_1^{*(7)}) dS = 0 \quad \int_{S_b} (\varepsilon_6 \varepsilon_6^{*(7)}) dS = 0, \\
\int_{S_a} (\varepsilon_1 \varepsilon_1^{*(8)}) dS = 0 \quad \int_{S_a} (\varepsilon_2 \varepsilon_2^{*(8)}) dS = 0 \quad \int_{S_a} (\varepsilon_1 \varepsilon_2^{*(8)} + \varepsilon_2 \varepsilon_1^{*(8)}) dS = 1 \quad \int_{S_a} (\varepsilon_6 \varepsilon_6^{*(8)}) dS = 0, \\
\int_{S_b} (\varepsilon_1 \varepsilon_1^{*(8)}) dS = 0 \quad \int_{S_b} (\varepsilon_2 \varepsilon_2^{*(8)}) dS = 0 \quad \int_{S_b} (\varepsilon_1 \varepsilon_2^{*(8)} + \varepsilon_2 \varepsilon_1^{*(8)}) dS = 0 \quad \int_{S_b} (\varepsilon_6 \varepsilon_6^{*(8)}) dS = 0.
\end{array} \right. \quad (16)$$

So, directly identify  $Q_{11a}, Q_{11b}, Q_{12a}, Q_{12b}, Q_{22a}, Q_{22b}, Q_{66a},$  and  $Q_{66b}$  using the abovementioned four special virtual displacement fields. If the noise is

ignored, approximate parameters expressed as  $\mathbf{Q}^{app}$  are identified. The components of which are defined as equation (17) (see Appendix B2 for the detailed equation derivations).

$$\left\{ \begin{aligned}
Q_{11a}^{\text{app}} &= \int_{L_f} T_i u_i^{*(1)} dl - Q_{22a} \int_{S_a} \varepsilon_2 \varepsilon_2^{*(1)} dS - Q_{12a} \int_{S_a} (\varepsilon_1 \varepsilon_2^{*(1)} + \varepsilon_2 \varepsilon_1^{*(1)}) dS - Q_{66a} \int_{S_a} \varepsilon_6 \varepsilon_6^{*(1)} dS \\
&\quad - Q_{11b} \int_{S_b} \varepsilon_1 \varepsilon_1^{*(1)} dS - Q_{22b} \int_{S_b} \varepsilon_2 \varepsilon_2^{*(1)} dS - Q_{12b} \int_{S_b} (\varepsilon_1 \varepsilon_2^{*(1)} + \varepsilon_2 \varepsilon_1^{*(1)}) dS - Q_{66b} \int_{S_b} \varepsilon_6 \varepsilon_6^{*(1)} dS, \\
Q_{22a}^{\text{app}} &= \int_{L_f} T_i u_i^{*(2)} dl - Q_{11a} \int_{S_a} \varepsilon_1 \varepsilon_1^{*(2)} dS - Q_{12a} \int_{S_a} (\varepsilon_1 \varepsilon_2^{*(2)} + \varepsilon_2 \varepsilon_1^{*(2)}) dS - Q_{66a} \int_{S_a} \varepsilon_6 \varepsilon_6^{*(2)} dS \\
&\quad - Q_{11b} \int_{S_b} \varepsilon_1 \varepsilon_1^{*(2)} dS - Q_{22b} \int_{S_b} \varepsilon_2 \varepsilon_2^{*(2)} dS - Q_{12b} \int_{S_b} (\varepsilon_1 \varepsilon_2^{*(2)} + \varepsilon_2 \varepsilon_1^{*(2)}) dS - Q_{66b} \int_{S_b} \varepsilon_6 \varepsilon_6^{*(2)} dS, \\
Q_{12a}^{\text{app}} &= \int_{L_f} T_i u_i^{*(3)} dl - Q_{11a} \int_{S_a} \varepsilon_1 \varepsilon_1^{*(3)} dS - Q_{22a} \int_{S_a} \varepsilon_2 \varepsilon_2^{*(3)} dS - Q_{66a} \int_{S_a} \varepsilon_6 \varepsilon_6^{*(3)} dS \\
&\quad - Q_{11b} \int_{S_b} \varepsilon_1 \varepsilon_1^{*(3)} dS - Q_{22b} \int_{S_b} \varepsilon_2 \varepsilon_2^{*(3)} dS - Q_{12b} \int_{S_b} (\varepsilon_1 \varepsilon_2^{*(3)} + \varepsilon_2 \varepsilon_1^{*(3)}) dS - Q_{66b} \int_{S_b} \varepsilon_6 \varepsilon_6^{*(3)} dS, \\
Q_{66a}^{\text{app}} &= \int_{L_f} T_i u_i^{*(4)} dl - Q_{11a} \int_{S_a} \varepsilon_1 \varepsilon_1^{*(4)} dS - Q_{22a} \int_{S_a} \varepsilon_2 \varepsilon_2^{*(4)} dS - Q_{12a} \int_{S_a} (\varepsilon_1 \varepsilon_2^{*(4)} + \varepsilon_2 \varepsilon_1^{*(4)}) dS \\
&\quad - Q_{11b} \int_{S_b} \varepsilon_1 \varepsilon_1^{*(4)} dS - Q_{22b} \int_{S_b} \varepsilon_2 \varepsilon_2^{*(4)} dS - Q_{12b} \int_{S_b} (\varepsilon_1 \varepsilon_2^{*(4)} + \varepsilon_2 \varepsilon_1^{*(4)}) dS - Q_{66b} \int_{S_b} \varepsilon_6 \varepsilon_6^{*(4)} dS, \\
Q_{11b}^{\text{app}} &= \int_{L_f} T_i u_i^{*(5)} dl - Q_{22b} \int_{S_b} \varepsilon_2 \varepsilon_2^{*(5)} dS - Q_{12b} \int_{S_b} (\varepsilon_1 \varepsilon_2^{*(5)} + \varepsilon_2 \varepsilon_1^{*(5)}) dS - Q_{66b} \int_{S_b} \varepsilon_6 \varepsilon_6^{*(5)} dS \\
&\quad - Q_{11a} \int_{S_a} \varepsilon_1 \varepsilon_1^{*(5)} dS - Q_{22a} \int_{S_a} \varepsilon_2 \varepsilon_2^{*(5)} dS - Q_{12a} \int_{S_a} (\varepsilon_1 \varepsilon_2^{*(5)} + \varepsilon_2 \varepsilon_1^{*(5)}) dS - Q_{66a} \int_{S_a} \varepsilon_6 \varepsilon_6^{*(5)} dS, \\
Q_{22b}^{\text{app}} &= \int_{L_f} T_i u_i^{*(6)} dl - Q_{11b} \int_{S_b} \varepsilon_1 \varepsilon_1^{*(6)} dS - Q_{12b} \int_{S_b} (\varepsilon_1 \varepsilon_2^{*(6)} + \varepsilon_2 \varepsilon_1^{*(6)}) dS - Q_{66b} \int_{S_b} \varepsilon_6 \varepsilon_6^{*(6)} dS \\
&\quad - Q_{11a} \int_{S_a} \varepsilon_1 \varepsilon_1^{*(6)} dS - Q_{22a} \int_{S_a} \varepsilon_2 \varepsilon_2^{*(6)} dS - Q_{12a} \int_{S_a} (\varepsilon_1 \varepsilon_2^{*(6)} + \varepsilon_2 \varepsilon_1^{*(6)}) dS - Q_{66a} \int_{S_a} \varepsilon_6 \varepsilon_6^{*(6)} dS, \\
Q_{12b}^{\text{app}} &= \int_{L_f} T_i u_i^{*(7)} dl - Q_{11b} \int_{S_b} \varepsilon_1 \varepsilon_1^{*(7)} dS - Q_{22b} \int_{S_b} \varepsilon_2 \varepsilon_2^{*(7)} dS - Q_{66b} \int_{S_b} \varepsilon_6 \varepsilon_6^{*(7)} dS - Q_{11a} \int_{S_a} \varepsilon_1 \varepsilon_1^{*(7)} dS \\
&\quad - Q_{22a} \int_{S_a} \varepsilon_2 \varepsilon_2^{*(7)} dS - Q_{12a} \int_{S_a} (\varepsilon_1 \varepsilon_2^{*(7)} + \varepsilon_2 \varepsilon_1^{*(7)}) dS - Q_{66a} \int_{S_a} \varepsilon_6 \varepsilon_6^{*(7)} dS, \\
Q_{66b}^{\text{app}} &= \int_{L_f} T_i u_i^{*(8)} dl - Q_{11b} \int_{S_b} \varepsilon_1 \varepsilon_1^{*(8)} dS - Q_{22b} \int_{S_b} \varepsilon_2 \varepsilon_2^{*(8)} dS - Q_{12b} \int_{S_b} (\varepsilon_1 \varepsilon_2^{*(8)} + \varepsilon_2 \varepsilon_1^{*(8)}) dS \\
&\quad - Q_{11a} \int_{S_a} \varepsilon_1 \varepsilon_1^{*(8)} dS - Q_{22a} \int_{S_a} \varepsilon_2 \varepsilon_2^{*(8)} dS - Q_{12a} \int_{S_a} (\varepsilon_1 \varepsilon_2^{*(8)} + \varepsilon_2 \varepsilon_1^{*(8)}) dS - Q_{66a} \int_{S_a} \varepsilon_6 \varepsilon_6^{*(8)} dS,
\end{aligned} \right. \quad (17)$$

To minimize the effect of noise, taking  $Q_{11a}$  as an example, the variance of  $Q_{11a}$  is as follows:

$$\begin{aligned}
V(Q_{11a}) &= \gamma^2 E \left( \left[ Q_{11a}^{\text{app}} \int_{S_a} \varepsilon_1^{*(1)} \mathcal{N}_1 dS + Q_{22a}^{\text{app}} \int_{S_a} \varepsilon_2^{*(1)} \mathcal{N}_2 dS + Q_{12a}^{\text{app}} \int_{S_a} (\varepsilon_2^{*(1)} \mathcal{N}_1 + \varepsilon_1^{*(1)} \mathcal{N}_2) dS + Q_{66a}^{\text{app}} \int_{S_a} \varepsilon_6^{*(1)} \mathcal{N}_6 dS \right]^2 \right. \\
&\quad \left. + \left[ Q_{11b}^{\text{app}} \int_{S_b} \varepsilon_1^{*(1)} \mathcal{N}_1 dS + Q_{22b}^{\text{app}} \int_{S_b} \varepsilon_2^{*(1)} \mathcal{N}_2 dS + Q_{12b}^{\text{app}} \int_{S_b} (\varepsilon_2^{*(1)} \mathcal{N}_1 + \varepsilon_1^{*(1)} \mathcal{N}_2) dS + Q_{66b}^{\text{app}} \int_{S_b} \varepsilon_6^{*(1)} \mathcal{N}_6 dS \right]^2 \right) \\
&\quad + \gamma^2 E \left( \left[ Q_{11b}^{\text{app}} \int_{S_b} \varepsilon_1^{*(1)} \mathcal{N}_1 dS + Q_{22b}^{\text{app}} \int_{S_b} \varepsilon_2^{*(1)} \mathcal{N}_2 dS + Q_{12b}^{\text{app}} \int_{S_b} (\varepsilon_2^{*(1)} \mathcal{N}_1 + \varepsilon_1^{*(1)} \mathcal{N}_2) dS + Q_{66b}^{\text{app}} \int_{S_b} \varepsilon_6^{*(1)} \mathcal{N}_6 dS \right]^2 \right) \\
&= V_A(Q_{11a}) + V_B(Q_{11a}).
\end{aligned} \quad (18)$$

As described above, the virtual fields are expanded by polynomial basis functions based on equation (11). The unknown coefficients  $A_{ij}$  and  $B_{ij}$  are included in vector  $\mathbf{Y}$  as follows:

$$\mathbf{Y} = \begin{bmatrix} A_{00} \\ \vdots \\ A_{30} \\ \vdots \\ A_{03} \\ \vdots \\ A_{33} \\ B_{00} \\ \vdots \\ B_{30} \\ \vdots \\ B_{03} \\ \vdots \\ B_{33} \end{bmatrix}. \quad (19)$$

The integrals of equation (15) are calculated using vectors  $\mathbf{B11}$ ,  $\mathbf{B22}$ ,  $\mathbf{B12}$ , and  $\mathbf{B66}$  through discrete sum approximation so that

$$\left\{ \begin{array}{l} \int_{S_a} (\varepsilon_1 \varepsilon_1^*) dS \approx Lw_a \overline{\varepsilon_{1a} \varepsilon_{1a}^*} = \mathbf{B11a} \cdot \mathbf{Y}, \\ \int_{S_a} (\varepsilon_2 \varepsilon_2^*) dS \approx Lw_a \overline{\varepsilon_{2a} \varepsilon_{2a}^*} = \mathbf{B22a} \cdot \mathbf{Y}, \\ \int_{S_a} (\varepsilon_1 \varepsilon_2^* + \varepsilon_2 \varepsilon_1^*) dS \approx Lw_a (\overline{\varepsilon_{1a} \varepsilon_{2a}^*} + \overline{\varepsilon_{2a} \varepsilon_{1a}^*}) = \mathbf{B12a} \cdot \mathbf{Y}, \\ \int_{S_a} (\varepsilon_6 \varepsilon_6^*) dS \approx Lw_a \overline{\varepsilon_{6a} \varepsilon_{6a}^*} = \mathbf{B66a} \cdot \mathbf{Y}, \\ \int_{S_b} (\varepsilon_1 \varepsilon_1^*) dS \approx Lw_b \overline{\varepsilon_{1b} \varepsilon_{1b}^*} = \mathbf{B11b} \cdot \mathbf{Y}, \\ \int_{S_b} (\varepsilon_2 \varepsilon_2^*) dS \approx Lw_b \overline{\varepsilon_{2b} \varepsilon_{2b}^*} = \mathbf{B22b} \cdot \mathbf{Y}, \\ \int_{S_b} (\varepsilon_1 \varepsilon_2^* + \varepsilon_2 \varepsilon_1^*) dS \approx Lw_b (\overline{\varepsilon_{1b} \varepsilon_{2b}^*} + \overline{\varepsilon_{2b} \varepsilon_{1b}^*}) = \mathbf{B12b} \cdot \mathbf{Y}, \\ \int_{S_b} (\varepsilon_6 \varepsilon_6^*) dS \approx Lw_b \overline{\varepsilon_{6b} \varepsilon_{6b}^*} = \mathbf{B66b} \cdot \mathbf{Y}. \end{array} \right. \quad (20)$$

The others that the definition from the virtual fields (vectors  $\mathbf{H11}$ ,  $\mathbf{H22}$ ,  $\mathbf{H12}$ , and  $\mathbf{H66}$ ) are related to the terms of equation (18).

$$\left\{ \begin{array}{l} \int_{S_a} (\varepsilon_1^*)^2 dS \approx \left( \frac{Lw_a}{\text{npointsa}} \right)^2 \mathbf{Y} \cdot \mathbf{H11a} \cdot \mathbf{Y} \\ \int_{S_a} (\varepsilon_1^*)^2 dS \approx \left( \frac{Lw_a}{\text{npointsa}} \right)^2 \mathbf{Y} \cdot \mathbf{H11a} \cdot \mathbf{Y}, \\ \int_{S_a} (\varepsilon_1 \varepsilon_2^*) dS \approx \left( \frac{Lw_a}{\text{npointsa}} \right)^2 \mathbf{Y} \cdot \mathbf{H11a} \cdot \mathbf{Y}, \\ \int_{S_a} (\varepsilon_6^*)^2 dS \approx \left( \frac{Lw_a}{\text{npointsa}} \right)^2 \mathbf{Y} \cdot \mathbf{H11a} \cdot \mathbf{Y}, \\ \int_{S_b} (\varepsilon_1^*)^2 dS \approx \left( \frac{Lw_b}{\text{npointsa}} \right)^2 \mathbf{Y} \cdot \mathbf{H11b} \cdot \mathbf{Y}, \\ \int_{S_b} (\varepsilon_1^*)^2 dS \approx \left( \frac{Lw_b}{\text{npointsa}} \right)^2 \mathbf{Y} \cdot \mathbf{H11b} \cdot \mathbf{Y}, \\ \int_{S_b} (\varepsilon_1 \varepsilon_2^*) dS \approx \left( \frac{Lw_b}{\text{npointsa}} \right)^2 \mathbf{Y} \cdot \mathbf{H11b} \cdot \mathbf{Y}, \\ \int_{S_b} (\varepsilon_6^*)^2 dS \approx \left( \frac{Lw_b}{\text{npointsa}} \right)^2 \mathbf{Y} \cdot \mathbf{H11b} \cdot \mathbf{Y}. \end{array} \right. \quad (21)$$

The first KA virtual field conditions of three-point bending are  $u_2^* = 0$ , when  $x1 = 0$ , and  $x2 = 0$ , which implies

$$B_{00} = 0. \quad (22)$$

The second KA virtual field conditions of three-point bending re  $u_1^* = 0$ , when  $x1 = L$ , which means that

$$\sum_{i=0}^m A_{ij} = 0, \quad j = 0, \dots, n. \quad (23)$$

The optimized virtual fields are totally defined. The following equations can identify the constitutive parameters:

$$\left\{ \begin{array}{l} Q_{11a} = \frac{F}{t} u_2^{*(a)}(x_1 = L, x_2 = w), \\ Q_{22a} = \frac{F}{t} u_2^{*(a)}(x_1 = L, x_2 = w), \\ Q_{12a} = \frac{F}{t} u_2^{*(a)}(x_1 = L, x_2 = w), \\ Q_{66a} = \frac{F}{t} u_2^{*(a)}(x_1 = L, x_2 = w), \\ Q_{11b} = \frac{F}{t} u_2^{*(a)}(x_1 = L, x_2 = w), \\ Q_{22b} = \frac{F}{t} u_2^{*(a)}(x_1 = L, x_2 = w), \\ Q_{12b} = \frac{F}{t} u_2^{*(a)}(x_1 = L, x_2 = w), \\ Q_{66b} = \frac{F}{t} u_2^{*(a)}(x_1 = L, x_2 = w). \end{array} \right. \quad (24)$$

### 3. Numerical Verification and Discussion

To evaluate the accuracy of the abovementioned optimized polynomial VFM, numerical experiments with FEM simulations and DIC simulations are employed in this section.

*3.1. Numerical Verification of Optimized Polynomial Virtual Fields with FEM Simulations.* In FEM simulation, in order to

$$W_{re} = \frac{|Q_{11a}^{ide} - Q_{11a}^{rfe}| + |Q_{22a}^{ide} - Q_{22a}^{re}| + |Q_{12a}^{ide} - Q_{12a}^{re}| + |Q_{66a}^{ide} - Q_{66a}^{rfe}| + |Q_{11b}^{ide} - Q_{11b}^{rfe}| + |Q_{22b}^{ide} - Q_{22b}^{rfe}| + |Q_{12b}^{ide} - Q_{12b}^{rfe}| + |Q_{66b}^{ide} - Q_{66b}^{rfe}|}{Q_{11a}^{rfe} + Q_{22a}^{rfe} + Q_{12a}^{rfe} + Q_{66a}^{rfe} + Q_{11b}^{rfe} + Q_{22b}^{rfe} + Q_{12b}^{rfe} + Q_{66b}^{rfe}} \quad (25)$$

It can be seen from Table 3 that the weighted relative error is lower than 1%. The relative error of  $Q_{66}$  of the two materials is the smallest. Although the relative errors of  $Q_{11}$  and  $Q_{22}$  of the two materials are slightly larger than  $Q_{66}$ , both of them are less than 2%. The relative error of  $Q_{12a}$  and  $Q_{12b}$

facilitate the simulation of bimaterials configuration, a two-dimensional rectangular beam specimen was adopted, and applied a three-point bending load to get inhomogeneous in-plane deformation fields. Based on the principle of the symmetry of three-point bending, only the left of the specimen was modelled, as shown in Figure 1.

The length, width, and thickness of the bimaterial beam specimen were set as  $L = 30$  mm,  $w = 20$  mm, and  $t = 2.3$  mm, respectively, and the width of the two material regions was the same:  $w_a = w_b = 10$  mm. The force was set as  $F = 2544$  N. The four-node plane-stress element with thickness (Solid-Quad 4 nodes 182/Plane strs w/thk) was employed. The displacement constraint  $u_y = 0$  is added in the lower left corner of the model, and the line constraint  $u_x = 0$  is added on the right side of the model.

The beam specimen was set as orthotropic materials. The engineering elastic constants in the FEM simulation are shown in Table 1, and the converted constitutive parameters in the elastic matrix are shown in Table 2.

The displacement fields and the strain fields of the three-point bending test of the orthotropic bimaterial obtained through FEM simulations using the commercial software ANSYS are shown in Figures 2 and 3.

Table 3 shows the identification results of the heterogeneous orthotropic bimaterials by using the optimized polynomial VFM, as shown in Section 2.2. To study the identification accuracy of the optimized polynomial VFM, the relative error of every constitutive parameter component and the weighted relative error  $W_{re}$  were calculated. Owing to there were 8 unknown constitutive parameters, the weighted relative error employed here can be expressed as follows:

is significantly higher than others, because  $\sigma_2$  must be included in the virtual fields to identify  $Q_{12}$ , while the stress data density of  $\sigma_2$  is low in the three-point bending test. The stress data density can be expressed by the following equation:

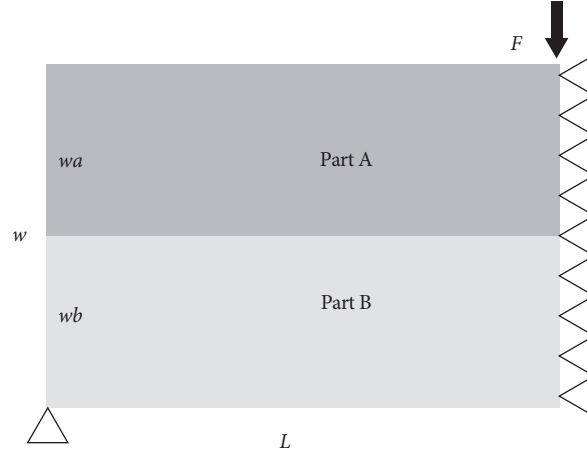


FIGURE 1: Two-dimensional bimaterial model of three-point bending established in FEM simulation.

TABLE 1: Engineering elastic constants of orthotropic bimaterial.

$E_{xa}$ (Mpa)	$E_{ya}$ (Mpa)	$E_{za}$ (Mpa)	$PR_{xya}$ (Mpa)	$PR_{yza}$ (Mpa)	$PR_{xza}$ (Mpa)	$G_{xya}$ (Mpa)	$G_{yza}$ (Mpa)	$G_{xza}$ (Mpa)
180000	30000	8300	0.17	0.25	0.31	5700	12000	12000
$E_{xb}$ (Mpa)	$E_{yb}$ (Mpa)	$E_{zb}$ (Mpa)	$PR_{xyb}$ (Mpa)	$PR_{yzb}$ (Mpa)	$PR_{xzb}$ (Mpa)	$G_{xyb}$ (Mpa)	$G_{yzb}$ (Mpa)	$G_{xzb}$ (Mpa)
175000	32000	8300	0.25	0.25	0.31	5700	12000	12000

TABLE 2: Reference constitutive parameters of orthotropic bimaterial.

$Q_{11a}$ (Mpa)	$Q_{22a}$ (Mpa)	$Q_{12a}$ (Mpa)	$Q_{66a}$ (Mpa)	$Q_{11b}$ (Mpa)	$Q_{22b}$ (Mpa)	$Q_{12b}$ (Mpa)	$Q_{66b}$ (Mpa)
181937.10	30719.68	5907.20	5700	178229.16	32976.51	8947.80	5700

$$\rho(\sigma_i) = \frac{\sum_{j=1}^{\text{bpoints}} |\sigma_i(M_j)|}{\text{npoints}}, \quad i = 1, 2, 6. \quad (26)$$

According to equation (7), the standard deviations of  $Q_{ij}$  are equal to  $\eta^{(i)}\gamma$ . If  $\gamma$  is the standard deviation of the strain noise, the coefficients of variations ( $CV(Q_{ij})$ ) of each stiffness component are given by

$$\left\{ \begin{array}{l} CV(Q_{11}) = \frac{\eta_{11}}{Q_{11}}\gamma, \\ CV(Q_{22}) = \frac{\eta_{22}}{Q_{22}}\gamma, \\ CV(Q_{12}) = \frac{\eta_{12}}{Q_{12}}\gamma, \\ CV(Q_{66}) = \frac{\eta_{66}}{Q_{66}}\gamma. \end{array} \right. \quad (27)$$

The ratio of coefficient of variation to the standard deviation of the strain noise can show the sensitivity to the noise. It indicates the rate at which the coefficient of variation increases with the increase of noise, which can be called the variation coefficient-to-noise ratio, and can be expressed as  $\eta_{ij}/Q_{ij}$ . The lower variation coefficient-to-noise ratio indicates that the corresponding identification constitutive parameters are less susceptible to noise. The variation coefficient-to-noise ratios  $\eta_{ij}/Q_{ij}$  of eight identification results are shown in Table 3. Significant differences on the variation coefficient-to-noise ratio and the coefficient-to-noise ratio of  $Q_{66}$  is the smallest, the next is  $Q_{11}$ , and then is the  $Q_{22}$ , and the biggest is  $Q_{12}$ . The quantitative results show that if  $Q_{11}$ ,  $Q_{22}$ , and  $Q_{66}$  are stable,  $Q_{12}$  is less robustly identified. This result shows that this configuration is unsuitable for the transverse stiffness.

*3.2. Comparison with Results of Piecewise Virtual Fields and Polynomial Virtual Fields.* This section will implement the same numerical experiment as Section 3.1 to compare the identified constitutive parameters of the piecewise virtual

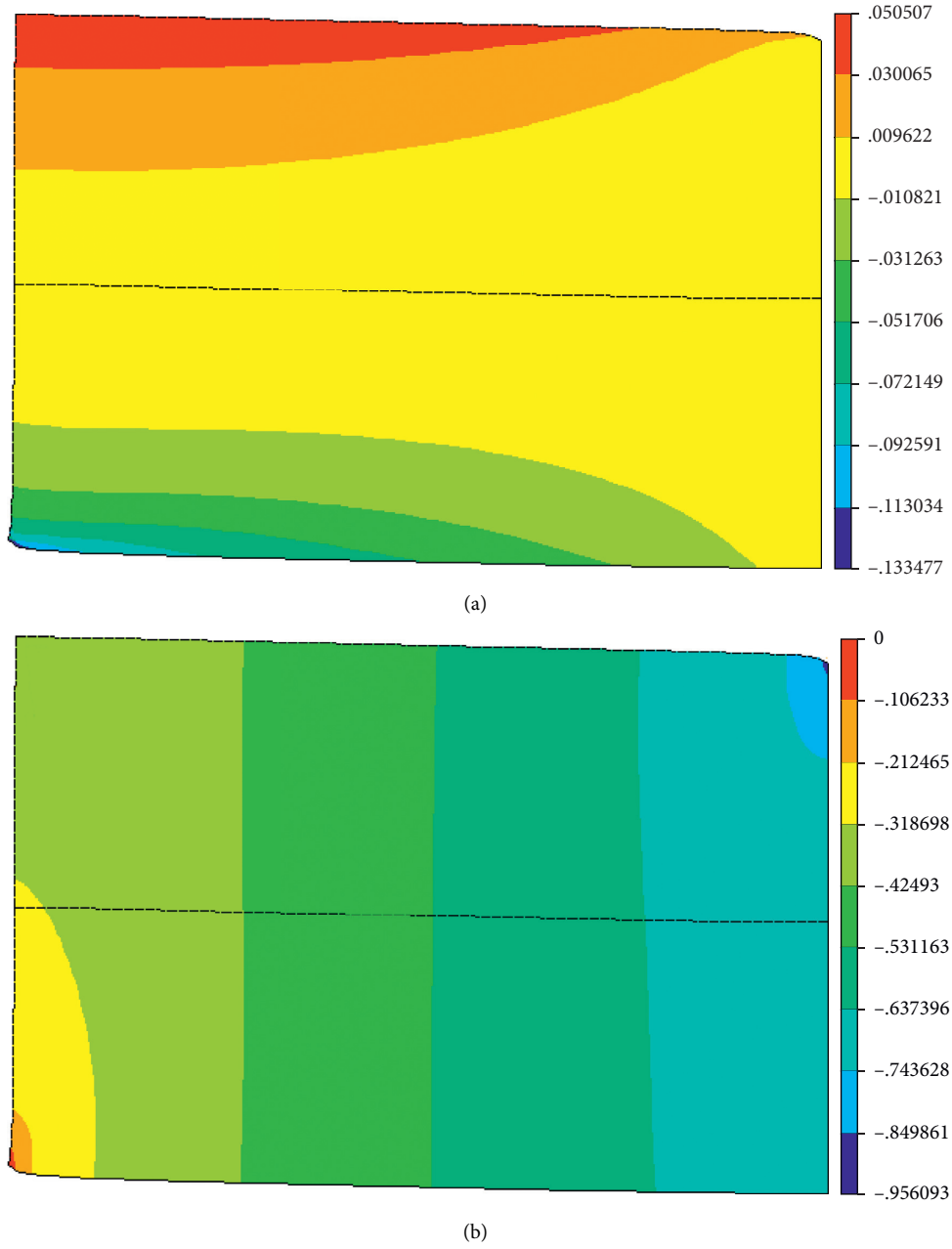


FIGURE 2: Displacement distributions of heterogeneous orthotropic bimetals: (a)  $u_1$ ; (b)  $u_2$  (unit: mm).

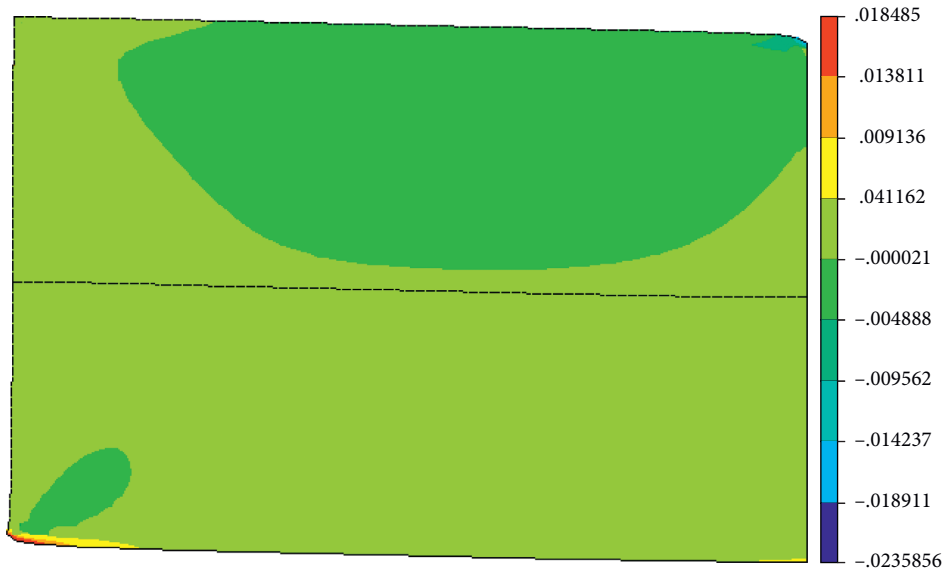
field and polynomial virtual field. At this situation, the bilinear shape function is used to interpolate the four-node element to represent the virtual field instead of the polynomial virtual field.

The piecewise function expansion of the virtual displacement field is similar to the interpolation of the real

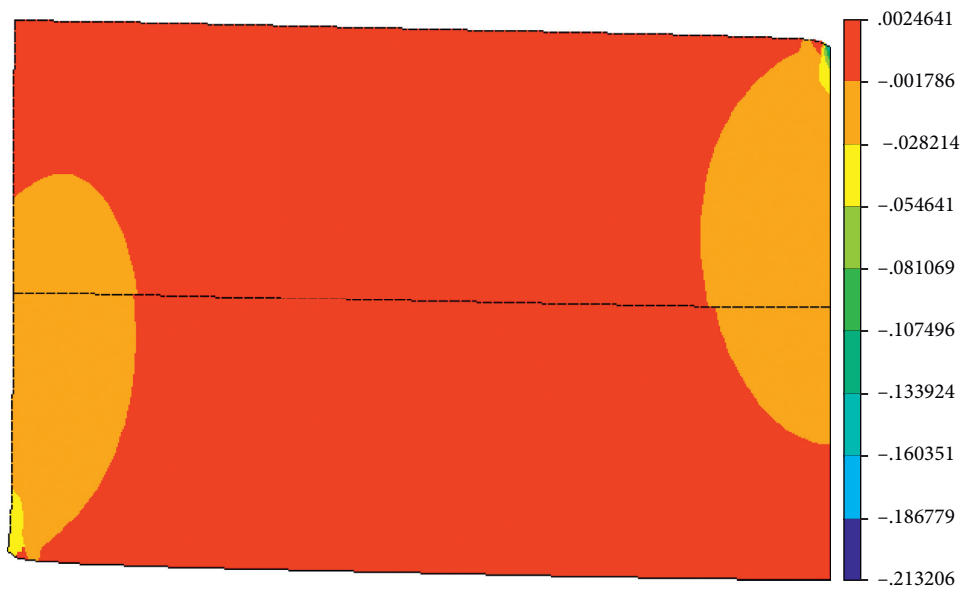
displacement in the FEM. Derived from the relationship between strain and displacement,

$$\boldsymbol{\varepsilon} = \mathbf{S}\mathbf{u}^*, \quad (28)$$

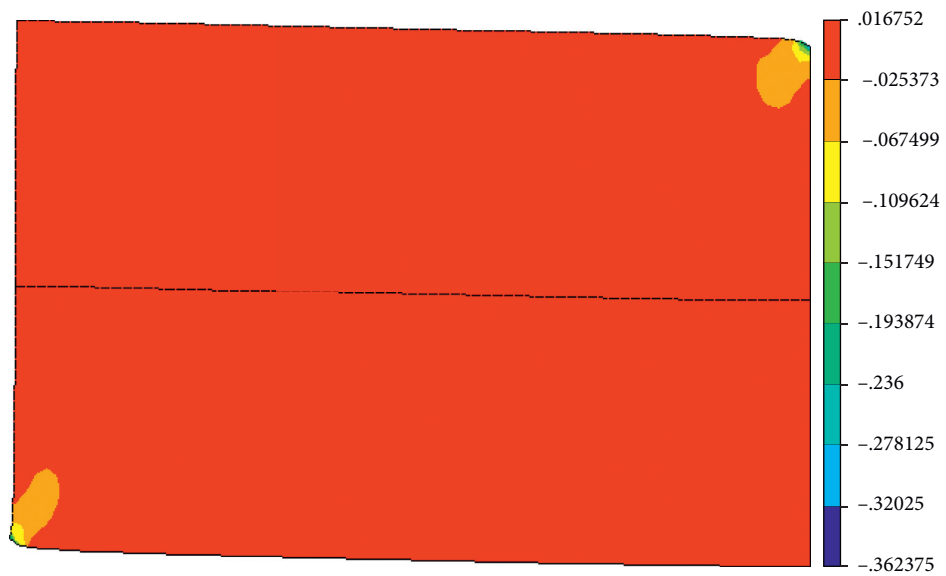
where



(a)



(b)



(c)

FIGURE 3: Strain distributions of heterogeneous orthotropic bimetals: (a)  $\epsilon_1$ ; (b)  $\epsilon_2$ ; (c)  $\epsilon_3$ .

TABLE 3: Identification results of constitutive parameters of orthotropic bimaterial using the optimized polynomial virtual fields.

	Reference (MPa)	Identification (MPa)	$\eta_{ij}/Q_{ij}$	Relative error (%)	Weighted relative error (%)
$Q_{11a}$	181937.10	181597.13	28.0642	-0.19	
$Q_{22a}$	30719.68	30350.43	10.6390	-1.20	
$Q_{12a}$	5907.20	4791.27	208.0530	-18.89	
$Q_{66a}$	5700	5701.02	5.3999	0.02	0.83
$Q_{11b}$	178229.16	177353.94	23.4711	-0.49	
$Q_{22b}$	32976.51	32595.46	9.1601	-1.16	
$Q_{12b}$	8947.80	8275.81	101.8827	-7.51	
$Q_{66b}$	5700	5698.79	5.9903	-0.02	

$$\boldsymbol{\varepsilon} = \begin{Bmatrix} \varepsilon_1 \\ \varepsilon_2 \\ \varepsilon_6 \end{Bmatrix},$$

$$\mathbf{u}^* = \begin{Bmatrix} u_1^* \\ u_2^* \end{Bmatrix},$$

$$\mathbf{S} = \begin{Bmatrix} \frac{\partial}{\partial x_1} & 0 \\ 0 & \frac{\partial}{\partial x_2} \\ \frac{\partial}{\partial x_2} & \frac{\partial}{\partial x_1} \end{Bmatrix}. \quad (29)$$

For the quadrilateral element, the virtual displacement can be expressed by the following formula:

$$\mathbf{u}^*(\xi_1, \xi_2) \approx \mathbf{u}^*(\xi_1, \xi_2) = \sum_{a=1}^4 \mathbf{N}^{(a)}(\xi_1, \xi_2) \mathbf{u}^{*(a)}, \quad (30)$$

where  $\mathbf{u}^*$  is the vector containing the virtual displacement of any point  $(\xi_1, \xi_2)$  in the element, and  $\mathbf{u}^{*(a)}$  is the vector containing the virtual displacement of the nodes in the element. The expression of  $\mathbf{N}^{(a)}$  is defined as

$$\mathbf{N}^{(a)}(\xi_1, \xi_2) = N^{(a)}(\xi_1, \xi_2) \mathbf{I}, \quad (31)$$

where  $\mathbf{I}$  is the identity matrix. The shape function expression of  $\mathbf{N}^{(a)}$  can be defined as follows:

$$\begin{cases} N^{(1)} = \frac{1}{4}(1 - \xi_1)(1 - \xi_2), \\ N^{(2)} = \frac{1}{4}(1 + \xi_1)(1 - \xi_2), \\ N^{(3)} = \frac{1}{4}(1 + \xi_1)(1 + \xi_2), \\ N^{(4)} = \frac{1}{4}(1 - \xi_1)(1 + \xi_2). \end{cases} \quad (32)$$

So, the virtual displacement can be expressed by the following formula:

$$\begin{cases} u_1^* \approx N^{(1)}\tilde{u}_1^{*(1)} + N^{(2)}\tilde{u}_1^{*(2)} + N^{(3)}\tilde{u}_1^{*(3)} + N^{(4)}\tilde{u}_1^{*(4)}, \\ u_2^* \approx N^{(1)}\tilde{u}_2^{*(1)} + N^{(2)}\tilde{u}_2^{*(2)} + N^{(3)}\tilde{u}_2^{*(3)} + N^{(4)}\tilde{u}_2^{*(4)}. \end{cases} \quad (33)$$

Therefore, the unknown coefficient vector  $\mathbf{Y}$  (equation (17)) in the polynomial virtual fields can be denoted on each node:

$$\mathbf{Y} = \begin{bmatrix} \tilde{u}_1^{*(1)} \\ \tilde{u}_2^{*(1)} \\ \vdots \\ \tilde{u}_1^{*(n)} \\ \tilde{u}_2^{*(n)} \end{bmatrix}, \quad (34)$$

where  $n$  is the total number of nodes.

Use the piecewise virtual field instead of the polynomial virtual field to perform the same experiment (Section 3.1). Table 4 shows the values of relative and weighted relative error of A and B. It can be seen from Table 4 that the identification results of piecewise virtual fields are similar to that of polynomial virtual fields. The weighted relative error is 0.97%, which is slightly larger than that of polynomial virtual fields. The relative error of  $Q_{66}$  of the two materials is the smallest. Although the relative errors of  $Q_{11}$  and  $Q_{22}$  of the two materials are slightly larger than  $Q_{66}$ , both of them are less than 2%. Similar to the results of polynomial virtual fields, the relative error of  $Q_{12a}$  and  $Q_{12b}$  is significantly higher than others, because  $\sigma_2$  must be included in the virtual fields to identify  $Q_{12}$ , while the data density of  $\sigma_2$  is low in the three-point bending test.

The variation coefficient-to-noise ratios of eight identification results are also shown in Table 4. Significant differences can be seen on the variation coefficient-to-noise ratios and the quantitative results show that if  $Q_{11}$ ,  $Q_{22}$ , and  $Q_{66}$  are stable,  $Q_{12}$  is less robustly identified. Compared with the polynomial virtual field, the variation coefficient-to-noise ratio of the eight identification parameters calculated by the optimized piecewise virtual field is larger.

**3.3. Influence of Noise on Identification Results.** The noise is inevitable in the experiments. To investigate the influence of noise on identification results, zero-mean Gaussian white

TABLE 4: Identification results of constitutive parameters of orthotropic bimaterial using the optimized piecewise virtual fields.

	Reference (MPa)	Identification (MPa)	$\eta_{ij}/Q_{ij}$	Relative error (%)	Weighted relative error (%)
$Q_{11a}$	181937.10	181236.94	29.7551	-0.38	
$Q_{22a}$	30719.68	30226.44	11.6049	-1.61	
$Q_{12a}$	5907.20	4979.48	245.8494	-58.71	
$Q_{66a}$	5700	5700.70	6.1965	0.01	0.97
$Q_{11b}$	178229.16	177249.89	25.0937	-0.55	
$Q_{22b}$	32976.51	32456.53	9.7825	-1.58	
$Q_{12b}$	8947.80	8184.67	125.9329	-8.53	
$Q_{66b}$	5700	5699.21	6.8896	-0.01	

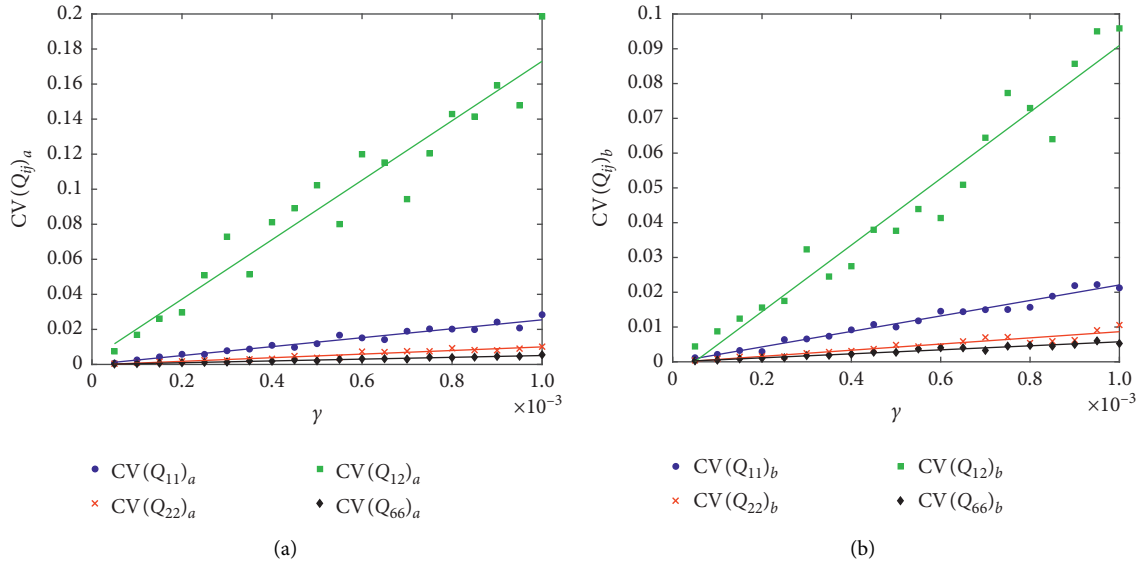


FIGURE 4: The coefficients of variation of the identified stiffness components. (a) Part A; (b) Part B.

noise with different amplitudes is added in the strain data of the orthotropic bimaterial specimen, and the above-mentioned experiments are repeated to obtain the coefficients of variation corresponding to the eight identification results with the increasing noise amplitudes. In order to assess the influence of noise on the identified parameters, it is necessary to discuss the standard deviation of strain noise. It can be seen from equation (27) that the coefficients of variation ( $CV(Q_{ij})_a$ ) are proportional to the uncertainty ( $\gamma$ ) of strain measurement. Since the coefficient of variation can be directly compared between different constitutive components, this article chose to discuss the coefficient of variation rather than standard deviation. Thus, coefficients of variation were used to discuss the sensitivity to noise.

The coefficients of variation of the identified stiffness components of the two materials were calculated for a range of strain noise standard deviation values. The strain noise standard deviation  $\gamma$  varies from  $5 \times 10^{-5}$  to  $1 \times 10^{-3}$  by steps of  $5 \times 10^{-5}$ . For each value of  $\gamma$ , the identification is repeated 30 times using the optimized polynomial virtual fields. The coefficients of variation ( $CV(Q_{ij})$ ) were calculated by equation (34). Figure 4 indicates the graph plotting, the coefficients of variations for the

TABLE 5: The fitted and the theoretical values of the variation coefficient-to-noise ratios.

	Fitted value	Theoretical value
$\eta_{11a}/Q_{11a}$	27.13	26.6534
$\eta_{22a}/Q_{22a}$	10.34	9.6984
$\eta_{12a}/Q_{12a}$	165.75	172.1564
$\eta_{66a}/Q_{66a}$	5.29	5.0576
$\eta_{11b}/Q_{11b}$	23.94	22.0878
$\eta_{22b}/Q_{22b}$	8.50	8.4713
$\eta_{12b}/Q_{12b}$	88.04	84.7326
$\eta_{66b}/Q_{66b}$	5.94	5.6006

eight stiffness components of the two materials, as a function of  $\gamma$ . The points are fitted by linear regression to calculate the slope, and the slope was compared to the theoretical value of the variation coefficient-to-noise ratio  $\eta_{ij}/Q_{ij}$ .

$$CV(Q_{ij}) = \sqrt{\frac{\sum (Q_{ij} - \overline{Q_{ij}})^2 / n - 1}{(\sum Q_{ij}) / n}} \quad (35)$$

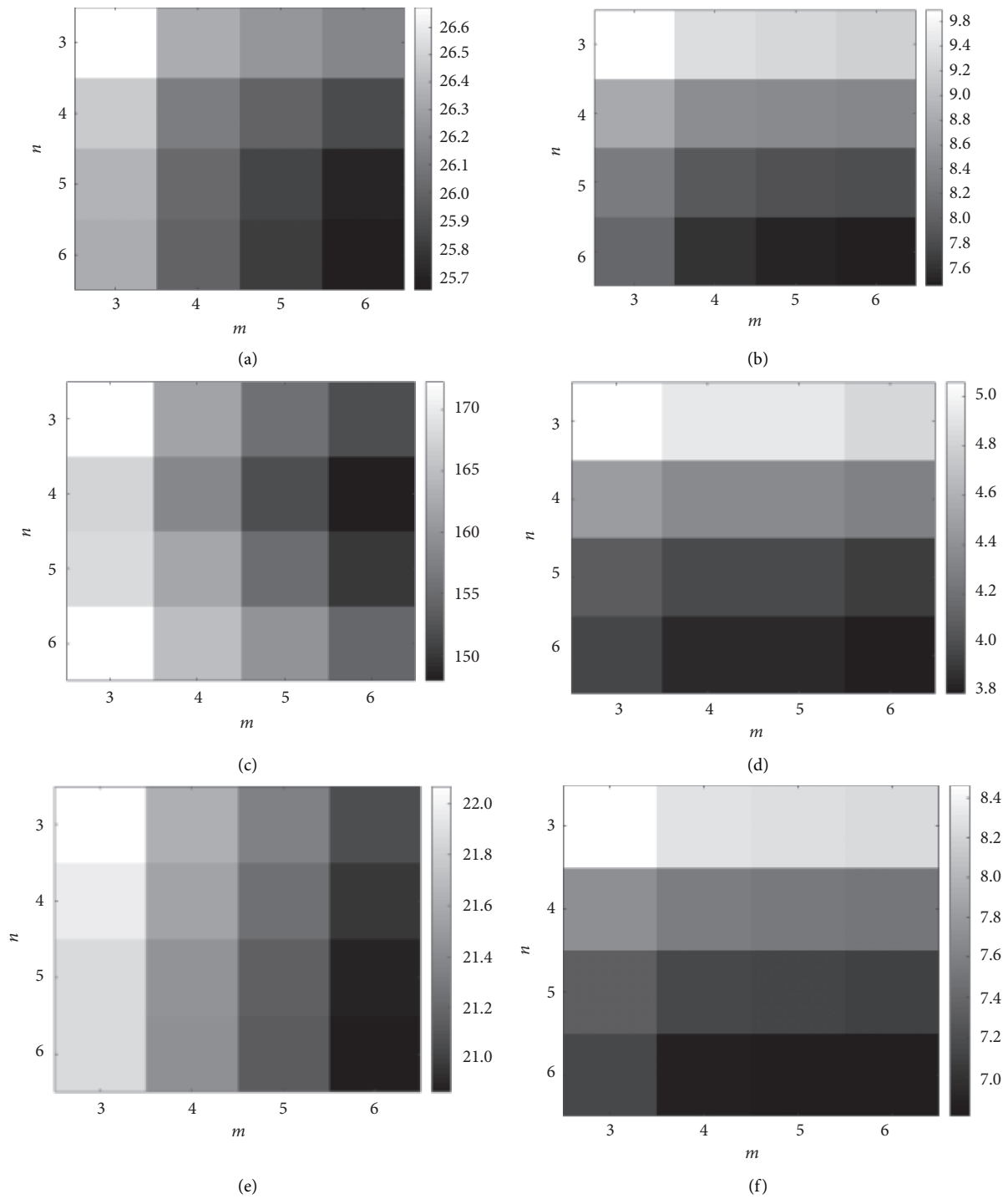


FIGURE 5: Continued.

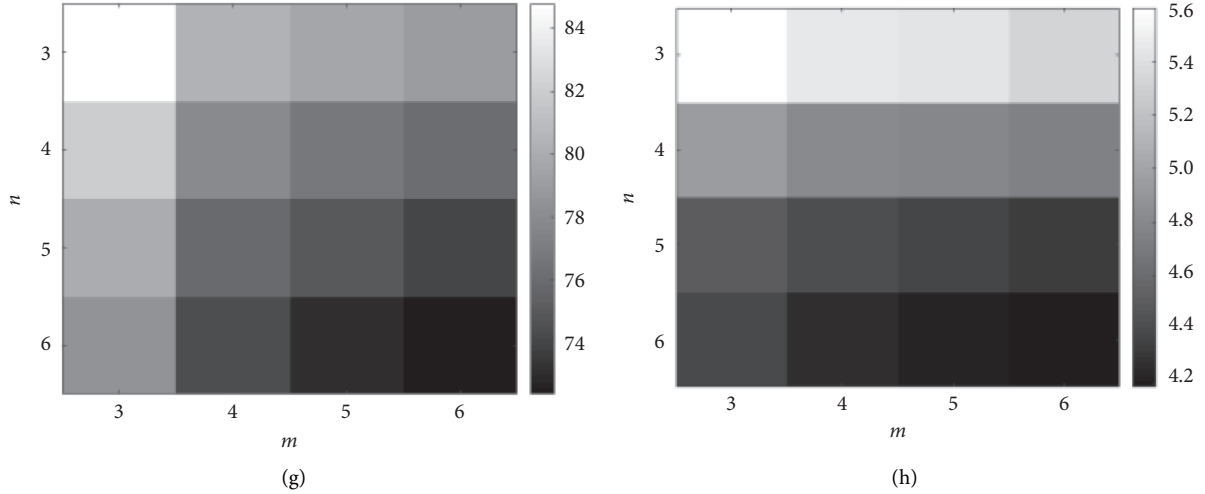


FIGURE 5: Values of  $\eta_{ij}/Q_{ij}$ . (a)  $\eta_{11a}/Q_{11a}$ , (b)  $\eta_{22a}/Q_{22a}$ , (c)  $\eta_{12a}/Q_{12a}$ , (d)  $\eta_{66a}/Q_{66a}$ , (e)  $\eta_{11b}/Q_{11b}$ , (f)  $\eta_{22b}/Q_{22b}$ , (g)  $\eta_{12b}/Q_{12b}$ , and (h)  $\eta_{66b}/Q_{66b}$ .

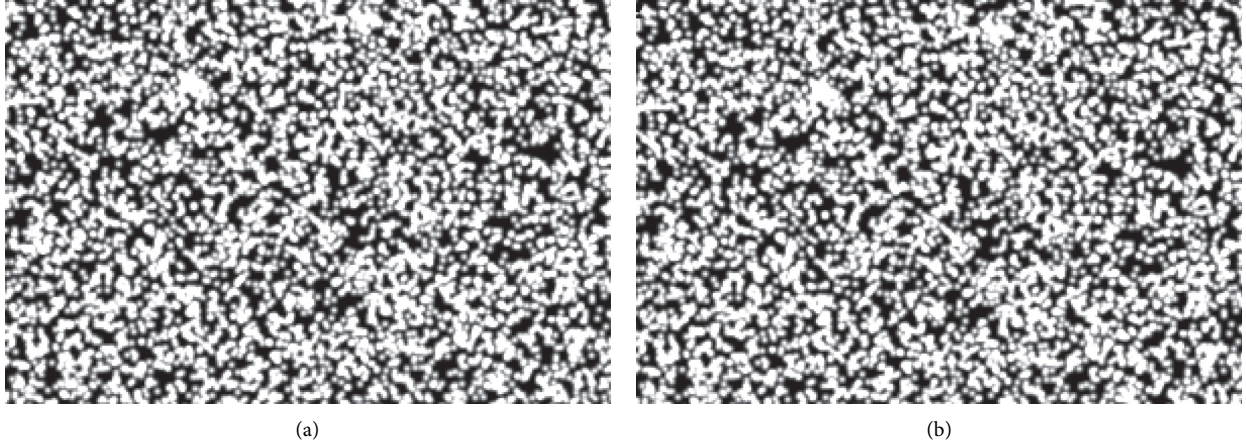


FIGURE 6: The reference and the deformation speckle pattern images. (a) Reference speckle pattern. (b) Deformed speckle pattern.

For both materials A and B, Figure 4 shows that the smallest coefficient of variation value is  $CV(Q_{66})$ . The results of Figure 4 are consistent with the variation coefficient-to-noise ratio studies in Section 3.1.  $Q_{66}$  was the most stable of the identified stiffness components.  $CV(Q_{22})$  was the second and  $CV(Q_{11})$  was the third, and finally  $CV(Q_{12})$ , which is also consistent with the results in Section 3.1. The slope of the fitted curve is the fitted variation coefficient-to-noise ratio. The comparisons of the fitted and theoretical value of the variation coefficient-to-noise ratio are listed in Table 5. Figure 4 and Table 5 not only show the linear relationship but also show that the theoretical  $\eta_{ij}/Q_{ij}$  values are consistent with the fitted ones. It suggests that the procedure can perform a priori evaluation of a confidence interval on the identified stiffness components. In addition, due to the hypothesis of equation (16), the straight line is unsuitable for the highest values of noise. Equation (16) shows the noise should be smaller than the signal.

**3.4. Influence of the Polynomial Degrees.** According to equation (10), when the basic functions to expand the virtual field is selected, the only parameters, the degrees of the  $x_1$  and  $x_2$  monomials, denoted as  $m$  and  $n$ , need to be selected.  $m$  and  $n$  are the polynomial degrees that represent the maximum number of monomials. The total number of polynomial degrees is  $2(m+1)(n+1)$ ; for the case of optimized polynomial virtual fields applied to the bimaterial without knowing any material constitutive parameters, the condition of equation (35) needs to be satisfied.

$$2(m+1)(n+1) > n+10. \quad (36)$$

For the optimized polynomial virtual fields, on the one hand,  $m$  and  $n$  cannot be selected too small, which will lead to too few polynomial degrees and thus cannot satisfy equation (35). On the other hand,  $m$  and  $n$  should not be selected too large, which will result in ill-conditioned matrix. Figure 5 shows the evolution of the variation coefficient-to-noise ratio  $\eta_{ij}/Q_{ij}$  as a function of  $m$  and  $n$ . It can be seen

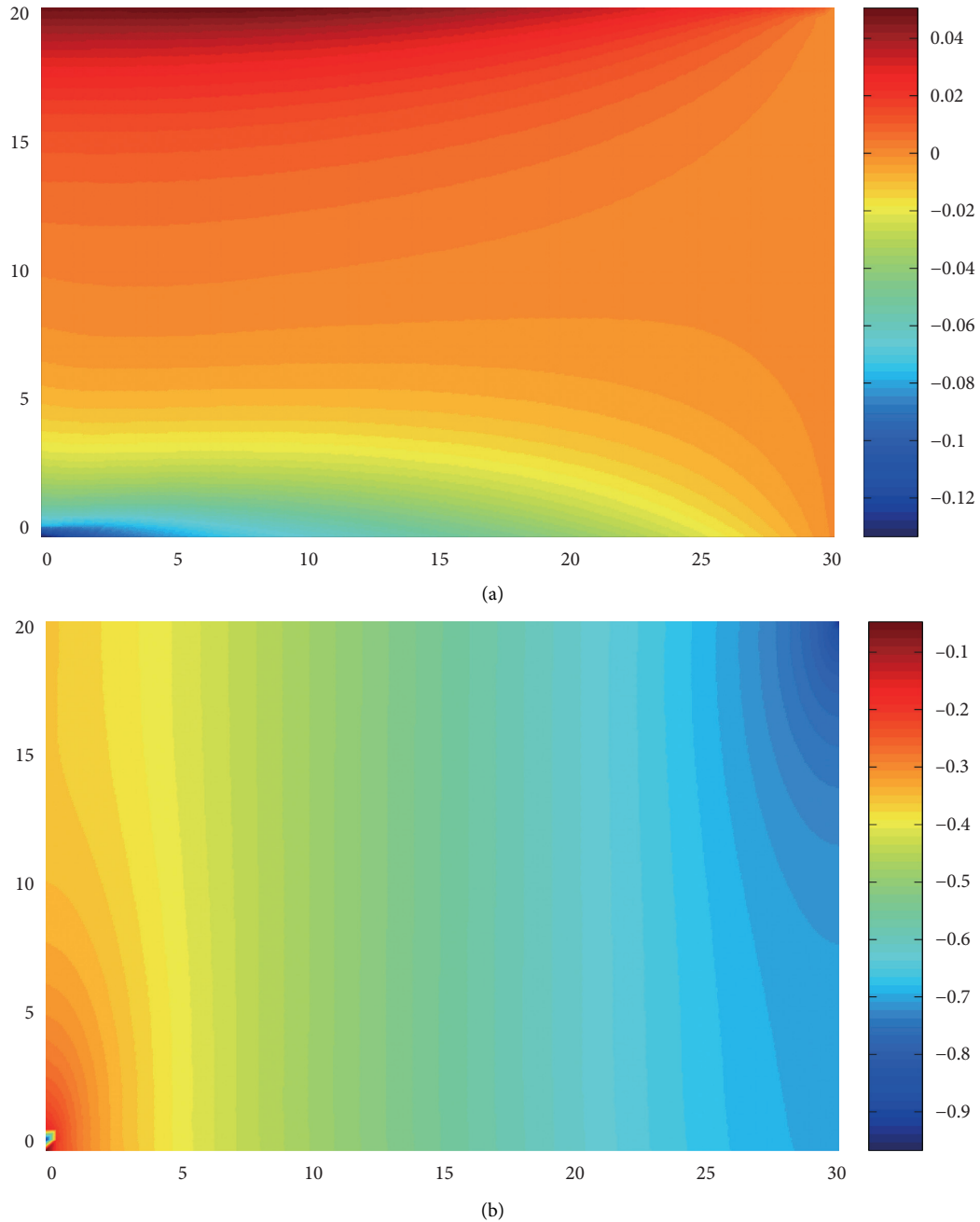


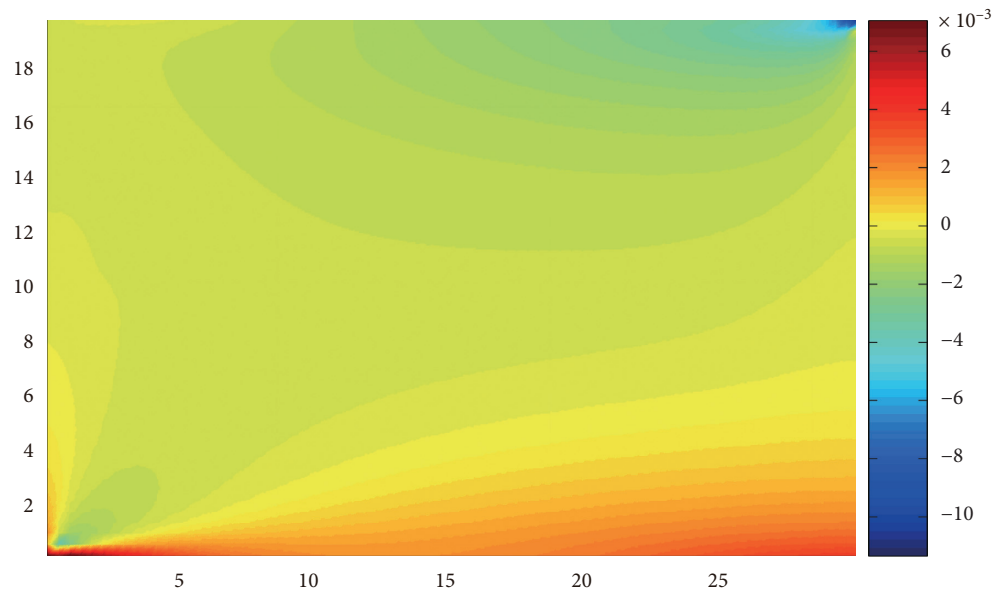
FIGURE 7: Displacement fields of speckle images using DIC: (a)  $u_1$ ; (b)  $u_2$ (unit: mm).

from Figure 5 that there are slight variations in the  $\eta_{ij}/Q_{ij}$  with higher gradients for the values related to  $Q_{12a}$  and  $Q_{12a}$ . Due to the three-point bending test configuration, these parameters are relatively less good identifiability. It can also show that the dependance on  $n$  is higher than that on  $m$ . This is because all the constraints affect the  $x_2$  monomials.

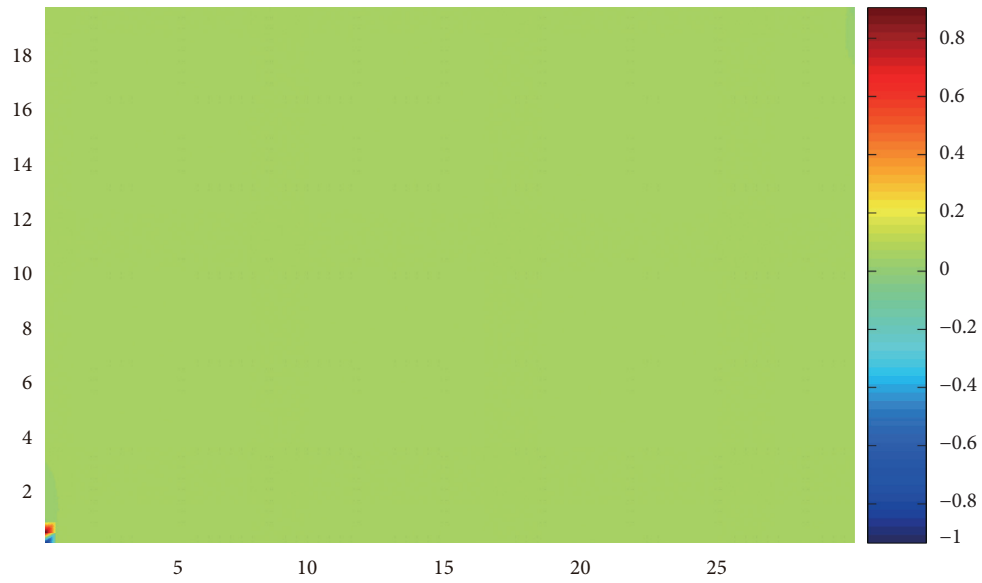
*3.5. Numerical Verification of Optimized Polynomial Virtual Fields with DIC Simulations.* In practice, to provide a more reliable strain input for the virtual fields method, digital image correlation (DIC) was applied to obtain deformation

fields. DIC is an effective optical technique for noncontact full-field deformation measurement for various materials and structures. The DIC computes the displacement of each image point by comparing the gray intensity of images of the test specimen surface in different loading states. The corresponding strain fields are calculated using a numerical differentiation method. In addition to the systematic error of DIC algorithm, aberration, distortion, and out-of-plane displacement will affect the accuracy of displacement measurement.

For the purpose of evaluating the simulated results of constitutive parameters for bimetals and the influence of



(a)



(b)

FIGURE 8: Continued.

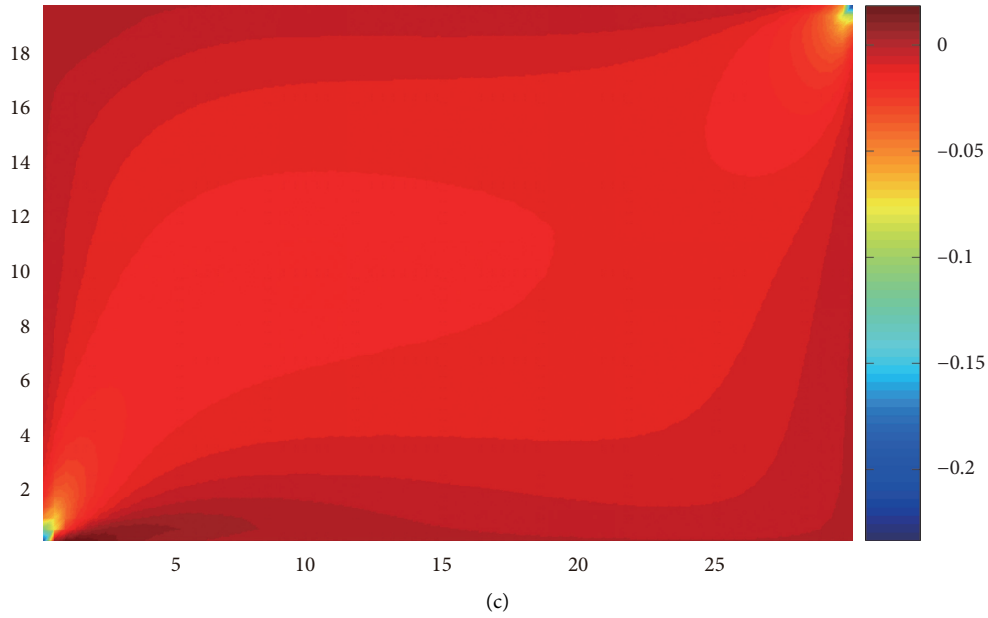
FIGURE 8: Strain fields of simulated speckle images using DIC: (a)  $\varepsilon_1$ ; (b)  $\varepsilon_2$ ; (c)  $\varepsilon_6$ .

TABLE 6: Identification results of constitutive parameters of orthotropic bimetals with speckle images.

	Reference (MPa)	Identification (MPa)	$\eta_{ij}/Q_{ij}$	Relative error (%)	Weighted relative error (%)
$Q_{11a}$	181937.10	180555.58	28.0682	-0.76	
$Q_{22a}$	30719.68	30448.46	10.5995	-0.88	
$Q_{12a}$	5907.20	4799.89	207.1620	-18.75	
$Q_{66a}$	5700	5678.47	5.4031	-0.38	
$Q_{11b}$	178229.16	178258.47	23.4412	0.02	1.14
$Q_{22b}$	32976.51	31730.88	8.9408	-3.78	
$Q_{12b}$	8947.80	7884.06	103.7439	-11.89	
$Q_{66b}$	5700	5725.27	5.9455	0.44	

strain input calculated by DIC on the identification of constitutive parameters, the simulated DIC results were used as the input of the VFM to exclude the influence of lens distortion and out-of-plane displacements. The displacement fields of the bimaterial beam specimen obtained through abovementioned FEM simulations were exported and converted to reference and deformed speckle patterns by Gaussian speckle [32], as shown in Figure 6. The displacement fields and strain fields obtained from DIC are shown in Figures 7 and 8, respectively.

Table 6 shows the identification results and the corresponding variation coefficient-to-noise ratio and relative error and weighted relative error for both materials. Similar to the results in Table 3, it shows significant differences on the variation coefficient-to-noise ratio and the coefficient-to-noise ratio of  $Q_{66}$ , which is the smallest, the next is  $Q_{11}$ , and then is the  $Q_{22}$ , and the biggest is  $Q_{12}$ . The lowest value is  $Q_{66}$ . This result is consistent with studies in Section 3.3.  $Q_{66}$  was the most stable of the four identified stiffness components in Section 3.3.  $Q_{11}$  is the second,  $Q_{22}$  is the third, and  $Q_{12}$  is the last. This result is also consistent with the studies in Section 3.3. As shown in Table 6, the relative errors of  $Q_{12a}$  and  $Q_{12b}$  are more than 10%, while

others are not more than 4%, and the weighted relative error is 1.14%, which is slightly larger than the results in Table 3. This indicates that the strain data calculated by DIC contains noise, resulting in an increase in the error of the identification results. This comparison result reveals the feasibility of the optimized polynomial virtual fields combined with DIC for extracting the constitutive parameters of the unknown bimaterial. It should be pointed out that in the actual DIC calculation, the displacement measurement errors caused by aberration and out-of-plane displacements will lead to additional strain noise, so the relative errors and weighted relative error of the identification results will be larger than the results in Table 6.

#### 4. Conclusions

In this article, optimized polynomial virtual fields are proposed to extract the constitutive parameters of the heterogeneous orthotropic bimetals without knowing any material constitutive parameters. Numerical experiments with FEM simulations are employed to investigate the accuracy of the optimized polynomial virtual fields method. The main conclusions are as follows:

- (1) The optimized polynomial virtual fields were proposed to identify the constitutive parameters of heterogeneous orthotropic bimetals under the condition that constitutive parameters of both materials are all unknown from a single test. The results show that the weighted relative error of the constitutive parameter is less than 1%. The stress data density was used to explain the difference in the relative error of the constitutive parameter. For heterogeneous orthotropic bimetals without knowing any material constitutive parameters, this method is suitable for extracting the constitutive parameters.
- (2) To investigate the effect of the noise, a series of numerical experiments with different strain noise amplitudes were used in FEM simulations. The variation coefficient-to-noise ratio and coefficients of variation are applied to quantify the influence of noise on the identification results, and the results suggest that the variation coefficient-to-noise ratio can perform a priori evaluation of a confidence interval on the identified stiffness components.
- (3) For comparison, piecewise virtual fields were used to extract the constitutive parameters of the heterogeneous orthotropic bimetals. The results denoted that the optimized polynomial virtual fields have a higher reliability than the optimized piecewise virtual fields.
- (4) To study the accuracy of the optimized polynomial VFM combined with DIC method, the numerical experiments with DIC simulations are employed. The comparison result shows the feasibility of the optimized polynomial virtual fields combined with DIC for extracting the constitutive parameters of the unknown bimetals. The result also indicates that the strain data calculated by DIC contains noise, resulting in an increase in the error of the identification results, and the weighted relative error is 1.14%.

## Nomenclature

$\sigma$ :	Cauchy stress tensor
$\mathbf{u}^*$ :	Virtual displacement vector
$\varepsilon^*$ :	Strain tensor
$\bar{\mathbf{T}}$ :	External force
$S$ :	Area of the specimen
$\mathbf{b}$ :	Vector of volume force
$V$ :	Specimen volume
$\mathbf{a}$ :	Distribution of acceleration
KA:	Virtual displacement field being kinematically admissible
$Q_{11}, Q_{22}, Q_{12}, Q_{66}$ :	In-plane constitutive parameters

$u^{*(1)}, u^{*(2)}, u^{*(3)}, u^{*(4)}$ :	Four independent KA virtual fields
$\varepsilon^{*(1)}, \varepsilon^{*(2)}, \varepsilon^{*(3)}, \varepsilon^{*(4)}$ :	Four independent KA virtual fields
$\mathcal{N}_1, \mathcal{N}_2, \mathcal{N}_6$ :	Processes of scalar zero-mean stationary Gaussian
$\varepsilon_1, \varepsilon_2, \varepsilon_6$ :	Strain components
$\gamma$ :	Measured amplitude of the random variable strain
$Q^{\text{app}}$ :	Approximate parameter components
$\ \varepsilon_i\  (i = 1, 2, 6)$ :	Norm of strain component
$V(Q_{11}), V(Q_{22}), V(Q_{12}), V(Q_{66})$ :	Variances of $Q_{11}, Q_{12}, Q_{22}$ , and $Q_{66}$
$\mathbf{Y}^*$ :	Vector concerning the coefficients of virtual strain fields
$\mathbf{H}$ :	Hessian matrix
$\mathcal{L}^{(i)}$ :	Lagrangian function
$\lambda^{(i)}$ :	Vector containing Lagrange multipliers
$Q_{11a}, Q_{22a}, Q_{12a}, Q_{66a}$ :	Constitutive parameters of material a
$Q_{11b}, Q_{22b}, Q_{12b}, Q_{66b}$ :	Constitutive parameters of material b
$L$ :	Typical dimensions of the $x_1$
$w$ :	Typical dimensions of the $x_2$
$F$ :	External force of the specimen
$W_{re}$ :	Weighted relative error of Q
$N^{(i)} (i = 1, 2, 3, 4)$ :	Shape function.

## Appendix

### A. Equation Derivation of Section 2.1

*A1. The Principle of Virtual Work for an Orthotropic Material in a Plane-Stress State.* The integral form of the mechanical equilibrium equation of the VFM based on virtual work for a continuous solid can be expressed as [31]

$$\begin{aligned}
 & - \int_S \boldsymbol{\sigma} : \boldsymbol{\varepsilon}^* dS + \int_S \bar{\mathbf{T}} \cdot \mathbf{u}^* dS + \int_V \mathbf{b} \cdot \mathbf{u}^* dV \\
 & = \int_V \rho \mathbf{a} \cdot \mathbf{u}^* dV \quad \forall \mathbf{u}^* \in \text{KA},
 \end{aligned} \tag{A.1}$$

where  $\boldsymbol{\sigma}$  is the Cauchy stress tensor,  $\mathbf{u}^*$  is the virtual displacement vector,  $\boldsymbol{\varepsilon}^*$  denotes the strain tensor corresponding to  $\mathbf{u}^*$ ,  $\bar{\mathbf{T}}$  represents the external force associated with the stress tensor  $\boldsymbol{\sigma}$  by the boundary,  $S$  is a vector which is the volume force applied over the volume  $V$  of the specimen, and  $\mathbf{a}$  denotes the distribution of acceleration. Such a distribution will cause an additional volumetric force

distribution equal to  $-\rho\mathbf{a}$  with D'Alembert's principle, the virtual displacement field being kinematically admissible (KA).

In the case of a quasistatic load, acceleration  $\mathbf{a}$  can be omitted. The volume force  $\mathbf{b}$  can usually also be omitted. Under this circumstance, equation (A.1) can be written as follows:

$$-\int_S \boldsymbol{\sigma} : \boldsymbol{\varepsilon}^* dS = \int_S \bar{\mathbf{T}} \cdot \mathbf{u}^* dS \quad \forall \mathbf{u}^* \text{ KA.} \quad (\text{A.2})$$

Equation (A.2) denotes the plane-stress problem. For an orthotropic material in a plane-stress state, the principle of virtual work becomes

$$\begin{aligned} & \int_S Q_{11} (\varepsilon_1 \varepsilon_1^*) dS + \int_S Q_{22} (\varepsilon_2 \varepsilon_2^*) dS + \int_S Q_{12} (\varepsilon_1 \varepsilon_2^* + \varepsilon_2 \varepsilon_1^*) dS \\ & + \int_S Q_{66} (\varepsilon_6 \varepsilon_6^*) dS = \int_{L_f} (T_i u_i^*) dl, \end{aligned} \quad (\text{A.3})$$

where  $Q_{11}, Q_{22}, Q_{12}$ , and  $Q_{66}$  are the in-plane stiffness components and equation (A.3) is linear. It is suitable for every KA virtual field. This equation uses four independent KA virtual fields  $\boldsymbol{\varepsilon}^{*(1)}, \boldsymbol{\varepsilon}^{*(2)}, \boldsymbol{\varepsilon}^{*(3)}$ , and  $\boldsymbol{\varepsilon}^{*(4)}$  instead of  $u^{*(1)}, u^{*(2)}, u^{*(3)}$ , and  $u^{*(4)}$ , respectively. So, the relationship between  $\mathbf{A}, \mathbf{Q}$ , and  $\mathbf{B}$  is as follows:

$$\mathbf{A}\mathbf{Q} = \mathbf{B}. \quad (\text{A.4})$$

*A2. The Principle of Virtual Work with Uncorrelated Noise.* The exact values and white noise constitute the measured strain component. So, equation (A.3) in Appendix A1 can be reexpressed as follows:

$$\begin{aligned} & Q_{11} \int_S (\varepsilon_1 - \gamma \mathcal{N}_1) \varepsilon_1^* dS + Q_{22} \int_S (\varepsilon_2 - \gamma \mathcal{N}_2) \varepsilon_2^* dS \\ & + Q_{12} \int_S [(\varepsilon_1 - \gamma \mathcal{N}_1) \varepsilon_2^* + (\varepsilon_2 - \gamma \mathcal{N}_2) \varepsilon_1^*] dS \\ & + Q_{66} \int_S (\varepsilon_6 - \gamma \mathcal{N}_6) \varepsilon_6^* dS = \int_{L_f} (T_i u_i^*) dl, \end{aligned} \quad (\text{A.5})$$

where  $\mathcal{N}_1, \mathcal{N}_2$ , and  $\mathcal{N}_6$  denote the processes of scalar zero-mean stationary Gaussian generalized by the corresponding strain components  $\varepsilon_1, \varepsilon_2$ , and  $\varepsilon_6$ , respectively, and  $\gamma$  denotes the measured amplitude of the random variable strain. Assume that the noise components are uncorrelated to each other, and presume that the noise between points is also uncorrelated. Equation (A.5) can be rewritten as follows:

$$\begin{aligned} & Q_{11} \underbrace{\int_S (\varepsilon_1 \varepsilon_1^*) dS}_{=1} + Q_{22} \underbrace{\int_S (\varepsilon_2 \varepsilon_2^*) dS}_{=0} + Q_{12} \underbrace{\int_S (\varepsilon_1 \varepsilon_2^* + \varepsilon_2 \varepsilon_1^*) dS}_{=0} + Q_{66} \underbrace{\int_S (\varepsilon_6 \varepsilon_6^*) dS}_{=0} - \\ & \gamma \left[ Q_{11} \int_S \varepsilon_1^* \mathcal{N}_1 dS + Q_{22} \int_S \varepsilon_2^* \mathcal{N}_2 dS + Q_{12} \int_S (\varepsilon_2^* \mathcal{N}_1 + \varepsilon_1^* \mathcal{N}_2) dS + Q_{66} \int_S \varepsilon_6^* \mathcal{N}_6 dS \right] = \int_{L_f} (T_i u_i^*) dl. \end{aligned} \quad (\text{A.6})$$

*A3. The Principle of Virtual Work with Ignored Noise.* Directly identify  $Q_{11}, Q_{22}, Q_{12}$ , and  $Q_{66}$  using these four special virtual displacement fields  $\boldsymbol{\varepsilon}^{*(1)}, \boldsymbol{\varepsilon}^{*(2)}, \boldsymbol{\varepsilon}^{*(3)}$ , and  $\boldsymbol{\varepsilon}^{*(4)}$ .

$$\begin{aligned} Q_{11} = & \gamma \left[ Q_{11} \int_S \varepsilon_1^{*(1)} \mathcal{N}_1 dS + Q_{22} \int_S \varepsilon_2^{*(1)} \mathcal{N}_2 dS + Q_{12} \int_S (\varepsilon_2^{*(1)} \mathcal{N}_1 + \varepsilon_1^{*(1)} \mathcal{N}_2) dS \right. \\ & \left. + Q_{66} \int_S \varepsilon_6^{*(1)} \mathcal{N}_6 dS \right] + \int_{L_f} (T_i u_i^{*(1)}) dl, \end{aligned} \quad (\text{A.7})$$

$$\begin{aligned} Q_{22} = & \gamma \left[ Q_{11} \int_S \varepsilon_1^{*(2)} \mathcal{N}_1 dS + Q_{22} \int_S \varepsilon_2^{*(2)} \mathcal{N}_2 dS + Q_{12} \int_S (\varepsilon_2^{*(2)} \mathcal{N}_1 + \varepsilon_1^{*(2)} \mathcal{N}_2) dS \right. \\ & \left. + Q_{66} \int_S \varepsilon_6^{*(2)} \mathcal{N}_6 dS \right] + \int_{L_f} (T_i u_i^{*(2)}) dl, \end{aligned} \quad (\text{A.8})$$

$$\begin{aligned} Q_{12} = & \gamma \left[ Q_{11} \int_S \varepsilon_1^{*(3)} \mathcal{N}_1 dS + Q_{22} \int_S \varepsilon_2^{*(3)} \mathcal{N}_2 dS + Q_{12} \int_S (\varepsilon_2^{*(3)} \mathcal{N}_1 + \varepsilon_1^{*(3)} \mathcal{N}_2) dS \right. \\ & \left. + Q_{66} \int_S \varepsilon_6^{*(3)} \mathcal{N}_6 dS \right] + \int_{L_f} (T_i u_i^{*(3)}) dl, \end{aligned} \quad (\text{A.9})$$

$$Q_{66} = \gamma \left[ Q_{11} \int_S \varepsilon_5^{*(4)} \mathcal{N}_1 dS + Q_{22} \int_S \varepsilon_2^{*(4)} \mathcal{N}_2 dS + Q_{12} \int_S (\varepsilon_2^{*(4)} \mathcal{N}_1 + \varepsilon_1^{*(4)} \mathcal{N}_2) dS \right. \\ \left. + Q_{66} \int_S \varepsilon_6^{*(4)} \mathcal{N}_6 dS \right] + \int_{L_f} (T_i u_i^{*(4)}) dl. \quad (\text{A.10})$$

If the noise is ignored, approximate parameters expressed as  $\mathbf{Q}^{\text{app}}$ , these components are defined by

$$\left\{ \begin{array}{l} Q_{11}^{\text{app}} = \int_{L_f} (T_i u_i^{*(1)}) dl, \\ Q_{22}^{\text{app}} = \int_{L_f} (T_i u_i^{*(2)}) dl, \\ Q_{12}^{\text{app}} = \int_{L_f} (T_i u_i^{*(3)}) dl, \\ Q_{66}^{\text{app}} = \int_{L_f} (T_i u_i^{*(4)}) dl, \end{array} \right. \quad (\text{A.11})$$

where  $\gamma$  can be negligible compared to the  $\|\varepsilon_1\|$ ,  $\|\varepsilon_2\|$  and  $\|\varepsilon_6\|$ , respectively, and the  $\|\varepsilon_i\|$  ( $i = 1, 2, 6$ ) is the norm of strain component  $L^2$ . Thus,

$$\gamma \ll \min(\|\varepsilon_1\|, \|\varepsilon_2\|, \|\varepsilon_6\|). \quad (\text{A.12})$$

Equations (A.7)–(A.10) mentioned above can be reexpressed by the actual values of the  $Q_{ij}$  instead of the approximate counterparts. Thus,

$$\left\{ \begin{array}{l} Q_{11} = \gamma \left[ Q_{11}^{\text{app}} \int_S \varepsilon_1^{*(1)} \mathcal{N}_1 dS + Q_{22}^{\text{app}} \int_S \varepsilon_2^{*(1)} \mathcal{N}_2 dS + Q_{12}^{\text{app}} \int_S (\varepsilon_2^{*(1)} \mathcal{N}_1 + \varepsilon_1^{*(1)} \mathcal{N}_2) dS \right. \\ \left. + Q_{66}^{\text{app}} \int_S \varepsilon_6^{*(1)} \mathcal{N}_6 dS \right] + Q_{11}^{\text{app}}, \\ Q_{22} = \gamma \left[ Q_{11}^{\text{app}} \int_S \varepsilon_1^{*(2)} \mathcal{N}_1 dS + Q_{22}^{\text{app}} \int_S \varepsilon_2^{*(2)} \mathcal{N}_2 dS + Q_{12}^{\text{app}} \int_S (\varepsilon_2^{*(2)} \mathcal{N}_1 + \varepsilon_1^{*(2)} \mathcal{N}_2) dS \right. \\ \left. + Q_{66}^{\text{app}} \int_S \varepsilon_6^{*(2)} \mathcal{N}_6 dS \right] + Q_{22}^{\text{app}}, \\ Q_{12} = \gamma \left[ Q_{11}^{\text{app}} \int_S \varepsilon_1^{*(3)} \mathcal{N}_1 dS + Q_{22}^{\text{app}} \int_S \varepsilon_2^{*(3)} \mathcal{N}_2 dS + Q_{12}^{\text{app}} \int_S (\varepsilon_2^{*(3)} \mathcal{N}_1 + \varepsilon_1^{*(3)} \mathcal{N}_2) dS \right. \\ \left. + Q_{66}^{\text{app}} \int_S \varepsilon_6^{*(3)} \mathcal{N}_6 dS \right] + Q_{12}^{\text{app}}, \\ Q_{66} = \gamma \left[ Q_{11}^{\text{app}} \int_S \varepsilon_1^{*(4)} \mathcal{N}_1 dS + Q_{22}^{\text{app}} \int_S \varepsilon_2^{*(4)} \mathcal{N}_2 dS + Q_{12}^{\text{app}} \int_S (\varepsilon_2^{*(4)} \mathcal{N}_1 + \varepsilon_1^{*(4)} \mathcal{N}_2) dS \right. \\ \left. + Q_{66}^{\text{app}} \int_S \varepsilon_6^{*(4)} \mathcal{N}_6 dS \right] + Q_{66}^{\text{app}}. \end{array} \right. \quad (\text{A.13})$$

*A4. The Variance of Identified Constitutive Parameters.* To lower the effect of noise, the objective function can be denoted as the difference between the real parameters  $\mathbf{Q}$  and

approximate parameters  $\mathbf{Q}^{\text{app}}$ . For instance, the variance for  $Q_{11}$  can be written as follows:

$$V(Q_{11}) = \gamma^2 E \left( \left[ Q_{11}^{\text{app}} \int_S \varepsilon_1^{*(1)} \mathcal{N}_1 dS + Q_{22}^{\text{app}} \int_S \varepsilon_2^{*(1)} \mathcal{N}_2 dS + Q_{12}^{\text{app}} \int_S (\varepsilon_2^{*(1)} \mathcal{N}_1 + \varepsilon_1^{*(1)} \mathcal{N}_2) dS + Q_{66}^{\text{app}} \int_S \varepsilon_6^{*(1)} \mathcal{N}_6 dS \right]^2 \right). \quad (\text{A.14})$$

Using the rectangle method to discretize the above-mentioned integrals,

$$V(Q_{11}) = \gamma^2 \left( \frac{S}{n} \right)^2 E \left( \left[ Q_{11}^{\text{app}} \sum_{i=1}^n \varepsilon_1^{(1)}(M_i) \mathcal{N}_1(M_i) + Q_{22}^{\text{app}} \sum_{i=1}^n \varepsilon_2^{*(1)}(M_i) \mathcal{N}_2(M_i) + \right. \right. \\ \left. \left. Q_{12}^{\text{app}} \sum_{i=1}^n (\varepsilon_2^{*(1)}(M_i) \mathcal{N}_1(M_i) + \varepsilon_1^{*(1)}(M_i) \mathcal{N}_2(M_i)) + Q_{66}^{\text{app}} \sum_{i=1}^n \varepsilon_6^{*(1)}(M_i) \mathcal{N}_6(M_i) \right]^2 \right), \quad (\text{A.15})$$

where  $S$  is the specimen area, and  $n$  is the number of rectangular elements by discretizing the specimen geometry.

Derived from the abovementioned equations are the following total six different types of  $S_i$ ;  $i = 1, 2, \dots, 6$ :

$$\left\{ \begin{array}{l} S_1 = \sum_{i=1}^n \sum_{j=1}^n \varepsilon_k(M_i) \varepsilon_k(M_j) E[\mathcal{N}_1(M_i) \mathcal{N}_l(M_j)] \quad i \neq j \& k, l = 1, 2, 6, \\ S_2 = \sum_{i=1}^n \varepsilon_k^2(M_i) E[\mathcal{N}_k^2(M_i)] \quad k = 1, 2, 6, \\ S_3 = \sum_{i=1}^n \varepsilon_k(M_i) \varepsilon_l(M_i) E[\mathcal{N}_k^2(M_i)] \quad k, l = 1, 2 \& k \neq l, \\ S_4 = \sum_{i=1}^n \sum_{j=1}^n \varepsilon_k(M_i) \varepsilon_k(M_j) E[\mathcal{N}_k(M_i) \mathcal{N}_k(M_j)] \quad i \neq j \& k, l = 1, 2, \\ S_5 = \sum_{i=1}^n \sum_{j=1}^n \varepsilon_k(M_i) \varepsilon_l(M_j) E[\mathcal{N}_p(M_i) \mathcal{N}_q(M_j)] \quad k, l, p, q = 1, 2 \& p \neq q, \\ S_6 = \sum_{i=1}^n \sum_{j=1}^n \varepsilon_k(M_i) \varepsilon_6(M_j) E[\mathcal{N}_1(M_i) \mathcal{N}_6(M_j)] \quad k, l = 1, 2. \end{array} \right. \quad (\text{A.16})$$

Due to the autocorrelation of functions  $\mathcal{N}_i$ ,  $i = 1, 2, 6$ , the mathematical expectation in the abovementioned equation is equal to 0 or 1; then,

$$\left\{ \begin{array}{l} S_1, S_4, S_5, S_6 = 0, \\ S_2 = \sum_{i=1}^n \varepsilon_k^2(M_i), \quad k = 1, 2, 6, \\ S_3 = \sum_{i=1}^n \varepsilon_k(M_i) \varepsilon_l(M_i), \quad k, l = 1, 2 \& k \neq l. \end{array} \right. \quad (\text{A.17})$$

Hence,  $V(Q_{11})$  can be rewritten as follows:

$$V(Q_{11}) = \gamma^2 \left( \frac{S}{n} \right)^2 \left[ \left( (Q_{11}^{\text{app}})^2 + (Q_{12}^{\text{app}})^2 \right) \sum_{i=1}^n (\varepsilon_1^{*(1)}(M_i))^2 + \right. \\ \left( (Q_{22}^{\text{app}})^2 + (Q_{12}^{\text{app}})^2 \right) \sum_{i=1}^n (\varepsilon_2^{*(1)}(M_i))^2 + 2(Q_{11}^{\text{app}} + Q_{22}^{\text{app}}) Q_{12}^{\text{app}} \sum_{i=1}^n \varepsilon_1^{*(1)}(M_i) \varepsilon_2^{*(1)}(M_i) \\ \left. + (Q_{66}^{\text{app}})^2 \sum_{i=1}^n (\varepsilon_6^{*(1)}(M_i))^2 \right]. \quad (\text{A.18})$$

Similar results are obtained for  $Q_{22}$ ,  $Q_{12}$ , and  $Q_{66}$ . Denoting  $V(Q)$ , the vector containing the variances of  $Q_{11}$ ,  $Q_{22}$ ,  $Q_{12}$ , and  $Q_{66}$ , one can write

$$\begin{cases} V(Q_{11}) = \gamma^2 \left(\frac{S}{n}\right)^2 \mathbf{Q}^{\text{app}} \mathbf{G}^{(1)} \mathbf{Q}^{\text{app}}, \\ V(Q_{22}) = \gamma^2 \left(\frac{S}{n}\right)^2 \mathbf{Q}^{\text{app}} \mathbf{G}^{(2)} \mathbf{Q}^{\text{app}}, \\ V(Q_{12}) = \gamma^2 \left(\frac{S}{n}\right)^2 \mathbf{Q}^{\text{app}} \mathbf{G}^{(3)} \mathbf{Q}^{\text{app}}, \\ V(Q_{66}) = \gamma^2 \left(\frac{S}{n}\right)^2 \mathbf{Q}^{\text{app}} \mathbf{G}^{(4)} \mathbf{Q}^{\text{app}}, \end{cases} \quad (\text{A.19})$$

where  $\mathbf{G}^{(j)}$ ,  $j = 1, 2, 3, 4$  is the following square matrix:

$$\begin{bmatrix} \sum_{i=1}^n (\varepsilon_1^{*(j)}(M_i))^2 & 0 & \sum_{i=1}^n \varepsilon_1^{*(j)}(M_i) \varepsilon_2^{*(j)}(M_i) & 0 \\ 0 & \sum_{i=1}^n (\varepsilon_2^{*(j)}(M_i))^2 & \sum_{i=1}^n \varepsilon_1^{*(j)}(M_i) \varepsilon_2^{*(j)}(M_i) & 0 \\ \sum_{i=1}^n \varepsilon_1^{*(j)}(M_i) \varepsilon_2^{*(j)}(M_i) & \sum_{i=1}^n \varepsilon_1^{*(j)}(M_i) \varepsilon_2^{*(j)}(M_i) & \sum_{i=1}^n (\varepsilon_1^{*(j)}(M_i))^2 + \sum_{i=1}^n (\varepsilon_2^{*(j)}(M_i))^2 & 0 \\ 0 & 0 & 0 & \sum_{i=1}^n (\varepsilon_6^{*(j)}(M_i))^2 \end{bmatrix}. \quad (\text{A.20})$$

These variances are proportional to  $\gamma^2$ , expressing

$$(\eta^{(i)})^2 = \left(\frac{S}{n}\right)^2 \mathbf{Q}^{\text{app}} \mathbf{G}^{(i)} \mathbf{Q}^{\text{app}}. \quad (\text{A.21})$$

Equation (A.19) can be rewritten as

$$\begin{cases} V(Q_{11}) = (\eta^{(1)})^2 \gamma^2, \\ V(Q_{22}) = (\eta^{(2)})^2 \gamma^2, \\ V(Q_{12}) = (\eta^{(3)})^2 \gamma^2, \\ V(Q_{66}) = (\eta^{(4)})^2 \gamma^2. \end{cases} \quad (\text{A.22})$$

**A5. The Linear System of KA Virtual Fields.** The KA condition can produce several linear equations, and the number of these equations is depending on the number of supports. The special virtual field condition also leads to several linear equations, the number of which depends on the type of constitutive model of specimen material. The two types of conditions can produce the following linear system:

$$\mathbf{A} \mathbf{Y}^{*(i)} = \mathbf{Z}^{(i)}. \quad (\text{A.23})$$

Using the Lagrange multiplier approach, the Lagrangian function  $\mathcal{L}^{(i)}$  can be constructed for each constitutive parameter sought, and its constraint is equation (23), and the objective function is  $(\eta^{(i)})^2$ . Therefore, the expression of the Lagrange function is

$$\mathcal{L}^{(i)} = \frac{1}{2} \mathbf{Y}^{*(i)} \mathbf{H} \mathbf{Y}^{*(i)} + \lambda^{(i)} (\mathbf{A} \mathbf{Y}^{*(i)} - \mathbf{Z}^{(i)}), \quad (\text{A.24})$$

where  $\lambda^{(i)}$  is the vector containing Lagrange multipliers. Equation (A.23) can be re-expressed as the following linear relationship:

$$\begin{bmatrix} \mathbf{H} & \mathbf{A} \\ \mathbf{A} & \mathbf{0} \end{bmatrix} \begin{pmatrix} \mathbf{Y}^{(i)} \\ \lambda^{(i)} \end{pmatrix} = \begin{pmatrix} \mathbf{0} \\ \mathbf{Z}^{(i)} \end{pmatrix}. \quad (\text{A.25})$$

## B. Equation Derivation of Section 2.2

*B1. The Governing Equation of the Virtual Fields Method for the Total Specimen.* For the plane-stress specimen with two different materials A and B, and both of them are set with the elastic orthotropic material. But the constitutive parameters of A and B are unknown. The governing equation of the virtual fields method for the total specimen is as follows:

$$\begin{aligned} & Q_{11a} \int_{S_a} \varepsilon_1 \varepsilon_1^* dS + Q_{22a} \int_{S_a} \varepsilon_2 \varepsilon_2^* dS + Q_{12a} \int_{S_a} (\varepsilon_1 \varepsilon_2^* + \varepsilon_2 \varepsilon_1^*) dS + Q_{66a} \int_{S_a} \varepsilon_6 \varepsilon_6^* dS + \\ & Q_{11b} \int_{S_b} \varepsilon_1 \varepsilon_1^* dS + Q_{22b} \int_{S_b} \varepsilon_2 \varepsilon_2^* dS + Q_{12b} \int_{S_b} (\varepsilon_1 \varepsilon_2^* + \varepsilon_2 \varepsilon_1^*) dS + Q_{66b} \int_{S_b} \varepsilon_6 \varepsilon_6^* dS = \int_{L_f} (T_i u_i^*) dl. \end{aligned} \quad (\text{B.1})$$

As mentioned above, the sum of exact values and white noise is the measured strain as equation (B.1) can be reexpressed as follows:

$$\begin{aligned} & Q_{11a} \int_{S_a} (\varepsilon_1 - \gamma \mathcal{N}_1) \varepsilon_1^* dS + Q_{22a} \int_{S_a} (\varepsilon_2 - \gamma \mathcal{N}_2) \varepsilon_2^* dS + Q_{12a} \int_{S_a} [(\varepsilon_1 - \gamma \mathcal{N}_1) \varepsilon_2^* + (\varepsilon_2 - \gamma \mathcal{N}_2) \varepsilon_1^*] dS \\ & + Q_{66a} \int_{S_a} (\varepsilon_6 - \gamma \mathcal{N}_6) \varepsilon_6^* dS + Q_{11b} \int_{S_b} (\varepsilon_1 - \gamma \mathcal{N}_1) \varepsilon_1^* dS + Q_{22b} \int_{S_b} (\varepsilon_2 - \gamma \mathcal{N}_2) \varepsilon_2^* dS + \\ & Q_{12b} \int_{S_b} [(\varepsilon_1 - \gamma \mathcal{N}_1) \varepsilon_2^* + (\varepsilon_2 - \gamma \mathcal{N}_2) \varepsilon_1^*] dS + Q_{66b} \int_{S_b} (\varepsilon_6 - \gamma \mathcal{N}_6) \varepsilon_6^* dS = \int_{L_f} (T_i u_i^*) dl. \end{aligned} \quad (\text{B.2})$$

Assume that the noise components are uncorrelated to each other, and presume that the noise between points is also

uncorrelated. Therefore, equation (B.2) can be rewritten as follows:

$$\begin{aligned} & Q_{11a} \int_{S_a} \varepsilon_1 \varepsilon_1^* dS + Q_{22a} \int_{S_a} \varepsilon_2 \varepsilon_2^* dS + Q_{12a} \int_{S_a} (\varepsilon_1 \varepsilon_2^* + \varepsilon_2 \varepsilon_1^*) dS + Q_{66a} \int_{S_a} \varepsilon_6 \varepsilon_6^* dS + \\ & Q_{11b} \int_{S_b} \varepsilon_1 \varepsilon_1^* dS + Q_{22b} \int_{S_b} \varepsilon_2 \varepsilon_2^* dS + Q_{12b} \int_{S_b} (\varepsilon_1 \varepsilon_2^* + \varepsilon_2 \varepsilon_1^*) dS + Q_{66b} \int_{S_b} \varepsilon_6 \varepsilon_6^* dS - \\ & \gamma \left[ Q_{11a} \int_{S_a} \varepsilon_1^* \mathcal{N}_1 dS + Q_{22a} \int_{S_a} \varepsilon_2^* \mathcal{N}_2 dS + Q_{12a} \int_{S_a} (\varepsilon_2^* \mathcal{N}_1 + \varepsilon_1^* \mathcal{N}_2) dS + Q_{66a} \int_{S_a} \varepsilon_6^* \mathcal{N}_6 dS \right. \\ & \left. + Q_{11b} \int_{S_b} \varepsilon_1^* \mathcal{N}_1 dS + Q_{22b} \int_{S_b} \varepsilon_2^* \mathcal{N}_2 dS + Q_{12b} \int_{S_b} (\varepsilon_2^* \mathcal{N}_1 + \varepsilon_1^* \mathcal{N}_2) dS + Q_{66b} \int_{S_b} \varepsilon_6^* \mathcal{N}_6 dS \right] = \int_{L_f} (T_i u_i^*) dl. \end{aligned} \quad (\text{B.3})$$

B2. *The Principle of Virtual Work with Ignored Noise.* Directly identify  $Q_{11a}$ ,  $Q_{11b}$ ,  $Q_{12a}$ ,  $Q_{12b}$ ,  $Q_{22a}$ ,  $Q_{22b}$ ,  $Q_{66a}$ , and  $Q_{66b}$  using the abovementioned four special virtual

displacement fields  $\varepsilon^{*(1)}$ ,  $\varepsilon^{*(2)}$ ,  $\varepsilon^{*(3)}$ , and  $\varepsilon^{*(4)}$ . For instance,  $u^{*(1)}$  is a special virtual field that identifies  $Q_{11a}$ , which can be written as follows:

$$\begin{aligned} Q_{11a} = & -Q_{22a} \int_{S_a} \varepsilon_2 \varepsilon_2^{*(1)} dS - Q_{12a} \int_{S_a} (\varepsilon_1 \varepsilon_2^{*(1)} + \varepsilon_2 \varepsilon_1^{*(1)}) dS - Q_{66a} \int_{S_a} \varepsilon_6 \varepsilon_6^{*(1)} dS - \\ Q_{11b} \int_{S_b} \varepsilon_1 \varepsilon_1^{*(1)} dS & - Q_{22b} \int_{S_b} \varepsilon_2 \varepsilon_2^{*(1)} dS - Q_{12b} \int_{S_b} (\varepsilon_1 \varepsilon_2^{*(1)} + \varepsilon_2 \varepsilon_1^{*(1)}) dS - Q_{66b} \int_{S_b} \varepsilon_6 \varepsilon_6^{*(1)} dS + \\ \gamma \left[ Q_{11a} \int_{S_a} \varepsilon_1^{*(1)} \mathcal{N}_1 dS + Q_{22a} \int_{S_a} \varepsilon_2^{*(1)} \mathcal{N}_2 dS + Q_{12a} \int_{S_a} (\varepsilon_2^{*(1)} \mathcal{N}_1 + \varepsilon_1^{*(1)} \mathcal{N}_2) dS + Q_{66a} \int_{S_a} \varepsilon_6^{*(1)} \mathcal{N}_6 dS \right. \\ Q_{11b} \int_{S_b} \varepsilon_1^{*(1)} \mathcal{N}_1 dS & + Q_{22b} \int_{S_b} \varepsilon_2^{*(1)} \mathcal{N}_2 dS + Q_{12b} \int_{S_b} (\varepsilon_2^{*(1)} \mathcal{N}_1 + \varepsilon_1^{*(1)} \mathcal{N}_2) dS + Q_{66b} \int_{S_b} \varepsilon_6^{*(1)} \mathcal{N}_6 dS \left. \right] + \int_{L_f} (T_i u_i^*) dl. \end{aligned} \quad (\text{B.4})$$

## Data Availability

The data used to support the findings of this study are available from the corresponding author upon request.

## Conflicts of Interest

The authors declare that there are no conflicts of interest regarding the publication of this paper.

## Acknowledgments

This research was funded by the Fundamental Research Fund for the Central Universities (Grant nos. 2018ZY08 and 2015ZCQ-GX-02) and the National Natural Science Foundation of China (Grant no. 11502022).

## References

- [1] J. Xavier, S. Avril, F. Pierron, and J. Morais, "Novel experimental approach for longitudinal-radial stiffness characterisation of clear wood by a single test," *Holzforschung*, vol. 61, no. 5, pp. 573–581, 2007.
- [2] J. Xavier and F. Pierron, "Measuring orthotropic bending stiffness components of pinus pinaster by the virtual fields method," *The Journal of Strain Analysis for Engineering Design*, vol. 53, no. 8, pp. 556–565, 2018.
- [3] P. Wang, F. Pierron, M. Rossi, P. Lava, and O. T. Thomsen, "Optimised experimental characterisation of polymeric foam material using DIC and the virtual fields method," *Strain*, vol. 52, no. 1, pp. 59–79, 2015.
- [4] L. Zhang, S. G. Thakku, M. R. Beotra et al., "Verification of a virtual fields method to extract the mechanical properties of human optic nerve head tissues in vivo," *Biomechanics and Modeling in Mechanobiology*, vol. 16, no. 3, pp. 871–887, 2017.
- [5] X. Dai and H. Xie, "Constitutive parameter identification of 3D printing material based on the virtual fields method," *Measurement*, vol. 5, pp. 38–43, 2015.
- [6] M. Zhou and H. Xie, "An identification method of mechanical properties of materials based on the full-field measurement method based on the fringe pattern," *Strain*, vol. 55, no. 5, Article ID 12326, 2019.
- [7] S. Avril, M. Bonnet, A. S. Bretelle et al., "Overview of identification methods of mechanical parameters based on full-field measurements," *Experimental Mechanics*, vol. 48, no. 4, pp. 381–402, 2008.
- [8] E. Markiewicz, B. Langrand, and D. Nottacuvier, "A review of characterisation and parameters identification of materials constitutive and damage models: from normalised direct approach to most advanced inverse problem resolution," *International Journal of Impact Engineering*, vol. 110, pp. 371–381, 2017.
- [9] M. Grediac, E. Toussaint, and F. Pierron, "Special virtual fields for the direct determination of material parameters with the virtual fields method. 1-Principle and definition," *International Journal of Solids and Structures*, vol. 39, no. 10, pp. 2691–2705, 2002.
- [10] M. Grediac, E. Toussaint, and F. Pierron, "Special virtual fields for the direct determination of material parameters with the virtual fields method," 2-Application to in-plane properties," *International Journal of Solids and Structures*, vol. 39, no. 10, pp. 2707–2730, 2002.
- [11] S. Cooreman, D. Lecompte, H. Sol, J. Vantomme, and D. Debruyne, "Identification of mechanical material behavior through inverse modeling and DIC," *Experimental Mechanics*, vol. 48, no. 4, pp. 421–433, 2008.
- [12] L. Bruno, "Mechanical characterization of composite materials by optical techniques: a review," *Optics and Lasers in Engineering*, vol. 104, pp. 192–203, 2017.
- [13] R. Delorme, P. Diehl, I. Tabiai, L. L. Lebel, and M. Lévesque, "Extracting constitutive mechanical parameters in linear elasticity using the virtual fields method within the ordinary state-based peridynamic framework," *Journal of Peridynamics and Nonlocal Modeling*, vol. 2, no. 2, pp. 111–135, 2020.
- [14] M. Yue and S. Avril, "On improving the accuracy of non-homogeneous shear modulus identification in incompressible elasticity using the virtual fields method," *International Journal of Solids and Structures*, vol. 178–179, pp. 136–144, 2019.
- [15] J. Fu, W. Xie, J. Zhou, and L. Qi, "A method for the simultaneous identification of anisotropic yield and hardening constitutive parameters for sheet metal forming," *International Journal of Mechanical Sciences*, vol. 181, pp. 1–43, 2020.
- [16] T. T. Nguyen, J. M. Huntley, I. A. Ashcroft, P. D. Ruiz, and F. Pierron, "A Fourier-series-based virtual fields method for the identification of three-dimensional stiffness distributions and its application to incompressible materials," *Strain*, vol. 53, no. 5, Article ID 12229, 2017.
- [17] T. T. Nguyen, J. M. Huntley, I. A. Ashcroft, P. D. Ruiz, and F. Pierron, "A Fourier-series-based virtual fields method for

- the identification of 2-d stiffness and traction distributions,” *Strain*, vol. 50, no. 5, pp. 454–468, 2014.
- [18] A. Marek, F. M. Davis, and F. Pierron, “Sensitivity-based virtual fields for the non-linear virtual fields method,” *Computational Mechanics*, vol. 60, no. 3, pp. 409–431, 2017.
- [19] N. Nigamaa and S. J. Subramanian, “Identification of orthotropic elastic constants using the eigenfunction virtual fields method,” *International Journal of Solids and Structures*, vol. 51, no. 2, pp. 295–304, 2014.
- [20] W. Hao, Y. Zhang, and Y. Yuan, “Eigenfunction virtual fields method for thermo-mechanical parameters identification of composite materials,” *Polymer Testing*, vol. 50, pp. 224–234, 2016.
- [21] K. Syedmuhammad, E. Toussaint, M. Grediac, S. Avril, and J. Kim, “Characterization of composite plates using the virtual fields method with optimized loading conditions,” *Composite Structures*, vol. 85, no. 1, pp. 70–82, 2008.
- [22] J. Kim, F. Barlat, F. Pierron, and M. Lee, “Determination of anisotropic plastic constitutive parameters using the virtual fields method,” *Experimental Mechanics*, vol. 54, no. 7, pp. 1189–1204, 2014.
- [23] J. Xavier, S. Avril, F. Pierron, and J. Morais, ““Variation of transverse and shear stiffness properties of wood in a tree” *Composites Part A*,” *Applied Science and Manufacturing*, vol. 40, no. 12, pp. 1953–1960, 2009.
- [24] E. Toussaint, G. Michel, and F. Pierron, “The virtual fields method with piecewise virtual fields”” *International Journal of Mechanical Sciences*, vol. 48, no. 3, pp. 256–264, 2006.
- [25] Q. Cao, Y. Li, and H. Xie, “Orientation-Identified virtual fields method combined with moiré interferometry for mechanical characterization of single crystal Ni-based superalloys,” *Optics and Lasers in Engineering*, vol. 125, no. 123, pp. 1–9, 2020.
- [26] K. Syed-Muhammad, E. Toussaint, and M. Grediac, “Optimization of a mechanical test on composite plates with the virtual fields method,” *Structural and Multidisciplinary Optimization*, vol. 38, no. 1, pp. 71–82, 2009.
- [27] M. Grediac and F. Pierron, “Numerical issues in the virtual fields method,” *International Journal for Numerical Methods in Engineering*, vol. 59, no. 10, pp. 1287–1312, 2004.
- [28] M. Rossi and F. Pierron, “On the use of simulated experiments in designing tests for material characterization from full-field measurements,” *International Journal of Solids and Structures*, vol. 49, no. 3, pp. 420–435, 2012.
- [29] X. Gu and F. Pierron, “Towards the design of a new standard for composite stiffness identification,” *Composites Part A: Applied Science and Manufacturing*, vol. 91, pp. 448–460, 2016.
- [30] J. Fu, W. Xie, and L. Qi, “An identification method for anisotropic plastic constitutive parameters of sheet metals,” *Procedia Manufacturing*, vol. 47, pp. 812–815, 2020.
- [31] F. Pierron and M. Grédiac, “*The Virtual Fields Method. Extracting Constitutive Mechanical Parameters from Full-Field Deformation Measurements*,” Springer Verla, New York, NY, USA, 2012.
- [32] P. Zhou and K. E. Goodson, “Subpixel displacement and deformation gradient measurement using digital image/speckle correlation (DISC),” *Optical Engineering*, vol. 40, no. 8, pp. 1613–1620, 2001.

## Research Article

# The Influence of Blade Angle on the Performance of Plastic Centrifugal Pump

Jun Li , Lingfeng Tang, and Yaoyao Zhang

School of Mechanical and Automotive Engineering, Anhui Polytechnic University, Wuhu, Anhui 241000, China

Correspondence should be addressed to Jun Li; 2190110106@stu.ahpu.edu.cn

Received 19 April 2020; Revised 25 July 2020; Accepted 28 July 2020; Published 25 August 2020

Academic Editor: Candido Fabrizio Pirri

Copyright © 2020 Jun Li et al. This is an open access article distributed under the Creative Commons Attribution License, which permits unrestricted use, distribution, and reproduction in any medium, provided the original work is properly cited.

In order to obtain the influence of blade placement angle on the performance of plastic centrifugal pumps, this article used the velocity modulus method. Based on the method, the hydraulic design of the flow passage components of the plastic centrifugal pump was carried out, and the two-dimensional model and three-dimensional model diagram of the flow components were established. The flow field of the impeller model under different working conditions was simulated and the results were analyzed by ANSYS CFX. The influence of different fluid loads on the solid structure under design conditions on the structure characteristics of the impeller was studied by ANSYS Workbench. Impeller models with different outlet angles were established to study the influence of the outlet angle on the performance of pump, and fluid-structure interaction for different impeller models was utilized to study the influence of the outlet angle on the structural characteristics of the impeller. According to the Stepanoff velocity modulus method, considered the import prerotation, the wrap angle design method and the blade inlet angle design method were proposed. In order to study the influence of different inlet angles on the performance of pump, the inlet angle was changed to establish multiple sets of impeller models, 3D printing technology was used to print out each impeller, and performance experiments were performed on the pump equipped with the impeller. The result of the experiments showed that working pressure of plastic centrifugal pump exceeding 5 atm would cause impeller structure damage. When the outlet angle was 35°, the plastic centrifugal pump reached the highest efficiency of 81.0161% and the highest  $H$  of 35.8029. The maximum deformation caused by the flow field load on the impeller increased with the increase of the outlet angle. With the increase of the inlet angle, the efficiency and  $H$  of the plastic centrifugal pump were reduced. Under normal pressure load, the deformation of the impeller first decreased and then increased, and when  $\beta_1$  was 13°, the total deformation of the impeller was the smallest.

## 1. Introduction

Plastic centrifugal pumps have advantages such as outstanding corrosion resistance, light weight, and low price. They are widely used in various fields of national economic production [1]. In recent years, with the improvement of computer level and the continuous development of numerical simulation methods, Guo [2] studied the law of radial force and rotor mode on the blade of low specific speed by two-way fluid-structure interaction. Liu et al. [3] studied the influence of two-way fluid-structure interaction on the external characteristic parameters of centrifugal pump and analyzed the pressure fluctuation at the outlet of the impeller. Wang et al. [4] carried out numerical analysis and optimization of three kinds of volute structure and

obtained the matched deformation between the volute and the blade by the method of one-way fluid-structure interaction. Huang et al. [5] analyzed the whole flow field of IS100-65-200 centrifugal pump considering the flow field loads on the impeller, volute, and the front and back cavities of the impeller. Fontanls and Alfred [6] studied the influence of rotor stator interaction (RSI) on the vibration and acoustic characteristics of the centrifugal pump and studied the interaction between the impeller and diffuser of centrifugal pump with CFD to study its pressure fluctuation. Mou [7] analyzed the stress-strain distribution of the cantilever centrifugal pump impeller under different cantilever ratios by one-way fluid-structure interaction and studied the dynamic characteristics of the centrifugal pump rotor under different cantilever ratios under prestress and nonprestress.

Tang et al. [8] carried on the thermo-solid coupling analysis to the plastic pump. Wang and Huo [9] have carried out multiobjective optimization design and experiment on the centrifugal pump.

Gu et al. [10] reduced drag by studying the synergistic drag reduction of polymers and surfactants. The above research studies on fluid-structure interaction of the centrifugal pump are all aimed at metal pumps. The strength of the impeller of plastic centrifugal pump is relatively low, so under the fluid load, the elastic deformation of the impeller of plastic centrifugal pump is significantly larger than that of the metal pump. When the fluid load is large enough, the blade will produce obvious deformation and lead to the structural failure of the plastic centrifugal pump impeller. In this paper, a low specific speed plastic centrifugal pump is taken as the research object, and the influence of the blade angle of plastic centrifugal pumps on the pump performance is studied based on one-way fluid-structure interaction.

## 2. Structural Design of Plastic Centrifugal Pump

Basic parameters of the plastic centrifugal pump:  $Q = 12.5 \text{ m}^3/\text{h}$ ,  $H = 32 \text{ m}$ ,  $n = 2900 \text{ r/min}$ , and  $NPSHa = 4 \text{ m}$ , inlet diameter  $D_S = 50 \text{ mm}$ , inlet velocity  $v_s = 1.77 \text{ m/s}$ , outlet diameter  $D_d = 40 \text{ mm}$ , outlet velocity  $V_D = 2.765 \text{ m/s}$ , and  $n_s = 46.36$ . When the flow rate increases, the design parameters of the plastic centrifugal pump become  $Q = 20.375 \text{ m}^3/\text{h}$ ,  $H = 30.825 \text{ m}$ , and  $n_s = 60.871$ . Efficiency of the plastic centrifugal pump:  $\eta = 0.691$ ; motor power:  $P_C = 2.972 \text{ kw}$ .

**2.1. Determination of Impeller Inlet Diameter.** Equivalent diameter of the impeller inlet:  $D_0 = 56.24 \text{ mm}$ . For a cantilever impeller, impeller inlet diameter  $D_j = 58 \text{ mm}$ , blade inlet width  $b_1 = 23.43 \text{ mm}$ , impeller outlet diameter  $D_2 = 158.5 \text{ mm}$ . In the hydraulic design of low specific speed plastic centrifugal pump, in order to improve the efficiency of plastic centrifugal pump, the impeller outlet width is  $b_2 = 10 \text{ mm}$ .

In this paper, the angle of the blade is  $20^\circ$ , the angle of the blade outlet is  $\beta_2 = 30^\circ$ , the number of blades is  $Z = 5$ , and the diameter of the blade outlet is  $D_2 = 162 \text{ mm}$ .

Outlet shaft speed:  $v_{m2} = 1.38 \text{ m/s}$ , outlet peripheral speed:  $U_2 = 24.51 \text{ m/s}$ , and blade wrap angle  $\phi = 130^\circ$ .

### 2.2. Design of Main Structural Parameters of Pressurized Water Chamber

**2.2.1. The Area of Each Section of Vortex Chamber.** Each section of the vortex chamber presents a gradually increasing mode, and the area of each section is obtained by formula (1) and shown in Table 1:

$$F_\phi = F_8 \frac{\phi}{360}. \quad (1)$$

$F_\phi$ : area of each section of vortex chamber,  $\text{cm}^2$ .

$\phi$ : wrap angle of vortex chamber section.

### 2.2.2. Vortex Chamber Width

$$b_3 = (1.5 \sim 2.0)b_2. \quad (2)$$

According to the empirical formula of vortex chamber width and  $b_2 = 10 \text{ mm}$ ,  $b_3$  is  $20 \text{ mm}$ . Considering that the material of the impeller is a polymer material, a certain margin needs to be left to compensate the rotor series and manufacturing errors, so  $b_3$  is  $33 \text{ mm}$ .

### 2.2.3. Base Circle Diameter

$$D_3 = (1.03 \sim 1.08)D_2. \quad (3)$$

From the empirical formula of base circle diameter and  $D_2 = 158.5 \text{ mm}$ , substitute the value, then  $D_3 = 174.96 \text{ mm}$  and  $D_3 = 175 \text{ mm}$ .

**2.3. Model Diagram of Overcurrent Parts.** According to the structural parameters of the impeller calculated in the last section, the two-dimensional model diagram of the impeller is drawn.

**2.3.1. Two-Dimensional Design Drawing of Overcurrent Parts.** In [11], a method of drawing cylindrical blade with controllable wrap angle was proposed. In this paper, the blade thickness is uniformly thickened from the inlet to the outlet, the real thickness of the blade inlet is  $4 \text{ mm}$ , and the real thickness of the outlet is  $8 \text{ mm}$ . According to the above method of drawing profile, the two-dimensional design drawing of the impeller is shown in Figure 1, and the two-dimensional design drawing of volute is shown in Figure 2.

**2.3.2. Three-Dimensional Design Drawing of Overcurrent Parts.** Use SolidWorks 2017 to draw the three-dimensional model of the impeller, as shown in Figures 3(a) and 3(b), and the impeller water model diagram, as shown in Figure 3(c), and establish the three-dimensional model of the volute water body according to the two-dimensional design drawing of the volute, as shown in Figure 3(d).

## 3. Flow Field Simulation and Fluid-Structure Interaction Analysis of Impeller

Based on the results of fluid-structure interaction analysis, the deformation of the impeller under design condition is obtained.

**3.1. Simulation of Internal Flow Field of Plastic Centrifugal Pump.** The flow field simulation steps of the plastic centrifugal pump are as follows.

**3.1.1. Mesh Generation.** Due to the complex model of the overcurrent parts of the plastic centrifugal pump and the large change of curvature, after comparative analysis, an unstructured mesh is used for mesh generation, and the steps are shown in Figure 4.

TABLE 1: The area of each section of the vortex chamber.

Section	1	2	3	4	5	6	7	8
Wrap angle $\varphi_0$	45	90	135	180	225	270	315	360
Area $F\varphi/cm^2$	0.6	1.2	1.8	2.4	3	3.6	4.2	4.8

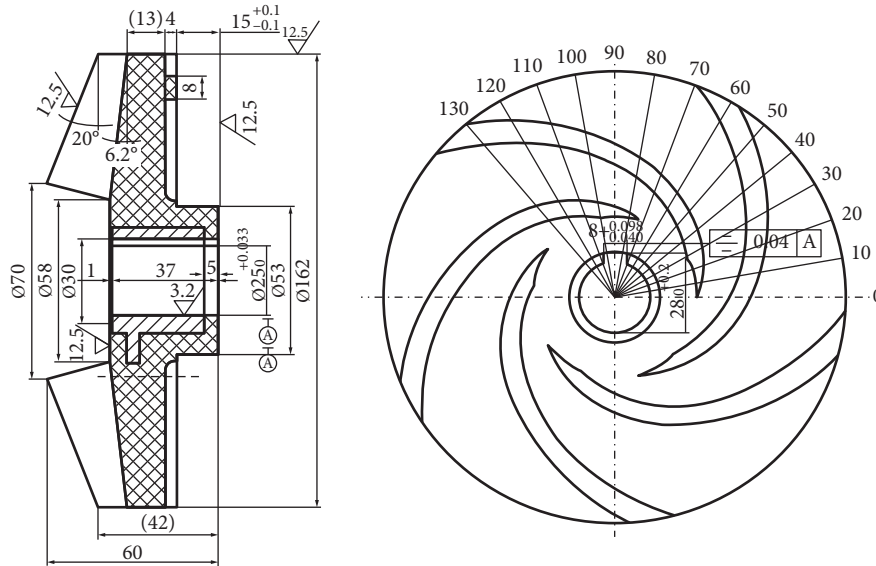


FIGURE 1: Two-dimensional design of the impeller.

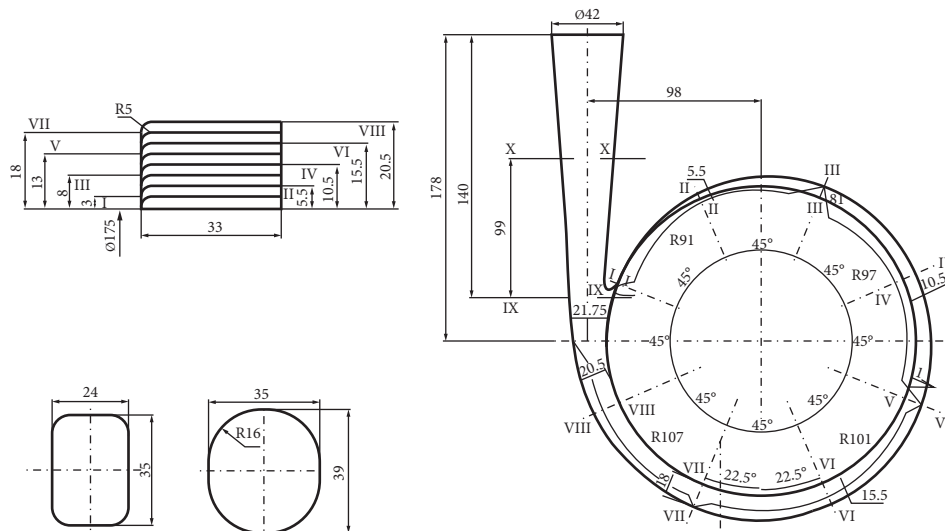


FIGURE 2: Two-dimensional design drawing of the volute.

The calculation domain of the whole flow field of the plastic centrifugal pump mainly includes the volute part, the rotating area of the impeller, and the extension of the inlet and outlet. The mesh distribution of each calculation domain is shown in Table 2 and mesh division model is shown in Figure 5.

3.1.2. Analysis of Numerical Simulation Results. Figure 6 shows the pressure cloud chart of the impeller model under the conditions of  $0.6Q$  and  $1.4Q$  ( $Q$  is the flow at the design

working point). It can be seen from the figure that, under the off-design working condition, the pressure distribution on the impeller is uneven, which will cause flow separation, water loss, and vibration of the pump and will reduce the service life of the pump. With the increase of  $Q$ , the pressure difference between the impeller outlet and inlet becomes smaller, and the pressure at the impeller inlet decreases, so the centrifugal pump is more prone to generate cavitation. It can also be seen clearly from Figure 7 that the effect of flow velocity on the efficiency of centrifugal pump. The flow distribution in the impeller is uneven, which is most obvious

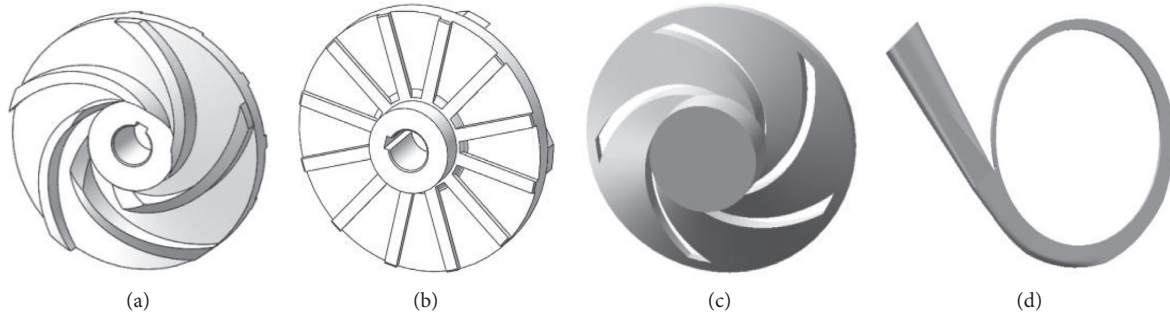


FIGURE 3: Three-dimensional design of the impeller. (a) Front view of the impeller model. (b) Back view of the impeller model. (c) Impeller water model. (d) Volute water model.

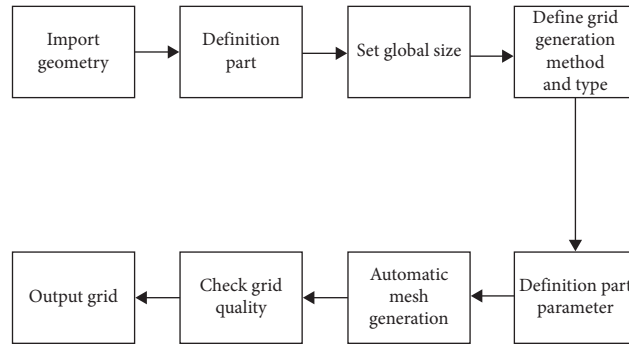


FIGURE 4: Unstructured mesh generation steps.

TABLE 2: Mesh distribution.

Computational domain	Inlet extension	Impeller	Volute	Outlet extension
Number	362444	715419	653367	238182

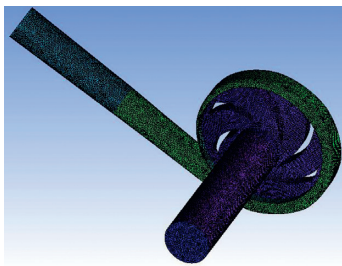


FIGURE 5: Mesh division model.

under the condition of the small flow rate. This situation is basically consistent with the result of the pressure cloud chart.

In order to study the cavitation performance of the plastic centrifugal pump under the design condition, the inlet pressure of the plastic centrifugal pump is continuously reduced until the cavitation occurs. The gas volume on the blades with a different NPSH is shown in Figure 8. Serious cavitation occurs in the experimental plastic centrifugal pump, which is consistent with the actual situation.

**3.2. Research on Structural Characteristics of Impeller Based on One-Way Fluid-Structure Interaction.** Two-way fluid-structure interaction is to solve unknowns in the solid domain and the fluid domain simultaneously, which requires higher requirements on computers. Considering the small flow rate and slow speed of the designed impeller, this paper only considers the effect of the fluid on the impeller and adopts one-way fluid-structure interaction to study the structural characteristics of the plastic centrifugal pump impeller [12, 13]. In this paper, a different pressure is applied to the fluid, and the corresponding pressure load is applied to the impeller to study the deformation of the impeller under different pressures. In mechanical, the equivalent stress and deformation of the impeller are obtained, as shown in Figures 9 and 10, respectively.

It can be seen from Figure 10 that

- (1) Under the combined action of centrifugal force load and fluid pressure load, the deformation of the impeller is basically axisymmetric. From the impeller inlet to the impeller outlet, the deformation of the impeller increases gradually, and the maximum deformation occurs at the outer edge of the impeller.
- (2) When 1 atm pressure is applied to the fluid in the pump, the maximum equivalent stress on the impeller is about 10 MPa and the maximum deformation on the impeller is 0.53256 mm. The strength and deformation of the impeller meet the requirements.

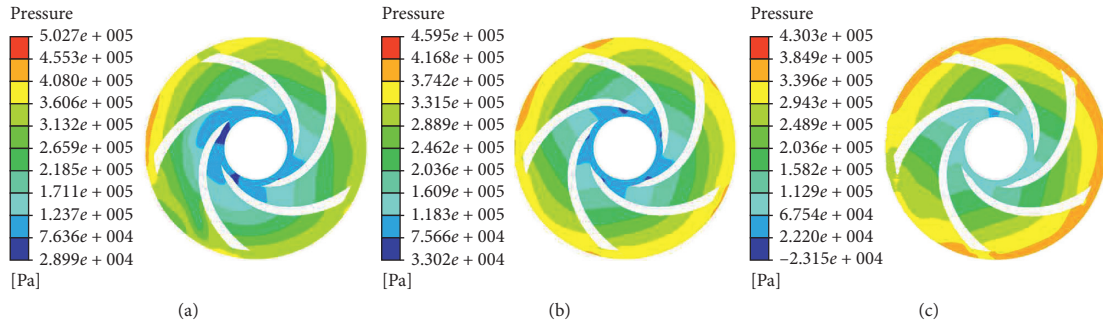


FIGURE 6: Pressure cloud chart under different working conditions. (a) 0.6Q, (b) Q, and (c) 1.4Q.

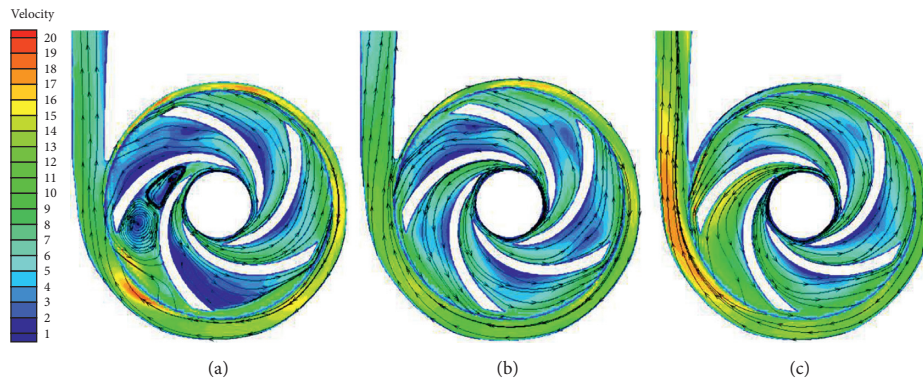


FIGURE 7: Velocity cloud chart and streamline chart under different working conditions. (a) 0.6Q, (b) Q, and (c) 1.4Q.

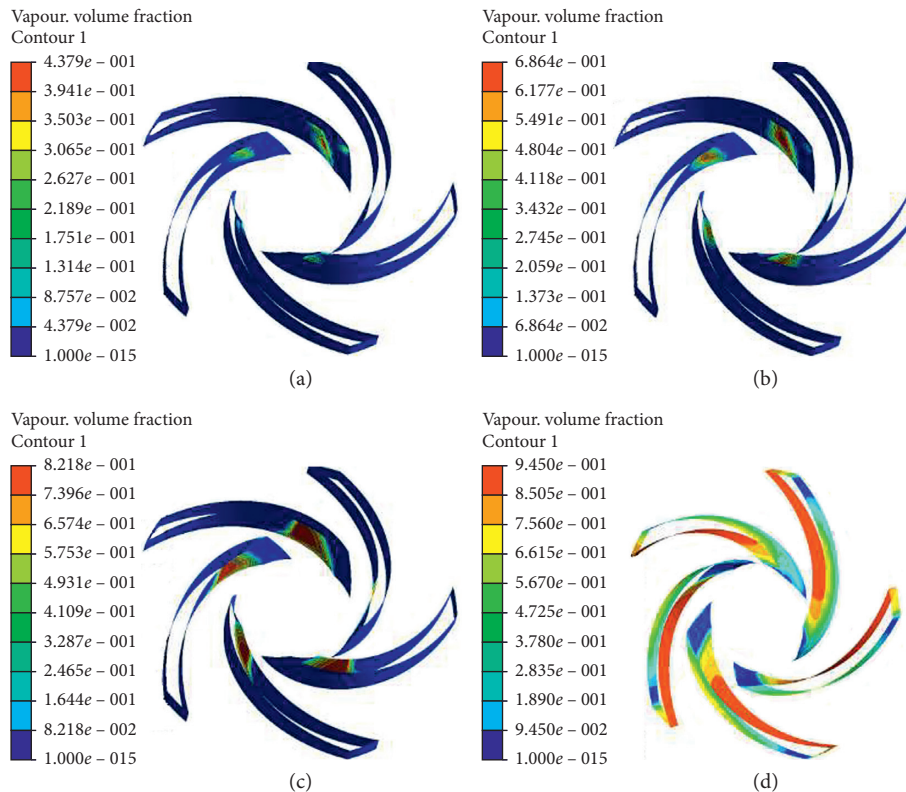


FIGURE 8: Cavitation on the blades with different NPSHs. (a) NPSH = 5 m. (b) NPSH = 3.5 m. (c) NPSH = 2 m. (d) NPSH = 1 m.

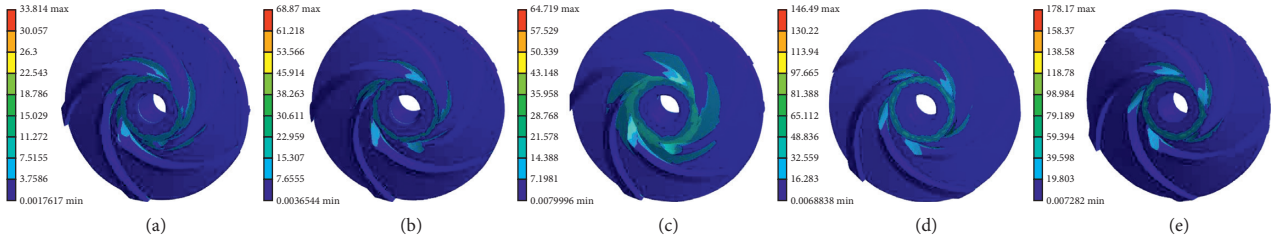


FIGURE 9: Equivalent stress diagram of the impeller surface. (a) 1 atm. (b) 3 atm. (c) 5 atm. (d) 8 atm. (e) 10 atm.

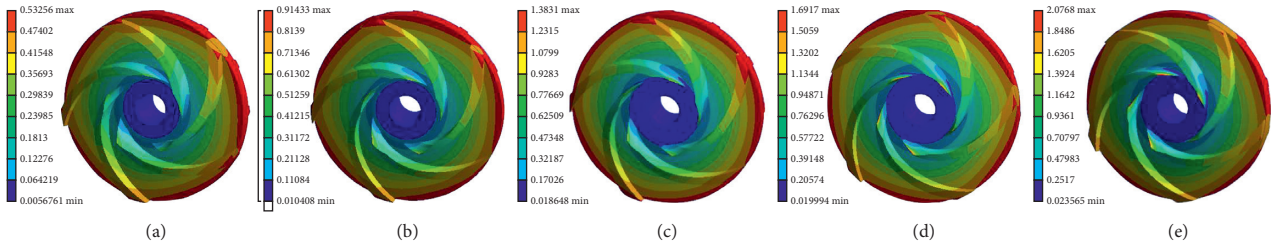


FIGURE 10: Deformation diagram of the impeller surface. (a) 1 atm. (b) 3 atm. (c) 5 atm. (d) 8 atm. (e) 10 atm.

- (3) When the force applied to the fluid is increasing, the total deformation of the impeller increases obviously. When  $P = 5$  atm, the maximum deformation of the blade reaches 1.3831 mm and the deformation at the blade inlet reaches more than 0.5 mm. The equivalent stress has exceeded its yield strength, or even greater than its tensile strength, and there is a risk of structural damage.
- (4) When  $P = 8$  atm, the maximum deformation of the impeller reaches 1.6917 mm and the equivalent stress of the blade inlet reaches above 35 MPa. The impeller structure has failed.
- (5) When  $P = 10$  atm, the deformation of the impeller inlet reaches more than 1 mm, and the equivalent stress is far greater than its tensile strength. The root position of the impeller breaks, resulting in the failure of the impeller structure.

#### 4. Research on the Influence of Blade Outlet Angle on the Performance of Plastic Centrifugal Pump

In the hydraulic design of the plastic centrifugal pump, the blade outlet angle is often an independent variable, which is determined according to engineering experience. A large setting angle can effectively reduce the disc friction loss of the plastic centrifugal pump, but it will cause severe blade bending and flow passage diffusion, strengthen the jet-wake structure of the plastic centrifugal pump, and reduce the efficiency of the plastic centrifugal pump [14]. In order to study the influence of the outlet angle on the performance of the plastic centrifugal pump, the impeller models with outlet angles of 25°, 30°, 35°, and 40° are established in this paper, and numerical simulation is carried out at different working points.

**4.1. Influence of Outlet Angle on External Characteristics of Plastic Centrifugal Pump.** Figure 11 shows the corresponding external characteristic curve of the impeller model with different outlet angles. Figure 11(a) shows the  $Q-\eta$  curve. With the increase of  $Q$ , the efficiency of the plastic centrifugal pump basically shows an upward trend. When  $\beta_2$  reaches 40°, the efficiency of the plastic centrifugal pump begins to decline; Figure 11(b) shows the  $Q-H$  curve. The blade outlet angle has a reasonable range to meet the performance requirements of the plastic centrifugal pump; Figure 11(c) shows the  $Q-P$  curve. The value of  $P$  is different under different  $Q$ .

**4.2. Influence of Outlet Angle on Internal Flow Field in Plastic Centrifugal Pump.** The internal flow field of the plastic centrifugal pump is simulated, and the pressure and velocity cloud charts of each impeller model at different working points (0.6 $Q$ ,  $Q$ , and 1.4 $Q$ ) are obtained, as shown in Figures 12 and 13, respectively. It can be seen from Figure 12 that the pressure distribution on the impeller cross-section is more uniform than that under off-working condition. It can be seen from Figure 13 that the velocity distribution in the impeller passage is relatively uniform, and the vortex is greatly reduced. With the increase of the outlet angle, the flow pattern in the flow channel is significantly improved, but the flow channel becomes shorter, and the binding force restriction of the channel wall on the fluid is insufficient, which results in the vortex.

When  $NPSHr = 1$  m, gas volume fraction chart with different outlet angles is shown in Figure 14. With the increase of the outlet angle, the overall gas volume fraction increases, and the bubbles gradually fill the whole impeller flow channel, and the cavitation performance of the impeller gradually becomes poor.

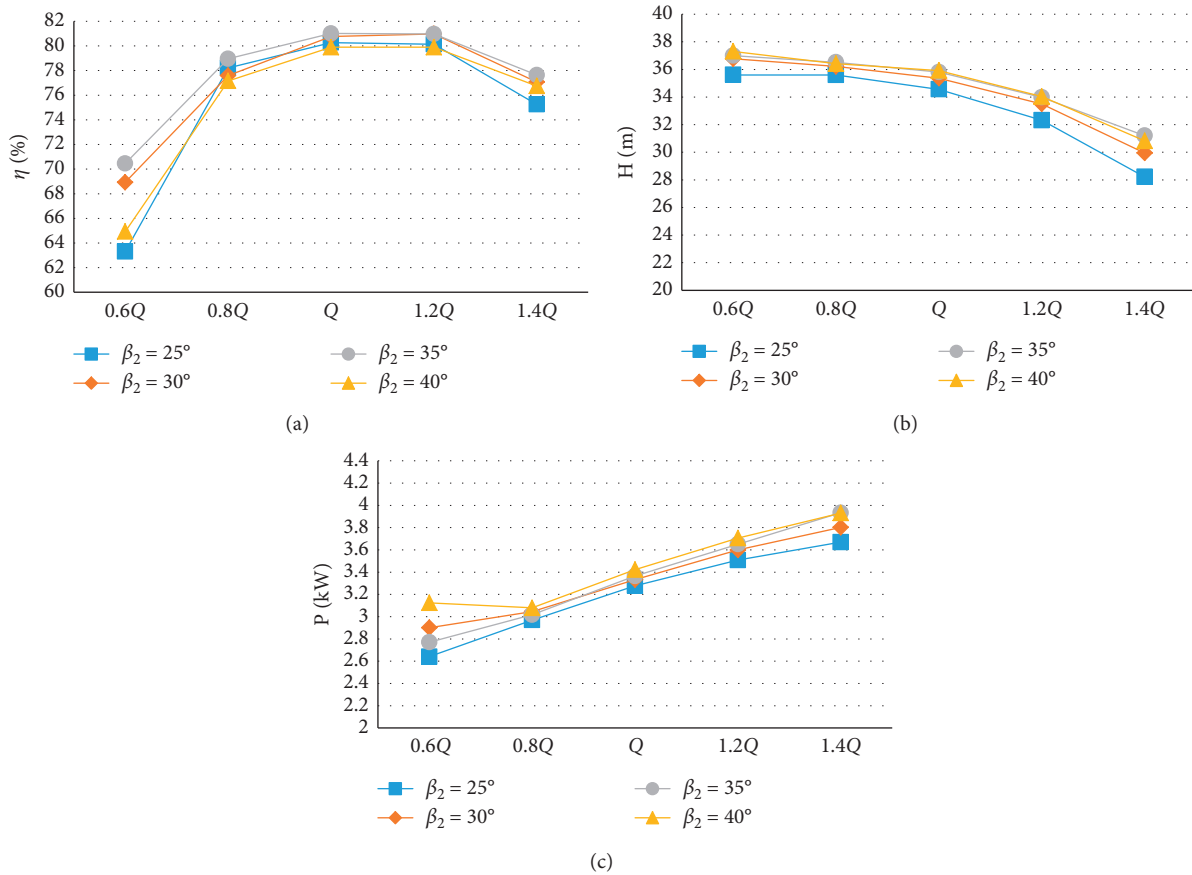


FIGURE 11: External characteristic curve of the impeller model with different outlet angles.

4.3. Research on the Influence of the Blade Outlet Angle on the Structural Characteristics of the Plastic Centrifugal Pump Based on Fluid-Structure Interaction. Figure 15 shows the equivalent stress diagram of each impeller under different fluid loads. It can be seen from the figure that the maximum equivalent stress exists at the impeller inlet and the whole blade root. When the plastic centrifugal pump transports the fluid under normal pressure, the impeller strength can meet the requirements; with the increase of working pressure, when  $P = 5$  atm, the impeller inlet and root have different degrees of structural damage.

According to the one-way fluid-structure interaction, the deformation of each impeller under different fluid loads is obtained, as shown in Figure 16. It can be seen from Figure 16 that when the plastic centrifugal pump works under the same pressure, the blade deformation basically increases with the increase of the outlet angle. When the working pressure increases, the difference of blade deformation under different angles is bigger. When the plastic centrifugal pump works under the condition of atmospheric pressure and negative pressure, the difference of impeller deformation is not obvious with the increase of the outlet angle, but when the plastic centrifugal pump works under the condition of high pressure (the impeller does not have structural damage), the difference of blade deformation is obvious with the increase of outlet angle. The effect of large deformation of the blade on flow field should be considered. When the

larger outlet angle is determined in the hydraulic design, the blade should be thickened properly.

## 5. Research on the Influence of Blade Inlet Angle on the Performance of Plastic Centrifugal Pump

In order to study the influence of the blade inlet angle on the performance of the plastic centrifugal pump, a design method of the blade inlet angle is proposed in this section. The paper first determines the value of the wrap angle and studies the influence of the wrap angle on the performance of the plastic centrifugal pump. This paper takes the outlet angle  $\beta_2 = 30^\circ$  as an example to determine the research scheme of the inlet angle.

5.1. Research on the Influence of Blade Wrap Angle on the Performance of Plastic Centrifugal Pump. In the design of impeller structural parameters, parameters that cannot be determined directly are often selected by experience. The wrap angle is one of the key structural parameters that affect the performance of the plastic centrifugal pump. In existing studies, three-dimensional models are used for numerical simulation to determine the value of the wrap angle. However, numerical simulation is complex and not widely used in engineering. Most workers engaged in the plastic

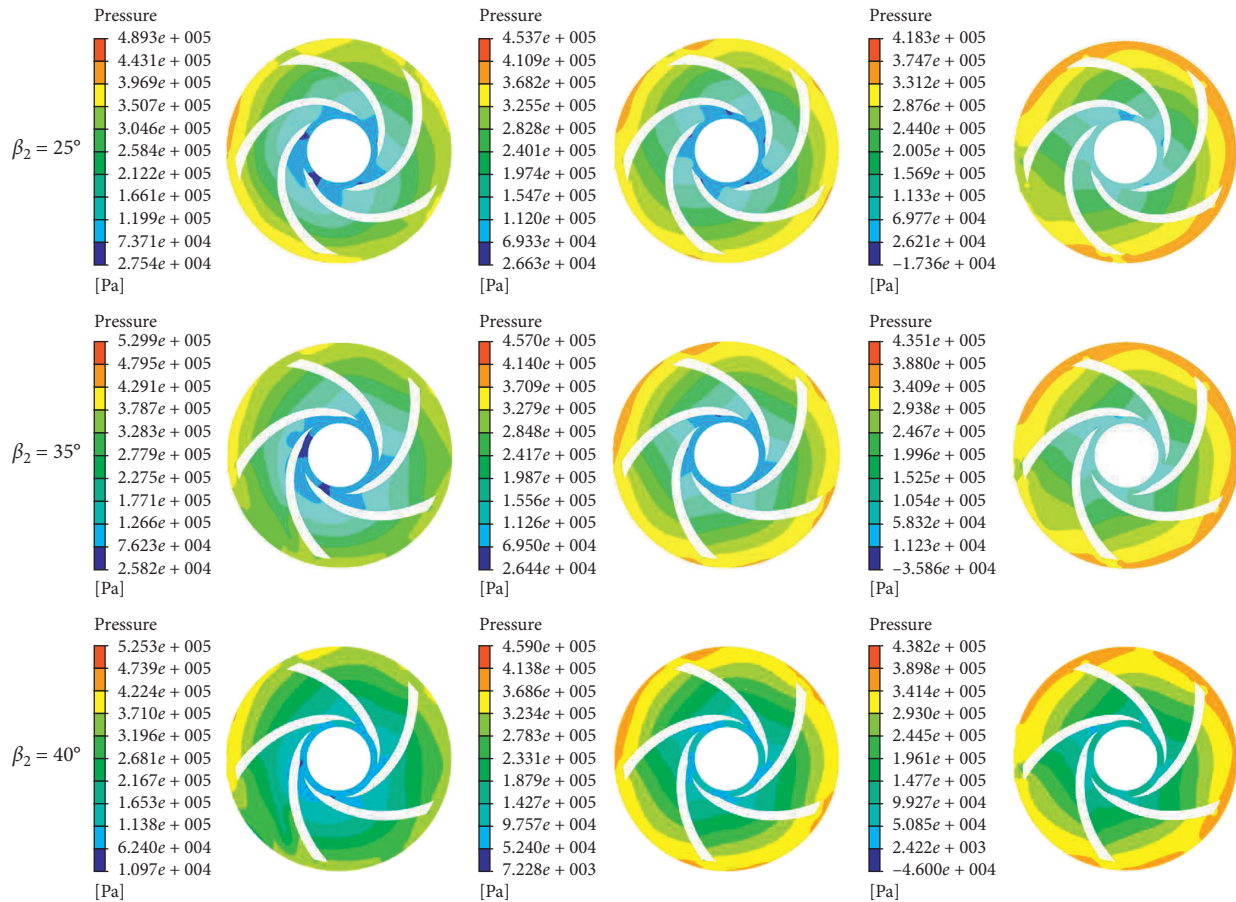


FIGURE 12: Pressure cloud chart with different outlet angles.

centrifugal pump still face great obstacles in numerical simulation [15, 16]. In this paper, the wrap angle design of the plastic centrifugal pump is considered to be related to the inlet and outlet parameters of the plastic centrifugal pump, and the functional relationship between the wrap angle and the inlet and outlet parameters is established, which makes the wrap angle design reasonable. Based on the above considerations, this paper proposes a design method of the wrap angle, which establishes the functional relationship between the inlet angle, outlet angle, and wrap angle of the plastic centrifugal pump. Figure 17 is the design diagram of the wrap angle.

In the design of impeller structural parameters, some experience parameters are often needed, and these experience parameters were first proposed by [17, 18]. According to Stepanoff velocity modulus, it can be found from Figures 7–9 in [19] that when the  $n_s = 60.871$  and  $K_{MI} = 0.128$ , the wrap angle is  $\varphi = 122.2^\circ$ .

**5.1.1. Research on the Influence of Blade Wrap Angle on the External Characteristics of Plastic Centrifugal Pump.** Figure 18 shows the external characteristic curve of the plastic centrifugal pump under six different wrap angles. It can be seen from Figure 18(a) that, under the design condition, other parameters are unchanged and only the wrap angle of the blade is changed.

It can be seen from Figure 18(b) that the trend of  $Q-H$  curve changes more and more steeply with the increase of the wrap angle. According to Figure 18(c), when  $\varphi = 110^\circ$ , the  $P$  is the largest. When  $\varphi$  is larger than  $110^\circ$ , the  $P$  decreases with the increase of the wrap angle.

In summary, when the  $Q$  is small, the impeller flow channel diffuses, and boundary layer separation is prone to occur during fluid flow, which leads to the lower hydraulic efficiency of the plastic centrifugal pump. With the increase of the wrap angle, the blade becomes longer, the impeller flow channel diffuses better, and the possibility of flow separation in the impeller decreases gradually. However, when the wrap angle continues to increase, the friction loss in the plastic centrifugal pump increases, and the  $H$  curve will decrease more and more steeply.

**5.1.2. Influence of Blade Wrap Angle on Internal Flow Field of Plastic Centrifugal Pump.** Figure 19 shows the pressure cloud chart of the impeller model section under different working conditions ( $0.6Q$ ,  $Q$ , and  $1.4Q$ ). It can be seen that the pressure on the pressure surface of the blade is greater than that on the suction surface pressure when the fluid in the impeller flows under the same radius and the reverse pressure gradient; under the same wrap angle, with the increase of  $Q$ , the overall pressure of the impeller presents a downward trend, and the pressure distribution under the

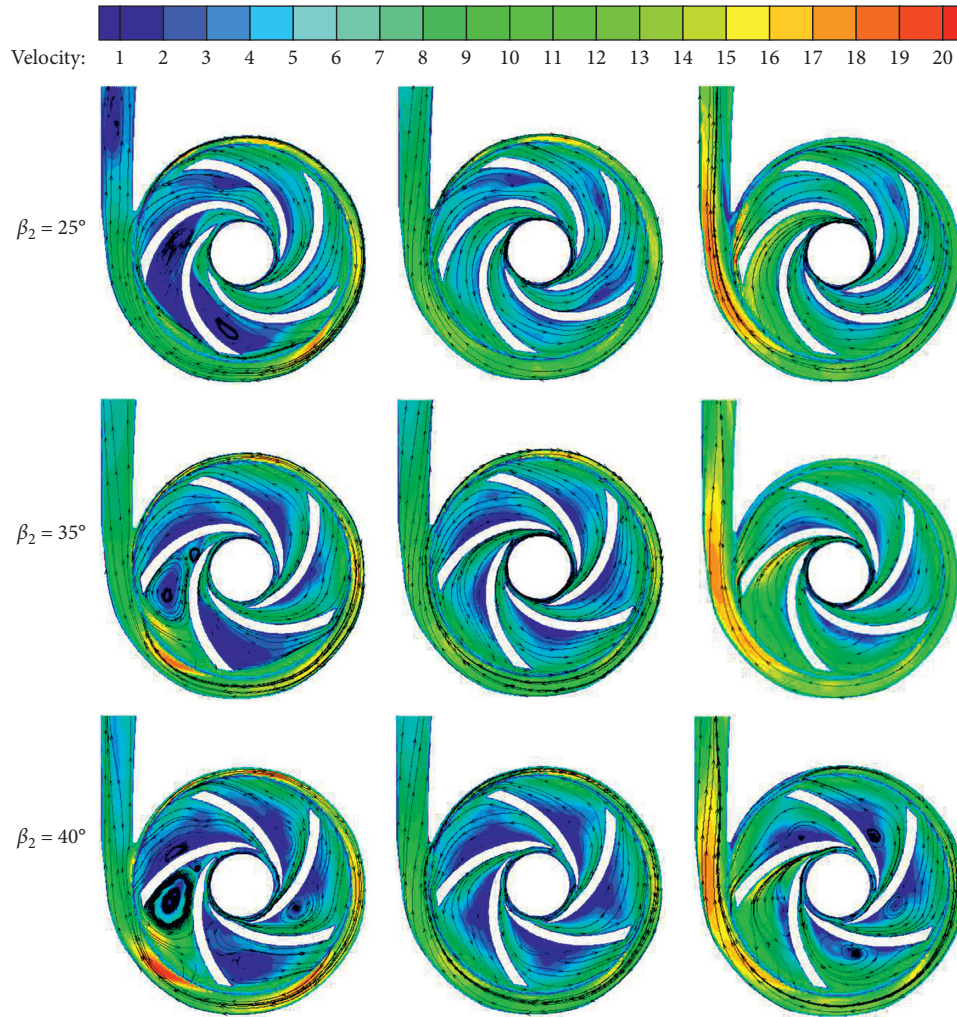


FIGURE 13: Velocity cloud chart with different outlet angles.

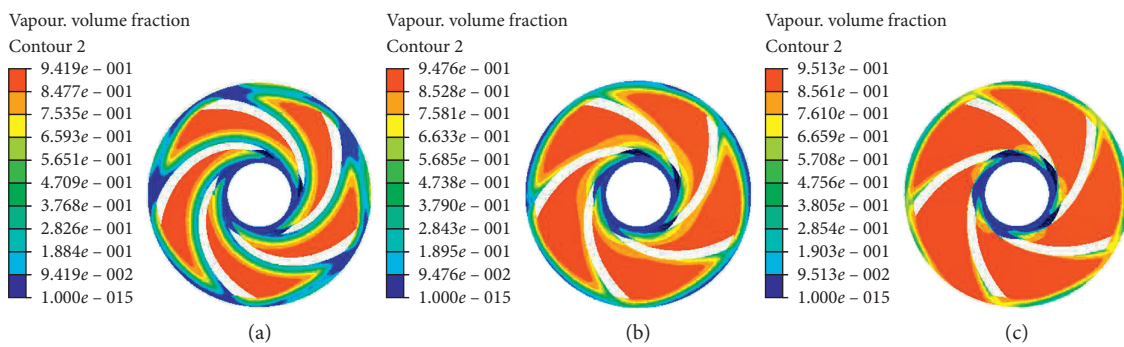


FIGURE 14: Gas volume fraction chart with different outlet angles. (a)  $\beta_2 = 25^\circ$ . (b)  $\beta_2 = 35^\circ$ . (c)  $\beta_2 = 40^\circ$ .

design working condition is more uniform than that under the off-design working condition. At the same working point, with the increase of the wrap angle, the low pressure area at the impeller inlet increases, the pressure gradient decreases gradually, and the pressure distribution is more uniform.

When the plastic centrifugal pump is running under the condition of small  $Q$ , the inlet pressure of the impeller

increases gradually, and the range of low pressure area increases. When  $\varphi = 140^\circ$  and  $\varphi = 150^\circ$ , the pressure distribution in the impeller is more uniform than that in other impeller; when it is running under the design working condition, the inlet pressure of the impeller increases gradually, when  $\varphi$  increases to  $140^\circ$ , the inlet pressure of the impeller is the largest, and when  $\varphi$  increases to  $150^\circ$ , the inlet pressure begins to decrease; when it is running under the

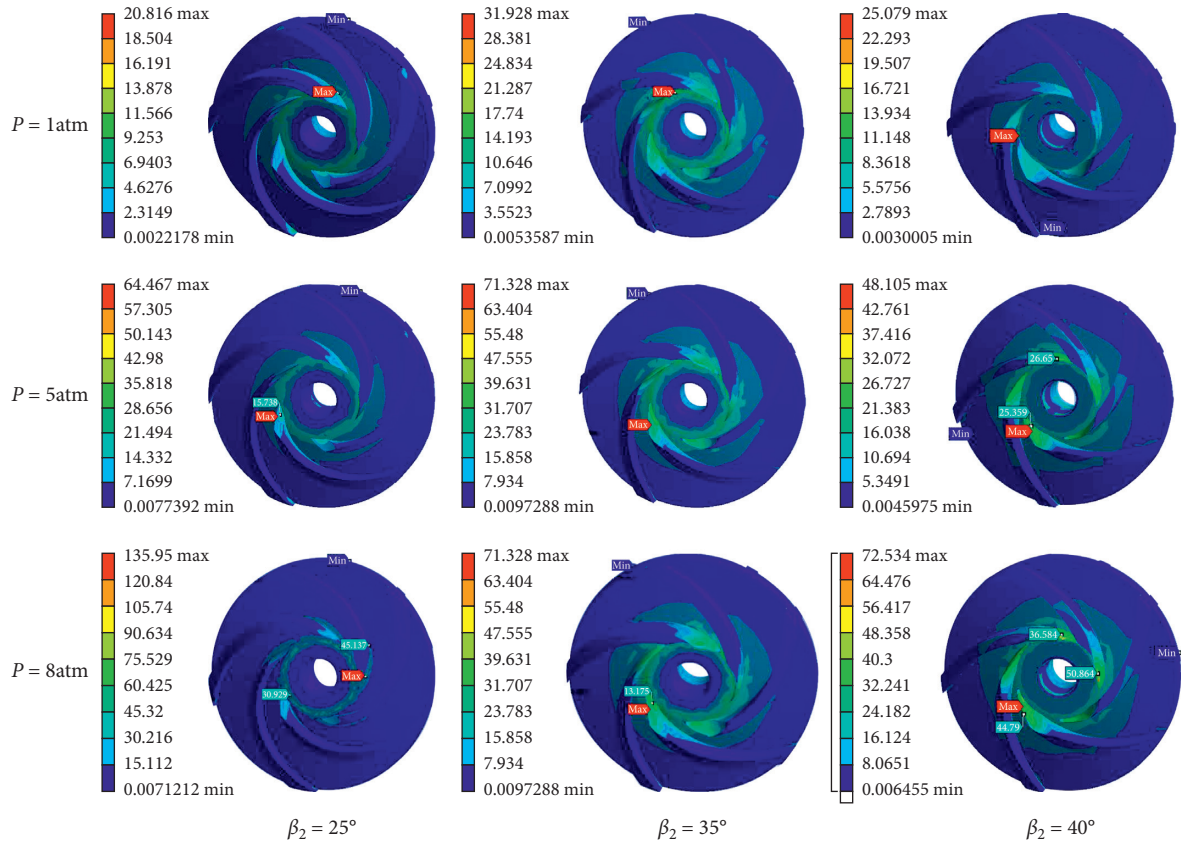


FIGURE 15: The equivalent stress diagram of each impeller under different fluid loads.

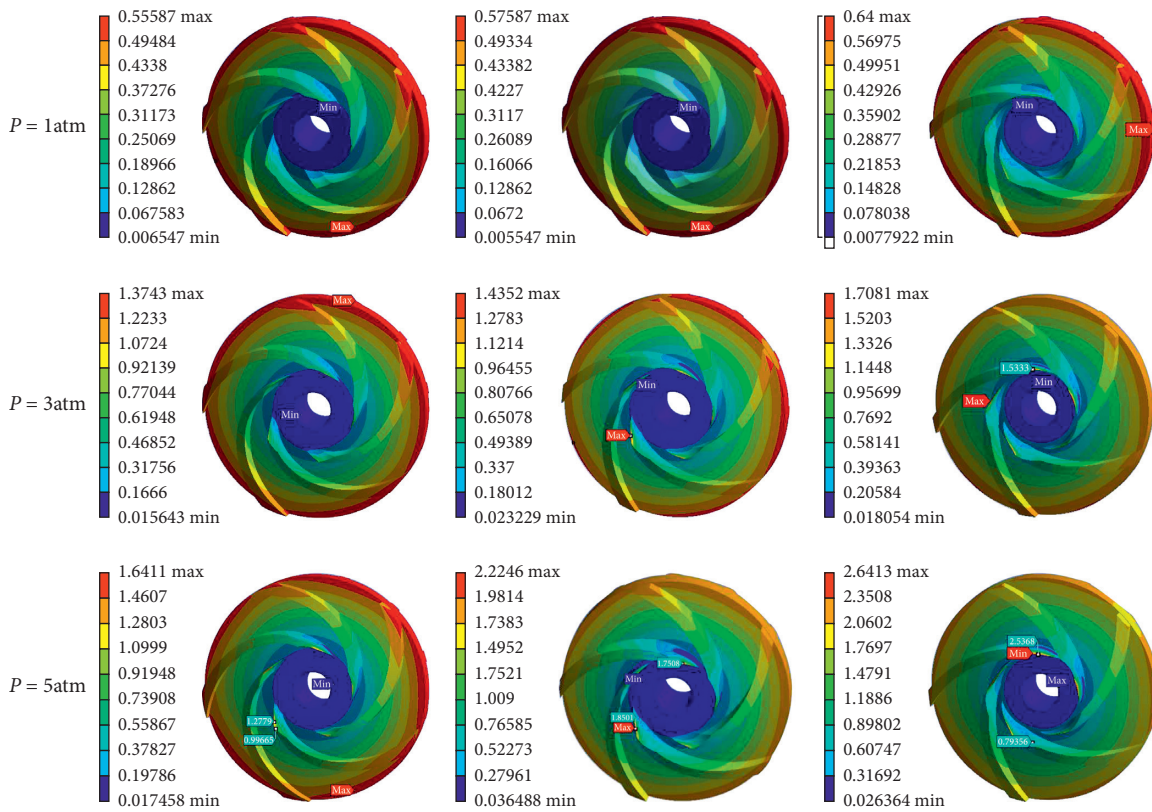


FIGURE 16: Impeller deformation under different outlet angles.

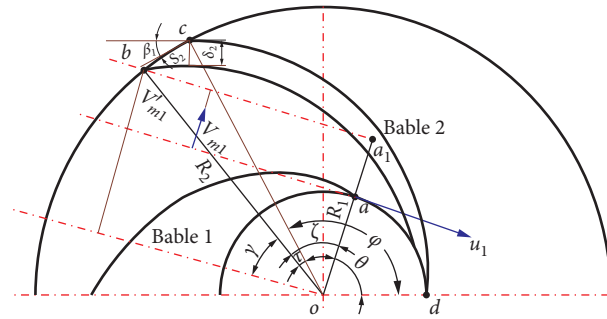


FIGURE 17: Design diagram of the wrap angle.

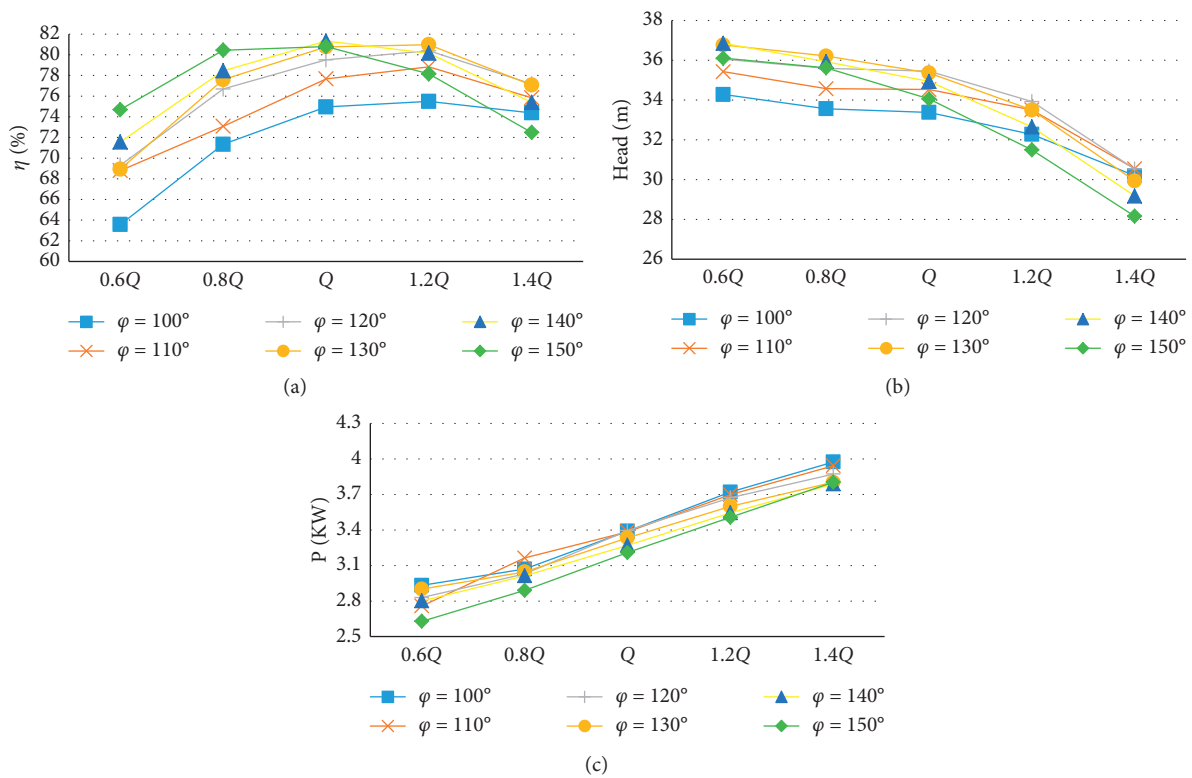


FIGURE 18: External characteristic curve of the plastic centrifugal pump under different wrap angles.

condition of large  $Q$ , the uneven pressure distribution on the impeller is obvious, and the change trend of impeller inlet pressure is basically consistent with the design working condition.

It can be seen from Figure 20 that the internal flow of impellers with different wrap angles meets the following laws: the internal velocity in impellers increases continuously from the inlet to the outlet, and with the increase of  $Q$ , the internal velocity in impellers becomes more uniform and the flow is more stable. The smaller the  $Q$  is, the greater the flow gradient is and the worse the performance of the plastic centrifugal pump is. The larger the  $Q$  is, the more uniform the velocity change is.

Under the condition of small  $Q$ , the uneven velocity in the impeller flow channel near the volute tongue is more obvious. Influenced by the impact of the volute tongue, a large number of low-speed vortex and backflow appear in

the impeller flow channel. With the increase of the wrap angle, the vortex and backflow phenomenon are improved.

Under the working condition, when  $\varphi = 110^\circ$ , due to the short flow channel and serious diffusion, the turbulent flow causes a lot of backflow and vortex in the impeller flow channel near the volute tongue, which leads to a lot of hydraulic loss and reduces the hydraulic efficiency of the plastic centrifugal pump. With the increase of the wrap angle, fluid flows smoothly in the plastic centrifugal pump, vortex, and backflow decrease, and the hydraulic efficiency of the plastic centrifugal pump is improved.

Under the condition of large  $Q$ , the flow in the impeller is obviously improved. With the increase of the wrap angle, the wake area in the blade decreases, and the flow separation phenomenon is improved. However, when the wrap angle  $\varphi$  increases to  $140^\circ$  and  $150^\circ$ , the low-speed area in the flow channel decreases, and the overall flow velocity in the flow

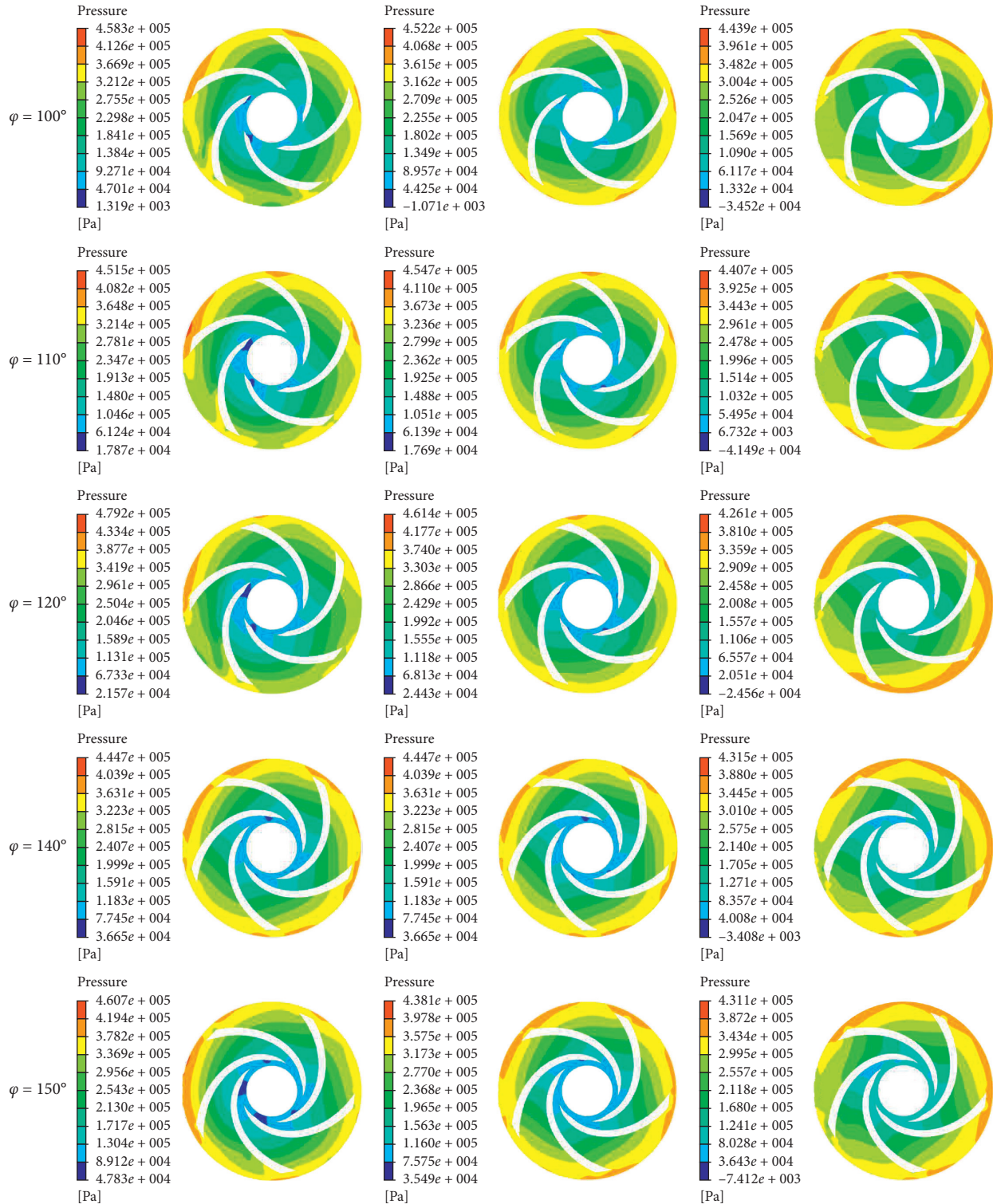


FIGURE 19: Pressure cloud chart of the impeller model section.

channel increases, which increases the friction resistance loss and reduces the efficiency of the plastic centrifugal pump.

5.1.3. Influence of Blade Wrap Angle on Impeller Deformation Based on Fluid-Structure Interaction. Figure 21 is the

impeller deformation with different wrap angles when the plastic centrifugal pump is working under normal pressure. It can be seen that when  $\varphi = 100^\circ$ , the maximum deformation on the impeller is 0.91441 mm, the maximum deformation at the outlet of the blade suction surface profile is 1.0231 mm, and the minimum deformation at the blade inlet is

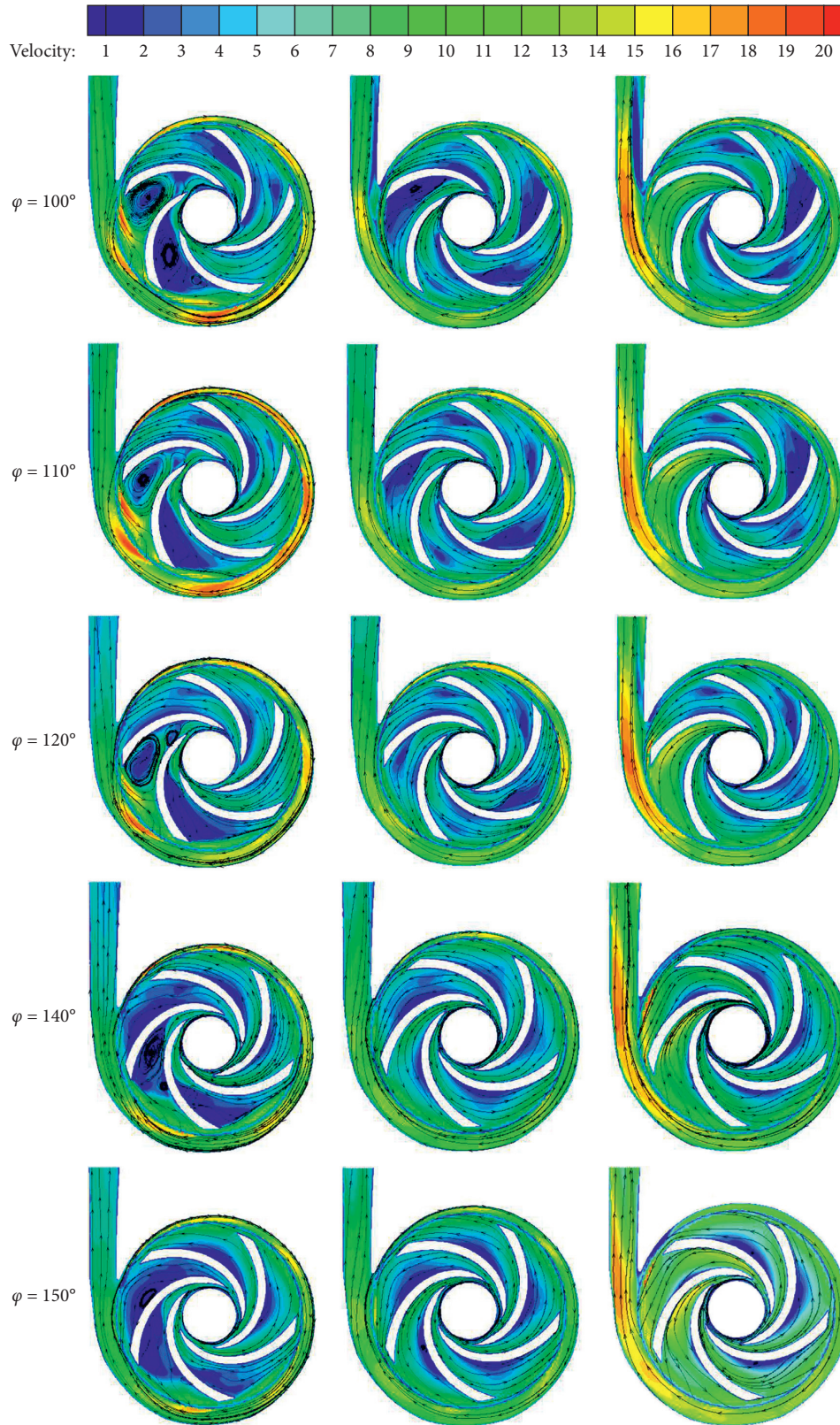


FIGURE 20: Velocity cloud chart and streamline chart of the impeller.

0.15362 mm. With the increase of the wrap angle, the deformation on the impeller decreases. When  $\varphi = 120^\circ$ , the maximum deformation on the impeller is 0.53984 mm, and the minimum deformation at the blade inlet is 0.065317 mm,

which is basically consistent with the maximum deformation of the impeller when  $\varphi = 130^\circ$  and  $\varphi = 140^\circ$ . However, when the wrap angle of the impeller increases to  $150^\circ$ , due to the uneven pressure distribution, the deformation of the

impeller presents obvious asymmetry, and the maximum deformation of the impeller is 0.96362 mm and the minimum deformation is 0.13622 mm.

## 5.2. Research on the Influence of Blade Inlet Angle on the Performance of Plastic Centrifugal Pump

**5.2.1. Design of Blade Inlet Angle.** In order to study the influence of the blade inlet angle on the performance of the plastic centrifugal pump, this chapter relates the design of the blade inlet angle with other structural parameters of the blade and proposes a design method of the blade inlet angle. In the conventional design, when calculating the fluid flow angle, the inlet without prerotation is considered for design [20]. In this paper, the factors of inlet prerotation are taken into account, and the segment between points  $a$  and  $b$  is determined as the absolute velocity direction, and the inlet angle under the corresponding wrap angle is calculated (the following inlet angles do not include the impact angle). Figure 22 is a schematic diagram of blade geometric parameters.

According to the research in Section 4.1, the wrap angle is  $\varphi = 122.2^\circ$ , and the inlet angle  $\beta_1 = 7^\circ$  is calculated from Figure 22.

It can be seen from the above that the design of the inlet angle is related to the wrap angle and the outlet angle. When the outlet angle is constant, the inlet angle is changed, and the blade wrap angle is also changed. As shown in Figure 23, when  $\beta_1 = 0$  and  $\alpha_1 = 180^\circ$ , the corresponding wrap angle is

$$\varphi = a \cos\left(\frac{R_2}{R_1}\right) + \theta - \tau. \quad (4)$$

Substitute the value  $\varphi = 129.8473^\circ$ .

In the actual process, the  $V_{m1}$  is impossible to be 0, so the wrap angle  $\varphi < 129.8473^\circ$ . According to the research results in Section 4.1, when  $\varphi > 130^\circ$ , the performance of the plastic centrifugal pump with  $\varphi = 140^\circ$  does not increase compared with that of the plastic centrifugal pump with  $\varphi = 130^\circ$ . When  $\varphi = 150^\circ$ , the performance of the plastic centrifugal pump decreases, which is consistent with the research here.

From Figure 24, according to the relationship between velocity components, when  $\varphi = \theta - \tau$  and  $\varphi = 60.6319^\circ$ , the value of the inlet angle is

$$\beta_1 = a \tan\left(\frac{v_{m1}}{u_1}\right). \quad (5)$$

By substituting the data, we can get  $\beta_1 = 15.3426^\circ$ .

According to the above research, six groups of impeller models can be preliminarily established, as shown in Table 3.

For the impeller models in Table 3, it is found in the process of drawing the impeller model that when the thickness of the inlet and outlet remains unchanged and the thickness is uniformly thickened from the inlet to the outlet, if  $\varphi \leq \theta - \tau$  ( $\varphi \leq 60.6319^\circ$ ), there is no intersection between the suction surface profile of the blade and the outer diameter of the impeller, and the blade profile does not converge, so the value range of the blade inlet angle is  $0 < \theta < 15.3426^\circ$  and the range of the wrap angle corresponding to the blade inlet angle is

$60.6319^\circ < \varphi < 129.8473^\circ$ . It can be seen from the actual drawing that when the inlet angle reaches  $14.5^\circ$ , the blade profile is not convergent, so the range of the above angle needs further study.

**5.2.2. Influence of Blade Inlet Angle on Internal Flow Field in Plastic Centrifugal Pump.** In order to study the influence of the inlet angle on the performance of the pump, this paper establishes several groups of models for numerical simulation according to different angles and uses ANSYS CFX to simulate the flow field. Table 4 is the external characteristic parameter obtained by the simulation of the design model under the working condition. It can be seen from Table 4 that when the outlet angle is constant, the absolute speed direction of the inlet is changed, and the inlet angle increases gradually, and the efficiency and head of the plastic centrifugal pump decrease.

Take  $\beta_2 = 30^\circ$  as an example, analyze the internal velocity cloud chart of the impeller with different inlet angles, as shown in Figure 25. It can be seen that, with the increase of the inlet angle, the low velocity area on the pressure surface of the blade becomes more obvious, the possibility of boundary layer separation increases, the low velocity area on the suction surface of the blade becomes larger, resulting in a large number of vortices and flow separation, and the structure of jet wake in the impeller increases. The main reason is that the increase of the inlet angle causes weakness of the blade on fluid control.

**5.2.3. Research on the Influence of Blade Inlet Angle on the Structural Characteristics of the Impeller of Plastic Centrifugal Pump.** Figure 26 shows the deformation of impeller models with different inlet angles under constant pressure load of  $\beta_2 = 30^\circ$ . It can be seen from the figure that, under normal pressure load, with the increase of the inlet angle, the blade deformation decreases and then increases. When  $\beta_1 = 7^\circ$ , the load on the impeller is obviously uneven, the maximum deformation reaches 0.97388 mm, and the maximum deformation of the blade inlet is about 0.3 mm; when  $\beta_1 = 13^\circ$ , the maximum deformation of the blade is about 0.57258 mm, the overall deformation is significantly reduced, but the deformation of the blade inlet increases about 0.3 mm; with the further increase of the blade inlet angle, the overall deformation of the impeller continues to increase, when  $\beta_1 = 14^\circ$ , the impeller inlet bears the maximum load, and the deformation reaches 0.81869 mm.

## 6. Optimization of Blade Angle Based on Hydraulic Loss

**6.1. Optimization of Blade Angle Based on Hydraulic Loss.** In order to find the optimal outlet angle and the added impact angle, this paper takes the minimum hydraulic loss and cavitation loss in the impeller as the objective to establish an optimization model for optimization. In [21], the hydraulic loss in the impeller is divided into five kinds, and the loss coefficient under different  $N_s$  is obtained according to linear regression, which improves the accuracy of hydraulic loss calculation. Because the blade angle has obvious influence on the cavitation of the plastic centrifugal pump,

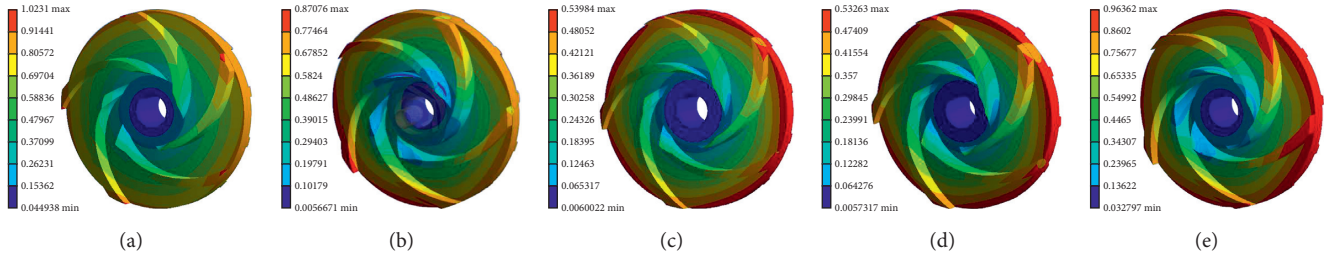


FIGURE 21: Impeller deformation with different wrap angles. (a)  $\varphi = 100^\circ$ . (b)  $\varphi = 110^\circ$ . (c)  $\varphi = 120^\circ$ . (d)  $\varphi = 140^\circ$ . (e)  $\varphi = 150^\circ$ .

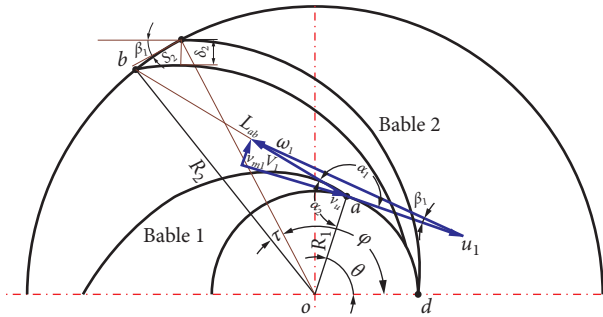


FIGURE 22: Schematic diagram of blade geometric parameters.

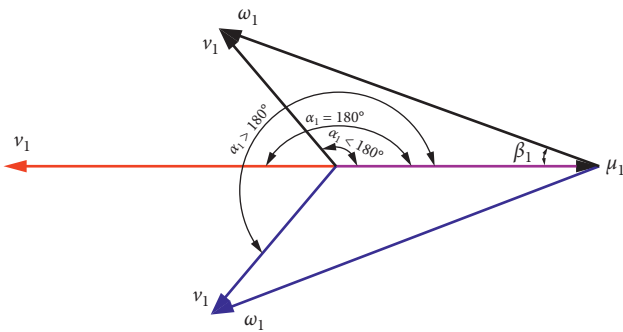


FIGURE 23: Schematic diagram for determination of the range of the inlet angle.

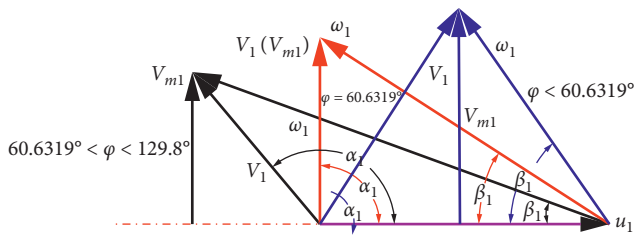


FIGURE 24: Inlet speed triangle under different inlet setting angles.

only optimizing the efficiency cannot guarantee its cavitation performance. If we want to reduce the *NPSH* of the plastic centrifugal pump, we usually change the inlet diameter of the plastic centrifugal pump and the blade angle, so we still need to introduce the minimum objective function

TABLE 3: Parameters of impeller models.

Model	Inlet angle $\beta_1$ ( $^\circ$ )	Wrap angle $\varphi$ ( $^\circ$ )
Model 1	7	122.3022
Model 2	9	117.5788
Model 3	11	109.4721
Model 4	13	93.8815
Model 5	14	81.2838
Model 6	15.3426	60.6319
Model 7	16	51.1620

of cavitation. In this paper, we use the method of the weight coefficient to deal with the multiobjective function. For the weight of each objective, the efficiency is twice as much as cavitation, and the inlet angle and outlet angle are selected as optimization variables. The range of the outlet angle is

$$15^\circ \leq \beta_2 \leq 40^\circ. \quad (6)$$

According to the calculation, the range of the inlet angle is

$$6^\circ \leq \beta_1 \leq 35^\circ. \quad (7)$$

Use MATLAB to program and get the optimized data, as shown in Table 5.

Based on the hydraulic loss, taking the highest hydraulic efficiency and the minimum *NPSH* as the objective function, the optimal angles are  $\beta_1 = 19^\circ$  and  $\beta_2 = 33^\circ$ .

## 7. Experimental Verification

In order to verify the effect of the blade angle on the performance of the plastic centrifugal pump, several points were selected and 3D models were printed.

**7.1. Impeller Model Printing.** In order to verify the performance of the design models and summarize the influence of the blade angle on the performance of the pump from the experiment, this paper used 3D printing technology to print out the impeller models of the plastic centrifugal pump and carried out the performance experiments on the models. Table 6 is the performance table of 3D material (*UTR9000*), and Figure 27 is the impeller models printed by 3D printing technology.

The printing impellers were operated on the test bench for 4 hours, there was no obvious wear and damage on the impeller appearance, and the impeller strength met the requirements.

TABLE 4: External characteristic parameter under different model working conditions.

Number	Outlet angle $\beta_2/^\circ$	Inlet angle $\beta_1/^\circ$	Wrap angle $\varphi/^\circ$	Hydraulic efficiency $\eta_h/(\%)$	Head H/m	Shaft power P/kW
1	25	7	120.1309	78.2025	34.9143	3.3992
2		9	115.4908	77.319	34.2364	3.37129
3		11	107.3851	75.8128	33.2508	3.33928
4		13	91.7944	73.1623	32.3427	3.36576
5	30	7	122.3022	78.6326	35.5208	3.43933
6		9	117.5788	77.5703	35.1021	3.44634
7		11	109.4721	74.6859	33.1619	3.38061
8		13	93.8815	73.2596	32.4081	3.36808
9	35	14	81.2838	71.9816	32.8627	3.47597
10		7	123.7650	79.7254	35.5934	3.3913
11		9	119.0406	77.6532	35.6254	3.49296
12		11	110.9349	76.7474	35.315	3.50339
13	40	13	95.3443	72.6208	33.1782	3.47845
14		14	82.7465	71.8342	33.1818	3.51692
15		15	67.4184	73.1426	34.5774	3.59928
16		7	124.8358	76.545	36.0313	3.5839
17	40	9	120.1115	75.8269	35.4806	3.56256
18		11	112.0058	74.915	35.1326	3.57056
19		13	96.4151	73.1767	34.1683	3.55503
20		14	83.8174	71.1099	32.6869	3.45837
21		15	68.4893	72.2672	35.2507	3.71381

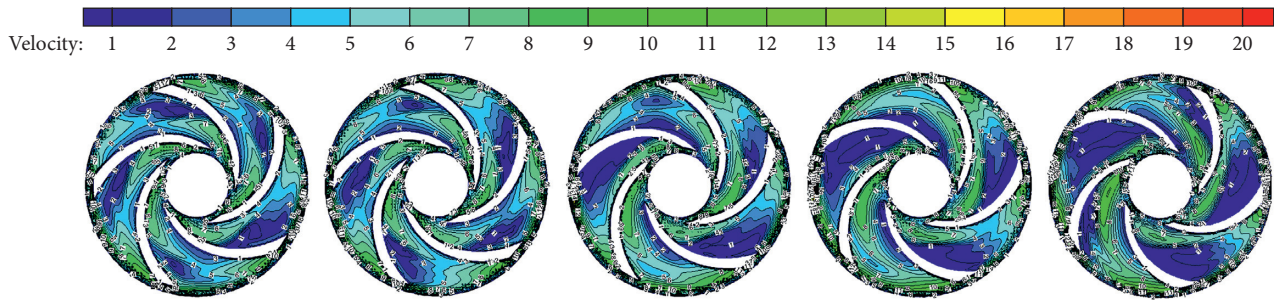


FIGURE 25: Velocity cloud chart of the impeller with different inlet angles.

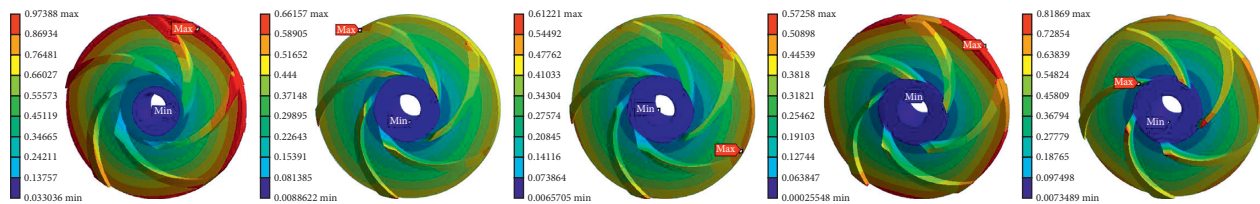


FIGURE 26: Cloud chart of impeller deformation under different inlet angles.

TABLE 5: Optimization results of the blade angle of the plastic centrifugal pump.

Parameter	$\beta_1 (^\circ)$	$\beta_2 (^\circ)$	$\Phi (^\circ)$
After optimization	19	33	123

## 7.2. Performance Experiments of Plastic Centrifugal Pump

7.2.1. Data Analysis. According to the above impeller models, external characteristic experiments were carried out, respectively, and the fitting data are shown in Figure 28.

It can be seen that when the outlet angle  $\beta_2$  is constant, the performance parameters of the plastic centrifugal pump basically increase first and then decrease with the increase of the inlet angle  $\beta_1$ . With the increase of the outlet angle and inlet angle, the optimal performance of the plastic

TABLE 6: Performance parameters of 3D printing materials.

	Performance parameter	Numerical value
Mechanical properties of cured materials	Density (g/cm <sup>3</sup> )	1.16
	Thermal deformation temperature (°C)	52
	Tensile strength (MPa)	27~31
	Bending strength (MPa)	69~74

Note: in the figure, the first number represents the size of the inlet angle ( $7^\circ \leq \beta_1 \leq 15^\circ$ ), the second number represents the size of the outlet angle ( $25^\circ \leq \beta_2 \leq 40^\circ$ ), and the third number represents the size of the wrap angle.

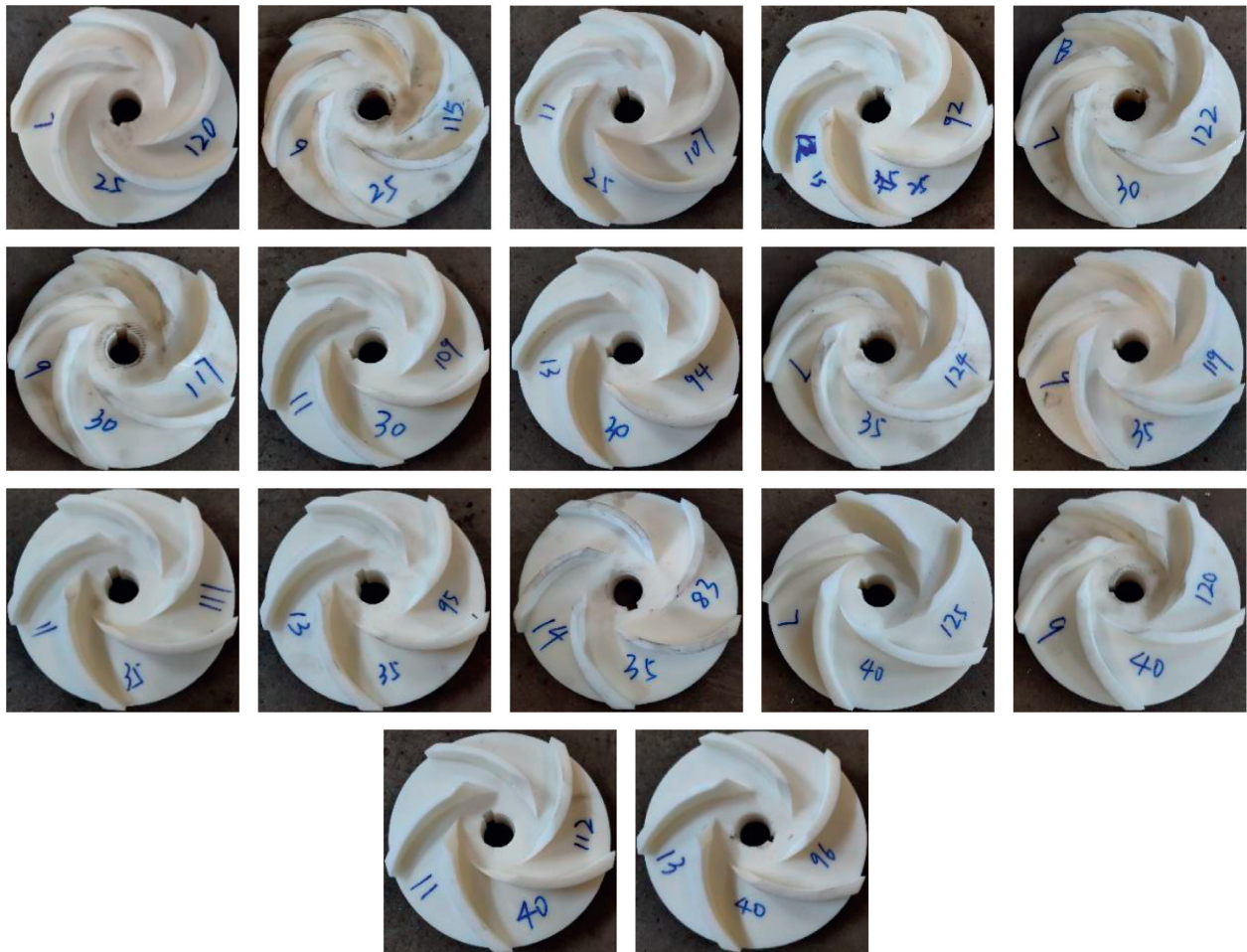


FIGURE 27: 3D printing impeller models of the impeller.

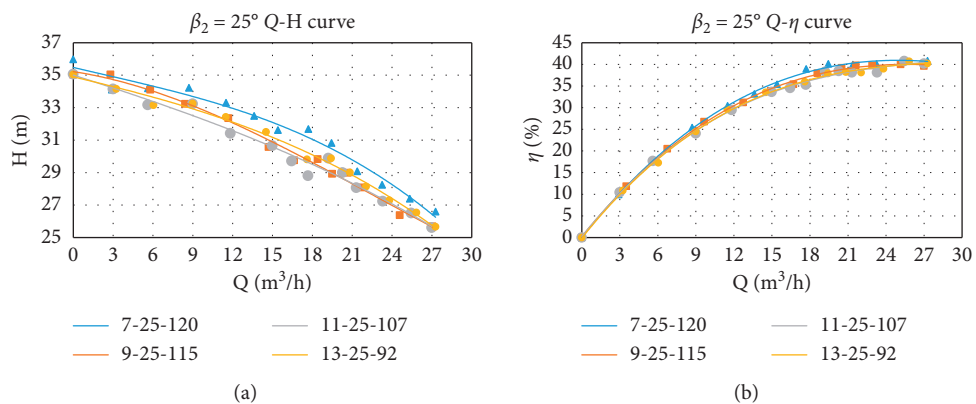


FIGURE 28: Continued.

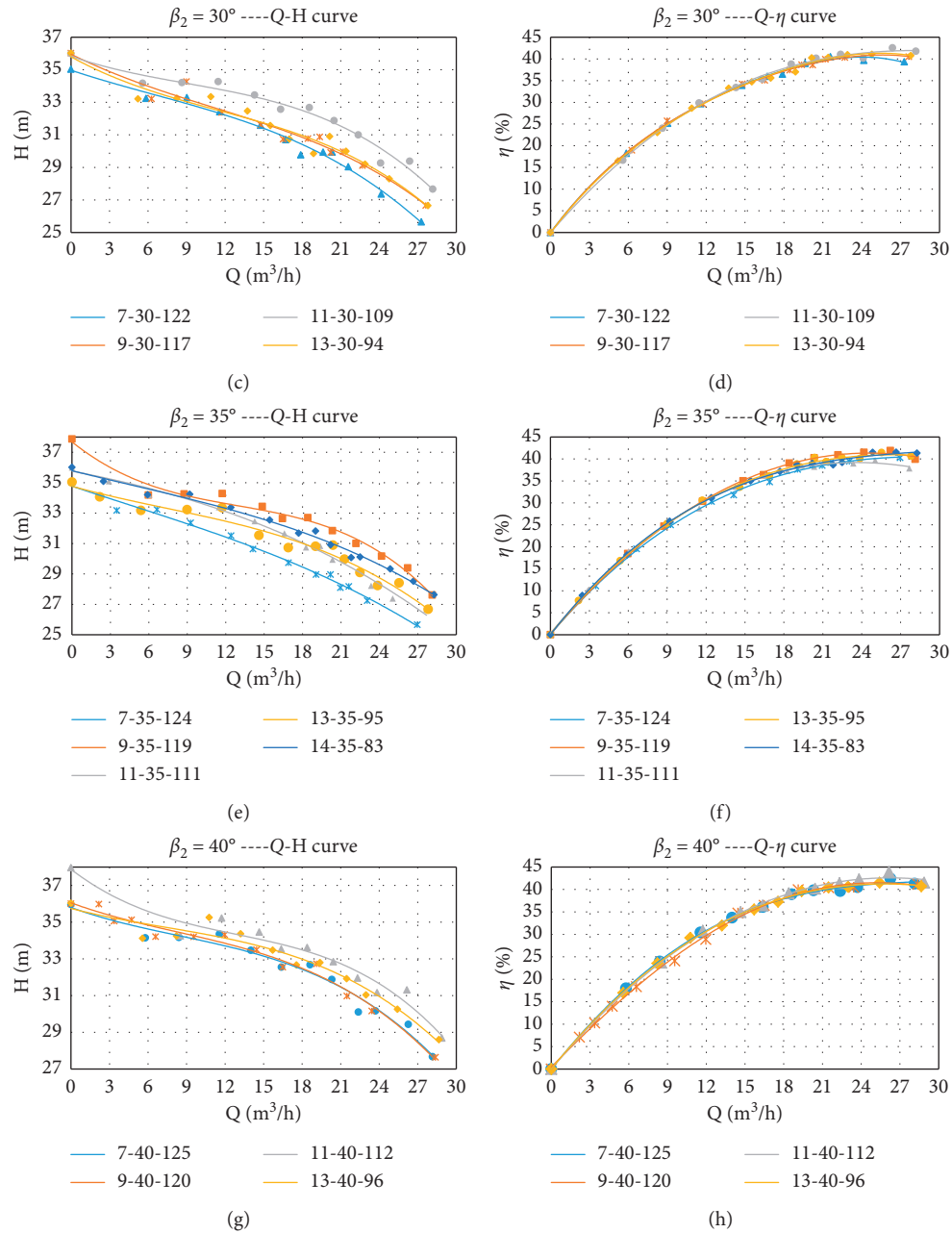


FIGURE 28: External characteristic curve of the plastic centrifugal pump.

centrifugal pump can be guaranteed. Of course, we can also adopt other methods, such as the development of an environment-friendly marine antifouling paint proposed by Gu et al. [22], which can be used to reduce the wear of the plastic centrifugal pump.

## 8. Conclusion

The blade angle of the plastic centrifugal pump is the key structural parameter that affects the performance of the plastic centrifugal pump. In the current research, the design of the blade angle of the plastic centrifugal pump is not effectively related to other structural parameters, and the

relationship between the blade angle and performance parameters of the plastic centrifugal pump is more irregular. This paper studies the effect of the blade angle on the performance of the plastic centrifugal pump combined with experiments based on fluid-structure interaction. The main research results of this paper are as follows:

- (1) The simulation results of the internal flow field were analyzed. When the plastic centrifugal pump worked under the off-design working condition, the flow field pressure distribution and velocity distribution were obviously uneven. When it worked at the small  $Q$  condition, there was vortex in the impeller flow channel, the hydraulic performance of the plastic centrifugal

pump was low, and the flow in the impeller improved with the increase of the  $Q$ . After the cavitation analysis of the plastic centrifugal pump, when the pressure dropped to 1 atm, the bubble filled the whole flow channel, the gas volume fraction reached 0.945, and serious cavitation occurred in the plastic centrifugal pump. Based on ANSYS Workbench, the influence of different fluid loads on the structural characteristics of the impeller under the working conditions was studied. The results showed that the deformation of the impeller was basically axisymmetric distribution, and the deformation gradually increased from the impeller inlet to the impeller outlet. When the impeller bore the pressure of about 5 atm, the impeller structure was destroyed.

- (2) Under the working condition, when the outlet angle was  $35^\circ$ , the plastic centrifugal pump could reach the highest efficiency of 81.0161% and the highest  $H$  of 35.8029 m. When the outlet angle continued to increase, the efficiency and  $H$  of the plastic centrifugal pump would decrease. According to the analysis of the internal flow field, it was found that, with the increase of the outlet angle, the low pressure area at the inlet of the impeller increased obviously and the pressure gradient decreased. However, when the outlet angle increased to  $40^\circ$ , the pressure distribution at the inlet of the impeller was not uniform, and the overall cavitation performance of the impeller changed. After one-way fluid-structure interaction, it was found that, under the same working pressure, the maximum deformation of the impeller caused by flow field load at different outlet angles increased with the increase of the outlet angle, and the difference increased with the increase of working pressure of the plastic centrifugal pump.
- (3) With the increase of the inlet angle, the efficiency and  $H$  of the plastic centrifugal pump showed a decreasing trend. According to the results of internal flow field analysis, the low-speed area on the pressure surface and suction surface of the blade expands, resulting in a large number of vortices and flow separation. According to the results of fluid-structure interaction, under the normal pressure load, the deformation of the blade first decreased and then increased. When  $\beta_1 = 13^\circ$ , the deformation of the blade was the most small, 0.57258 mm.

### Data Availability

The data used to support the findings of this study are included within the article.

### Conflicts of Interest

The authors declare that they have no conflicts of interest.

### Acknowledgments

This article belongs to the project of the “The University Synergy Innovation Program of Anhui Province” (GXXT-2019-004) and “Teaching Research Project of Anhui Education Department” (2019jyxm0229).

### References

- [1] X. Yang, “Analysis of the current situation and development direction of domestic plastic centrifugal pump,” *Chemical Equipment Technology*, vol. 36, no. 6, pp. 44–46, 2015.
- [2] W. Guo, *Analysis of Unsteady Flow and Vibration Characteristics of Low Specific Speed Centrifugal Pump Based on Two-Way Fluid Solid Coupling*, Zhejiang University of Technology, Hangzhou, China, 2017.
- [3] H. Liu, H. Xu, X. Wu et al., “Effect of fluid solid coupling on internal and external characteristics of centrifugal pump,” *Journal of Agricultural Engineering*, vol. 28, no. 13, pp. 82–87, 2012.
- [4] H. Wang, D. Zhang, W. Shi, and L. Zhang, “Structural analysis and optimization of centrifugal pump volute based on fluid solid coupling,” *Journal of Drainage and Irrigation Machinery Engineering*, vol. 32, no. 6, pp. 472–476, 2014.
- [5] S. Huang, X. Zhang, X. Su, and G. Qu, “Fluid structure coupling analysis based on the whole flow field of centrifugal pump,” *Fluid Machinery*, vol. 43, no. 11, pp. 38–42, 2015.
- [6] G. Fontanals and E. Alfred, “Numerical study of the fluid-structure interaction in the diffuser passage of a centrifugal pump,” *Computational Methods for Coupled Problems Inence & Engineering IV*, vol. 30, no. 6, pp. 986–995, 2011.
- [7] L. Zheng, “Design and experimental research of plastic chemical centrifugal pump,” *Rubber Technology and Equipment*, vol. 42, no. 12, pp. 89–90, 2016.
- [8] L. Tang, M. Liu, and F. Ma, “Thermosetting coupling analysis and parameter optimization of the plastic lining pump structure,” *Advances in Materials Science and Engineering*, vol. 2019, pp. 1–15, 2019.
- [9] Y. Wang and X. Huo, “Multiobjective optimization design and performance prediction of centrifugal pump based on orthogonal test,” *Advances in Materials Science and Engineering*, vol. 2018, pp. 1–10, 2018.
- [10] Y. Gu, S. Yu, J. Mou, D. Wu, and S. Zheng, “Research progress on the collaborative drag reduction effect of polymers and surfactants,” *Materials*, vol. 13, no. 2, p. 444, 2020.
- [11] Y. Jing, J. Zhang, M. He, and T. Wang, “Profile equation of cylindrical blade with controllable wrap angle of centrifugal pump,” *Irrigation and Drainage Machinery*, vol. 2008, no. 5, pp. 46–49, 2008.
- [12] J. Zheng, C. Yang, L. Zhu, and N. Jia, “Rotating solid coupling analysis of centrifugal pump blades,” *Fluid Machinery*, vol. 41, no. 2, pp. 25–29, 2013.
- [13] M. Bongert, J. Wüst, M. Geller et al., “Comparison of two biological aortic valve prostheses inside patient-specific aorta model by bi-directional fluid-structure interaction,” *Current Directions in Biomedical Engineering*, vol. 4, no. 1, pp. 59–62, 2018.
- [14] S. Kim, U.-B. Jeong, K.-Y. Lee, J.-H. Kim, J.-Y. Yoon, and Y.-S. Choi, “Multi-objective optimization for mixed-flow pump with blade angle of impeller exit and diffuser inlet,” *Journal of Mechanical Science and Technology*, vol. 31, no. 11, pp. 5099–5106, 2017.
- [15] Y. Bai, F. Kong, S. Yang, K. Chen, and T. Dai, “Effect of blade wrap angle in hydraulic turbine with forward-curved blades,” *International Journal of Hydrogen Energy*, vol. 42, no. 29, pp. 18709–18717, 2017.
- [16] J. Du, H. Yang, and Z. Shen, “Study on the impact of blades wrap angle on the performance of pumps as turbines used in water supply system of high-rise buildings,” *International Journal of Low-Carbon Technologies*, vol. 13, no. 1, pp. 102–108, 2018.

- [17] J. Stepanoff, *Centrifugal and Axial Pumps*, John Wiley & Sons, New York, NY, USA, 1957.
- [18] Z. Pan, Y. Cao, W. Cao, and Y. Ni, "Selection principle of design coefficient of centrifugal impeller," *Irrigation and Drainage Machinery*, vol. 2008, no. 3, pp. 34–38, 2008.
- [19] X. Guan, *Modern Pump Theory and Design*, China Aerospace Press, Beijing, China, 2011.
- [20] T. Wang, F. Kong, B. Xia, Y. Bai, and C. Wang, "The method for determining blade inlet angle of special impeller using in turbine mode of centrifugal pump as turbine," *Renewable Energy*, vol. 109, pp. 518–528, 2017.
- [21] O. Minggao, H. Liu, and S. Yuan, "Calculation of hydraulic loss of centrifugal pump," *Journal of Jiangsu University (Natural Science Edition)*, vol. 2007, no. 5, pp. 405–408, 2007.
- [22] Y. Gu, L. Yu, J. Mou et al., "Research strategies to develop environmentally friendly marine antifouling coatings," *Marine Drugs*, vol. 18, no. 7, p. 371, 2020.

## Research Article

# Prediction of Tool Lifetime and Surface Roughness for Nickel-Based Waspaloy

Shao-Hsien Chen<sup>1</sup> and Chung-An Yu<sup>2</sup>

<sup>1</sup>The Graduate Institute of Precision Manufacturing, National Chin-Yi University of Technology, No. 57, Section 2, Zhongshan Road, Taiping District, Taichung 41170, Taiwan

<sup>2</sup>Department of Mechanical Engineering, National Chin-Yi University of Technology, No. 57, Section 2, Zhongshan Road, Taiping District, Taichung 41170, Taiwan

Correspondence should be addressed to Shao-Hsien Chen; e6036@ncut.edu.tw

Received 12 June 2020; Accepted 27 June 2020; Published 27 July 2020

Academic Editor: Jinyang Xu

Copyright © 2020 Shao-Hsien Chen and Chung-An Yu. This is an open access article distributed under the Creative Commons Attribution License, which permits unrestricted use, distribution, and reproduction in any medium, provided the original work is properly cited.

In recent years, most of nickel-based materials have been used in aircraft engines. Nickel-based materials applied in the aerospace industry are used in a wide range of applications because of their strength and rigidity at high temperature. However, the high temperatures and high strength caused by the nickel-based materials during cutting also reduce the tool lifetime. This research aims to investigate the tool wear and the surface roughness of Waspaloy during cutting with various cutting speeds, feed per tooth, cutting depth, and other cutting parameters. Then, it derives the formula for the tool lifetime based on the experimental results and explores the impacts of these cutting parameters on the cutting of Waspaloy. Since the impacts of cutting speed on the cutting of Waspaloy are most significant in accordance with the experimental results, the high-speed cutting is not recommended. In addition, the actual surface roughness of Waspaloy is worse than the theoretical surface roughness in case of more tool wear. Finally, a set of mathematical models can be established based on these results, in order to predict the surface roughness of Waspaloy cut with a worn tool. The errors between the predictive values and the actual values are 5.122%~8.646%. If the surface roughness is within the tolerance, the model can be used to predict the residual tool lifetime before the tool is damaged completely. The errors between the predictive values and the actual values are 8.014%~20.479%.

## 1. Introduction

In recent years, the development of engine design aims at the applications under high pressure and high temperature, in order to improve the fuel efficiency and to save the related costs. Some parts which adopt stainless steel, aluminum alloys, magnesium alloys, and titanium alloys in the past, such as compressor housings, combustor combustion chambers, and turbine blades, have adopted nickel-based alloys gradually as shown in Figure 1, to meet the requirements of the applications in the special corrosion-resistant environments, high-temperature corrosion environments, or the equipment with high-temperature mechanical strength.

Nickel-based alloys are the alloys containing more than 30 wt% nickel, and the nickel-based parts available on the market often contain more than 50 wt% nickel. Nickel-based alloys were researched and developed in the late 1930s and were first produced by the British in 1941. They support high hardness, high-temperature strength, good thermal stability, and corrosion resistance. They support, especially, better high-temperature resistance than low-alloy steel and stainless steel in case the temperature is higher than 650°C. In recent years, they have been widely used in aerospace industry, petrochemical industry and other fields. Among these applications, the aerospace industry supports the highest output value accounting for 33% of the total output value [2, 3].

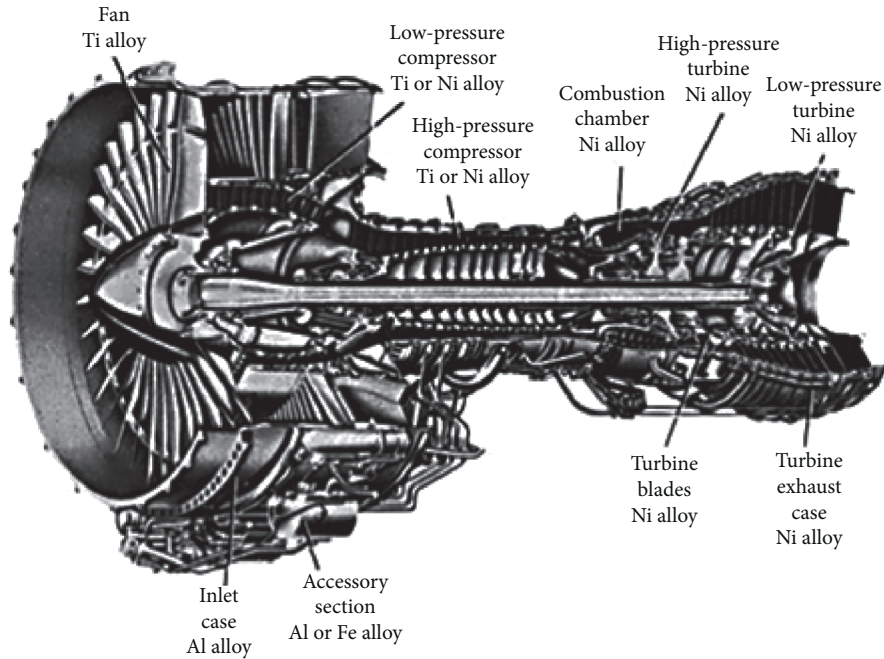


FIGURE 1: Parts of jet engine [1].

Hanasaki et al. [4] discovered that the coated tool supports better resistance on the groove wear and the tool wear when cutting a nickel-based alloy with a tungsten carbide tool with a specific coating. They also pointed out that the tool lifetime depends on the tool chipping and the adhesion wear during the low-speed cutting and depends on the wear caused by the tool temperature increases during the high-speed cutting.

In the research on the cutting Inconel-718 alloy with ceramic tools and ceramic tools, Nalbant [5] figured out that carbide tools are more suitable than ceramic tools for cutting Inconel-718 alloy. According to the comparison of different cutting speeds, they discovered that ceramic tools are suitable for high-speed cuttings, and carbide tools are suitable for low-speed cuttings. Moreover, the cutting force is inversely proportional to the cutting speed.

Jawaid et al. [6] explored the cutting performance and the wear resistance of tungsten carbide tools with and without TiN coating on the face milling of Inconel-718 alloy.

Zetek et al. [7] cooled down and changed the tool angle with the cutting fluids to cut Inconel-718 alloys. The tool lifetime was improved by 35% by improving the tool geometrical shape.

After applying the Ti-based and Cr-based metal tool coated with diamond-like films to mill aluminum alloys, X-H, Wang and Su [8] figured out that the surface roughness is worse than those milled with tools without coating. However, the tool wear is better, and this of Cr-based metal tools is better than this of Ti-based metal tools.

The thesis on machining mostly issue on tool wear and optimization parameter, this study mainly objects at the simultaneous prediction of tool wear and surface roughness to specifically for the nickel-based alloy Waspaloy.

## 2. Cutting Principle and Material Property

**2.1. Cutting Property of Nickel-Based Materials.** Waspaloy is one of the nickel-based alloys and contains about fifteen alloy elements. Among these elements, the additional aluminum (Al) and chromium (Cr) can improve the high-temperature oxidation resistance, the additional chromium (Cr) and titanium (Ti) can prevent hot corrosion caused by sulfides, and other elements also can provide corresponding features. After the aging treatment, nickel-based alloys will coherently precipitate the fine spherical  $\gamma'$ -phase on the base ( $\gamma$ -phase) of the face-centered cubic (FCC) and then generate the coherency strain. The generation of  $\gamma'$ -phase affects the high-temperature properties of nickel-based alloys, and more generations cause better high-temperature properties. Moreover, the solidified aluminum (Al) and titanium (Ti) contribute to the generation of the  $\gamma'$ -phase, and cobalt (Co) can increase the  $\gamma'$ -phase melting temperature and raise the high-temperature strength and stability. Because Waspaloy contains more aluminum (Al) and titanium (Ti), it has more  $\gamma'$ -phase, and better high-temperature strength, creep, oxidation, and corrosion resistance. However, it also causes more processing difficulties [9, 10].

The increase of the  $\gamma'$ -phase precipitations enhances both the tensile strength and the falling strength of the alloy but reduces the toughness. In addition, the carbon elements contained in the alloy also cause the absolute influences on the properties of the nickel-based alloy. Carbon does not combine with nickel to form carbides, but it can combine with other alloy elements to form intermetallic compounds. The carbides that precipitated from nickel-based alloys are MC,  $M_6C$ ,  $M_7C_3$ , and  $M_{23}C_6$  as shown in Figure 2. Material scientists discovered that MC (high-temperature tungsten

carbide phase) would be precipitated in the form of a mass, which is not beneficial for alloy materials and  $M_6C$  is often precipitated at the grain boundary in the form of a mass to control the grain size. Moreover,  $M_7C_3$  will be generated in the intervals between crystal grains. If it is discontinuously distributed, it will strengthen the alloy material. On the contrary, if it is precipitated at the grain boundaries, it may cause the embrittlement of the alloy.

The toughness of Waspaloy is relative to the precipitated carbides at the forging deformation grain boundary, the large-angle recrystallization grain boundary, and the deformation twin rather than the size and distribution of  $\gamma'$ -phase. At above the  $\gamma'$ -phase dissolution temperature (above 1080°C), MC will be autolysis. During the subsequent solid solution process, the MC precipitations result in a twin structure and may generate a carbide film at the grain boundary. The content of major elements in the high-temperature superalloys leads to a great influence on microstructure, structural stability, and final properties. In the production process, the content of major elements in the  $\gamma'$ -phase and the carbide may be not the same, and their precipitation quantities, precipitations, and solid solution temperature may also be different. [12, 13].

**2.2. Strengthening Mechanism of Waspaloy Superalloy.** Nickel-based alloys have good strength and ductility at medium and low temperatures. The strengthening factors come from a combination of various mechanisms, including the solid solution strengthening, the precipitation strengthening, and the grain boundary strengthening as the following summarization [14–16].

**2.2.1. Austenitic-Base Solid Solution Strengthening.** Since the alloy contains about Cr and Mo and the atomic volumes of Cr and Mo are both larger than this of Ni, the substitutional solid solution will be generated when the alloy is solid solubilized in the base. Then, the grain lattice of base will be distorted to generate the strain and the strengthening effect.

**2.2.2.  $\gamma'$ -Phase Precipitation Strengthening.** The precipitation strengthening is relative to the interaction between the precipitation phase and the dislocation. Since the  $\gamma'$ -phase is regular and coherent precipitates, the strengthening effect on the precipitates is generally caused by the inversed phase boundary and defect hardening when the dislocation generates precipitates, the proportion of size and the volume of precipitates affects the important factors of the coherency strain.

**2.2.3. Grain Boundary Strengthening.** It is the strengthening effect caused by the precipitating carbides generated at the grain boundary to block the grain boundary sliding. A small amount of boron (B) segregates the precipitated carbides at the grain boundary and reduces the grain boundary diffusion. Also, the grain size and direction can be controlled to generate the strengthening effect. In case of the higher creep resistance of fine grain at the medium temperature and high

stress, the control factor of creep is the dislocation sliding. In case of the higher creep resistance of coarse grain at the high temperature and low stress, the control factor of creep is the dislocation climbing. The main precipitation strengthening mechanism in the nickel-based alloy is  $\gamma'$ . This mechanism and the coherency strain generated in the base support higher strength for the nickel-based alloy at the medium or low temperature environment.

### 2.3. Cutting Principle

**2.3.1. Tool Life and Wear.** The experiment method used in this research is face milling. For the tool lifetime predictions and cutting research, the feed per tooth, cutting speed, and depth are the essential cutting parameters. Since a disposable insert of circular is adopted in the cutting process, the feed per tooth and the cutting depth are relative, as shown in Figure 3. Thus, the feed per tooth is calculated as follows [17, 18]:

$$f_z = \frac{H_{ex}C_i}{2\sqrt{a_p C_i - a_a^2}} \quad (1)$$

$$a_p^2 - C_i a_p + \left(\frac{H_{ex}C_i}{2f_z}\right)^2 = 0. \quad (2)$$

Generally, the cutting tool lifetime research is divided into qualitative method and quantitative method. The research adopts the quantitative method for the investigations and analysis mainly. In each set of the cutting parameters, the total travel length is 1410 mm. For each 282 mm, the tool wear and the surface roughness are measured for each 282 mm. Therefore, there are 5 values of the tool wear and the surface roughness for each set of the cutting parameters. Based on these measurement results, the tool lifetime for each set of the cutting parameters can be derived at the tool wear  $VB=0.3$  mm, and then it can be substituted into the formula as follows [19, 20]:

$$V \times T^n \times f_z^a \times ap^b = C. \quad (3)$$

Substitute the known values of the cutting speed,  $V_1, V_2,$  and  $V_3$ ; the feed per tooth,  $f_{z1}, f_{z2},$  and  $f_{z3}$ ; cutting depth,  $ap_1, ap_2,$  and  $ap_3$ ; and tool lifetime,  $T_1, T_2,$  and  $T_3$  into the above formula:

$$\begin{cases} V_1 T_1^n f_{z1}^a ap_1^b = C, \\ V_2 T_2^n f_{z2}^a ap_2^b = C, \\ V_3 T_3^n f_{z3}^a ap_3^b = C. \end{cases} \quad (4)$$

Since the previous formula with each set of the cutting parameters can derive a constant value  $C$ , it can be derived as follows:

$$V_1 T_1^n f_{z1}^a ap_1^b = V_2 T_2^n f_{z2}^a ap_2^b = V_3 T_3^n f_{z3}^a ap_3^b. \quad (5)$$

After the further derivations, the cutting parameters, feed per tooth, cutting speed, and depth are proportional and can be presented as follows:

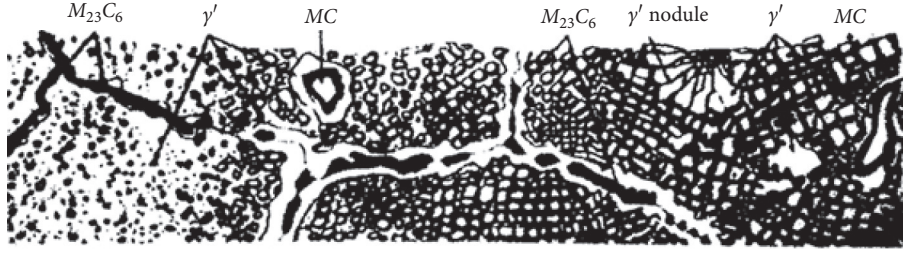


FIGURE 2: Grain structure of nickel-based materials [11].

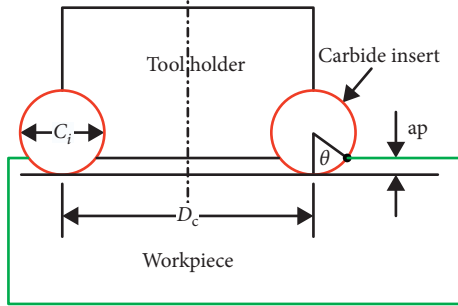


FIGURE 3: Geometry and labeling of a cutting tool.

$$\begin{cases} \left(\frac{T_1}{T_2}\right)^n \left(\frac{f_{z1}}{f_{z2}}\right)^a \left(\frac{ap_1}{ap_2}\right)^b = \frac{V_2}{V_1}, \\ \left(\frac{T_2}{T_3}\right)^n \left(\frac{f_{z2}}{f_{z3}}\right)^a \left(\frac{ap_2}{ap_3}\right)^b = \frac{V_3}{V_2}, \\ \left(\frac{T_1}{T_3}\right)^n \left(\frac{f_{z1}}{f_{z3}}\right)^a \left(\frac{ap_1}{ap_3}\right)^b = \frac{V_3}{V_1}, \end{cases} \quad (6)$$

Rewrite the above formula in a matrix as follows:

$$\begin{bmatrix} \ln\left(\frac{T_1}{T_2}\right) & \ln\left(\frac{f_{z1}}{f_{z2}}\right) & \ln\left(\frac{ap_1}{ap_2}\right) \\ \ln\left(\frac{T_2}{T_3}\right) & \ln\left(\frac{f_{z2}}{f_{z3}}\right) & \ln\left(\frac{ap_2}{ap_3}\right) \\ \ln\left(\frac{T_1}{T_3}\right) & \ln\left(\frac{f_{z1}}{f_{z3}}\right) & \ln\left(\frac{ap_1}{ap_3}\right) \end{bmatrix} \begin{bmatrix} n \\ a \\ b \end{bmatrix} = \begin{bmatrix} \ln\left(\frac{V_2}{V_1}\right) \\ \ln\left(\frac{V_3}{V_2}\right) \\ \ln\left(\frac{V_3}{V_1}\right) \end{bmatrix}. \quad (7)$$

Based on the previous formula, the variables,  $n$ ,  $a$ , and  $b$  and each set of the cutting parameters can be derived and substituted into formula (3) for the constant value  $C$ , and then the formula of tool lift-time on the cutting of superalloy, Waspaloy, can be derived finally. Also, the impacts of cutting parameters on the cutting of superalloy, Waspaloy, can be derived based on the formula of tool lift-time.

The machining time required for the tool to reach flank wear, mainly for continuous cutting test of single blade and then the tool wear process, is (1) initial wear rate, (2) uniform wear rate, and (3) accelerating wear rate, for uniform wear is

0.3 mm and nonuniform wear is 0.6 mm (tool life criterion); this study is based on the ISO-8688-1/1994 standard for testing and analysis.

**2.3.2. Tool Wear and Surface Roughness.** For most of the sets of cutting parameters, the actual surface roughness is less than the theoretical one. The theoretical surface roughness can be defined as the surface roughness under conditions of a complete tool. However, the cutting of a worn tool is a straight-line as shown in Figure 4(b) rather than a circular arc as shown in Figure 4(a). Moreover, the surface roughness generated by a worn tool is less than the theoretical one based on Figure 4. Thus, the straight-line generated by the tool shape will be impacted by the tool wear as shown in Figure 5. The surface roughness is relative to the feed per tooth in accordance with the surface roughness theory, the feed per tooth in the first set of cutting parameters is 0.3 mm/tooth, and the straight-line (C2) by the tool wear is much more than the feed per tooth. Therefore, the tool wear and the shape of worn tool may impact the surface roughness in addition to the feed per tooth in this experiment.

The tool wear and the surface roughness are relative. Thus, the tool wear straight-line is calculated as follows:

$$a = VB \times \tan 7^\circ, \quad (8)$$

$$b = R - a \quad (9)$$

$$C1 = \sqrt{R^2 - b^2}, \quad (10)$$

$$C2 = 2C1, \quad (11)$$

where  $VB$  is the tool wear (mm) and  $R$  is the radius of tool (fixed value: 6 mm).

### 3. Experimental Procedure and Equipment

**3.1. Experimental Plan.** The research contains the variable factors, resolution, cutting depth, and feed rate and adopts the disposable insert tool coated TiAlN to perform the experiment. Through the generalized formula of tool lifetime and the substitution of a set of cutting parameter into the formula to derive the constant value  $C$ , the formula of tool lift-time on the cutting of superalloy, Waspaloy, can be derived finally. Moreover, the relations between surface roughness and the tool wear can be established through the formula of surface roughness, and the impacts of cutting

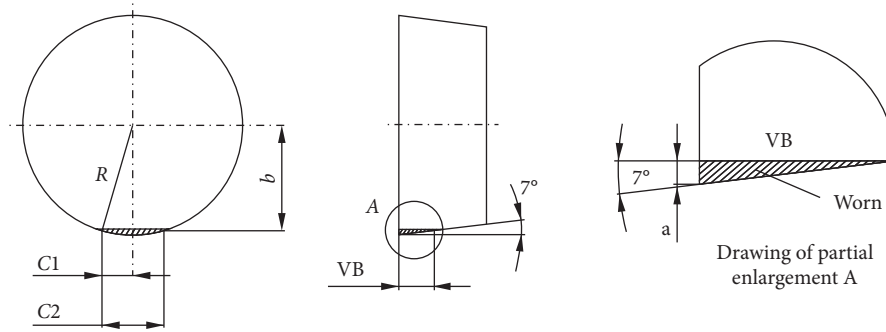


FIGURE 4: Effects of tool wear on surface roughness.

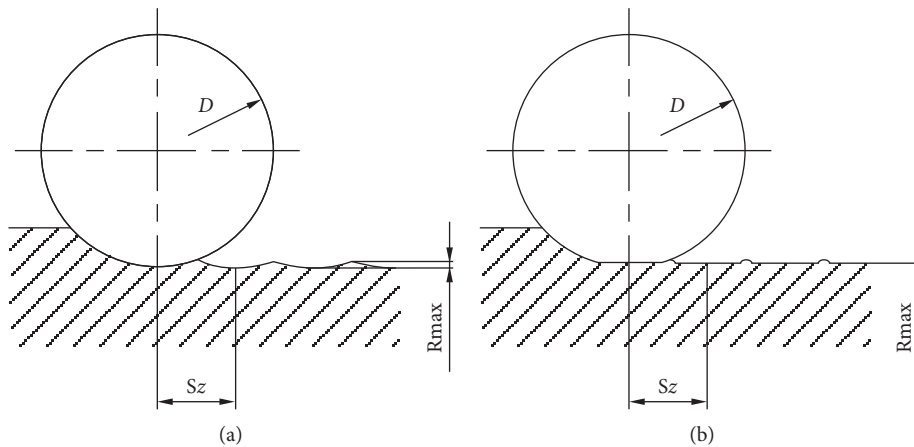


FIGURE 5: Effects of tool wear on tool shape. (a) Surface roughness of complete tool. (b) Surface roughness of worn tool.

parameters on the cutting of superalloy, Waspaloy, can be derived based on the formula of tool lift-time. This experiment adopts the cutting speed, the feed per tooth, and the cutting depth as the variables in accordance with the recommendations of the tool catalog on the cutting of nickel-based alloy, such that the cutting speed ( $V_c$ ) is 40~36.5 (m/min) and the feed per tooth ( $f_z$ ) is 0.28~0.42 (mm/tooth). The experimental procedure is described in Figure 6 and Table 1.

#### 4. Result and Discussion

**4.1. The Relationship between Tool Wear and Time.** The cutting experimental results show the tool wear is more with the longer cutting travel length or the cutting time. The tool lifetime aims to explore the relations between the cutting time and tool wear, and this experiment observes the impacts of cutting travel length on the tool wear. Therefore, the travel length can be converted into the cutting time in the following tables and figures. In addition, the feed rate ( $F$ ) can be derived based on the cutting conditions mentioned. The cutting travel length is directly proportional to the cutting time and inversely proportional to the feed rate.

The cutting parameters adopted in the first experiment for tool wear are the cutting speed ( $V$ ) = 40 m/min, the feed per tooth ( $f_z$ ) = 0.3 mm/tooth, the cutting depth ( $a_p$ ) = 0.3 mm, and the travel length ( $L$ ) = 282 mm, 564 mm, 846 mm, 1128 mm, and 1410 mm. As shown in Figure 7, the longer travel length will

increase the tool wear. It is caused by the effects of tool usage mainly.

Based on the experimental results, the relations between time and tool wear can be drawn as shown in Figure 7. With the method of least squares, a curve approaching the experimental point can be derived, and the formula of fitting curve can be described as follows:

$$VB = 0.084 \times e^{0.157t} \tag{12}$$

Through the above formula, at the 0.3 mm of tool wear (i.e.,  $VB = 0.3$ ), the time is 8.108 min. It is the tool lifetime ( $T$ ) under conditions of the first cutting parameters, where  $VB$  is tool wear (mm) and  $t$  is the cutting time (min). The cutting parameters adopted in the second experiment for tool wear are the cutting speed ( $V$ ) = 37.5 m/min, the feed per tooth ( $f_z$ ) = 0.35 mm/tooth, the cutting depth ( $a_p$ ) = 0.25 mm, and the travel length ( $L$ ) = 282 mm, 564 mm, 846 mm, 1128 mm, and 1410 mm as shown in Figure 8.

Based on the experimental results, the relations between time and tool wear can be drawn as Figure 8. With the method of least squares, a curve approaching the experimental point can be derived, and the formula of fitting curve can be described as follows:

$$VB = 0.066 \times e^{0.177t} \tag{13}$$

Through the above formula, at the 0.3 mm of tool wear (i.e.,  $VB = 0.3$ ), the time is 8.544 min. It is the tool lifetime ( $T$ ) under conditions of the second cutting parameters. The

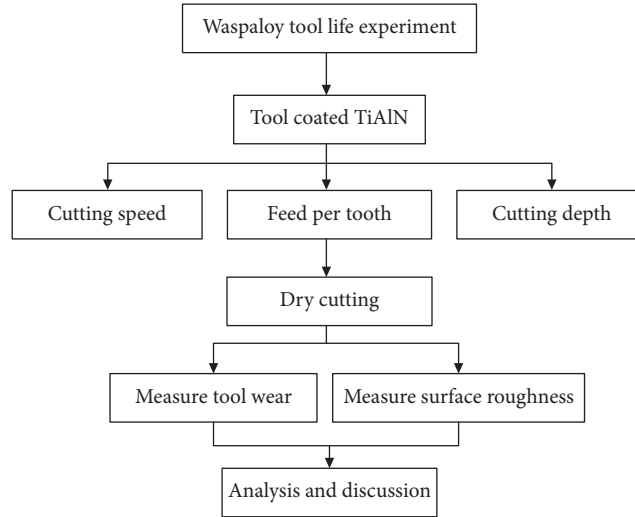


FIGURE 6: Experimental procedure.

TABLE 1: Cutting condition design.

Parameter set no.	Cutting speed (m/min)	Feed per tooth (mm/tooth)	Cutting depth (mm)
1	40	0.3	0.3
2	37.5	0.35	0.25
2	35	0.4	0.2

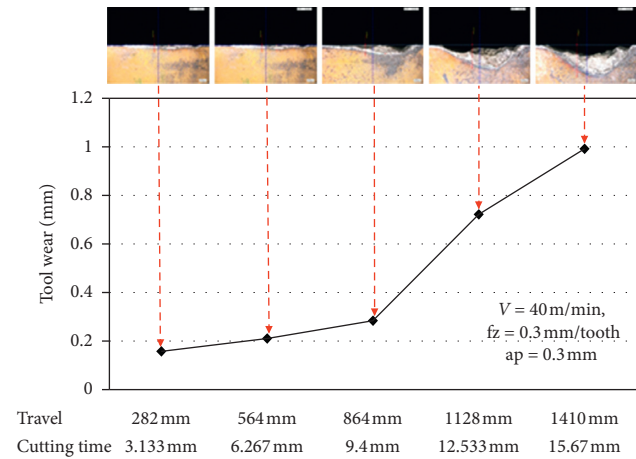


FIGURE 7: Tool wear under conditions of  $V = 40$  m/min,  $f_z = 0.3$  mm/tooth, and  $a_p = 0.3$  mm.

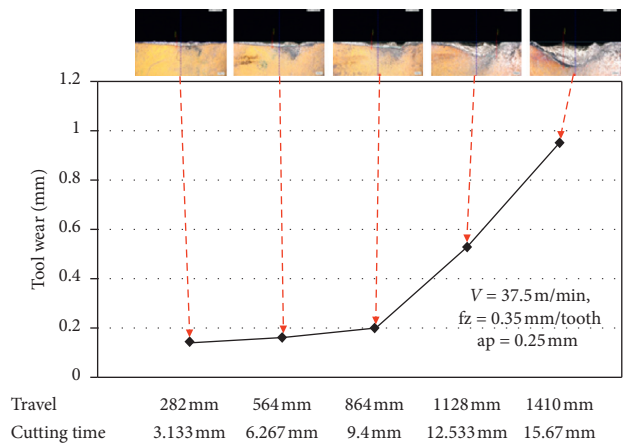


FIGURE 8: Tool wear under conditions of  $V = 37.5$  m/min,  $f_z = 0.35$  mm/tooth, and  $a_p = 0.25$  mm.

cutting parameters adopted in the third experiment for tool wear are the cutting speed ( $V$ ) = 35 m/min, the feed per tooth ( $f_z$ ) = 0.4 mm/tooth, the cutting depth ( $a_p$ ) = 0.2 mm, and the travel length ( $L$ ) = 282 mm, 564 mm, 846 mm, 1128 mm, and 1410 mm as shown in Figure 9.

Based on the experimental results, the relations between time and tool wear can be drawn as in Figure 9. With the method of least squares, a curve approaching the experimental point can be derived, and the formula of fitting curve can be described as follows:

$$VB = 0.081 \times e^{0.119t} \quad (14)$$

Through the above formula, at the 0.3 mm of tool wear (i.e.,  $VB = 0.3$ ), the time is 11.003 min. It is the tool lifetime ( $T$ ) under conditions of the third cutting parameters. Summarily, the above experimental results can be listed in Table 2.

Substituting all known values into formula (3) and calculating the matrix can derive the results:  $n = 0.036$ ,  $a = 0.302$ , and  $b = -0.088$ . Substituting these values into formula (5) can derive the formula as follows:

$$VT^{-0.036} f_z^{0.302} a_p^{-0.088} = C. \quad (15)$$

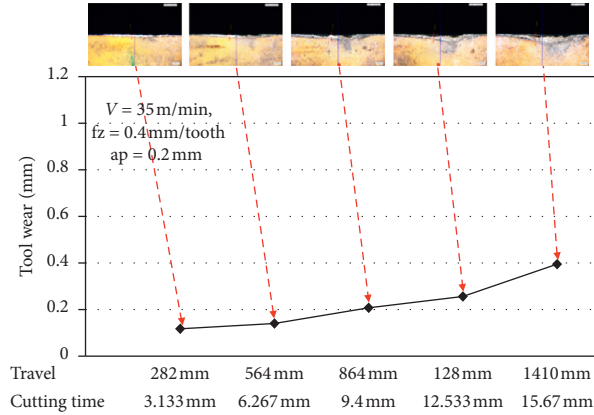


FIGURE 9: Tool wear under conditions of  $V = 35$  m/min,  $fz = 0.4$  mm/tooth, and  $ap = 0.2$  mm (conti.).

TABLE 2: Tool lifetime for cutting parameters.

Parameter set no.	Cutting speed (m/min)	Feed per tooth (mm/tooth)	Cutting depth (mm)	Tool lifetime (min)
The first group	40	0.3	0.3	8.108
The second group	37.5	0.35	0.25	8.554
The third group	35	0.4	0.2	11.003

Substituting the first set of cutting parameters, including the cutting speed ( $V$ ), feed per tooth ( $fz$ ), cutting depth ( $ap$ ), and tool lifetime ( $T$ ), into the above formula can derive the constant value  $C = 33.334$ . Finally, the formula for tool lifetime can be derived as follows:

$$VT^{0.036} fz^{0.302} ap^{-0.088} = 33.334. \quad (16)$$

4.2. *Experimental Parameters and Significant Factor Analysis.* Based on the formula of tool lifetime, the relations between the cutting speed ( $V$ ) and the tool lifetime ( $T$ ) can be derived when the feed per tooth ( $fz$ ) and the cutting depth ( $ap$ ) are set to 1. Similarly, the relations between the feed per tooth and the tool lifetime and between the cutting depth and the tool lifetime can also be derived. These procedures can be described as follows [20]:

$$\begin{cases} fz = 1, ap = 1, \\ V = 1, ap = 1, \\ V = 1, fz = 1. \end{cases} \quad (17)$$

They are substituted into formula (16):

$$\Rightarrow \begin{cases} VT^{0.036} = 33.334, \\ T^{0.036} fz^{0.302} = 33.334, \\ T^{0.036} ap^{-0.088} = 33.334, \end{cases} \quad (18)$$

$$\Rightarrow \begin{cases} \ln(V) + 0.036 \ln(T) = 3.507, \\ 0.036 \ln(T) + 0.302 \ln(fz) = 3.507, \\ 0.036 \ln(T) - 0.088 \ln(ap) = 3.507, \end{cases} \quad (19)$$

$$\Rightarrow \begin{cases} \ln(T) = -27.778 \ln(V) + 97.417, \\ \ln(T) = -8.389 \ln(fz) + 97.417, \\ \ln(T) = 2.444 \ln(ap) + 97.417. \end{cases} \quad (20)$$

According to formula (20),  $\ln(T)$  will be reduced 27.778 when  $\ln(V)$  increases 1. That is,  $T$  will be multiplied by  $8.633 \times 10^{-13}$  when  $\ln(V)$  increases 1. Second,  $\ln(T)$  will be reduced 8.389 when  $\ln(fz)$  increases 1. That is,  $T$  will be multiplied by  $2.274 \times 10^{-4}$  when  $\ln(fz)$  increases 1. Third,  $\ln(T)$  will be reduced 2.444 when  $\ln(ap)$  increases 1. That is,  $T$  will be multiplied by 11.519 when  $\ln(ap)$  increases 1. Based on these results, the larger slope of the formula leads to more impacts on the tool lifetime. Therefore, the impacts of the cutting speed on the cutting of Waspaloy are larger, and the impacts of the cutting depth are smaller as shown in Figure 10.

4.3. *Relations between Tool Wear and Surface Roughness.*

As the experimental procedure, not only the tool wear but also the surface roughness of Waspaloy is measured when the travel length is 282 mm, 564 mm, 846 mm, 1128 mm, and 1410 mm for each set of the cutting parameters. In addition to the tool wear and surface roughness at each travel length, Table 3 also lists the theoretical surface roughness for further discussion. The derivation of theoretical surface roughness is mentioned in surface roughness theory in (31). However, this theoretical surface roughness is described by the maximum surface roughness ( $R_{max}$ ), and the experiment applies the average surface roughness at the central line ( $R_a$ ). Thus, the theoretical surface roughness shall be converted through the formula as follows [20]:

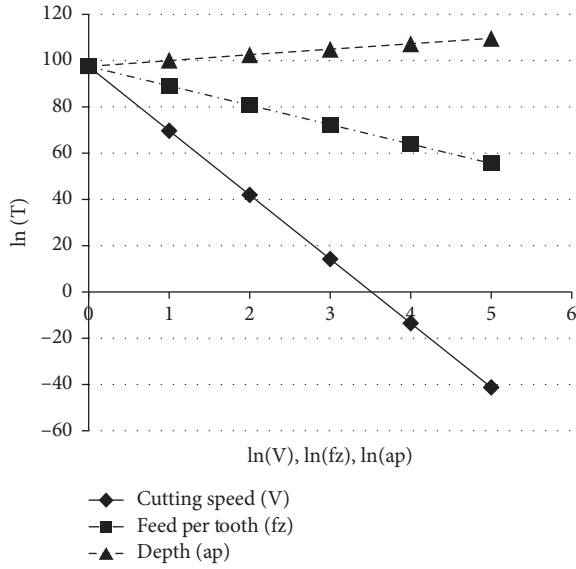


FIGURE 10: Impacts of cutting parameters on tool lifetime.

TABLE 3: Tool wear and surface roughness of Waspaloy for cutting parameters.

The first group cutting parameters	$V = 40$ m/min, $fz = 0.3$ mm/tooth, $ap = 0.3$ mm				
Theoretical surface roughness (Ra)	0.469 $\mu$ m				
Travel length (mm)	282	564	864	1128	1410
Tool wear (mm)	0.157	0.21	0.285	0.721	0.989
Surface roughness ( $\mu$ m)	0.297	0.328	0.325	0.729	0.483
The second group cutting parameters	$V = 37.5$ m/min, $fz = 0.35$ mm/tooth, $ap = 0.25$ mm				
Theoretical surface roughness (Ra)	0.638 $\mu$ m				
Travel length (mm)	282	282	282	282	282
Tool wear (mm)	0.142	0.142	0.142	0.142	0.142
Surface roughness ( $\mu$ m)	0.330	0.312	0.341	0.419	0.537
The third group cutting parameters	$V = 35$ m/min, $fz = 0.4$ mm/tooth, $ap = 0.2$ mm				
Theoretical surface roughness (Ra)	0.833 $\mu$ m				
Travel length (mm)	282	282	282	282	282
Tool wear (mm)	0.116	0.116	0.116	0.116	0.116
Surface roughness ( $\mu$ m)	0.322	0.322	0.322	0.322	0.322

$$Ra = \frac{1}{4} R_{max}, \quad (21)$$

where Ra is the average surface roughness at the central line and Rmax is the maximum surface roughness.

As shown in Table 3, for most of the sets of cutting parameters, the actual surface roughness is less than the theoretical one. The theoretical surface roughness can be defined as the surface roughness under conditions of a complete tool. For example, the first set of cutting parameters shall present the 0.469  $\mu$ m of the theoretical surface roughness at the 282 mm of the travel length, and the actual surface roughness is 0.297  $\mu$ m only. It shall be caused by the tool shape as shown in Figures 4 and 5. Take 0.157 mm of

tool wear at 282 mm of travel length for the first set of cutting parameter as an example; that is, VB is 0.157 mm of tool wear in Figure 11. Therefore,  $a$  is 0.019 mm and C2 is 0.954 mm.

For the impacts of tool wear on the surface roughness, the relation between the tool wear and the surface roughness can be established based on the data in Table 4. For each set of the cutting parameters, the more tool wear will cause more surface roughness. However, the data at several experimental points is not in compliance with the trend. In addition to the tool wear, these symptoms may be caused by the tool adhesion, the cuttings which are not cleared and adhered on the workpiece surface, or other phenomena influencing the surface roughness of tool during the cutting.

If these experimental points are treated as noise and removed, the relation between tool wear and the surface roughness becomes linear as shown clearly in Figure 11, and the impacts of feed per tooth on the tool wear and surface roughness can be discovered. For each set of the cutting parameters, both of the impacts of cutting speed (V) and the cutting depth (ap) are decreasing, and the impacts of the feed per blade are increasing. Moreover, under conditions of the same tool wear, the increased feed per tooth causes more surface roughness. Therefore, the three fitting curves approaching the experimental curves can be derived through the method of least squares and are shown in Table 4.

4.4. Tool Wear and Surface Roughness to Prediction. The research aims to predict that the surface roughness of workpiece after cutting meets the requirements or not in case of worn tool and how long such tool can be used subsequently. Based on the relations between the tool wear and surface roughness, the tool wear and the feed per tooth cause a certain influence on the surface roughness. Therefore, here assume a formula about the tool wear, the feed per tooth, and the surface roughness as follows [20]:

$$a \times VB + b \times fz + c = SR. \quad (22)$$

The unknown values,  $a$ ,  $b$ , and  $c$ , in formula (21) can be derived by substituting the results of the tool wear, the feed per tooth, and the surface roughness into formula (22) as follows:

$$\begin{cases} a \times VB_1 + b \times fz_1 + c = SR_1, \\ a \times VB_2 + b \times fz_2 + c = SR_2, \\ \vdots \\ a \times VB_n + b \times fz_n + c = SR_n. \end{cases} \quad (23)$$

Formula (23) can be described as the following matrix, where the experimental results of tool wear, feed per tooth, and surface roughness are

$$\begin{bmatrix} VB_1 & fz_1 & 1 \\ VB_2 & fz_2 & 1 \\ \vdots & \vdots & \vdots \\ VB_n & fz_n & 1 \end{bmatrix} \begin{bmatrix} a \\ b \\ c \end{bmatrix} = \begin{bmatrix} SR_1 \\ SR_2 \\ \vdots \\ SR_n \end{bmatrix}. \quad (24)$$

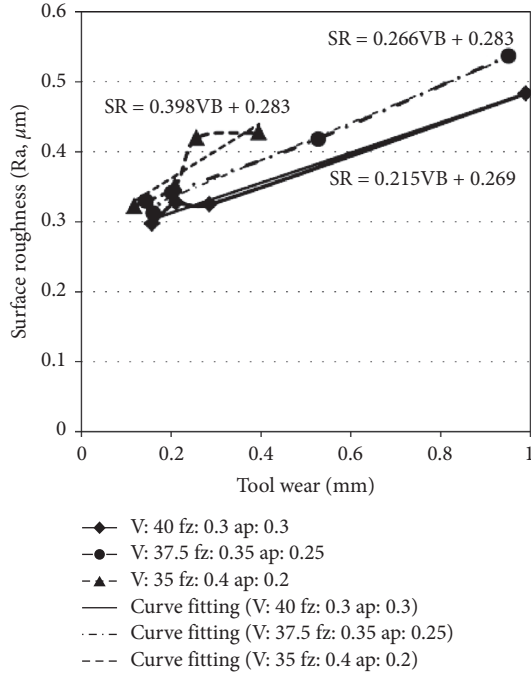


FIGURE 11: Relation between tool wear and surface roughness.

TABLE 4: Linear formula of tool wear on surface roughness, where SR is the surface roughness ( $R_a, \mu\text{m}$ ) and VB is the tool wear (mm).

Cutting parameters	Linear formula
$V = 40 \text{ m/min}$ , $fz = 0.3 \text{ mm/tooth}$ , $ap = 0.3 \text{ mm}$	$SR = 0.215VB + 0.269$
$V = 37.5 \text{ m/min}$ , $fz = 0.35 \text{ mm/tooth}$ , $ap = 0.25 \text{ mm}$	$SR = 0.266VB + 0.282$
$V = 35 \text{ m/min}$ , $fz = 0.4 \text{ mm/tooth}$ , $ap = 0.2 \text{ mm}$	$SR = 0.398VB + 0.283$

Solving the above matrix can derive  $a = 0.248$ ,  $b = 0.633$ , and  $c = 0.067$ ; then substitute these values into formula (22) as follows:

$$0.248VB + 0.633fz + 0.067 = SR. \quad (25)$$

By substituting the experimental results of the feed per tooth and the tool wear into formula (25) and drawing it as shown in Figure 12, it presents a corresponding trend line for each feed per tooth. Therefore, the predictive value of surface roughness after cutting can be derived after measuring the tool wear and substituting the value and the given feed per tooth into formula (25). Also, the predictive value of surface roughness can be used to determine the tool can be used subsequently or not. Table 5 shows the comparison for the experimental predictive surface roughness for each set of the cutting parameters.

**4.5. Tool Wear and Cutting Time to Prediction.** If the tool can be used in the cutting process subsequently, the next issue is how long the tool can be used subsequently. The cutting time, including the tool lifetime, is relative to the tool wear,

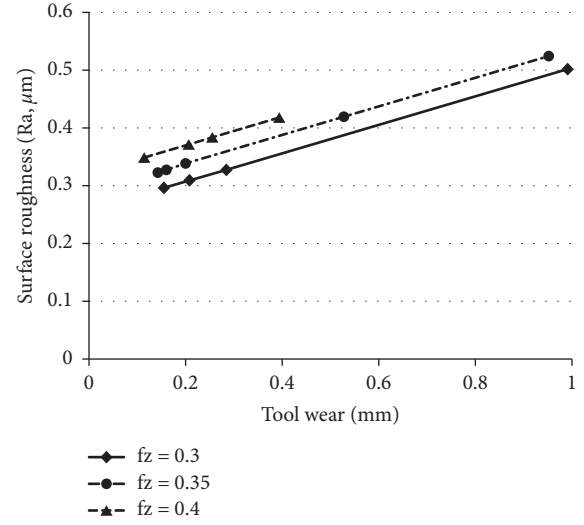


FIGURE 12: Trend of surface roughness prediction.

and the relation can be presented with a curve. Therefore, a formula of curve can be assumed to describe the relation between the cutting time and the tool wear as follows [20]:

$$A \times e^{Bt} = VB, \quad (26)$$

$$t = \frac{1}{B} \times \ln\left(\frac{VB}{A}\right). \quad (27)$$

$A$  and  $B$  in formula (27) are the factors influencing the formula of curve, and the values of  $A$  and  $B$  may be not the same under different cutting conditions as the fitting curve formula for each set of the cutting parameters. These results are listed in Table 6.

Since the  $A$  and  $B$  may be different with the set of cutting parameters, assume the  $A$  and  $B$  are relative to the cutting speed, the feed per tooth and the cutting depth as follows:

$$\{V^{a1} \times fz^{b1} \times ap^{c1} = A, \quad (28)$$

$$\{V^{a2} \times fz^{b2} \times ap^{c2} = B. \quad (29)$$

Formula (28) shows the relation of  $A$  to the cutting parameters, where  $a1$ ,  $b1$ , and  $c1$  are unknown values and impact on  $A$ .  $A$  can be derived by the following procedure:

$$V^{a1} \times fz^{b1} \times ap^{c1} = A. \quad (30)$$

Practicing the logarithm in the above formula can derive the following one:

$$a1 \times \ln(V) + b1 \times \ln(fz) + c1 \times \ln(ap) = \ln(A). \quad (31)$$

Substitute the corresponding values of  $A$  for each set of the cutting parameters into the above formula (e.g.,  $A_1 = 0.084$ ,  $A_2 = 0.066$ , and  $A_3 = 0.081$ ):

$$\begin{cases} a1 \times \ln(V_1) + b1 \times \ln(fz_1) + c1 \times \ln(ap_1) = \ln(A_1), \\ a1 \times \ln(V_2) + b1 \times \ln(fz_2) + c1 \times \ln(ap_2) = \ln(A_2), \\ a1 \times \ln(V_3) + b1 \times \ln(fz_3) + c1 \times \ln(ap_3) = \ln(A_3). \end{cases} \quad (32)$$

TABLE 5: Comparison for the experimental and predictive surface roughness for each set of the cutting parameters.

The first group cutting parameters		V = 40 m/min, fz = 0.3 mm/tooth, ap = 0.3 mm			
Experimental value ( $\mu\text{m}$ )	0.297	0.328	0.325	0.412	0.483
Predictive value ( $\mu\text{m}$ )	0.295836	0.308980	0.327580	0.429	0.502172
Error (%)	0.392	5.799	0.794	1.7	3.969
The second group cutting parameters		V = 37.5 m/min, fz = 0.35 mm/tooth, ap = 0.25 mm			
Experimental value ( $\mu\text{m}$ )	0.330	0.330	0.330	0.330	0.330
Predictive value ( $\mu\text{m}$ )	0.323766	0.323766	0.323766	0.323766	0.323766
Error (%)	1.889	1.889	1.889	1.889	1.889
The third group cutting parameters		V = 35 m/min, fz = 0.4 mm/tooth, ap = 0.2 mm			
Experimental value ( $\mu\text{m}$ )	0.322	0.332	0.351	0.420	0.427
Predictive value ( $\mu\text{m}$ )	0.348968	0.315	0.371536	0.383688	0.417664
Error (%)	8.375	1.7	5.851	8.646	2.186

TABLE 6: Fitting curve formula of each set of cutting parameter on the cutting time.

Cutting parameters	Curve formula
V = 40 m/min, fz = 0.3 mm/tooth, and ap = 0.3 mm	VB = 0.084 $\times e^{0.157t}$
V = 37.5 m/min, fz = 0.35 mm/tooth, and ap = 0.25 mm	VB = 0.066 $\times e^{0.177t}$
V = 35 m/min, fz = 0.4 mm/tooth, and ap = 0.2 mm	VB = 0.081 $\times e^{0.119t}$

TABLE 7: Comparison for the experimental and predictive cutting time for each set of the cutting parameters.

The first group cutting parameters		V = 40 m/min, fz = 0.3 mm/tooth, ap = 0.3 mm			
Experimental value (min)	3.133	6.267	9.4	12.533	15.667
Predictive value (min)	3.992036	5.845427	7.791341	13.705577	15.719503
Error (%)	27.419	6.727	17.113	9.356	0.335
Average magnitude of error (%)			12.190		
The second group cutting parameters		V = 37.5 m/min, fz = 0.35 mm/tooth, ap = 0.25 mm			
Experimental value (min)	3.82	5.64	7.46	11.28	14.1
Predictive value (min)	4.335873	4.974936	6.271479	11.736453	15.077437
Error (%)	13.5	11.792	15.95	4.047	6.932
Average magnitude of error (%)			10.4458		
The third group cutting parameters		V = 35 m/min, fz = 0.4 mm/tooth, ap = 0.2 mm			
Experimental value (min)	2.564	5.127	7.691	10.255	12.818
Predictive value (min)	3.027042	4.607661	7.894739	9.680498	13.283241
Error (%)	18.059	10.129	2.649	5.602	3.630
Average magnitude of error (%)			8.014		

Then, solving the matrix of the above formula can derive  $a1 = -5.666$ ,  $b1 = -10.095$ , and  $c1 = -5.207$ . Then, solving the matrix of the above formula can derive  $a2 = 5.191$ ,  $b2 = 10.804$ , and  $c2 = 6.639$ . Finally, substitute the values,  $a1$ ,  $a2$ ,  $b1$ ,  $b2$ ,  $c1$ , and  $c2$ , into formulas (28) and (29) to derive the prediction formula as follows:

$$\left\{ t = \frac{1}{B} \times \ln\left(\frac{VB}{A}\right), \right. \quad (33)$$

$$\left\{ V^{-5.666} \times fz^{-10.095} \times ap^{-5.207} = A, \right. \quad (34)$$

$$\left\{ V^{5.191} \times fz^{10.804} \times ap^{6.639} = B. \right. \quad (35)$$

Summarily, there are two sets of derived formulas. The first set, formula (25), can predict the feasibility of a worn tool in the cutting process. The second set, formulas (32)–(34), can predict the residual cutting time of such worn tool. Tables 5 and 6 show the comparison for the experimental predictive cutting time for each set of the cutting parameters. For example, practicing a cutting process with the first set of

cutting parameter, the cutting speed ( $V$ ) = 40 m/min, the feed per tooth ( $fz$ ) = 0.3 mm/tooth, the cutting depth ( $ap$ ) = 0.3 mm, and the given tool wear ( $VB$ ) = 0.157 mm; then the surface roughness and the residual cutting time can be derived as follows.

Substitute the tool wear ( $VB$ ) and the feed per tooth ( $fz$ ) into formula (24):

$$0.248VB + 0.633fz + 0.067 = SR, \quad (36)$$

$$SR = 0.248 \times 0.157 + 0.633 \times 0.3 + 0.067 = 0.296 (\mu\text{m}). \quad (37)$$

Solving the above formulas can derive the surface roughness ( $SR$ ) = 0.296  $\mu\text{m}$  at the tool wear ( $VB$ ) = 0.157 mm. The result can be used to determine the surface roughness processed by the tool meets the requirement or not. If the tool is available, substitute the cutting speed ( $V$ ) = 40 m/min, the feed per tooth ( $fz$ ) = 0.3 mm/tooth, and the cutting depth ( $ap$ ) = 0.3 mm into formulas (33) and (34) and

derive the influence factors of the predictive formula of cutting time, A and B:

$$A = V^{-5.666} \times fz^{-10.095} \times ap^{-5.207} = 40^{-5.666} \times 0.3^{-10.095} \times 0.3^{-5.207} = 0.084,$$

$$B = V^{5.191} \times fz^{10.804} \times ap^{6.639} = 40^{5.191} \times 0.3^{10.804} \times 0.3^{6.639} = 0.157. \quad (38)$$

Substitute the derived A and B into formula (33) to derive the predictive formula of cutting time as follows:

$$t = \frac{1}{0.157} \times \ln\left(\frac{VB}{0.084}\right). \quad (39)$$

Substitute the tool wear (VB) = 0.157 mm into the above formula to derive the time of the tool used under the given cutting parameters. Assume the tool is unavailable at the tool wear (VB) = 0.3 mm or more. Then, the cutting time at the tool wear (VB) = 0.3 mm can be derived. By subtracting the cutting time at the tool wear (VB) = 0.157 mm from the cutting time at tool wear (VB) = 0.3 mm, the residual time of the tool can be derived as 4.124 (min), as shown in Table 7.

## 5. Conclusion

- (1) Tool wear curve: based on the experiments of the first and the second sets of cutting parameters, the tool wear is significant after the cutting time is more than 9 minutes. Since the tool wear can be divided into three stages, namely, the burst stage, the stable stage, and the damage stage, the significant tool wear is caused that the tool wear has exceeded the stable stage and reached the damage stage.
- (2) Factors impacting tool lifetime: according to the experimental results, the impacts of the cutting speed on the tool lifetime are the most significant, and the impacts of the cutting depth on the tool lifetime are the least. The experimental results are similar to most of research results. In addition, the impacts of the feed per tooth on the surface roughness are more, followed by the impacts of the tool wear.
- (3) Comparison of experimental and predicted surface roughness: in the prediction of surface roughness, the maximum error between the actual value and the predicted value for the first set of cutting parameters is 5.799%, this for the second set of cutting parameters is 5.122%, and this of the third set of cutting parameters is 8.375%.
- (4) Comparison of experimental and predicted cutting time: in the prediction of cutting time, the average magnitude of error between the actual value and the predicted value for the first set of cutting parameters is 12.19%, this for the second set of cutting parameters is 10.4458%, and this of the third set of cutting parameters is 8.014%.

## Nomenclature

V:	Cutting speed (m/min)
VB:	Tool wear (mm)
Ap:	Cutting depth (mm)
H:	Cutting thickness (fixed value: 0.1 mm)
Ci:	Diameter of throwaway tool (fixed value: 12 mm)
T:	Cutting time (min)
Fz:	Feed per tooth (mm/tooth)
SR:	Surface roughness (Ra, $\mu\text{m}$ )
a1, a2, b1, b2, c1, and c2:	Constant values
A, B:	Influence factors

### The experimental results of tool wear (mm)

fz_1,	Experimental results of feed per tooth
fz_2, ..., fz_n:	(mm/tooth)
SR_1,	Experimental results of surface roughness
SR_2, ..., SR_n:	(Ra, $\mu\text{m}$ ).

## Data Availability

The raw/processed data required to reproduce these findings cannot be shared at this time as the data also form part of an ongoing study.

## Conflicts of Interest

The authors declare that they have no conflicts of interest.

## References

- [1] F. Campbell, "Chapter 6-super alloys," in *Manufacturing Technology for Aerospace Structural Materials*, F. Campbell, Ed., pp. 211–272, Elsevier Science, Oxford, MI, USA, 2006.
- [2] E. O. Ezugwu, Z. M. Wanga, and R. Machado, "The machinability of nickel-based alloys: a review," *Journal of Materials Processing Technology*, vol. 86, no. 1–3, pp. 1–16, 1999.
- [3] R. Polvorosa, A. Suárez, L. N. L. de Lacalle, I. Cerrillo, A. Wretland, and F. Veiga, "Tool wear on nickel alloys with different coolant pressures: comparison of Alloy 718 and Waspaloy," *Journal of Manufacturing Processes*, vol. 26, pp. 44–56, 2017.
- [4] S. Hanasaki, J. Fujiwara, M. Touge, Y. Hasegawa, and K. Uehara, "Tool wear of coated tools when machining a high nickel alloy," *CIRP Annals*, vol. 39, no. 1, pp. 77–80, 1990.
- [5] M. Nalbant, A. Altın, and H. Gökkaya, "The effect of cutting speed and cutting tool geometry on machinability properties of nickel-base Inconel 718 super alloys," *Materials & Design*, vol. 28, no. 4, pp. 1334–1338, 2007.
- [6] A. Jawaid, S. Koksai, and S. Sharif, "Cutting performance and wear characteristics of PVD coated and uncoated carbide tools in face milling Inconel 718 aerospace alloy," *Journal of Materials Processing Technology*, vol. 116, no. 1, pp. 2–9, 2001.
- [7] M. Zetek, I. Česáková, and V. Švarc, "Increasing cutting tool life when machining Inconel 718," *Procedia Engineering*, vol. 69, pp. 1115–1124, 2014.
- [8] S. H. Wang and Y. L. Su, *Tribology Potential of DLC Coated Milling Inserts*, National Cheng Kung University the Degree of Master, Tainan, Taiwan, 1998.

- [9] C. T. Sims and W. Hagel, *The Superalloys*, Wiley-Interscience, New York, NY, USA, 1972.
- [10] H. Bhadeshia, *Nickel Based Super-alloys*, University Of Cambridge, Cambridge, England, 2002.
- [11] H.-Y. Bor, *A Study on the Elevated Temperature Brittleness and Fracture Mechanism of Mar-M247 Superalloy*, National Chiao Tung University the Degree of Master, Hsinchu, Taiwan, 1998.
- [12] B. H. Kear, J. M. O'blak, and A. F. Giami, "Stacking faults in gamma prime precipitation hardened nickel-base alloys," *Metallurgical Transactions*, vol. 1, pp. 2477–2486, 1970.
- [13] C. M. Hong, Z. H. Yao, M. C. Zhang, J. X. Dong, and Y. F. Zhang, "The thermodynamic calculation of Waspaloy alloy carbide and  $\gamma'$  phase precipitation law," *Journal of University of Science and Technology Beijing*, vol. 30, no. 9, pp. 1018–1023, 2008.
- [14] A. S. Abdulhakim and A. C. Okafor, "Effects of geometric parameters of wavy-edge bull-nose helical end-mill on cutting force prediction in end-milling of Inconel 718 under MQL cooling strategy," *Journal of Manufacturing Processes*, vol. 23, pp. 102–114, 2016.
- [15] S. H. Chen, "Study on application of grey prediction model in superalloy MAR-247 machining," *Advances in Materials Science and Engineering*, vol. 2015, Article ID 704143, 10 pages, 2015.
- [16] S. H. Chen and Yu-L. Ho, "Lifespan of super-alloy Waspaloy cutting tools," *Heliyon*, vol. 5, no. 4, Article ID e01388, 2018.
- [17] P. Nieslony, G. M. Krolczyk, S. Wojciechowski, R. Chudy, K. Zak, and R. W. Maruda, "Surface quality and topographic inspection of variable compliance part after precise turning," *Applied Surface Science*, vol. 434, pp. 91–101, 2018.
- [18] R. W. Maruda, G. M. Krolczyk, S. Wojciechowski, K. Zak, W. Habrat, and P. Nieslony, "Effects of extreme pressure and anti-wear additives on surface topography and tool wear during MQCL turning of AISI 1045 steel," *Journal of Mechanical Science and Technology*, vol. 32, no. 4, pp. 1585–1591, 2018.
- [19] S. E. Oraby and D. R. Hayhurst, "Tool life determination based on the measurement of wear and tool force ratio variation," *International Journal of Machine Tools and Manufacture*, vol. 44, no. 12-13, pp. 1261–1269, 2004.
- [20] C. A. Yu and S. H. Chen, *The Prediction of Tool Life in Milling Waspaloy*, NCUT the Degree of Master, Taichung, Taiwan, 2016.